

**INTEGRATION OF REDOX-REGULATED SIGNALING AND METABOLISM IN
HEAD AND NECK CANCER**

BY

JADE T. MOORE

A Dissertation Submitted to the Graduate Faculty of

WAKE FOREST UNIVERSITY GRADUATE SCHOOL OF ARTS AND SCIENCES

In Partial Fulfillment of the Requirements

for the Degree of

DOCTOR OF PHILOSOPHY

in Molecular Medicine and Translational Science

May, 2017

Winston-Salem, North Carolina

Approved By:

Cristina M. Furdul, Ph.D., Advisor

Glen Marrs, Ph.D., Chair

Anthony J. Molina, Ph.D.

John S. Parks, Ph.D.

Mercedes Porosnicu, MD

ACKNOWLEDGEMENTS

Thanks to Cristina for being my advisor and mentor for the past four years. Her dedicated interest in science has helped me grow as a scientist, taught me patience beyond the bench, and taught me science is always a party. Joining Cristina's lab provided me with a faux advisor in Allen. I appreciate Allen for always keeping me on my toes and challenging me to question every piece of data until thoroughly proven otherwise. I am also thankful to postdocs past and present, including Nidhi B., Julie R.H., Nelmi D.B., Elsa S.L., and Xiaofei C., who have all added a positive perspective to research, engaging conversations and helped me grow as a scientist. Thanks to everyone on my committee who has assisted me in achieving my research goals from protocols to imaging, building interpersonal skills beyond the bench and guiding me to completion of my Ph.D.

Thanks to my parents and parents-in-law for supporting me through the last five years with phone calls, emails, holidays and creating positive memories. Special thanks to my immediate and extended family of friends and loved ones who have supported me for many years and helped me create lasting memories over the last five years. I must also acknowledge two individuals, Brittany E. and Jessica S., who have been on this ride with me from our first drink at Burke Street to our endless study nights and Thursday night dance parties to weddings and everything else in between.

The most thanks goes to my husband, Jeremy, and dog, Monty, who have been there with me from applying to graduate school through the program and more than anyone has endured the worse and best days with me. I am forever grateful for their continuous love, support and belief in my ability to achieve my goals.

You are the company you keep, 'for he that walketh with wise men shall be wise: but a companion of fools shall be destroyed'.

TABLE OF CONTENTS

| | Page |
|--|-----------|
| LIST OF FIGURES..... | vi |
| LIST OF ABBREVIATIONS..... | xi |
| ABSTRACT..... | xx |
| CHAPTER 1..... | 1 |
| INTRODUCTION | |
| Head and Neck Squamous Cell Carcinoma..... | 1 |
| Treatment of Head and Neck Squamous Cell Carcinoma..... | 6 |
| Redox Regulation by Endogenous and Irradiation-Induced Reactive Oxygen Species..... | 17 |
| Therapeutic Resistance Mechanisms in Head and Neck Squamous Cell Carcinoma..... | 25 |
| Preclinical Models of Radiation Resistance in Head and Neck Squamous Cell Carcinoma | 32 |
| Bioinformatics and Computational Modeling in Head and Neck Squamous Cell Carcinoma..... | 36 |
| Literature Cited..... | 39 |

| | |
|---|------------|
| CHAPTER 2..... | 65 |
| Broad Phenotypic Changes Associated with Gain of Radiation Resistance in Head and Neck Squamous Cell Cancer. | |
| Published in <i>Antioxidant Redox Signaling</i> – 2014 July, 21(2):221 – 236 | |
| CHAPTER 3..... | 102 |
| Energy Metabolism in a Matched Model of Radiation Resistance for Head and Neck Squamous Cell Cancer | |
| Published in <i>Radiation Research</i> – 2015 March, 183(3) – 291 – 304 | |
| CHAPTER 4..... | 140 |
| Integration of Signaling and Metabolism in a Head and Neck Cancer Cell Model of Radiation Resistance using COSM ^{RO} | |
| <i>In preparation to be submitted</i> | |
| CHAPTER 5..... | 197 |
| Unpublished Results | |
| Investigation of Lipid Raft Signaling through Proteomics Analysis..... | 197 |
| Lipid Raft Modulation in other Radioresistant Head and Neck Cell Lines..... | 200 |
| Mitochondrial Reactive Oxygen Species Cycling..... | 203 |
| CHAPTER 6..... | 207 |

DISCUSSION

| | |
|---|-----|
| Head and Neck Cancer Matched Model..... | 207 |
| Epidermal Growth Factor Signaling..... | 208 |
| Energy Metabolism..... | 210 |
| Redox Metabolism..... | 215 |
| Cell Survival..... | 217 |
| Innovation..... | 219 |
| Future Direction..... | 220 |
| Literature Cited..... | 224 |

APPENDIX

| | |
|---|------------|
| Chapter II Appendix Figures and Tables..... | 229 |
| Chapter IV Appendix Figures and Tables..... | 251 |
| CURRICULUM VITAE..... | 281 |

LIST OF FIGURES

CHAPTER 1

Figure 1: Current therapeutic options for Head and Neck Squamous Cell Carcinoma patients.

Figure 2: Endogenous sources of reactive oxygen species and cellular defense against reactive oxygen species formation.

CHAPTER 2

Figure 1: rSCC-61 exhibits increased resistance to radiation and increased sensitivity to Erlotinib in comparison to SCC-61.

Figure 2: Summary of quantitative proteomic analysis of SCC-61 and rSCC-61.

Figure 3: Functional network analysis—Human Protein Reference Database (HPRD) interaction subnetworks.

Figure 4: rSCC-61 cells are associated with mesenchymal-to-epithelial transition (MET).

Figure 5: The stoichiometry of LDH-A and LDH-B determines the pyruvate/lactate equilibrium.

Figure 6: rSCC-61 have decreased ROS and reduced DNA damage.

Figure 7: Western blot and immunofluorescence analysis of γ H2AX.

Figure 8: Lipid rafts and response to radiation and EGFR inhibition.

CHAPTER 3

Figure 1: Glucose uptake and dependence on cell growth on glucose metabolism in SCC-61 and rSCC-61 cells.

Figure 2: Contribution of PPP to cellular proliferation in SCC-61 and rSCC-61.

Figure 3: Glutamine utilization in SCC-61 and rSCC-61 cells.

Figure 4: rSCC-61 has decreased OXPHOS capabilities.

Figure 5: Fatty acid synthase is overexpressed and correlated to radioresistance in rSCC-61.

Figure 6: Inhibition of FASN decreases rSCC-61 survival.

Figure 7: Summary overview of the differential carbohydrate and lipid metabolism in SCC-61 and rSCC-61 cells.

CHAPTER 4

Figure 1: Mathematical approach to integrate ROS-mediated effects on signaling and metabolism contributing to radiation resistance in HNSCC.

Figure 2: Inferred Network

Figure 3: Inferred Pathway Predicts Differential Regulation of AKT2 and AKT1/3 in Radiation Resistant Cells.

Figure 4: Network Predicts Flux through Pentose Phosphate Pathway to Increase NADPH in Radiation Resistant Cells.

Figure 5: Cysteine and Glutathione Biosynthesis Critical for Cell Survival in Radiation Resistant Cells.

Figure 6: Inferred Pathway Connects AMPK Activity to Fatty Acids and Cholesterol Metabolism.

Figure 7: Cholesterol regulation in lipid raft formation and response to radiation.

CHAPTER 5

Figure 1: Identifying lipid raft proteins.

Figure 2: Lipid Raft Formation and Response to Irradiation.

Figure 3: Mitochondrial ROS Cycling.

CHAPTER 6

Figure 1: Central role of reactive oxygen species and cholesterol metabolism in Head and Neck Squamous Cell Carcinoma in response to therapies.

APPENDIX

Supplemental Information for Chapter II

Figure 1: Cellular localization and molecular functions of proteins identified in proteomic analysis.

Figure 2: Functional network analysis-KEGG interaction network.

Table 1: List of calculated values of D_0 , α and β parameters for the clonogenic assays in SCC-61 and rSCC-61.

Table 2: List of proteins with expression ratio <0.01 in rSCC-61 and SCC-61 generated by the SILAC proteomics analysis.

Table 3: List of the top upregulated proteins in rSCC-61 generated by the SILAC proteomics analysis.

Table 4: Fold change in a subset of proteins predicted to decrease cell death and apoptosis in rSCC-61 obtained from the SILAC proteomics analysis.

Table 5A: Fold change in a subset of proteins involved in DNA replication and base-excision repair obtained from the SILAC proteomics analysis.

Table 5B: Fold change in a subset of proteins involved in ECM-receptor interaction obtained from the SILAC proteomics analysis.

Table 5C: Fold change in a subset of proteins involved in regulation of cell cycle obtained from the SILAC proteomics analysis.

Table 5D: Fold change in a subset of proteins involved in focal adhesion obtained from the SILAC proteomics analysis.

Table 5E: Fold change in a subset of proteins involved in regulation of actin cytoskeleton obtained from the SILAC proteomics analysis.

Table 6: Fold change in proteins predicted to decrease ROS in rSCC-61 obtained from the SILAC proteomics analysis.

Table 7: Fold change in expression of subset of proteins predicted to decrease DNA damage in rSCC-61 obtained from the SILAC proteomics analysis.

Table 8: Primers and PCR conditions for Vimentin and E-cadherin.

Supplemental Information for Chapter IV

Figure 1: Metabolomics Analysis.

Figure 2: Redox Proteomics.

Figure 3: Targeted Western Blot Analysis.

Figure 4: Generic Network.

Figure 5: Signaling Sub-Network Represented as a Boolean Network.

Figure 6: Cholesterol Synthesis and Trafficking.

Table 1: Screened redox-sensitive proteins from redox proteomics data.

Table 2: Redox-regulated proteins.

Table 3: Validation for the prediction of our optimized specific pathway network on five interested proteins.

Dataset 1: Redox proteomics.

Dataset 2: Signaling Proteins.

Dataset 3: Signaling reactions.

Dataset 4: Metabolites.

Dataset 5: Metabolic reactions.

LIST OF ABBREVIATIONS

| | |
|--------|--|
| 2D | two dimensional |
| 2-DG | 2-deoxy-D-glucose |
| 3D | three dimensional |
| 5-FU | 5-fluorouracil |
| 6AN | 6-aminonicotinamide |
| ABC | ATP-binding cassette |
| AC | acid ceramidase |
| ACC | acetyl-CoA carboxylase |
| ADCC | antibody-dependent cellular cytotoxicity |
| ADH | alcohol dehydrogenase |
| AhpC | alkyl hydroperoxide reductase subunit C |
| AKT | protein kinase B |
| AMFR | autocrine motility factor receptor |
| AMPK | AMP-activated protein kinase |
| ATM | ataxia telangiectasia mutated |
| ATP | adenosine triphosphate |
| BAX | Bcl-2-associated X protein |
| BCA | bicinchoninic acid |
| Bcl-2 | b-cell lymphoma 2 |
| Bcl-xL | b-cell lymphoma extra large |
| BP1 | biotin-1,3-cyclopentanedione |
| BSA | bovine serum albumin |
| CAMMK | calmodulin-dependent protein kinase |
| CasP | Cascade Propagation subtyping |

| | |
|--------------------|--|
| CAT | catalase |
| CBS | cystathionine β -synthase |
| CD | cluster differentiation |
| ChiP | chromatin immunoprecipitation |
| CONCERT | CONcomitant chemotherapy and/or EGFR inhibition with radiation therapy |
| COSM ^{ro} | constraint-based systemic modeling of redox regulation |
| CRT | chemoradiotherapy |
| Cs | cesium |
| CS | cigarette smoke |
| CSC | cancer stem cell |
| CSE | cystathionine γ -lyase |
| CT | computerized tomography |
| CT-B | cholera toxin subunit B |
| CTLA-4 | cytotoxic T-lymphocyte associated protein 4 |
| CTP | cytidine triphosphate |
| CTR | copper transporter |
| CYP | cytochrome p450 |
| Cys | cysteine |
| DAHANCA | Danish head and neck cancer group |
| DAVID | Database for Annotation, Visualization, and Integrated Discovery |
| DCF | dichlorofluorescein |
| DDR | DNA damage response |
| DHFR | dihydrofolate reductase |
| DMEM | Dulbecco's modified Eagle medium |
| DNA | deoxyribonucleic acid |
| DSBs | double strand breaks |

| | |
|----------|---|
| DTT | dithiothreitol |
| DUT | deoxyuridine 5'-triphosphate nucleotidohydrolase |
| ECAR | extracellular acidification rate |
| ECM | extracellular matrix |
| EDTA | ethylenediaminetetraacetic acid |
| EEF2 | eukaryotic translation elongation factor 2 |
| EGF | epidermal growth factor |
| EGFR | epidermal growth factor receptor |
| EGFRvIII | truncated EGFR-variant 3 |
| EMT | epithelial-to-mesenchymal transition |
| EORTC | European organization for research and treatment of cancer |
| ERCC-1 | excision repair cross-complementation group 1 |
| ERK | extracellular signal regulated kinases |
| ETC | electron transfer chain |
| EXTREME | Erbix in first-line treatment of recurrent or metastatic head and neck cancer |
| F6P | fructose-6-phosphate |
| FAs | fatty acids |
| FAO | fatty acid oxidation |
| FASN | fatty acid synthase |
| FBS | fetal bovine serum |
| FCCP | trifluorocarbonylcyanidephenylhydrazine |
| FDA | Food and Drug Administration |
| FTIs | farnesyl transferase inhibitors |
| G3P | glyceraldehyde-3-phosphate |
| G6PD | glucose-6-phosphate dehydrogenase |

| | |
|-------------------------------|---|
| GAPDH | glyceraldehyde 3-phosphate dehydrogenase |
| GCL | glutamate-cysteine ligase |
| GCLC | glutamate-cysteine ligase catalytic subunit |
| GLUT1 | glucose transporter 1 |
| GPX | glutathione peroxidase |
| GRX | glutaredoxin |
| GSH | glutathione |
| GSK3 β | glycogen synthase kinase 3 beta |
| GSR | glutathione reductase |
| GSS | glutathione synthetase |
| GSSG | oxidized glutathione |
| GST | glutathione S-transferase |
| H ₂ O | water |
| H ₂ O ₂ | hydrogen peroxide |
| HBSS | Hanks' balanced salt solution |
| HCA | heterocyclic amines |
| HIFs | hypoxia inducible factors |
| HMGCR | 3-hydroxy-3-methylglutaryl-CoA reductase |
| HMR | human metabolic reaction |
| HNC | head and neck cancer |
| HNE | 4-hydroxy-2-noneal |
| HNSCC | head and neck squamous cell carcinoma |
| HPA | Human Protein Atlas |
| HPLC | high-performance liquid chromatography |
| HPRD | Human Protein Reference Database |
| HPV | human papilloma virus |

| | |
|--------|---|
| HPV- | HPV-negative |
| HPV+ | HPV-positive |
| HR | homologous recombination |
| HRP | horse radish peroxidase |
| HSP | heat shock protein |
| IDH | isocitrate dehydrogenase |
| IgG1 | immunoglobulin G1 |
| IL | interleukin |
| INSIG | insulin-induced gene 1 protein |
| IPA | Ingenuity Pathway Analysis |
| IR | ionizing radiation |
| JNK | Jun amino-terminal kinase |
| KEGG | Kyoto Encyclopedia of Genes and Genomes |
| KOH | potassium hydroxide |
| KRT | keratins |
| LDH | lactate dehydrogenase |
| LDL | low density lipoprotein |
| LDLR | low density lipoprotein receptor |
| LOOH | lipid hydroperoxide |
| mAbs | monoclonal antibodies |
| MDA | malondialdehyde |
| MEHGAN | Cetuximab in squamous cell carcinoma of the head and neck |
| MET | mesenchymal-to-epithelial transition |
| MIP | mixed integer programming |
| MitoPQ | MitoParaquat |
| MnSOD | manganese superoxide dismutase |

| | |
|------------------------------|--|
| MRI | magnetic resonance imaging |
| mRNA | messenger RNA |
| MTHFD | C-1-tetrahydrofolate synthase |
| mTOR | mechanistic target of rapamycin |
| MTT | 3-(4,5-dimethylthiazol-2-yl)-2, 5-diphenyltetrazolium bromide |
| MTX | methotrexate |
| M β CD | methyl- β -cyclodextrin |
| NAD | nicotinamide adenine dinucleotide |
| NADPH | nicotinamide adenine dinucleotide phosphate |
| NCI | national cancer institute |
| NCR | nucleus-to-cytoplasm ratio |
| NF- κ B | nuclear factor kappa light chain enhancer of activated B cells |
| NFR2 | nuclear factor erythroid 2 related factor 2 |
| NHEJ | non-homologous end joining |
| NIH | national institute of health |
| NMR | nuclear magnetic resonance |
| NOX | NADPH oxidase |
| O ₂ | oxygen |
| O ₂ ^{•-} | superoxide |
| OCR | oxygen consumption rate |
| OCT | organic cation transporter |
| ODE | ordinary differential equation |
| OH | hydroxyl radical |
| ONOO- | peroxynitrite |
| OS | overall survival |
| OXPHOS | oxidative phosphorylation |

| | |
|-----------------|----------------------------------|
| PAH | polycyclic aromatic hydrocarbons |
| PARP | poly(ADP-ribose) polymerase |
| P-ATP | p-type ATPase |
| PBS | phosphate buffered saline |
| PCR | polymerase chain reaction |
| PD-1 | programmed cell death protein 1 |
| PD-L1/2 | programmed death-ligand 1 or 2 |
| PDXs | patient derived xenografts |
| PEG | polyethylene glycol |
| PET | positron emission tomography |
| PFS | progression free survival |
| PGD | 6-phosphogluconate dehydrogenase |
| PGM | phosphoglycerate mutase |
| PHA | polyhydroxyalkanoates |
| PI3K | phosphoinositide 3-kinase |
| PKM2 | pyruvate kinase isozyme M1/M2 |
| pO ₂ | oxygen partial pressure |
| PPP | pentose phosphate pathway |
| PRX | peroxiredoxins |
| PTEN | phosphatase and tensin homolog |
| PTPs | protein tyrosine phosphatases |
| PUFAs | polyunsaturated fatty acids |
| R5P | ribose-5-phosphate |
| Rb | retinoblastoma |
| redox | reduction and oxidation |
| RIPA | radioimmunoprecipitation assay |

| | |
|-------------------|--|
| RNA | ribonucleic acid |
| ROS | reactive oxygen species |
| RPIA | ribulose-5-phosphate |
| rSCC-61 | radiation resistant squamous cell carcinoma 61 |
| RT | radiation therapy |
| RTOG | radiation therapy oncology group |
| Ru5P | ribulose-5-phosphate |
| SAS | sulfasalazine |
| SCC | squamous cell carcinoma |
| SDS | sodium dodecyl sulfate |
| SHMT | serine hydroxymethyltransferase |
| SILAC | stable isotope labeling with amino acids in cell culture |
| siRNA | small interfering ribonucleic acid |
| SO ₂ H | Sulfinic acid |
| SO ₃ H | sulfonic acid |
| SOD | superoxide dismutase |
| SOH | sulfenic acid |
| SQS | squalene synthase |
| SRB | sulforhodamine B |
| SREBP | sterol regulatory element-binding protein |
| SRX | sulfiredoxin |
| SSBs | single strand breaks |
| STAT3 | signal transducer and activator of transcription 3 |
| STR | short tandem repeats |
| TCA | trichloroacetic acid |
| TCA cycle | citric acid cycle |

| | |
|-------|---|
| TCGA | the cancer genome atlas |
| TCPA | the cancer proteome atlas |
| TIGAR | TP53-inducible glycolysis and apoptosis regulator |
| TKIs | tyrosine kinase inhibitors |
| TP53 | tumor protein p53 |
| TR | thioredoxin reductase |
| Tregs | regulatory T cells |
| US | United States |
| VEGF | vascular endothelial growth factor |
| VIP | variable importance in the projection |
| WT | wild type |
| xCT | Cystine transporter |
| XP | Xerodermic pigmentosum |

ABSTRACT

Moore, Jade

INTEGRATION OF REDOX-REGULATED SIGNALING AND METABOLISM IN HEAD AND NECK CANCER

Dissertation under the direction of Cristina M. Furdui, Ph.D., Associate Professor Molecular
Medicine & Translational Science

Head and Neck Squamous Cell Carcinoma (HNSCC) is a complex disease characterized by genetic and metabolic changes. Radiation therapy alone or combined with systemic chemotherapy is widely used for treatment of HNSCC as definitive treatment or as adjuvant treatment after surgery. Resistance to radiation therapy significantly impacts the ability to achieve local and regional remission to ultimately cure cancer. The disease heterogeneity, invasiveness and resistance to radiation constitute significant roadblocks for treatment and patients' quality of life despite improvements in treatment modality over the last two decades and the emergence of new therapies. The research presented in this dissertation focuses on better understanding the underlying molecular mechanisms that elicit resistance to radiation treatment and drug-targeted therapy in HNSCC. To systematically study the molecular mechanisms contributing to radiation resistance, we developed a matched model of radiation resistance (SCC-61/rSCC-61 system) in HNSCC. We initially characterized differences between SCC-61 and rSCC-61 using quantitative mass spectrometry and complementary validation assays. We identified broad changes in signaling and metabolic pathways indicating mesenchymal-to-epithelial transition, increased DNA repair, and increased expression of antioxidant proteins (e.g. PRX, GSTpi). To further integrate signaling and metabolism in HNSCC, we developed a constraint-based computational model (COSM^{ro}) which combines multiple 'omics' (i.e. proteomics, redox proteomics, metabolomics, lipidomics) data and takes into consideration the relationships among signaling proteins, metabolic flux distribution, and the thermodynamic and stoichiometric characteristics of metabolites in the network. The application of COSM^{ro} to the matched model of radiation

resistance demonstrates that multiple signaling and metabolic pathways converge to produce the radiation resistance phenotype. The findings highlight potential radiation resistance signatures including (1) decreased ROS and cholesterol levels, (2) increased flux through pentose phosphate pathway for increased production of NADPH, ribonucleotides and endogenous fatty acids, and (3) increased glutathione production, which together with increased NADPH and increased expression of ROS metabolizing enzymes, maintain decreased ROS and coordinate redox regulation of signaling and metabolic pathways. The rSCC-61/SCC-61 system provides opportunity for future investigations of redox-regulated mechanisms of response to radiation and drug-targeted therapy with potential for translation to clinic.

CHAPTER 1 – INTRODUCTION

Head and Neck Cancer

Cancer is a global public health problem and the second leading cause of death in the United States (Siegel 2017). As of 2012, there were an estimated 1.689 million new cases and approximately 600,000 deaths in the US alone (Dobrossy 2005). Head and neck squamous cell carcinoma (HNSCC) makes up 55,000 and 12,000 of estimated new cases and deaths annually (Dobrossy 2005). HNSCC is a broad term encompassing malignancies of the squamous epithelium in the upper aerodigestive tract including the oral cavity (i.e. lip, base of tongue, floor of mouth and palate), the pharynx (i.e. oro-, hypo-, and nasopharynx), the larynx and other sites (i.e. salivary glands, thyroid) (Dobrossy 2005). About 40% of head and neck tumors occur in the oral cavity with the remaining 15, 20, and 25% arising in the pharynx, larynx and remaining sites (Dobrossy 2005). Thus, HNSCC in this region can destroy vital structures necessary for survival such as the larynx or tongue and reduce function of organs involved in breathing, voice, speech, swallowing, taste, smell and hearing. Due to the location of tumor development and ability of the tumor to easily advance locally, sometimes it is difficult to determine the exact stage at which a patient presents with HNSCC. The three primary parameters to determine stage of development include (1) primary tumor size, (2) degree to which lymph nodes are involved in tumor development, and (3) absence or presence of distant metastases. Most patients present with loco-regionally advanced disease or stage III and IV cancers that have spread to lymph nodes on one side or both sides of the neck. Cure is targeted with a multi-modality approach involving surgery and/or a combination of radiotherapy and chemotherapy. Multifactorial interactions between environment and genetic mutations play a critical role in the development and complexities of staging HNSCC. Key factors associated with HNSCC are due to tobacco smoking, alcohol consumption, and genetic factors. More recently, the role of human papilloma virus (HPV) emerged as an important etiological factor especially for head and neck cancer localized in the oropharynx (Dobrossy 2005).

Tobacco Smoke It is estimated that 74% of the HNSCC can be attributed to smoking alone (Dobrossy 2005). Studies show that each puff of smoke contains 5,000 carcinogenic compounds such as nitrosamines, aromatic amines, polycyclic aromatic hydrocarbons (PAH), and heterocyclic amines (Derry 2013, Galbiatti 2013), that produce 10^{15} free radical molecules in the gas phase (Goldkorn 2014). These compounds enter the alimentary tract and are metabolized either by the cytochrome p450 (CYP) super family of proteins (CYP1A1, CYP1A2, CYP2E1, CYP2A6) leading to deoxyribonucleic acid (DNA) adduct formation or by glutathione *S*-transferases (GSTs) (GSTM1, GSTT1, GSTP1) leading to excretion (Derry 2013). Exposure to cigarette smoke (CS) increases oxidative damage rate by 30–50% (Loft 1996), and generation of 100–800 μM hydrogen peroxide (H_2O_2) per cigarette drives the oxidative stress response. CS exposure can induce cell death via ceramide generation and induce proliferation via epidermal growth factor receptor (EGFR) activation (Goldkorn 2010). For example, cells exposed to endogenous or exogenous H_2O_2 can induce (a) ceramide generation and apoptosis in a dose- and time-dependent manner (Laventiadou 2001), (b) non-canonical phosphorylation of EGFR resulting in impaired EGFR degradation by E3 ubiquitin ligase, and (c) caveolae-mediated trafficking to the perinuclear region where it causes downstream activation of protein kinase B (PKB or Akt) and extracellular signal regulated kinases (ERK) 1/2 survival and proliferation pathways (Goldkorn 2010). EGFR is expressed in all cells of epithelial origin but is 50-80% overexpressed in squamous cell carcinomas including HNSCC (Hirsch 2003). Prolonged exposure to CS leads to increased oxidized glutathione (GSSG) thereby activating inflammatory pathways involving nuclear factor kappa-light-chain-enhancer of activated B cells (NF- κ B) and nuclear factor-erythroid 2-related factor 2 (NRF2) (Derry 2013, Flora 2008). These result in increased gene expression and release of cytokines (Goldkorn 2014) through mechanisms involving epigenetic modifications (Derry 2013) amongst others.

Alcohol consumption Tobacco smoking and alcohol consumption in conjunction may increase HNSCC risk (Dobrossy 2005). Excessive alcohol consumption increases mucosa

permeability to toxins and reduces epithelial thickness leading to damage of vital structures and tumor formation as alcoholic beverages contain potential carcinogens or precursors such as ethanol, nitrosamine *N*-nitrosodiethylamine and polyhydroxyalkanoates (PHA) (Malik 2016). Ethanol can be metabolized to carcinogenic acetaldehyde by alcohol dehydrogenase (ADH) in the mitochondria or nicotinamide adenine dinucleotide phosphate (NADPH) dependent CYP2E1 in the microsomal ethanol oxidizing system, and be converted to fatty acid ethyl esters by fatty acid ethyl ester synthase (Dobrossy 2005). Catalase (CAT) can also oxidize ethanol to acetaldehyde in peroxisomes in the presence of H₂O₂. Both acetaldehyde and reactive oxygen species (ROS) interact with proteins and nucleic acids to form stable and unstable adducts, interfering with cellular functions such as DNA synthesis and repair (Dobrossy 2005).

Genetic Factors Variant alleles of genes involved in carcinogen metabolism, alcohol and folate metabolism, and DNA repair and cell cycle control are thought to play a role in development of HNSCC tumors. Most meta-analyses have focused on carcinogen metabolism enzymes such as CYP super family of enzymes, which activate tobacco carcinogens and oxidize alcohol, and GSTs, which are responsible for metabolizing xenobiotics (Albano 1991, Landi 1994). For example, several studies have demonstrated an increased risk of HNSCC in individuals with an isoleucine to valine substitution at codon 105 in GSTP1 associated with increased DNA oxidative products (Katoh 1999, Matthias 1998, Park 1999). Presence of the null GSTM μ 1 genotype versus the positive genotype also increases the risk for HNSCC (Cheng 1999, Coutelle 1997, Hong 2000, Park 1999). Genetic variants in DNA repair gene, xeroderma pigmentosum (XP) complementary group D (XPD), and cell cycle control gene, *TP53*, are also common in HNSCC and increase risk by 83 and 75% (Birgander 1996, Huang 2005, Kietthubthew 2006, Lu 2007, Majumder 2007, Sturgis 2000, Ramachandran 2006). Individuals with homozygous variant genotype of XPD have suboptimal DNA repair capacity (Qiao 2002). The G to C polymorphism in codon 72 of exon 4 results in an arginine to proline substitution in *TP53*. Though both variants are wild-type (WT), the proline/proline genotype has been

demonstrated to be less effective in suppressing cellular transformation and showed a higher risk for HNSCC than individuals with the arginine/arginine genotype (Birgander 1996, Hamel 2000, Nagpal 2002). Relations between polymorphisms in other genes, such as folate metabolic and extracellular degradation enzymes (e.g. methylenetetrahydrofolate reductase, serine hydroxymethyltransferase (SHMT), TNF-related apoptosis-inducing ligand and immune response factors (e.g. interleukin (IL)-8, toll-like receptor 10), have been investigated. However, the number of such studies is limited, and difficult to draw definite conclusions.

Human papillomavirus The incidence of HNSCC with tobacco and excessive alcohol consumption etiology is decreasing, while there is an increase in incidence of HNSCC in younger white individuals and non-smokers. This cancer has been linked to infection with high-risk serotypes of human papillomavirus (HPV). Human papillomaviruses are small non-enveloped DNA viruses that can infect mucosal (α -HPV) or cutaneous (β -HPV) epithelial cells. The virus generates lesions in the form of warts and papilloma and uses the host-cell DNA replication machinery to support viral replication (Giroglou 2001, Rampias 2014). A subgroup of HPVs known as “high-risk” HPVs cause precancerous lesions which will develop into cancer many years after the original infection. HPV⁺ subtype 16 accounts for 87% of all HPV⁺ tumors. The HPV viral genes are divided into “early” genes (E1-7) and “late” genes (L1, L2). Two “early” genes (E6, E7) are considered oncoproteins. HPV-E6 protein induces ubiquitin-mediated degradation of the TP53 tumor suppressor protein by binding directly to E6-associated protein, a specific ubiquitin-ligase for TP53 degradation. HPV-E7 protein destabilizes the retinoblastoma (Rb) tumor suppressor protein and members of the Rb family required for cellular DNA synthesis and cell cycle progression (e.g. cyclin A and E, DNA polymerase α , p21) (Boyer 1996, Dyson 1989, Gonzalez 2001, Munger 1989) and targets Rb and family members for degradation (Boyer 1996). TP53 and Rb-independent mechanisms of oncogenesis have also been described for E6 and E7 proteins (e.g. E6 binding to PDZ domain containing proteins with tumor suppressor activity (Gewin 2001, Veldman 2001). Together, E6 and E7 oncoproteins modulate many cellular

signaling pathways including Wnt/ β -catenin and PI3K/Akt/mTOR (mTOR - mechanistic target of rapamycin). Currently, HPV⁺ patients receive the same standard of care treatment, discussed later, as HPV⁻ patients despite better response to therapy, improved locoregional control and better overall survival. These patients will outlive their cancer and have to endure long-term side effects associated with aggressive radiotherapy. For example, studies have shown that stroke or occlusive carotid artery disease occurs within 10–12 years after cancer treatment in HPV⁺ patients (Travis 2012, Wang 2011). Thus, it is vital to modify current treatment modalities for HPV⁺ patients to improve their quality of life.

Symptoms and Detection Because HNSCC is a broad term covering the entire upper aerodigestive tract, patients can present with various precancerous conditions and lesions depending on the tumor location within specific areas of the head and neck. For example, oral cavity cancers have symptoms associated with white or red patches on gums, tongue or lining of mouth while pharynx symptoms are more commonly associated with trouble breathing, speaking or pain swallowing. The most common symptoms presented by HNSCC patients include chronic sore throat, difficulty swallowing, a change or hoarseness in the voice and a lump or sore that does not heal. The disease is often detected at locally advanced stages. In addition, smokers have a high risk of second primary tumors resulting in an overall poor prognosis for patients. However, early detection and appropriate treatment increases cure rate to 80% and results in improved quality of life (Mager 2005, Silverman Jr 2001). Visual examination of mouth in asymptomatic patients is the primary screening method followed by biopsy and histopathological analysis (Guerra 2016). Diagnostic evaluations in symptomatic patients may include indirect pharyngoscopy and laryngoscopy, panendoscopy, or others including computerized tomography (CT), magnetic resonance imaging (MRI) or positron emission tomography (PET) scan, and finally biopsy. There are currently no biomarkers for early HNSCC detection. Preclinical studies have been done to identify possible markers for early cancer detection, however, results remain exploratory. Two combinatory serum biomarkers were proposed to predict early stages of

HNSCC: (1) EGFR, cyclin D1, and squamous cell carcinoma antigen, or (2) IL-8, choline, pipercolinic acid, L-phenylalanine and S-carboxymethyl-L-cysteine (Guerra 2016). Serum antioxidants such as CAT and glutathione (GSH), and sex hormone, prolactin have also shown promise in predicting the early stages of HNSCC. DNA methylation patterns appear gradually due to environmental influences (i.e. tobacco and alcohol use), and were thus considered as potential source of biomarkers. Epigenetic modifications are essential for regulation of cell cycle control (i.e. p16, p14), DNA repair, and apoptosis. Longitudinal studies reported higher hypermethylation of p16 in precancerous lesions leads to increased tumor progression compared to hypomethylation of p16 in precancerous lesions leading to tumor regression. Therefore, hypermethylation of p16 promoter has also been proposed as a prognostic biomarker to determine if a patient will have increased (i.e. hypomethylation p16) or decreased (i.e. hypermethylation p16) progression free survival (PFS) of oral and oropharyngeal cancers (Cao 2009, Hall GL 2008). Thus, these data point to dynamic alterations of methylation patterns occurring during disease progression as potential biomarkers.

Treatment of Head and Neck Cancer

About 50-60% of HNSCC patients present with loco-regionally advanced cancer. Lack of biomarkers contributes to the late diagnosis and aggressive treatment of head and neck tumors causing patients to develop serious functional changes in their upper aerodigestive tract that can affect their overall quality of life including mental health, appearance, employment, social life and family living.

Standard of Care The treatment plan for patients with HNSCC is determined from three parameters including (1) location of tumor, (2) stage of cancer, and (3) person's age and overall performance status (Ribeiro 2001). Surgery followed by fractionated radiotherapy is the standard of care for resectable primary and secondary malignancy with the goal of obtaining negative or tumor-free surgical margins (Haque 2006). However, negative surgical margins often results in

removal of normal tissue causing impairment of critical functions, such as chewing and swallowing, and an adverse quality of life (Haque 2006). In most cases, positive surgical margins (i.e. residual cancer remains) are obtained to preserve vital organs, such as carotid artery. As a result, surgery is followed up with aggressive radiation and chemotherapy to kill remaining tumor cells. Patients generally undergo fractionated doses of 2 Gy each in five weekly sessions for 5 ½-6 weeks for a total dose of 60–66 Gy (Bernier 2004) (**Fig. 1A**). Surgery, followed by radiation, can also increase the adverse side effects and overall quality of life in some cases leading to permanent loss of voice, tongue and neck deformities and scars and paralysis of cranial nerves (Haque 2006). Postoperative follow-up is every two months for the first six months, every four months for the next two years then every six months for the following two years and annually thereafter (Bernier 2004). Patients with unresectable tumors receive radiotherapy alone or in combination with chemotherapy (Galbiatti 2013). This treatment also comes with many side effects including soreness in mouth or throat, dry mouth, trouble swallowing, changes in taste, nausea or swelling in the gums, throat or neck (Jham 2006).

Biomarkers to assess tumor characteristics pre- and post-treatment are critical in making therapeutic choices for patients. HPV status is most often used to stratify patients but is not enough to determine course of treatment. The most common biomarkers to assess tumor characteristics post-treatment include (a) DNA damage (e.g. γ H2AX), (b) changes in tumor microenvironment (e.g. hypoxia) and (c) differences in cancer stem cells (CSC) versus non-CSC (e.g. CD133⁺, CD44⁺) (Chiou 2008). Currently, γ H2AX, a histone protein phosphorylated after DNA double strand breaks (DSBs), is the most frequently used biomarker to assess DNA damage post-treatment (Koch 2013). While accumulation of γ H2AX foci correlates with increased radiosensitivity, γ H2AX alone is unable to consistently predict treatment response due to high foci background (Yaromina 2012). However, γ H2AX foci colocalization in hypoxic tumor areas is able to predict local tumor control (Menegakis 2011). Ku80, a DNA repair protein, overexpression predicts locoregional failure and death following RT. Opportunities also exist to

identify tumor radiation resistance/sensitivity biomarkers to escalate/de-escalate radiation dose and to spare normal tissue toxicity (Baumann 2016). For example, overexpression of anti-apoptotic proteins Bcl-2 and Bcl-xl is correlated with chemotherapy and radiation resistance because inhibition of apoptosis favors DNA repair (Kumar 2008). Increased intake of dietary antioxidants (e.g. Vitamin D, carotenoids) before beginning of treatment was associated with better PFS. Interestingly, those antioxidants are decreased after radiotherapy partly due to increased utilization of antioxidants to quench radiation-induced free radicals. The difference in the antioxidant reserve pre- and post-treatment could potentially be used to predict response to radiation exposure.

Multimodality Treatment About 60% of patients present at locoregionally advanced stages with about 10% having distant metastases to pulmonary, bone, liver, skin, mediastinum and bone marrow (Ferlito 2001, Galbiatti 2013, Shin 2013). Standard of care for these patients is associated with a three year overall survival (OS) of 30–50% and locoregional recurrences or distant metastases occur in 40–60% of these patients (Adelstein 2003). Currently, cisplatin in combination with radiotherapy is the most commonly used treatment given at 100 mg/m² every 3 weeks during the course of radiation treatment for a total dose of 300 mg/m² (Bar-Ad 2014). Cisplatin is transported into the cell by copper transporters (CTR1/CTR2) or organic cation transporter (OCT), and it can be exported from the cell via membrane transporters, chemically neutralized by binding to sulfhydryl groups in proteins or can nonspecifically react with proteins, ribonucleic acid (RNA) or DNA (Hall MD 2008). The binding of cisplatin to DNA results in platinum adducts, such as N7-d(GpG) and N7-d(ApG), causing kinking of the DNA (Li 2000) and preventing cells from replicating until DNA damage is repaired or the cell dies (Amable 2016) (**Fig. 1B**). Other platinum agents such as taxane, 5-fluorouracil (5-FU), methotrexate (MTX) and ifosfamide have been tested alone or in various combinations in clinical trials for metastatic disease and are being explored in preclinical settings as potential definitive curative therapeutics. Only cisplatin with 5-FU has shown higher response rates and decreased side effects

than cisplatin alone but it did not increase OS (Bar-Ad 2014, Shin 2013). The major side effects associated with high dose cisplatin are adverse and include peripheral neuropathy, hearing loss, renal dysfunction, marked nausea and vomiting (Bar-Ad 2014). It is important to note that taxane-based induction chemotherapy such as docetaxel before radiotherapy or chemoradiotherapy has been shown to reduce risk of distant metastases compared with cisplatin with 5-FU regimen (Hitt 2005, Lorch 2011, Vermorken 2007). Systemic chemoradiotherapy has also been tested in a postoperative setting for high-risk positive surgical margin (e.g. nodal extracapsular spread, lymphovascular invasion, perineural invasion and positive lymph nodes) patients (Bernier 2005, Cooper 2004). The EORTC 22931 clinical trial, comparing postoperative chemoradiotherapy versus radiotherapy alone, showed significant reduction in risk of locoregional recurrence and OS with chemoradiotherapy. As of now the optimal timetable for multimodality treatment in managing loco-regionally advanced HNSCC remains concurrent chemotherapy with cisplatin and radiotherapy.

EGFR messenger RNA (mRNA) and protein is overexpressed in 90% and 40% of HNSCC patients (Bei 2004, Ongkeko 2005) making EGFR a possible target to help improve locally advanced HNSCC (Galbiatti 2013). It is a transmembrane glycoprotein that includes a tyrosine kinase enzyme in its intracellular domain (Dobrossy 2005) and is a critical signaling hub for tumor cell growth, angiogenesis and invasion. Currently, Cetuximab (Erbiximab®) is the only targeted therapy approved by US Food and Drug Administration (FDA) to be used in combination with radiotherapy for locally advanced HNSCC (Bonner 2006). Cetuximab is a recombinant immunoglobulin G1 (IgG1) monoclonal antibody directed at the extracellular domain of EGFR to block ligand-mediated activation of the EGFR pathway, inhibition of downstream signaling, and stimulate antibody-dependent cellular cytotoxicity (ADCC) (Taylor 2009) (**Fig. 1C**). Cetuximab combined with radiotherapy improves PFS from 14.9 to 24.4 months and median OS rates from 20.3 to 54.0 months but does not decrease rates of distant metastases in patients with locally advanced HNSCC compared to RT alone (Ang 2011, Bar-Ad 2014).

Cetuximab is also FDA approved for use as a single agent or in combination with chemotherapy in metastatic HNSCC. Cetuximab combined with platinum and 5-FU was tested in the EXTREME clinical trial. The study showed improved outcome in all end points including (a) increased PFS from 2.7 to 4.2 months, (b) increased OS from 8.0 to 9.2 months, (c) one year survival rate from 31.7 to 38.6%, and (Siegel 2017) locoregional control from 60 to 80% with no compromise in quality of life (Shin 2013).

Emerging Therapy Despite decades of research, the best treatment modality yielding significant efficacy with reduced side effects, organ function and overall quality of life has yet to be determined. Most research has focused on identifying radiation sensitizing therapies with decreased side effects. There are many new emerging therapies on the horizon including monoclonal antibodies (mAbs), tyrosine kinase inhibitors (TKIs), and immunotherapies.

Monoclonal antibodies Other mAbs, similar to Cetuximab such as Nimotuzumab, Zalutumumab, Duligotuzumab and Panitumumab, have proved promising in preclinical research. However, when tested for first-line treatment of recurrent and metastatic HNSCC, they were unable to demonstrate improved locoregional control and OS compared to Cetuximab (Chapman 2016, Eriksen 2014/DAHANCA19, Giralt 2015/CONCERT2,). A successful phase II clinical trial with Nimotuzumab led to drug approval for advanced HNSCC in China and currently has orphan status in Europe and US for glioblastoma. Compared to Cetuximab, it has milder side effects resulting in weaker allergic reactions (Guo 2015, Lu 2016). Duligotuzumab is a dual-action humanized IgG1 antibody against EGFR and erbB3 (also known as HER3) that blocks ligand binding, inhibits signaling from all ligand-dependent HER dimers, and elicits ADCC. MEHGAN clinical trial proved dual inhibition was not associated with improved efficacy compared to Cetuximab even when biomarkers were used to predict response and help with patient selection (Fayette 2016). One significant take away from the study is that HPV⁻ patients had higher response rates to Cetuximab and Duligotuzumab than HPV⁺ patients (Fayette 2016). A new promising mAb currently in clinical trial for HNSCC by Symphogen is Sym004. It is a 1:1

mixture of two synergistic full-length anti-EGFR antibodies (992, 1024) which bind to two separate non-overlapping epitopes on EGFR (Pedersen 2010). The mechanism of action is similar to Cetuximab but unique in its ability to induce EGFR internalization and degradation by cross-linking receptors (Skartved 2011). A phase II clinical trial tested weekly infusions of Sym004 as a palliative care in incurable, recurrent and/or metastatic HNSCC patients with acquired resistance to anti-EGFR mAb treatment. Out of 26 patients, 12% were progression free after 6 months, 31% had decreased tumor size, and 50% of patients had stable disease (Machiels 2015). Symphogen also has Sym013, a pan-HER mAb, in preclinical pipeline that induces simultaneous downregulation of all three targets, prevents receptor upregulation and has demonstrated *in vivo* ability to inhibit tumor cell proliferation in HNSCC and ability to inhibit Cetuximab-resistant HNSCC cell lines in combination with radiation (Francis 2006). In general, newly developed EGFR mAbs combined with chemoradiotherapy or radiotherapy have not improved oncologic outcomes or demonstrated superiority over chemoradiotherapy but promising attempts at enhancement continue.

Tyrosine kinase inhibitors EGFR TKIs target the receptor catalytic domain. Overall, lack of survival benefit for EGFR TKIs alone or in combination with systemic chemoradiotherapy or radiotherapy alone in clinical trials have had difficulty obtaining FDA approval for HNSCC. Some associated challenges with EGFR TKIs are (1) EGFR mutations in the catalytic domain such as T790M, (2) too toxic in combination with chemotherapeutics, (3) increased potency inhibits WT-EGFR leading to increased toxicities and clinical dose limitations (Cheng 2016), and (4) lack of biomarkers to identify which patients will respond favorably to EGFR TKIs. For example, Erlotinib (Tarceva®) and Gefitinib (Iressa®) clinical trials have shown modest single agent response rate of only 4% and 10%, in recurrent or metastatic HNSCC. However, in combination with cisplatin, the response improved to 21% but the combination of cisplatin, radiation and Erlotinib has not been well tolerated in HNSCC clinical trials (Siu 2007, Soulieres 2004).

Second generation EGFR TKIs, such as Afatinib (Giotrif®), have shown increased cellular potency against EGFR (Engelman 2007, Miller 2012). Afatinib is an irreversible pan-EGFR TKI targeting a reactive cysteine in the active site of EGFR (**Fig. 1C**). Afatinib has been compared to both MTX and Cetuximab and is the only TKI that has demonstrated comparable activity to Cetuximab in recurrent or metastatic HNSCC patients with a response rate twice that of other TKIs (Seiwert 2014). Afatinib demonstrated increased disease control and median PFS of 38.9% and 15.85 weeks, respectively, compared to 18.8% and 13.9 weeks by Cetuximab (Seiwert 2014) in platinum-resistant and recurrent or metastatic HNSCC patients. The LUX-Head and Neck 1 phase III clinical trial compared oral dose of Afatinib (40 mg/day) to MTX infusion (40 mg/m², once weekly) in recurrent or metastatic HNSCC patients who progressed after first-line platinum-based chemotherapy. Patients who received Afatinib had significantly delayed deterioration of global health status, pain and swallowing compared to MTX. Other TKIs targeting vascular endothelial growth factor (VEGF) and mTOR are being studied but have not provided any evidence of significant therapeutic efficacy in HNSCC patients. Tools to better predict patient response to EGFR inhibitors will provide new opportunities for increased efficacy and newly identified mutations in the EGFR catalytic domain that confer sensitivity to EGFR TKIs promise to open new doors to use EGFR TKIs in the future.

Immunotherapy HNSCC is considered an immunosuppressive disease because of its ability to (a) deregulates the cytokine profile (e.g. chemokine and VEGF overexpression), (b) impair immune effector cells functions (e.g. upregulating IL-6), and (c) cause abnormalities in tumor-associated antigen presentation (Ferris 2006). The interplay between the tumor and the host's immune system has become an increased area of research for HNSCC therapeutics. Tumor progression or relapse is believed to be associated with the inability of the immune system to eliminate cancer (Schoenfeld 2015, Varilla 2013). Immune checkpoints are critical in regulating T cell response and co-inhibitory molecules are new exciting targets of inhibition for HNSCC. The two most common targets include (1) programmed cell death protein 1 (PD-1 or cluster

differentiation (CD) 279) and (2) cytotoxic T-lymphocyte-associated protein 4 (CTLA-4 or CD152). PD-1 is expressed on T cells and pro-B cells and binds its ligands, programmed death-ligand 1 or 2 (PD-L1 or PD-L2), to prevent T cell activation by promoting apoptosis in antigen specific T cells and reducing apoptosis of regulatory T cells (Tregs) (Pardoll 2012). CTLA-4 is a surface protein receptor expressed by activated T cells and Tregs. CTLA-4 transmits an inhibitory signal to T cells by outcompeting CD28, which sends a stimulatory signal to T cells, binding to CD80 and CD86 antigen presenting cells (Linsley 1991). However, the exact mechanism of action in T cells remains elusive and controversial. Blocking PD-1 and CTLA-4 prevents PD-1 ligand binding and releases stimulatory receptors to bind T cells resulting in an immune response against tumors (**Fig. 1D**).

There are currently two promising PD-1 inhibitors for HNSCC, including Pembrolizumab and Nivolumab, that have shown efficacy irrespective of tumor PD-L1 expression (> 1%) or HPV status (Ferris 2016). Pembrolizumab (Keytruda ®) is a mAb against PD-1 containing a high-affinity mouse anti-PD-1 derived variable region attached to a human IgG4 molecule with an engineered Fc region for stabilization (Philips 2015). The initial clinical trial to determine safety and clinical activity of Pembrolizumab for treatment of recurrent or metastatic HNSCC demonstrated its efficacy in tumors and had limited toxicity and drug-related adverse events with 63% of patients tolerating treatment (KEYNOTE-012, Seiwert 2016). Success of the clinical trial led to accelerated approval of Pembrolizumab by the FDA for treatment of recurrent or metastatic HNSCC following platinum-resistance. Full approval is contingent upon KEYNOTE-040 results, which is evaluating Pembrolizumab efficacy as a monotherapy against standard treatment options. Nivolumab (Opdivo ®) is also a promising human IgG4 mAb against PD-1 that has recently been FDA approved. In Checkmate141 clinical trial in recurrent HNSCC patients whose disease progressed within six months of platinum-based chemotherapy, Nivolumab outperformed the standard single-agent in all categories including (a) response rate up to 13.3% from 9.9%, (b) increased PFS at 6 months from 9.9 to 19.7%, (c) increased median OS from 5.1 to 6.5 months,

(d) 1-year survival rate increased from 16.6 to 36%, and (e) treatment related adverse events (i.e. fatigue, nausea, rash, decreased appetite and pruritus) occurred only 13.1% of the time in Nivolumab group versus 35.1% in standard-therapy group (Ferris 2016 NCT02105636). The success of Pembrolizumab and Nivolumab has led to a cascade of clinical trials testing their efficacy in HNSCC (KEYNOTE-048, KEYNOTE-055, NCT02641093, NCT02609503, NCT02586207, NCT02280209; CheckMate358, NCT021248450, ECHO-24, NCT02335918, NCT02426892).

As of now, no CTLA-4 mAbs have FDA approval for HNSCC treatment due to their severe toxicity profile with potentially life-threatening adverse events such as colitis (Economopoulou 2016). However, there are several open-label dose escalation clinical trials with Durvalumab (anti-PDL-1 mAb), and Ipilimumab or Tremelimumab against CTLA-4. Preclinical data also suggests there is increased efficacy when PD-1 and CTLA-4 immunotherapies are combined because they regulate T cell induction and maturation at different phases. There are three major ongoing clinical trials testing combinatory inhibition of PD-1 and CTLA-4 including (1) Durvalumab plus Tremelimumab as first-line treatment for advanced HNSCC (KESTREL), (2) Durvalumab plus Tremelimumab in platinum-resistant patients (EAGLE), and (3) combination of two mAbs in patients with PD-L1 negative platinum resistance disease (CONDOR) (Economopoulou 2016).

HPV Vaccine It is important to note with the increase of HPV⁺ HNSCC patients, HPV preventative vaccines have become a focus of cervical cancer and HNSCC research. Currently, Gardasil® and Cervarix® are the only two commercially available HPV vaccines and their role in HPV-related HNSCC is being evaluated (Herrero 2013). HPV preventative vaccines act by eliciting virus-neutralizing antibody responses that prevent initial infection (Venuti 2015). DNA vaccines, produce non-living antigens to induce T-helper and B-cell immunity, and peptide vaccines, incorporate amino acid sequences that are synthesized to form an immunogenic peptide

molecule presenting the specific epitope to bind onto HLA, are being explored in clinical trial as well (NCT00010110).

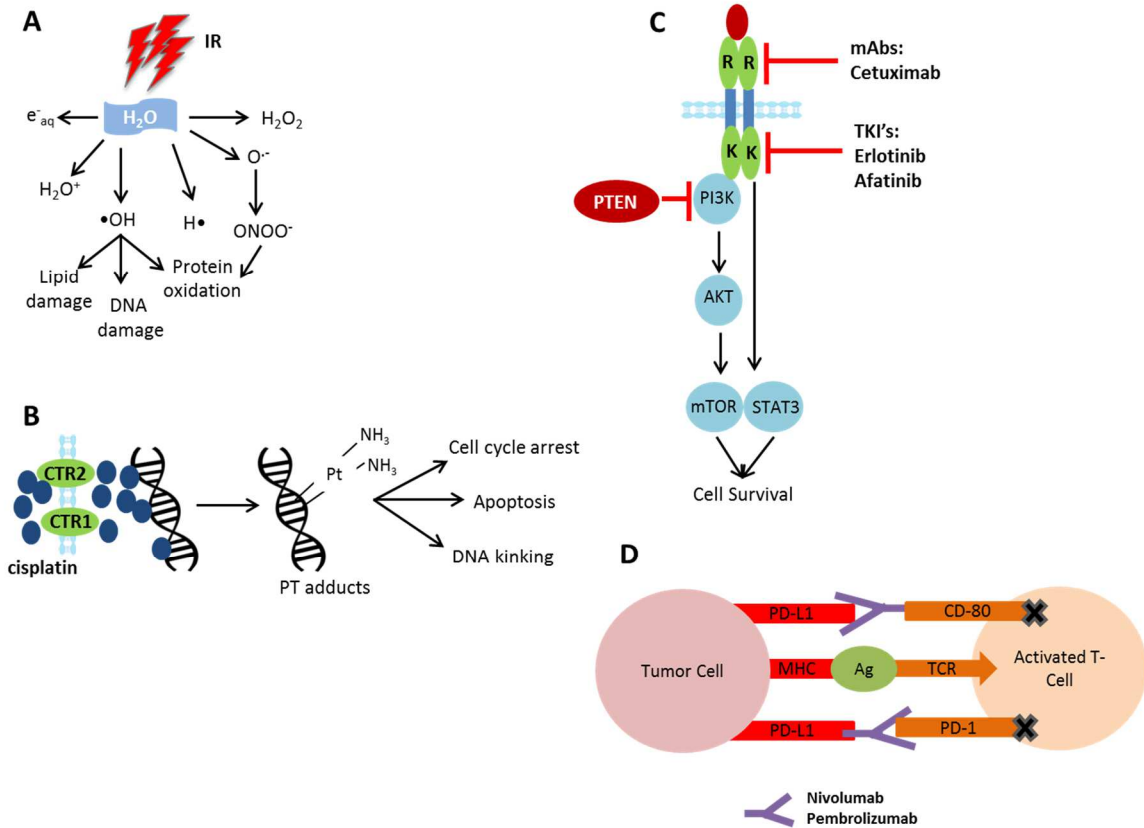


FIG. 1. Current therapeutic options for Head and Neck Squamous Cell Carcinoma patients. **A.** Radiation therapy leads to reactive oxygen species formation and ultimately lipid damage, DNA damage, and protein oxidation. **B.** Chemotherapy, with cisplatin, leads to platinum adduct formation and ultimately cell cycle arrest, apoptosis, and DNA kinking. **C.** Epidermal growth factor receptor inhibition at the extracellular domain by monoclonal antibody, Cetuximab, or inhibition at the catalytic domain by tyrosine kinase inhibitors, Erlotinib and Afatinib leading to PI3K/Akt/mTOR and STAT3 abrogation and reduced cell survival. **D.** Immunotherapies, Nivolumab and Pembrolizumab, inhibit tumor cell immune signaling by activating T-cell activity leading to immune response against tumors.

Redox Regulation by Endogenous and IR-induced ROS

Oxygen (O₂) homeostasis is the balance between oxidants and antioxidants which are maintained through a series of reduction and oxidation (redox) reactions. It is estimated that 1–3% of the O₂ consumed in the body is converted to ROS (Sohal 1996). The three major species of ROS, including superoxide (O₂^{•-}), H₂O₂ and hydroxyl radical (·OH), are also metabolic byproducts generated by mitochondria and membrane bound NADPH oxidase (NOX) (McCord 2000). At low or moderate concentrations, these reactions are critical for normal physiological cellular processes (Valko 2006). For example, oxidative burst within the cell generates low concentrations of ROS, which can activate EGFR leading to recruitment of accessory proteins and activation of Ras and downstream signaling (Johnson 2002, Li 2003). High concentrations of ROS can cause oxidative stress disrupting redox homeostasis, normal cellular processes and cause damage to cellular lipids, proteins and DNA (Droge 2002). Important pathophysiological functions controlled by redox signaling include immune response, inflammation, and epithelial to mesenchymal transition (Valko 2006).

Mitochondrial Metabolism Mitochondria consume 80–90% of the body's O₂ and are the powerhouse of the cell driving the production of adenosine triphosphate (ATP) through the electron transport chain (ETC) and regulating ceramide-induced apoptotic cell death (Reisz 2014). Five complexes make up the ETC and undergo a series of redox reactions where O₂ serves as the final electron acceptor and is reduced to water (H₂O). The transfer of electrons is coupled with ejection of H⁺ creating a proton gradient. During energy transduction, 1-3% of electrons leak from mitochondrial complex I and III leading to reduction of O₂ to form O₂^{•-} and generate H₂O₂ by the activity of manganese superoxide dismutase (MnSOD), an antioxidant located exclusively in the mitochondria (Boveris 1976, Cadenas 2000) (**Fig. 2**). High levels of MnSOD suppress cell growth in early tumor development, but as tumors become more advanced, invasive and metastatic, MnSOD overexpression is correlated with poor prognosis in patients (Liu 1997). For example, MnSOD overexpression has been shown to indirectly activate matrix metalloproteinase

family of proteins to initiate cellular remodeling processes through elevated H_2O_2 levels (Wenk 1999). Superoxide in its anion form is too strongly charged to cross the inner mitochondrial membrane but $\text{O}_2^{\bullet-}$ made within the intermembrane space can escape to the cytoplasm through voltage-dependent anion channels and be converted to H_2O_2 where it can initiate intracellular signaling and release of cytochrome C to activate apoptotic cell death (Han 2003, Klimova 2008, Valko 2007). Hydrogen peroxide generated in the mitochondria is metabolized to H_2O by peroxiredoxin (PRX) 3 which is the first line of protection against H_2O_2 generated from the ETC (Noh 2009). During the catalytic cycle, PRX3 is oxidized by H_2O_2 and reduced by mitochondrial thioredoxin 2 (TRX2) and glutaredoxin 2 (GRX2) (Chae 1999, Hanschmann 2010). The active peroxidatic Cys residue, which typically cycles through sulfenic, disulfide with the resolving cysteine and reduced states, can be hyperoxidized to sulfinic acid ($-\text{SO}_2\text{H}$) or sulfonic acid ($-\text{SO}_3\text{H}$) during oxidative stress leading to PRX3 inactivation. The activity of PRX3 and other hyperoxidized 2-Cys PRXs can be recovered by sulfiredoxin (SRX) in the presence of ATP (Bae 2009, Noh 2009). PRX3 levels are elevated in all cancers except malignant mesothelioma and protect tumors against H_2O_2 dependent apoptosis due to enhanced elimination of H_2O_2 and decreased rates of mitochondrial membrane collapse (Noh 2009, Nonn 2003).

Nicotinamide adenine dinucleotide phosphate oxidase NOX is composed of two membrane-bound components, gp91phox and p22phox, which make up the catalytic core subunit. Five cytosolic proteins, including p67phox, p47phox, p40phox, RAC1 and RAC2, migrate to the cell membrane to activate the catalytic core (Babior 1999) after respiratory burst (DeCoursey 2005). Activation of this enzyme generates $\text{O}_2^{\bullet-}$ at the plasma membrane where it is released into the extracellular space, generates H_2O_2 through the action of Cu/Zn-SOD which then can transverse back through the plasma membrane into the cytosol. During respiratory burst, both, $\text{O}_2^{\bullet-}$ and NO^{\bullet} are produced and may react together to produce peroxynitrite anion (ONOO^-) (Valko 2007). Peroxynitrite is a potent oxidizing agent that can cause DNA fragmentation and lipid oxidation (Carr 2000).

IR-induced ROS There are two types of radiation including ionizing and non-ionizing that can emit high-energy particles capable of displacing atomic electrons facilitating a chain reaction of electron ejections. The major types of ionizing irradiation (IR) are alpha and beta particles, X-rays and gamma rays and all are used for therapeutic purposes capable of causing cellular damage (Lawrence 2008). The adult human body is composed of 60% of H₂O which absorbs energetic radiations causing both excitations and ionizations reactions leading to ROS production. Gamma irradiation of cellular H₂O rapidly generates ROS including ·OH and ionized water (H₂O⁺) as well as hydrogen radical (H[·]) and hydrated electrons (e⁻_{aq}) (**Fig. 1A**). Within one picosecond, O₂^{·-} and H₂O₂ are formed as secondary ROS products and this chemical cascade generates cell-damaging molecules (Singh 1983). It is estimated that individuals are exposed to about 2.4 x 10⁻³ Gy low dose non-IR from natural sources, such as ultraviolet rays and electromagnetic radiation (e.g. radio waves and microwaves), each year and that amount is increased in developing nations (Karagas 2002, Khong 2013, Zhang 2012). These free radicals attack macromolecules, induce mitochondrial ROS production, and upregulate NOX expression (Azzam 2012, Collins-Underwood 2008, Du 2009).

DNA damage IR causes DNA damage either by directly depositing energy into DNA molecules or by creating free radicals that interact with DNA strands (Mahaney 2009, Reisz 2013). The damaging events include the deleterious alterations of bases and sugars, cross-link formation, single and double strand breaks (SSBs) and DNA clustering (Duncan 2009, Thompson 2012). Hydroxyl radicals are considered the most abundant and destructive to nucleic acid molecules because they react with purine nucleobase at carbons 4, 5 and 8 generating reactive adduct radicals, such as 8-oxodG, a hallmark for oxidative DNA damage (Dizdaroglu 2012). After hydroxyl radical adducts are formed, these species react with O₂ producing peroxy radicals, hydroperoxides, ring-opening events and ring-contraction (Reisz 2013). While base damage and DNA SSBs occur more frequently, DNA DSBs are the most toxic lesions by which IR-induced damage and cell death occur. The ROS mediated DNA damage leads to the activation of the cell

cycle checkpoint response that initiates the DNA damage response (DDR) signaling (Solier 2009). The DDR central regulator protein, ataxia telangiectasia mutated (ATM) serine/threonine kinase, is recruited by the Mre11-Rad50-Nbs1 DNA binding complex and phosphorylates downstream components such as H2AX, BRCA1/2, ATM/ATR, checkpoint kinases 1/2 and poly(ADP-ribose) polymerase (Reisz 2013, Solier 2009). Repair of DNA double strand breaks is carried out by non-homologous end joining (NHEJ) and homologous recombination (HR) (Wu 2007) with NHEJ repairing most DNA DSBs because HR can only occur during late S and G2 phases of the cell cycle (Branzei 2008). NHEJ is an error prone repair that can result in loss of significant amounts of genetic material. Immediate recognition and repair of DNA damage post-IR is critical for normal cells because failure to repair may result in cell death or an accumulation of mutations and genomic instability (Helleday 2008).

Lipid modification Radiation also induces peroxidation of polyunsaturated fatty acids (PUFAs), such as linoleic and arachidonic acids, leading to an increase in membrane permeability, disruption of ion gradients, and altered activity of membrane-associated proteins (Corre 2010). PUFA's are oxidized to either lipid hydroperoxides (LOOH) or fragmented to small molecule reactive carbonyls (e.g. malondialdehyde (MDA), acrolein, and 4-hydroxy-2-noneal (HNE)). MDA and HNE have been shown to persist long enough intracellularly to modify proteins, nucleic acids and other molecules (Chung 1996, Petersen 2004). With respect to nucleic acid modification, MDA can react with deoxyguanosine residues while HNE can react with deoxyadenosine and deoxycytidine to yield adducts that can cause G:C to T:A transversions in the *TP53* gene (Brooks 1997, Seitz 2007). At moderate levels, LOOH is reduced by glutathione peroxidases (GPXs) and thioredoxin reductase (TR) to LOH and H₂O (Ursini 1987). Persistent or high levels of LOOH induce global damage to cell membrane and cause cell death by apoptosis and necrosis (Girotti 1998).

Protein modification Proteins can also be modified by ROS either directly (e.g. amino acid oxidation, oxidative cleavage of protein backbone or amino acid side chain) or indirectly through

lipid peroxidation (e.g. HNE reacting with nucleophilic cysteine residues on proteins) (Madian 2010). With more than 35 types of oxidative protein modifications (e.g. protein tyrosine nitration, S-thiolation and –nitrosylation), protein oxidative damage can alter protein structure, enzyme activity, susceptibility to aggregation and proteolysis, and uptake by cells ultimately impacting cellular signaling and metabolism (Schmidt-Ullrich 2003). Most IR-induced protein modifications are irreparable and critically affect protein stability. Reversible oxidation of amino acids in critical signaling molecules, such as kinases and phosphatases, can lead to amplification or dampening of signaling pathways. For example, EGFR has a critical cysteine (Cys) 797 in its catalytic site that when oxidized enhances its tyrosine kinase activity (Seo 2009). This site is also the target of the EGFR inhibitor Afatinib, described above. Overexpression of EGFR and HER3 in HNSCC correlates with elevated H₂O₂ levels and may suggest a need for thiol-targeted irreversible inhibitors. Under moderate oxidative stress, Cys residues can be oxidized to relatively unstable sulfenic acid (-SOH) which can be easily oxidized to -SO₂H and -SO₃H or form mixed disulfides (S-thiolation) between protein thiol groups (R-SH) and low molecular mass thiols such as GSH (Claiborne 1993). Disulfides are readily reduced to thiols by disulfide reductases in coupled reactions such as TRX/TR or GRX/GSH/GSR with NADPH as ultimate provider of reducing equivalents (Holmgren 1989) (GSR - glutathione reductase). Loss of function by disulfide formation is a regulatory mechanism by which proteins mediate the cellular response to oxidative stress. For example, phosphatase and tensin homolog (PTEN), which is mutated in HNSCC, has a catalytic Cys124 residue that when oxidized leads to disulfide bond formation with a neighboring Cys79 residue. The disulfide bond inactivates the phosphatase and protects the cysteine from hyperoxidation enabling re-activation of PTEN by TRX (Leslie 2003).

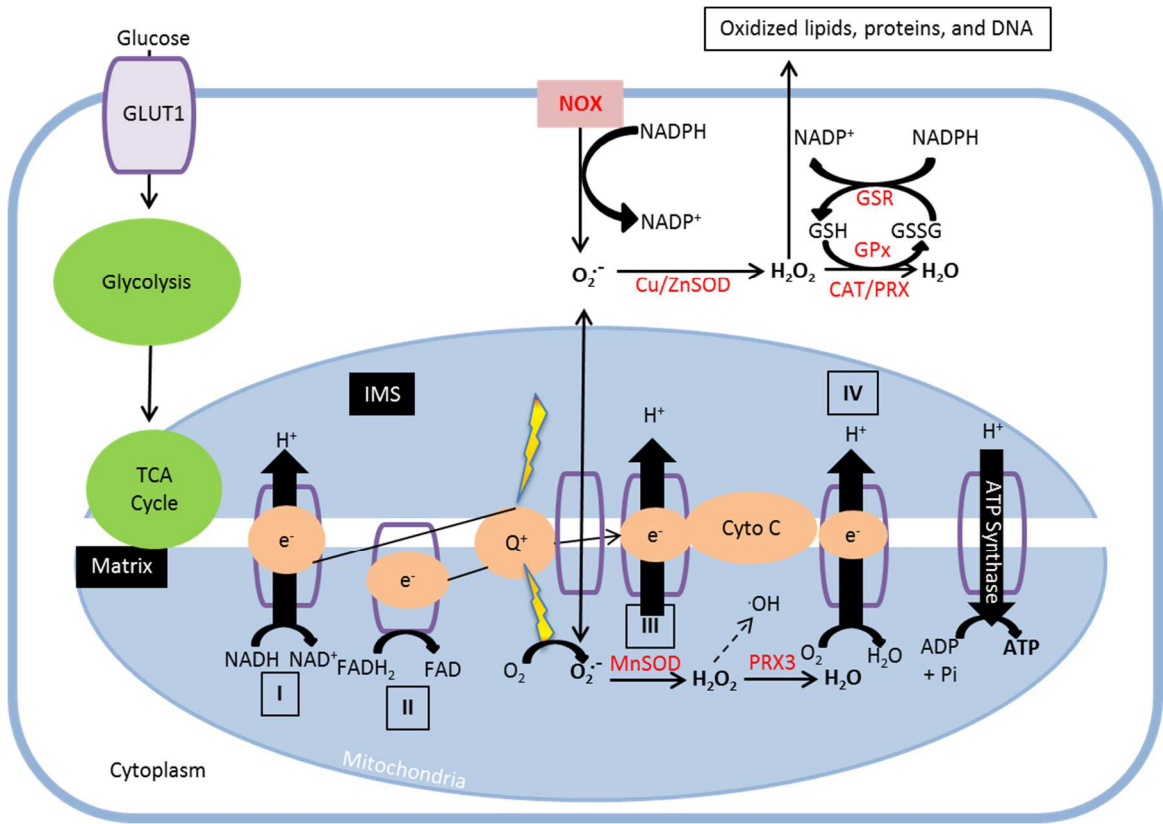


FIG. 2. Endogenous sources of ROS and cellular defense against ROS. GLUT1 = glucose transporter 1; TCA cycle = tricarboxylic acid cycle; NAD/NADH = nicotinamide adenine dinucleotide; FAD/FADH = Flavin adenine dinucleotide; Cu/ZnSOD = copper/zinc superoxide dismutase; MnSOD = manganese superoxide dismutase; PRX = peroxiredoxin; H₂O₂ = hydrogen peroxide; O₂ = oxygen; H₂O = water; ATP = adenosine triphosphate; ADP = adenosine diphosphate; Cyto C = Cytochrome C; CAT = catalase; GPx = glutathione peroxidase; GSR = glutathione reductase; GSH = reduced glutathione; GSSG = oxidized glutathione; NOX = NADPH oxidase; O₂⁻ = superoxide; IMS = intermembrane space; H⁺ = hydrogen; e⁻ = electron;

Cellular defense against ROS The body has developed a complex antioxidant defense mechanism against endogenous and exogenous free radical-induced oxidative stress. When ROS increases, cellular transcription factors, NRF2 and NF- κ B, are activated to help increase production of antioxidants (Bae 2009). Enzymatic (e.g. SOD, PRX, CAT) and non-enzymatic (e.g. GSH, NAD(P)H) antioxidants are some of the most well studied intracellular defenses against oxidative damage (**Fig. 2**). In addition to their antioxidant properties, several of these molecules are increasingly recognized as signaling molecules (Sharma 2012).

GSH is synthesized in the cytosol by sequential reactions catalyzed by glutamate-cysteine ligase (GCL) and glutathione synthetase (GSS). Cysteine availability is the rate-limiting factor in GSH biosynthesis and it can be either synthesized in cells from methionine through the activities of cystathionine β -synthase (CBS) and cystathionine γ -lyase (CSE or GCL) or imported by the cystine/glutamate transporter system (xCT). GSH donates reducing equivalent ($H^+ + e^-$) to molecules such as cysteine disulfides in oxidized proteins to shift their redox state to reduced forms. As a result, GSH becomes oxidized to GSSG which can be either excreted from the cell or reduced by glutathione reductase in an NADPH-dependent manner. In addition, glutathione's protective roles against oxidative stress include (1) acting as a cofactor of detoxifying enzymes, (2) participating in amino acid transport, (3) scavenging hydroxyl radical and singlet oxygen, and (4) regenerating other antioxidants back to their active forms (Masella 2005). The ratio of reduced GSH versus GSSG is an indicative measure of oxidative stress in the cell (Jones 2000). The typical ratio of GSH:GSSG in cells ranges from 100:1 under normal physiological conditions to as low as 1:1 under oxidative stress conditions with the total glutathione concentration (GSH + GSSG) being estimated in the millimolar range.

Thioredoxin is a disulfide-containing redox protein with two redox active Cys that can be oxidized to a disulfide and present in all subcellular organelles (Kern 2005). TRX is reduced to its active state TRX-(SH)₂ by TR in a NADPH-dependent manner (Watson 2004). In addition to its function in the PRX catalytic cycle, TRX plays critical roles in controlling cell growth through

redox regulation of DNA synthesis, cell signaling and apoptosis by regulating transcription factors and kinase cascades. For example, TRX acts as a reducing cofactor for ribonucleotide reductase, the first unique step in DNA synthesis and methionine sulfoxide reductase, which reduces methionine sulfoxide to methionine (Baker 1997). TRX also controls redox-sensitive points during apoptosis including activating caspases by reducing cysteine's (Ueda 1998) and by binding to apoptosis signal-regulated kinase-1 to create an inactive complex which when oxidized is activated and released from TRX (Morita 2001). Overexpression of TRX has been shown to protect cancer cells from oxidative stress-induced apoptosis and provide a survival and growth advantage to tumors (Valko 2006).

Peroxiredoxins, which were briefly introduced above in relation to their antioxidative function, are a family of thiol-dependent peroxidases that contain a conserved Cys residue to serve as the site of oxidation to catalyze the reduction of H_2O_2 , alkyl hydroperoxides and $ONOO^-$. There are six isoforms expressed ubiquitously in mammalian cells, which are broadly classified as typical 2-Cys PRXs (PRX1-4), atypical 2-Cys PRX (PRX5), and 1-Cys PRX (PRX6) (Wood 2003). A more refined classification using active site profiling of PRXs from all species was also reported showing PRXs could be divided into six subfamilies including AhpC/PRX1, PRX6, PRX5, Tpx, BCP/PRXQ, and AhpE based on key residues in their active site including Cp(Cys47), Pro39, Thr43, and Trp81 (Nelson 2011). PRXs have a high-affinity peroxide binding site making it highly sensitive to oxidation by peroxides to provide defense against toxic peroxide build up in the cell (Perkins 2015). They also function as regulators in growth factor signaling and cell cycle progression enabling localized build-up of H_2O_2 while simultaneously keeping peroxide away from targets until the floodgate has opened (Wood 2003). In this case, the transient inactivation of PRXs occurs by either hyperoxidation (Prx-SO_{2/3}) or phosphorylation at tyrosine or threonine residues (Woo 2010). For example, cells stimulated by EGFR can cause PRX1 association with lipid rafts and subsequent inactivation through selective phosphorylation at tyrosine 194 by Src kinase (Wood 2003, Woo 2010). The inactivation allows H_2O_2 to accumulate near lipid rafts and

mediate cell signaling. Therefore, PRXs play a critical role as a sensor and transducer of H₂O₂ signaling in cells and cancer cells, in particular. It has been shown that PRX2 forms a redox relay with transcription factor signal transducer and activator of transcription factor 3 (STAT3) by allowing oxidative equivalents to flow from PRX2 to STAT3 resulting in disulfide-linked oligomers ultimately attenuating transcriptional activity (Sobotta 2015). In HNSCC cells, PRX2 expression increased in cells after treatment with gamma radiation and overexpression blocked cells from radiation-induced cell death (Park 2000). Importantly, STAT3 is also expressed at high levels in HNSCC tumors and current therapeutics such as Cetuximab lacks the ability to abrogate STAT3 activity. Combined inhibition of EGFR and PRX2 activity could provide a path to improve Cetuximab-based therapies.

NADPH is a reducing equivalent critical for the maintenance of the redox status in cancer cells and also necessary for synthesis of nucleic acids and lipids (Vander Heiden 2011). NADPH is generated in cells *via* glucose and glutamine metabolism through the pentose phosphate pathway (PPP) enzyme glucose-6-phosphate dehydrogenase (G6PD), conversion of pyruvate to malate by malic enzymes and conversion of isocitrate to α -ketoglutarate by isocitrate dehydrogenase 1 and 2. Transcription factors NRF2 and TP53 modulate NADPH-production by increasing transcription of NADPH-generating enzymes and upregulating TP53-induced glycolysis and apoptosis regulator (TIGAR) which inhibits glycolysis and promotes PPP (Gorrini 2013). As previously described, NADPH is necessary to maintain reduced GSH and TRX during oxidative stress. Therefore, attenuation of the PPP or downregulation of NADPH production in tumors would reduce or inhibit the cells ability to handle ROS and inhibit critical biosynthetic pathways.

Therapeutic Resistance Mechanisms in HNSCC

Resistance to Radiation in HNSCC Radiation resistance is a major clinical problem for HNSCC patients compounded by origin, location and tumor grade that limits tumor control and affects patient quality of life (Perri 2015). A tumor is considered radioresistant if there is either

lack of tumor response or partial response resulting in recurrence a few weeks after an initial complete response. Resistance to IR in tumors is thought to be intrinsic or acquired through accumulation of genetic mutations and epigenetic changes or selection for increased proliferation and survival. Tumor size, location, grading and stem cell population play a critical role in driving radiation resistance. For example, larger, more differentiated tumors have a worse overall prognosis due to hypoxic cores and differentiated tumors have the ability to accelerate repopulation capacity during radiotherapy (Silva 2007). Rapid repopulation depends on the stem cells ability to activate checkpoints and DNA repair to enhance self-renewal and result in differentiation into heterogeneous cells (Eyler 2008). There are several well-studied mechanisms of resistance to radiation involving redox processes associated with hypoxia, autophagy, intracellular pathway alteration and metabolic reprogramming.

Hypoxia The cytotoxic effects of radiotherapy depend heavily on the presence of molecular O₂ to react with free radicals to produce ROS and irreparable DNA damage. However, under hypoxic conditions, O₂ availability is low due to either reduced perfusion or starvation of necessary O₂ and nutrients (Horsman 2016). It is estimated that HNSCC tumors contain three zones where O₂ tensions fluctuate between anoxic (0% O₂), hypoxic (1% / 7. mm Hg O₂) and normoxic (8% / 60 mm Hg O₂) (Vaupel 1989). A study measuring oxygen partial pressure (pO₂) in twenty-eight HNSCC patients reported an 80% post-radiotherapy PFS correlation with a median oxygen tension of pO₂ > 10 mm Hg (Brizel 1997). Transcription factors, such as hypoxia inducible factors (HIFs), respond to changes in O₂ availability in the cellular environment making them attractive targets in cancer therapeutics. HIFs (HIF-1 α / β , HIF2 α / β , and HIF3 α / β) are a family of highly conserved heterodimer transcription factors composed of an alpha and beta subunit. Under normoxic conditions, HIF's are hydroxylated by dioxygenases, prolyl hydroxylases and asparaginyl hydroxylase, leading to ubiquitination and protein degradation (Hirota 2005). However, under hypoxic conditions, HIFs interact with protein binding partners (e.g. p300/CREB-binding protein acetyltransferases) inducing transcription of > 800 genes

needed for tumor cells to survive in hypoxic environments (Semenza 2007, Semenza 2009). HIF-1 α is considered most active during initial intense short period of hypoxia (i.e. < 0.1% O₂ and < 24 h), while HIF-2 α is active under longer more chronic periods of hypoxia (i.e. < 5% O₂ and > 24 h) (Semenza 2003). Elevated expression of HIF-1 α and HIF-2 α is associated with radiation resistance in HNSCC tumors (Koukourakis 2006). In general, hypoxia contributes to radioresistance in several ways including (a) improving O₂ availability for angiogenesis and neovascularization, (b) aiding in cancer cell invasion and metastasis, (c) reprogramming of cell cycle, and (d) increasing tumor vasculature (Harada 2007, Zeng 2015). For example, HIF-1 α blocks cell cycle regulation at G1/S transition under hypoxic conditions through upregulation of cyclin-dependent kinase inhibitor 1A and inhibition of cell division cycle 25A, and upregulates VEGF causing increased tumor vasculature (Hammer 2007, Moeller 2004). New studies have shown HIF-1 α can also become active even in the presence of O₂ if three conditions are met including (1) decreased activity of dioxygenases (Selak 2005) (2) impaired E3 ubiquitin ligase function (Hirota 2005), and (3) increased transcription and translation initiation of HIF-1 α (Harada 2016).

Methods have been developed to detect levels of hypoxia in patients to determine their response to radiation. Those include measuring endogenous markers (e.g. HIF-1 α , glucose transporters, carbonic anhydrase IX), exogenous markers (e.g. pimonidazole, EF5), immunohistochemical estimates of intercapillary and vascular density, non-invasively using, MRI or PET, and tumor oxygenation levels (Koch 1995, Raleigh 1998). Unfortunately, there are limitations to accurately detecting hypoxia as most exogenous markers can only detect chronic hypoxia and endogenous markers may be upregulated due to stress factors that are not hypoxia related (Bayer 2011). However, PET studies using (¹⁸F) – fluoroazomycin arabinoside (Faza) to measure hypoxia and predict PFS showed that hypoxic tumors had a lower PFS of 60% compared with non-hypoxic tumors PFS of 93% (Serbagi-Vernat 2015). The clinical trial attempts at increasing tumor oxygenation before and during radiotherapy have included red blood cell transfusion,

erythropoietin administration and hyperbaric oxygen treatment but all have ended with conflicting or inconclusive results (Overgaard 2011). Inhibitors against HIFs such as acriflavine, YC-1, endostatin and TNP-470 have poor toxicity profiles and lack increased efficacy (Lee 2009, Lund 2000).

Autophagy Autophagy is the cellular recycling mechanism responsible for degrading dysfunctional cellular organelles in living cells to provide building blocks for metabolites and synthesis of macromolecules as a source of energy. Cell survival or death depends on the severity and length of autophagy (Dalby 2010). During early tumor development, autophagy is anticarcinogenic through removal of damaged mitochondria and protein aggregates (Marino 2007, Mo 2014). For example, short term exposure to arecoline, similar to nicotine, increases ROS and inflammatory cytokines leading to autophagy activation and removal of DNA damage or protein aggregates to prevent head and neck tumor formation. After tumor formation or radiation-induced oxidative stress, autophagy is upregulated and used by the tumor as a survival mechanism (Honscheid 2014). However, the exact mechanism by which autophagy contributes to radiation resistance is unclear. Some studies suggest autophagy is regulated by HIFs to clear ROS-producing damaged organelles and protein aggregates too large for proteasome removal (Zhang 2008). Overall, autophagy seems to have a dual role in cancer development and progression making it a potential therapeutic target and biomarker to determine tumor stage.

Reprogramming of cellular signaling and metabolism Radiation-induced cell death is accompanied by alterations in intracellular pathways primarily involved in DNA repair and cell cycle, proliferation, apoptosis and metabolic reprogramming. These insults can lead to radiation resistance over time. For example, TP53 regulates cell cycle arrest through cyclin-dependent kinase inhibitor 1 stimulation and programmed cell death in response to environmental stimuli. In the presence of cellular stressors, TP53 may undergo posttranslational modifications including phosphorylation, acetylation and poly ADP- ribosylation that lead to its activation. During cell cycle arrest in G1 phase, cells are able to repair DNA before its replication to avoid propagation

of nucleic acid alterations (Vousden 2002). However, TP53 may not be able to rescue a cell after repetitive insults leading to damage and apoptosis induction through upregulation of Bcl-2 associated X protein and TP53-upregulated modulator of apoptosis (Yu 2008). It is estimated 50% of HNSCC patients have small mutations in the gene encoding *TP53* (i.e. nonsense, missense, insertions or deletions of nucleotides) leading to inactivation or absence of protein (Somers 1992). These alterations impair the cells ability to arrest cell cycle and activate apoptosis leading to more genetic mutations, genetic instability, and clonal selection of radiation resistant cells. The origin and location of HNSCC in combination with the presence of TP53 mutations further increase tumor heterogeneity resulting in decreased survival and increased locoregional failure. As previously described, EGFR overexpression is correlated with poor prognosis in HNSCC. Radiation can induce autophosphorylation of EGFR causing protection from apoptosis (Schmidt-Ullrich 1996), increased cell proliferation and tumor repopulation after radiotherapy (Pedicini 2012). EGFR and TP53 expression and activity in HNSCC tumors are extremely important to therapeutic response. For example, HPV⁺ tumors are generally characterized by WT-TP53 and lower EGFR expression compared to HPV⁻ (Cattani 1998, Lassen 2009) resulting in high chemo-radiosensitivity. The metabolic reprogramming of cancer cells through the Warburg effect is also mediated by HIF-1 α . Activation of glycolytic enzymes, pyruvate dehydrogenase kinase 1 (Kim 2006) and G6PD, by HIF-1 α causes downregulation of aerobic respiration and upregulation of the PPP leading to increased production of NADPH and ribonucleotides (Peña-Rico 2011, Wanka 2012) to protect cells against apoptosis (Zhang 2008) during radiation-induced hypoxia and oxidative stress. HIF-2 α also regulates the expression of cytochrome c oxidase COX and MnSOD to increase mitochondrial ETC efficiency and suppressing ROS generation (Gordan 2007). Thus, tumor cell signaling and metabolism are connected by key enzymes and transcription factors to enhance resistance to radiation and chemotherapy by regulating energy production, proliferation and apoptosis.

Resistance to Chemotherapy in HNSCC Chemotherapy induces cell death primarily via DNA damage and apoptosis. Thus defective apoptotic initiation causes drug resistance (Maddika 2007). Cisplatin is the most commonly used chemotherapy but has significant patient variability related to outcome, efficacy and toxicity. Often the overall efficacy of the drug cannot be achieved due to harsh side effects (e.g. renal damage, deafness). In clinic, a cisplatin-sensitive patient is one who lived for more than two years from their last treatment session and has a 70% likelihood of responding to a second platinum-based therapy. To overcome disease resistance, cisplatin is used in combination with other chemotherapeutics, radiotherapy or drug targeted therapy. However, as the disease free period shortens, the response to platinum-based therapy decreases resulting in a platinum-resistant or refractory disease state. The primary mechanism of resistance to cisplatin at low levels (i.e. 10–15 fold above baseline) is due to altered DNA repair. At intermediate and high levels of cisplatin resistance, the resistance is due to reduced cellular accumulation and cytosolic inactivation of cisplatin (Amable 2016).

DNA damage alteration The balance of DNA damage versus DNA repair determines cancer cell death versus survival after cisplatin therapy (Metzger 1998). DNA excision repair protein, excision repair cross-complementation group 1 (ERCC-1), complexed with XP complementation group F (XPF) catalyzes the incision of the damaged DNA strand, the rate limiting step in the nucleotide excision repair pathway. High ERCC1 and XPF expression is indicative of increased removal of DNA platinum adducts and has a linear relationship with resistance to cisplatin in many cancers including HNSCC (Xuelei 2015). Polymorphisms have been identified in ERCC-1 and XPF but they have not correlated with increased sensitivity or resistance.

Platinum influx and efflux Moderate platinum resistance is mediated by decreased uptake or increased export thereby reducing platinum concentration (Kim 2012). Cisplatin can passively diffuse the cell membrane or is transported by copper uptake proteins CTR1/CTR2, and the organic cation transporter OCT2. Cisplatin resistant cells show decreased levels of CTR1 mRNA and reduced levels of copper but increased levels of CTR2 suggesting the CTR1 to CRT2 ratio

may be a useful biomarker for determining cisplatin response (Katano 2002). Cisplatin is exported out of the cell by P-type ATPase transporters (e.g. ATP7A, ATP7B) or ATP-binding cassette (ABC) transporters. These transporters are trafficked to the cell membrane to remove excessive copper (Amable 2016). As expected, increased ATP7A and ATP7B levels are associated with poor response to cisplatin (Li ZH 2012).

Platinum conjugation Cisplatin resistance can also be due to conjugation with proteins thiols (e.g., metallothionein, GSTs such as GST-pi and GST-M μ) leading to increased solubility, increased cellular export by transporters and less DNA damage. In HNSCC, there is a correlation between high expression of GST-pi and cisplatin resistance (Nishimura 1996). In breast cancer cells, GST-M μ 3 and GST-M μ 4 were decreased in cisplatin resistant cells but this phenomenon has not been investigated further (Smith 2007).

Other Mechanisms of Chemoresistance HIF's have been implicated in increased resistance to chemotherapeutics by increasing drug efflux and reducing DNA damage. HIF-2 ability to inhibit apoptotic pathways and activate anti-apoptotic signaling pathways results in enhanced CCND2 expression causing improved growth and resistance to DNA damage (Gordan 2007). Multidrug resistance 1 (ABCB1) is an ABC transporter protein, which can traffic substances across cellular membranes and cause efflux of many xenobiotics (Nakanishi 2012). It was also shown in colon and gastric cancer that ABC transporter, ABCG2, mediates resistance to chemotherapies under hypoxic conditions (Cuvillier 2012). Acid ceramidase (AC) plays a role in ceramide metabolism by converting ceramide into sphingosine to prevent ceramide induced apoptosis. AC is overexpressed in 70% of HNSCC malignant tissue and causes resistance to chemotherapeutic agents. An *in vitro* study demonstrated AC silencing regulated expression of wt or mutant TP53 by posttranscriptional processing and caspase-dependent mitochondrial apoptosis increased response to chemotherapy (Monsma 2013).

Resistance to EGFR-targeted therapies Monoclonal antibodies and TKIs target EGFR at the ligand binding or the catalytic domain, respectively, causing their efficacy and cytotoxicity

profiles to be different. Cetuximab resistance is associated with dysregulation of the internalization and degradation processing of EGFR. Forty-two percent of HNSCC tumors express an in-frame deletion in the ligand binding portion of the receptor resulting in a truncated EGFR-variant 3 (EGFRvIII) to be expressed (Sok 2006). EGFRvIII is constitutively phosphorylated, independent of ligand binding causing resistance to mAbs which target the ligand binding domain (Sok 2006). Downstream phosphotyrosine signal transducer and activator of transcription 3 (STAT3) is expressed at higher levels in HNSCC tumors with EGFRvIII. Cetuximab lacks the efficacy to abrogate EGFRvIII constitutive activation and STAT3 activity. On the other hand, resistance to TKIs is mostly attributed to (a) activation of redundant kinase signaling pathways such as tyrosine-protein kinase Met (c-MET) and HER family members and (b) EGFR-independent activation of downstream signaling pathways such as PI3K/Akt pathway (Cooper 2009, Lo Muzio 2004, Poetsch 2002). For example, recent studies have suggested overexpression of other members of the EGFR family, such as HER3, are involved in resistance to EGFR TKIs (Berghoff 2014). HER3 lacks tyrosine kinase activity but can be phosphorylated by c-MET or other receptor tyrosine kinases (Cortot 2013). C-MET is commonly overexpressed, mutated or has increased gene copy numbers in 60% of HNSCC (Lo Muzio 2004). MET amplification drives HER3 dependent activation of PI3K/Akt signaling bypassing the EGFR inhibition by TKI (She 2003, Soltoff 1994). Similarly, inhibitory PTEN mutations seen in many cancers including HNSCC (Soltoff 1994; She 2003), result in activation of Akt pathway and downstream effectors (Poetsch 2002).

Preclinical Models of Radiation Resistance in HNSCC

Challenges The standard of care has not changed markedly for HNSCC over the last two decades despite novel techniques for preclinical research and drug development to increase efficacy in clinical trials. Contributing factors include: (1) lack of biomarkers to detect early disease state or to assign disease stage accurately, (2) cytotoxicity of treatments decrease patient

functions and overall compliance, and (3) poor translation of laboratory findings to clinic. For example, chemoradiation therapies can overcome the intrinsic radioresistance of tumor cells but are not tumor specific and benefits are offset by normal tissue toxicity. A significant portion of HNSCC research has been dedicated to identifying drugs that increase radiosensitivity in tumors but sparing healthy normal tissue. Last year, a publication co-authored by experts in the field set forth guidelines to improve the translational potential of preclinical studies: (1) use of appropriate preclinical models that best represent the clinical setting of existent “standard-of-care” cancer therapy, (2) careful calibration and dosimetry testing of radiation sources, (3) detailed and accurate descriptions of experimental methodology and results, and (4) clinically relevant drugs, doses, schedules, and assay conditions (Coleman 2016).

In vitro models There are an estimated > 300 HNSCC cell lines characterized by various phenotypes: HPV⁺ and HPV⁻, resistance to cisplatin and/or radiation, TP53 or EGFRvIII mutations, and others. A panel of 9 human squamous cancer cell lines and 5 mouse cell lines are available from ATCC enabling a variety of studies including development of syngeneic *in vivo* models in immunocompetent mice. Approximately 85 cell lines taken from multiple sites of the head and neck region have been genomically validated by short tandem repeat (STR) profiling to facilitate future studies of the molecular, genetic and phenotypic diversity of HNSCC (Zhao 2011). It is becoming increasingly important to use genomically validated cell lines to prevent use of misidentification and cross-contamination of mammalian cell cultures resulting in false conclusions or discoveries resulting in failed clinical trials and a loss of research dollars. Currently the best method to authenticate cell lines is to perform STR profiling of control tissue from the tumor from which the cell line is derived to be used as a reference point for other researchers enabling better reproducibility. Standardized *in vitro* models and research methodology will help increase translation to clinic.

In recent years, there has also been great debate about the use of two dimensional (2D) versus three dimensional (3D) cell culture systems to determine drug efficacy. Currently, only about

10% of compounds tested in 2D cell culture progress successfully through clinical development due to lack of clinical efficacy or unacceptable toxicity (Breslin 2013, DiMasi 2007). This is mostly because a 2D monolayer culture provides an unnatural tumor microenvironment that cannot account for tumor oxygenation, immune cell infiltration or tumor vasculature (Coleman 2016). However, due to the cost and time of growing 3D cultures compared to 2D cultures, it has been suggested to first study growth inhibition and radiosensitivity in 2D using short term assay endpoints such as water soluble MTT (3-(4, 5-dimethylthiazol-2-yl)-2, 5-diphenyltetrazolium bromide) or trypan blue exclusion, or long term assays such as clonogenic or human tumor stem cell assay to measure tumor clonogens before moving to a 3D system. However, while MTT has long been regarded as the gold standard of cytotoxicity assays, there are a number of limitations associated with the assay including (1) less sensitive or accurate in detecting viable cell number compared to fluorescent and luminescent methods, (2) increased background absorbance values and assay artifacts caused by chemical interference due to non-enzymatic reduction of MTT to formazan by reducing compounds (i.e. GSH, coenzyme A) and (3) MTT reagent exhibits cytotoxic effects that may potentially be killing cells during the course of the experiment (Van Tonder 2015). Thus clonogenic assays or assays staining for nuclear features are preferable for 2D culture studies. Alternatively, cells can be grown in 3D cultures to form spheroids using scaffold/matrix (e.g. BD Matrigel™, Cultrex®, polyethylene glycol) (Breslin 2013, Gurski 2010, Tibbitt 2009) or in a scaffold-free manner (e.g. hanging drop method, forced floating method) (Breslin 2013). These methods add dimensionality and take into account how spatial and physical aspects effect interactions with surrounding cells, signal transduction from outside to inside, differentiation, morphology, and influence gene expression and cellular behavior (Lee 2008, Zietarska 2007). While 3D culture better mimic cell-cell interactions and cell-extracellular matrix (ECM) interactions, it still lacks complex vascular systems and thus proliferation rates of cells grown in 3D are significantly slower than cells grown in 2D (Kenny 2007). Overall 3D is a better system because cells exhibit gene expression more similar to those *in vivo* and response to

treatment is more predictive of *in vivo* drug responses. Recently the National Institute of Health (NIH) retired their National Cancer Institute (NCI)-60 panels in exchange for developing a repository of cancer models derived from patient derived xenografts (PDXs) (Ledford 2016).

In vivo models There are several animal models for HNSCC but none are ideal. The most ideal animal tumor model for HNSCC must be able to reproduce the characteristic features of the disease, and maintain clinical symptoms and laboratory abnormalities as well as be easy to use and progress rapidly enough to allow timely investigations. The most commonly used HNSCC models include chemically-induced *de novo* cancer, syngeneic animal tissue or cells transplanted into an immunocompetent mouse from the same strain, xenogeneic human tissue or cells transplanted into an immunodeficient animal environment subcutaneously or orthotopically (e.g. tongue or the floor of the mouth), and transgenic mice expressing *KRAS* or activated *AKT* with *TP53* loss (Smith 2006). Advantages include ability to study cancer development (*DMBA*-induced chemical carcinogenesis model), obtain information about tumor progression at all stages (e.g. hamster cheek pouch model), and resemble local and regional aggressiveness seen in clinic (e.g. syngeneic and xenograft orthotopic models). Some of the disadvantages are slow tumor growth, lack of local invasion and limited metastasis, and increased tumor burden in mice leading to short lifespan (Smith 2006). The ideal models correlating to clinical data are the orthotopic xenograft or orthotopic PDX models because these use either human cancer cells or human tissue in the correct anatomical site and therefore are better able to recapitulate the behavior of human tumors (Chung 2004, Cutz 2006). The PDX model also maintains histologic characteristics of primary tumor and response therapeutics. However, after successive generations, the population of cells becomes more homogenous and the gene expression profile diverges from that of the original tumor (Anderson 2003, Monsma 2013). The development of the NIH-NCI repository of cancer models derived from PDXs will hopefully increase access to primary human cells and tissue and decrease the cost associated with the establishment of *in vivo* models.

Bioinformatics and Computational Modeling in HNSCC

Systematic investigation integrates elements of the biological system such as genes, proteins, and metabolites with receptors, transcription factors or phenotypic effects using interdisciplinary approaches that can include a combination of physics, mathematics, chemistry and biology (Unger 2014). The integration of multiple factors allows the determination of causal relationships and the ability to identify perturbations in a signaling or metabolic pathway or network (Unger 2014) that are associated with specific disease, disease stage or response to treatment. Most studies characterize changes at the genome level using comparative genomic hybridization array or single nucleotide polymorphism microarray analysis and global methylation patterns by bisulfite-conversion of genomic DNA and hybridization of methylation sequences enriched by chromatin immunoprecipitation (ChiP) (Aparicio 2004, Davies 2005, LaFramboise 2009). Mass spectrometry based omics analysis allows characterization of the proteome, metabolome and lipidome (Geenen 2013) by detecting differentially expressed proteins, metabolites and lipids among different biological and clinical samples (Neilson 2011, Zhu 2010). For example, connecting gene expression with protein expression using transcription factors allows testing of potential associations either experimentally using ChiP-seq technology (Hoffman 2009) or *in silico* using algorithms such as graphical models or statistical associations to predict relationships (Kielbasa 2010). The benefit of modeling is the ability to use experimental measurements (e.g. protein expression) as elements in a network to predict correlations or causal relationships between perturbations and responses (Gagneur 2013). These predictions can provide key information about tumor development, response to therapeutics and treatment escalation/de-escalation. However, large-scale quantitative analysis can lead to high variability due to instrument related parameters or experimental conditions and network modeling comes with a certain level of uncertainty due to the potential for false positives or false negative findings (Karlebach 2008). Experimental variability can be corrected for at the level of data collection by using internal standards such as stable isotopically labeled internal standards (Stokvis 2005) and

validating data with other biological techniques (e.g. western blot, imaging). Network accuracy can be limited by level of detail, incomplete understanding of regulation to build accurate models or limited data availability resulting in no results or inconsistent results. For example, a HNSCC study attempted to understand mechanisms of radiation resistance and identify targets to overcome resistance using genome and miRNA data from archived clinical samples. The study used HPV status and individual mutations to identify candidate molecules. Unfortunately, they were unable to predict what effects are expected when applying certain doses of radiation, which genes are altered after radiation treatment or the occurrence of the primary radiation damage due to stochastic effects of radiation (Unger 2014). However, another study was able to determine a ten-gene signature to predict response of HNSCC patients to 5-FU induction chemotherapy by analyzing HNSCC biopsies with whole-genome microarrays and quantitative reverse transcriptase polymerase chain reaction (Tomkiewicz 2012). Some of the candidate genes identified play a role in response to redox stress such as heat shock protein 40 and thioredoxin domain containing 9 (Tomkiewicz 2012). Overall the major disadvantage of systematic investigations on determining radiation effects is the inability to predict the occurrence of the primary radiation damage (i.e. damage at DNA level). Specifically for HNSCC, integrating heterogeneous and high dimensionality data has limited the ability to determine the molecular mechanisms associated with the radiation-induced gene alterations. However, tumor resistance to radiation or tumor recurrence was found to be associated with molecular signatures identified in surviving cell population after treatment with ionizing radiation. Thus one can use systematic investigation of cells sensitive and resistant to radiation to better predict patient response to radiotherapy. A growing number of studies are using plasma or paraffin embedded human tissue samples when possible to provide more tumor specific experimental data and modeling of response to therapeutics or predicting biomarkers. Once optimized, systems biology will open new doors for precision medicine in determining precise course of action from patient to patient in the future. For example, a novel Cascade Propagation (CasP) subtyping approach, using the

cancer genome atlas (TCGA) data, was developed to investigate co-dependent immune signaling in HNSCC by using dynamic network modeling followed by stratifying somatic mutations. Using CasP subtyping, HNSCC patients can be stratified into two distinct groups including 1) patients with mutations in toll-like receptor signaling who have better overall survival, and 2) patients with mutations in T and B cell receptor signaling who have poorer survival. These findings will help predict patient response to therapeutics (Liu 2016). Also, another study identified genomic and/or epigenomic changes that lead to STAT3 activation in HNSCC using data generated by the TCGA and the cancer proteome atlas (TCPA) programs (Peysers 2016). The authors identified STAT3 expression is associated with disease stage, nodal status, tumor size, PFS, and OS in early stage oral HNSCC. These types of modeling techniques offer opportunities to better understand molecular signaling and identification of biomarkers as well as opportunities for therapeutic escalation/de-escalation. More importantly, the modeling presented in this dissertation further builds on signaling and metabolic interactions by combining the effects of intrinsic tumor redox state contributing to molecular signatures and altered response to therapeutics.

LITERATURE CITED

Adelstein DJ, Li Y, Adams GL, Wagner H Jr, Kish JA, Ensley JF, Schuller DE and Forastiere AA. Intergroup phase III comparison of standard radiation therapy and two schedules of concurrent chemoradiotherapy in patients with unresectable squamous cell head and neck cancer. *J Clin Oncol.* 21:92–8, 2003.

Albano E, Tomasi A, Persson JO, Terelius Y, Gorla-Gatti L, Ingelman-Sundberg M and Dianzani MU. Role of ethanol inducible cytochrome P450 (P450IIE1) in catalyzing the free radical activation of aliphatic alcohols. *Biochem Pharmacol.* 41:1895-1902, 1991.

Amable L. Cisplatin resistance and opportunities for precision medicine. *Pharmacol Res.* 106:27-36, 2016.

Anderson TM, Hess SD, Egilmez NK, Nwogu CE, Lenox JM, and Bankert RB. Comparison of human lung cancer/SCID mouse tumor xenografts and cell culture growth with patient clinical outcomes. *J Cancer Res Clin Oncol.* 129:565–568, 2003.

Ang KK, Zhang Q, Rosenthal DI, Nguyen-Tan PF, Sherman EJ, Weber RS, Galvin JM, Bonner JA, Harris J, EL-Naggar AK, Gillison ML, Jordan RC, Konski AA, Thorstad WL, Trotti A, Beitler JJ, Garden AS, Spanos WJ, Yom SS, and Axelrod RS. A randomized phase III trial (RTOG 0522) of concurrent accelerated radiation plus cisplatin with or without cetuximab for stage IIIIV head and neck squamous cell carcinomas (HNC). *J Clin Oncol.* 29 (Suppl 15s): Abstract 5500, 2011.

Aparicio O, Geisberg JV, and Struhl K. Chromatin immunoprecipitation for determining the association of proteins with specific genomic sequences in vivo. *Curr Protoc Cell Biol.* Chapter 17: Unit 17.7, 2004.

Azzam EI, Jay-Gerin JP, and Pain D. Ionizing radiation-induced metabolic oxidative stress and prolonged cell injury. *Cancer Lett.* 327(0):48-60, 2012.

Babior BM. NADPH oxidase: an update. *Blood.* 93:1464–1476, 1999.

Bae SH, Woo HA, Sung SH, Lee HE, Lee SK, Kil IS, and Rhee SG. Induction of sulfiredoxin via an Nrf2-dependent pathway and hyperoxidation of peroxiredoxin III in the lungs of mice exposed to hyperoxia. *Antioxid Redox Signal.* 11:937–948, 2009.

Baker A, Payne CM, Briehl MM, and Powis G. Thioredoxin, a gene found overexpressed in human cancer, inhibits apoptosis in vitro and in vivo. *Cancer Res.* 57:5162–5167, 1997.

Bar-Ad V, Palmer J, Yang H, Cognetti D, Curry J, Luginbuhl A, Tuluc M, Campling B, and Azelrod R. Current management of locally advanced head and neck cancer: the combination of chemotherapy with locoregional treatments. *Semin Oncol.* 41(6):798-806, 2014.

Baumann M, Krause M, Overgaard J, Debus J, Bentzen SM, Daartz J, Richter C, Zips D and Bortfeld T. Radiation oncology in the era of precision medicine. *Nat Rev Cancer.* 16:234–49, 2016.

Bayer C, Shi K, Astner ST, Maftai CA and Vaupel P. Acute versus chronic hypoxia: why a simplified classification is simply not enough. *Int J Radiat Oncol Biol Phys.* 80:965–8, 2011.

Bei R, Budillon A, Masuelli L, Cereda V, Vitolo D, Di Gennaro E, Ripavecchia V, Palumbo C, Ionna F, Losito S, Modesti A, Kraus MH, and Muraro R. Frequent overexpression of multiple ErbB receptors by head and neck squamous cell carcinoma contrasts with rare antibody immunity in patients. *J Pathol.* 204:317–25, 2004.

Berghoff AS, Bartsch R, Preusser M, Ricken G, Steger GG, Bago-Horvath Z, Rudas M, Streubel B, Dubsy P, Gnant M, Fitzal F, Zielinski CC and Birner P. Co-overexpression of HER2/HER3 is a predictor of impaired survival in breast cancer patients. *Breast.* 23: 637-43, 2014.

Bernier J, Cooper JS, Pajak TF, van Glabbeke M, Bourhis J, Forastiere A, Ozsahin EM, Jacobs JR, Jassem J, Ang KK and Lefebvre JL. Defining risk levels in locally advanced head and neck cancers: a comparative analysis of concurrent postoperative radiation plus chemotherapy trials of the EORTC (#22931) and RTOG (#9501). *Head Neck.* 27:843–50, 2005.

Bernier J, Dometge C, Ozsahin M, Matuszewska K, Lefebvre JL, Greiner RH, Giralt J, Maingon P, Rollan F, Bolla M, Cognetti F, Bourhis J, Kirkpatrick A, and van labeke M. Postoperative irradiation with or without concomitant chemotherapy for locally advanced head and neck cancer. *N Engl J Med.* 350(19):1945-52, 2004.

Birgander R, Sjalander A, Zhou Z, Fan C, Beckman L and Beckman G. p53 polymorphisms and haplotypes in nasopharyngeal cancer. *Hum Hered.* 46: 49-54, 1996.

Bonner JA, Harari PM, Giralt J, Azarnia N, Shin DM, Cohen RB, Jones CU, Sur R, Raben D, Jassem J, Ove R, Kies MS, Baselga J, Yousoufian H, Amellal N, Rowinsky EK, Ang KK. Radiotherapy plus cetuximab for squamous-cell carcinoma of the head and neck. *N Engl J Med.* 354:567–78, 2006.

Boveris A, Cadenas E, and Stoppani AO. Role of ubiquinone in the mitochondrial generation of hydrogen peroxide. *Biochem J.* 156:435–444, 1976.

Boyer SN, Wazer DE, and Band V. E7 protein of human papilloma virus-16 induces degradation of retinoblastoma protein through the ubiquitin-proteasome pathway. *Cancer Res.* 56:4620–4, 1996.

Branzei D and Foiani M. Regulation of DNA repair throughout the cell cycle. *Nat Rev Mol Cell Biol.* 9:297-308, 2008.

Breslin S and O’Driscoll L. Three-dimensional cell culture: the missing link in drug discovery. *Drug Discov Today.* 18:240–249, 2013.

Brizel DM, Sibley GS, Prosnitz LR, Scher RL and Dewhirst MW. Tumor hypoxia adversely affects the prognosis of carcinoma of the head and neck. *Int J Radiat Oncol Biol Phys.* 38(2):285-9, 1997.

Brooks PJ. DNA damage, DNA repair, and alcohol toxicity--a review. *Alcohol Clin Exp Res.* 21:1073-82, 1997.

Cadenas E and Davies KJ. Mitochondrial free radical generation, oxidative stress, and aging. *Free Radic Biol Med.* 29:222–230, 2000.

Cao J, Zhou J, Gao Y, Gu L, Meng H, Liu H, and Deng D. Methylation of p16 CpG island associated with malignant progression of oral epithelial dysplasia: a prospective cohort study. *Clin Cancer Res.* 15(16):5178–83, 2009.

Carr A, McCall MR, and Frei B. Oxidation of LDL by myeloperoxidase and reactive nitrogen species-reaction pathways and antioxidant protection. *Arterioscl Thromb Vasc Biol.* 20:1716–1723, 2000.

Cattani P, Hohaus S, Bellacosa A, Genuardi M, Caballo S, Rovella V, Almadori G, Cadoni G, Galli J, Maurizi M, Fadda G and Neri G. Association between cyclin D1 (CCND1) gene amplification and human papillomavirus infection in human laryngeal squamous cell carcinoma. *Clin Cancer Res.* 4:2585–2589, 1998.

Chae HZ, Kim HJ, Kang SW, and Rhee SG. Characterization of three isoforms of mammalian peroxiredoxin that reduce peroxides in the presence of thioredoxin. *Diabetes Res Clin Pract.* 45:101–112, 1999.

Chapman CH, Saba NF and Yom SS. Targeting epidermal growth factor receptor for head and neck squamous cell carcinoma: still lost in translation. *Ann Transl Med.* 4(4):80, 2016.

Cheng H, Nair SK and Murray BW. Recent progress on third generation covalent EGFR inhibitors. *Bioorg Med Chem Lett.* 26(8): 1861-8, 2016.

Cheng L, Sturgis EM, Eicher SA, Char D, Spitz MR and Wei Q. Glutathione-S-transferase polymorphisms and risk of squamous cell carcinoma of the head and neck. *Int J Cancer.* 84: 220-224, 1999.

Chiou SH, Kao CL, Chen YW, Chien CS, Hung SC, Lo JF, Chen YJ, Ku HH, Hsu MT, and Wong TT. Identification of CD133-positive radioresistant cells in atypical teratoid/rhabdoid tumor. *PLoS One.* 3:e2090, 2008.

Chung CH, Parker JS, Karaca G, Wu J, Funkhouser WK, Moore D, Butterfoss D, Xiang D, Zanation A, Yin X, Shockley WW, Weissler MC, Dressler LG, Shores CG, Yarbrough WG and Perou CM. Molecular classification of head and neck squamous cell carcinomas using patterns of gene expression. *Cancer Cell.* 5:489–500, 2004.

Chung F-L, Chen H-JC, and Nath RG. Lipid peroxidation as a potential endogenous source for the formation of exocyclic DNA adducts. *Carcinogenesis.* 17: 2105–2111, 1996.

Claiborne A, Miller H, Parsonage D, and Ross PR. Protein sulfenic acid stabilization and function in enzyme catalysis and gene regulation. *FASEB J.* 7:1483-1490, 1993.

Coleman CN, Higgins GS, Brown JM, Baumann M, Kirsch DG, Willers H, Prasanna PG, Dewhirst MW, Bernhard EJ and Ahmed MM. Improving the predictive value of preclinical studies in support of radiotherapy clinical trials. *Clin Cancer Res.* 22(13):3138-47, 2016.

Collins-Underwood JR, Zhao WL, Sharpe JG, and Robbins ME. NADPH oxidase mediates radiation-induced oxidative stress in rat brain microvascular endothelial cells. *Free Radic Biol Med.* 45: 929–938, 2008.

Cooper JB and Cohen EEW. Mechanisms of resistance to EGFR inhibitors in head and neck cancer. *Head Neck.* 31(8):1086-94, 2009.

Cooper JS, Pajak TF, Forastiere AA, Jacobs J, Campbell BH, Saxman SB, Kish JA, Kim HE, Cmelak AJ, Rotman M, Machtay M, Ensley JF, Chao KS, Schultz CJ, Lee N, Fu KK, and Radiation Therapy Oncology Group 9501/Intergroup. Postoperative concurrent radiotherapy and chemotherapy for high- risk squamous cell carcinoma of the head and neck. *N Engl J Med.* 350:1937–44, 2004.

Corre I, Niaudet C, and Paris F. Plasma membrane signaling induced by ionizing radiation. *Mutat Res.* 704: 61–67. 2010.

Cortot AB, Repellin CE, Shimamura T, Capelletti M, Zejnullahu K, Ercan D, Christensen JG, Wo-ng KK, Gray NS and Janne PA. Resistance to irreversible EGF receptor tyrosine kinase inhibitors through a multistep mechanism involving the IGF1R pathway. *Cancer Res.* 73: 834-843, 2013.

Coutelle C, Ward PJ, Fleury B, Quattrocchi P, Chambrin H, Iron A, Couzigou P and Cassaigne A. Laryngeal and oropharyngeal cancer, and alcohol dehydrogenase 3 and glutathione S-transferase M1 polymorphisms. *Hum Genet.* 99: 319-325, 1997.

Cutz JC, Guan J, Bayani J, Yoshimoto M, Xue H, Sutcliffe M, English J, Flint J, LeRiche J, Yee J, Squire JA, Gout PW, Lam S, and Wang YZ. Establishment in severe combined immunodeficiency mice of subrenal capsule xenografts and transplantable tumor lines from a variety of primary human lung cancers: potential models for studying tumor progression-related changes. *Clin Cancer Res.* 12:4043–4054, 2006.

Cuvillier O, Ader I, Bouquerel P, Brizuela L, Gstalder C, and Malavaud B. Hypoxia, therapeutic resistance, and sphingosine 1-phosphate. *Adv Cancer Res.* 117:117–41, 2012.

Dalby KN, Tekedereli I, Lopez-Berestein G, and Ozpolat B. Targeting the prodeath and prosurvival functions of autophagy as novel therapeutic strategies in cancer. *Autophagy.* 6:322–9, 2010.

Davies JJ, Wilson IM, and Lam WL. Array CGH technologies and their applications to cancer genomes. *Chromosome Res.* 13(3):237–248, 2005.

DeCoursey TE and Ligeti E. Regulation and termination of NADPH oxidase activity. *Cell Mol Life Sci.* 62:2173–2193, 2005.

Derry MM, Raina K, Agarwal C, and Agarwal R. Identifying molecular targets of lifestyle modifications in colon cancer prevention. *Front Oncol.* 3:119. 2013.

DiMasi JA and Grabowski HG. Economics of new oncology drug development. *J Clin Oncol.* 25:209–216, 2007.

Dizdaroglu M and Jaruga P. Mechanisms of free radical induced damage to DNA. *Free Radic Res.* 46: 382–419, 2012.

Dobrossy L. Epidemiology of head and neck cancer: magnitude of the problem. *Cancer Metastasis Rev.* 24:9-17, 2005.

Dröge, W. Free radicals in the physiological control of cell function. *Physiol Rev.* 82:47–95, 2002.

Du C, Gao Z, Venkatesha VA, Kalen AL, Chaudhuri L, Spitz DR, Cullen JJ, Oberley LW, and Goswami PC. Mitochondrial ROS and radiation induced transformation in mouse embryonic fibroblasts. *Cancer Biol Ther.* 8:1962–1971, 2009.

Duncan Lyngdoh RH and Schaefer HF. Elementary lesions in DNA subunits: electron, hydrogen atom, proton, and hydride transfers. *Acc Chem Res.* 42: 563–572, 2009.

Dyson N, Howley PM, Munger K, and Harlow E. The human papilloma virus-16 E7 oncoprotein is able to bind to the retinoblastoma gene product. *Science*. 243:934–7, 1989.

Economopoulou P, Perisanidis C, Giotakis EI, and Psyrri A. The emerging role of immunotherapy in head and neck squamous cell carcinoma (HNSCC): anti-tumor immunity and clinical applications. *Ann Transl Med*. 4(9):173, 2016.

Engelman JA, Zejnullahu K, Gale CM, Lifshits E, Gonzales AJ, Shimamura T, Zhao F, Vincent PW, Naumov GN, Bradner JE, Althaus IW, Gandhi L, Shapiro GI, Nelson JM, Heymach JV, Meyerson M, Wong KK, Jaenke PA. PF00299804, an irreversible pan-erbB inhibitor, is effective in lung cancer models with *egfr* and *erbB2* mutations that are resistant to gefitinib. *Cancer Res*. 67:11924, 2007.

Eriksen JG, Maare C, Johansen J, Primdahl H, Evensen JF, Kristensen CA, Andersen LJ, and Overgaard J. Evaluation of the EGFR-Inhibitor Zalutumumab Given With Primary Curative (Chemo)radiation Therapy to Patients With Squamous Cell Carcinoma of the Head and Neck: Results of the DAHANCA 19 Randomized Phase 3 Trial. *Int J Radiat Oncol Biol Phy*. 88(2) 465, 2014.

Eyler CE and Rich JN. Survival of the fittest: cancer stem cells in therapeutic resistance and angiogenesis. *J Clin Oncol*. 26:2839-2845, 2008.

Fayette J, Wirth L, Oprean C, Udrea A, Jimeno A, Rischin D, Nutting C, Harari PM, Csozsi T, Cernea D, O'Briend P, Hanley WD, Kapp AV, Anderson M, Penuel E, McCall B, Pirzkall A, and Vermorken JB. Randomized phase II study of duligotuzumab (MEHD7945A) vs. cetuximab in squamous cell carcinoma of the head and neck (MEHGAN Study). *Front Oncol*. 6:232, 2016.

Ferlito A, Shaha AR, Silver CE, Rinaldo A and Mondin V. Incidence and sites of distant metastases from head and neck cancer. *ORL J Otorhinolaryngol Relat Spec*. 63(4):202-7, 2001.

Ferris RL, Blumenschein G Jr, Fayette J, Guigay J, Colevas AD, Licitra L, Harington K, Kasper S, Vokes EE, Even C, Worden F, Saba NF, Iglesias Docampo LC, Haddad R, Rordorf T, Kiyota N, Tahara M, Monga M, Lynch M, Geese WJ, Kopit J, Shaw JW and Gillison ML. Nivolumab for recurrent squamous-cell carcinoma of the head and neck. *N Engl J Med*. 375(19):1856-1867, 2016.

Ferris RL, Whiteside TL, and Ferrone S. Immune escape associated with functional defects in antigen processing machinery in head and neck cancer. *Clin Cancer Res.*12:3890–5, 2006.

Flora SJ, Mittal M, and Mehta A. Heavy metal induced oxidative stress and its possible reversal by chelation therapy. *Indian J Med Res.*128:501–23, 2008.

Francis DM, Huang S, Armstrong EA, Wener LR, Hullett C, Li C, Morris ZS, Swick AD, Kragh M, Lantto J, Kimple RJ, and Harari PM. Pan-HER inhibitor augments radiation response in human lung and head and neck cancer models. *Clin Cancer Res.* 22(3):633-43, 2006.

Gagneur J, Stegle O, Zhu C, Jakob P, Tekkedil MM, Aiyar RS, Schuon A, Pe'er D, and Steinmetz LM. Genotype-environment interactions reveal causal pathways that mediate genetic effects on phenotype. *PLoS Genet.* 9(9):e1003803, 2013.

Galbiatti ALS, Padovani-Junior JA, Maniglia JV, Rodrigues CDS, Pavarino EC, and Goloni-Bertollo EM. Head and neck cancer: causes, prevention and treatment. *Braz J Otorhinolaryngol.* 79(2):239-47, 2013.

Geenen S, Cojocariu C, Gethings L, Isaac G, Fernandes L, Tonge R, Vissers J, Langrige J, Wilson I, and Martin L. Qualitative and Quantitative Characterization of the Metabolome, Lipidome and Proteome of Human Hepatocytes Stably Transfected with Cytochrome P450 2E1 Using Data Independent LC-MS. *J Biomol Tech.* 24(Suppl):S61—S62, 2013.

Gewin L and Galloway DA. E box-dependent activation of telomerase by human papillomavirus type 16 E6 does not require induction of c-myc. *J Virol.* 75:7198–201, 2001.

Giralt J, Trigo J, Nuyts S, Ozsahin M, Skladowski K, Hatoum G, Daisne JF, Anona ACY, Cmelak A, Mesia R, Zhang A, Oliner KS and VanderWalde A. Panitumumab plus radiotherapy versus chemoradiotherapy in patients with unresected, locally advanced squamous-cell carcinoma of the head and neck (CONCERT-2): a randomised, controlled, open-label phase 2 trial *Lancet Oncol.* 16:221-32, 2015.

Giroglou T, Florin L, Schafer F, Streeck RE, and Sapp M. Human papillomavirus infection requires cell surface heparan sulfate. *J Virol.* 75:1565–70, 2001.

Girotti AW. Lipid hydroperoxide generation, turnover, and effector action in biological systems. *J Lipid Res.* 39:1529–1542, 1998.

Goldkorn T and Filosto S. Lung injury and cancer: mechanistic insights into ceramide and EGFR signaling under cigarette smoke. *Am J Respir cell Mol Biol.* 4(3):259-268, 2010.

Goldkorn T, Filosto S, and Chung S. Lung injury and lung cancer caused by cigarette smoke-induced oxidative stress: molecular mechanisms and therapeutic opportunities involving the ceramide-generating machinery and epidermal growth factor receptor. *Antioxid Redox Signal.* 21(15):2149-2174, 2014.

Gonzalez SL, Stremlau M, He X, Basile JR, and Munger K. Degradation of the retinoblastoma tumor suppressor by the human papillomavirus type 16 E7 oncoprotein is important for functional inactivation and is separable from proteasomal degradation of E7. *J Virol* 75:7583–91, 2001.

Gordan JD, Bertout JA, Hu CJ, Diehl JA, and Simon MC. HIF-2 α promotes hypoxic cell proliferation by enhancing c-myc transcriptional activity. *Cancer Cell.* 11:335–47, 2007.

Gordan JD, Thompson CB, and Simon MC. HIF and c-Myc: sibling rivals for control of cancer cell metabolism and proliferation. *Cancer Cell.* 12:108–13, 2007.

Gorrini C, Harris IS, and Mak TW. Modulation of oxidative stress as an anticancer strategy. *Nat Rev Drug Discov.* 12(12):931-47, 2013.

Guerra ENS, Rego DF, Elias ST, Coletta RD, Mezzomo LAM, Gozal D and del Luca Canto G. *Crit Rev Oncol Hematol.* 101:93-118, 2016.

Guo JH, Chen MQ, Chen C, Lu HJ and Xu BH. Efficacy and toxicity of nimotuzumab combined with radiotherapy in elderly patients with esophageal squamous cell carcinoma. *Mol Clin Oncol.* 3(5):1135-1138, 2015

Gurski L, Petrelli N, Jia X, and Farach-Carson M. Three-dimensional matrices for anti-cancer drug testing and development. *Oncol Issues.* 25:20–25, 2010.

Hall GL, Shaw RJ, Field EA, Rogers SN, Sutton DN, Woolgar JA, Lowe D, Liloglou T, Field JK and Risk JM. P16 promoter methylation is a potential predictor of malignant transformation in oral epithelial dysplasia. *Cancer Epidemiol Biomarkers Prev.* 17 (8):2174–9, 2008.

Hall MD, Okabe M, Shen DW, Liang XJ, and Gottesman MM. The role of cellular accumulation in determining sensitivity to platinum-based chemotherapy, *Annu. Rev. Pharmacol. Toxicol.* 48:495–535, 2008.

Hamel N, Black MJ, Ghadirian P and Foulkes WD. No association between p53 codon 72 polymorphism and risk of squamous cell carcinoma of the head and neck. *Br J Cancer.* 82:757-759, 2000.

Hammer S, To KK, Yoo YG, Koshiji M and Huang LE. Hypoxic suppression of the cell cycle gene CDC25A in tumor cells. *Cell Cycle.* 6:1919–26, 2007.

Han D, Antunes F, Canali R, Rettori D, and Cadenas E. Voltage-dependent anion channels control the release of the superoxide anion from mitochondria to cytosol. *J Biol Chem.* 278:5557–5563, 2003.

Hanschmann EM, Lönn ME, Schütte LD, Funke M, Godoy JR, Eitner S, Hudemann C, and Lillig CH. Both thioredoxin 2 and glutaredoxin 2 contribute to the reduction of the mitochondrial 2-Cys peroxiredoxin Prx3. *J Biol Chem.* 285:40699–40705, 2010.

Haque R, Contreras R, McNicoll MP, Eckberg EC, and Petitti DB. Surgical margins and survival after head and neck cancer surgery. *BMC Ear, Nose, and Throat Disord.* 6:2, 2006.

Harada H, Kizaka-Kondoh S, Li G, Itasaka S, Shibuya K, Inoue M and Hiraoka M. Significance of HIF-1-active cells in angiogenesis and radioresistance. *Oncogene.* 26:7508–16, 2007.

Harada H. Hypoxia-inducible factor 1-mediated characteristic features of cancer cells for tumor radioresistance. *J Radiat Res.* 57(S1):i99-105, 2016.

Helleday T, Petermann E, Lundin C, Hodgson B and Sharma RA. DNA repair pathways as targets for cancer therapy. *Nat Rev Cancer.* 8:193-204, 2008.

Herrero R, Quint W, Hildesheim A, Gonzalez P, Struijk L, Katki HA, Porras C, Schiffman M, Rodriguez AC, Solomon D, Jimenez S, Schiller JT, Lowy DR, van Doorn LJ, Wacholder S, Kreimer AR and CVT Vaccine Group. Reduced prevalence of oral human papillomavirus (HPV) 4 years after bivalent HPV vaccination in a randomized clinical trial in Costa Rica. *PLoS One*. 8:e68329, 2013.

Hirota K and Semenza GL. Regulation of hypoxia-inducible factor 1 by prolyl and asparaginyl hydroxylases. *Biochem Biophys Res Commun*. 338:610–6, 2005.

Hirsch FR, Scagliotti GV, Langer CJ, Varella-Garcia M, and Franklin WA. Epidermal growth factor family of receptors in preneoplasia and lung cancer: perspectives for targeted therapies. *Lung Cancer*. 41:S29–S42, 2003.

Hitt R, Lopez-Pousa A, Martinez-Trufero J, Escrig V, Carles J, Rizo A, Isla D, Vega ME, Marti JL, Lobo F, Pastor P, Valenti V, Belon J, Sanchez MA, Chaib C, Pallares C, Anton A, Cervantes A, Paz-Ares L, and Cortes-Funes H. Phase III study comparing cisplatin plus fluorouracil to paclitaxel, cisplatin, and fluorouracil induction chemo-therapy followed by chemoradiotherapy in locally advanced head and neck cancer. *J Clin Oncol*. 23:8645, 2005.

Hoffman BG and Jones SJM. Genome-wide identification of DNA-protein interactions using chromatin immunoprecipitation coupled with flow cell sequencing. *J Endocrinol*. 201:1–13, 2009.

Holmgren A. Thioredoxin and glutaredoxin systems. *J Biol Chem*. 264: 13963-13966, 1989.

Hong YJ, Lee JK, Lee GH and Hong SI. Influence of glutathione S-transferase M1 and T1 genotypes on larynx cancer risk among Korean smokers. *Clin Chem Lab Med*. 38:917-919, 2000.

Honscheid P, Datta K, and Muders MH. Autophagy: detection, regulation and its role in cancer and therapy response. *Int J Radiat Biol*.90:628–35, 2014.

Huang WY, Olshan AF, Schwarts SM, Berndt SI, Chen C, Llaca V, Chanock SJ, Fraumeni JF Jr and Hayes RB. Selected genetic polymorphisms in *MGMT*, *XRCC1*, *XPB*, and *XRCC3* and risk of head and neck cancer: a pooled analysis. *Cancer Epidemiol Biomarkers Prev*. 14: 1747-1753, 2005.

Jham BC and da Silva Freire AR. Oral complications of radiotherapy in the head and neck. *Braz J Otorhinolaryngol.* 72(5): 704-8, 2006.

Johnson GL and Lapadat R. Mitogen-activated protein kinase pathways mediated by ERK, JNK, and p38 protein kinases. *Science.* 298:1911–2, 2002.

Jones DP, Carlson JL, Mody VC, Cai JY, Lynn MJ, and Sternberg P. Redox state of glutathione in human plasma. *Free Radic Bio Med.* 28, 625–635, 2000.

Karagas MR, Stannard VA, Mott LA, Slattery MJ, Spencer SK, and Weinstock MA. Use of tanning devices and risk of basal cell and squamous cell skin cancers. *J Natl Cancer Inst.* 94: 224–226, 2002.

Karlebach G and Shamir R. Modelling and analysis of gene regulatory networks. *Nat Rev Mol Cell Biol.* 9(10):770–780, 2008.

Katano K, Kondo A, Safaei R, Holzer A, Samimi G, Mishima M, Kuo YM, Rochdi M, and Howell SB. Acquisition of resistance to cisplatin is accompanied by changes in the cellular pharmacology of copper. *Cancer Res.* 62(22)6559–6565, 2002.

Katoh T, Kaneko S, Takasawa S, Nagata N, Inatomi H, Ikemura K, Itoh H, Matsumoto T, Kawamoto T and Bell DA. Human glutathione Stransferase P1 polymorphism and susceptibility to smoking related epithelial cancer; oral, lung, gastric, colorectal and urothelial cancer. *Pharmacogenetics.* 9: 165-169, 1999.

Kenny PA, Lee GY, Myers CA, Neve RM, Semeiks JR, Spellman PT, Lorenz K, Lee EH, Barcellos-Hoff MH, Peterson OW, Gray JW, and Bissell MJ. The morphologies of breast cancer cell lines in three-dimensional assays correlate with their profiles of gene expression. *Mol Oncol.* 1:84–96, 2007.

Kern JC and Kehrer JP. Free radicals and apoptosis: relationships with glutathione, thioredoxin and the BCL family of proteins. *Front Biosc.* 10:1727-1738, 2005.

Khong PL, Ringertz H, Donoghue V, Frush D, Rehani M, Appelgate K, and Sanchez R. Radiological protection in paediatric diagnostic and interventional radiology. *Ann ICRP.* 42: 1–63, 2013.

Kielbasa SM, Klein H, Roider HG, Vingron M, and Blüthgen N. Trans Find—predicting transcriptional regulators for gene sets. *Nucleic Acids Res.* 38(suppl 2):W275—W280, 2010.

Kietthubthew S, Sriplung H, Au WW and Ishida T. Polymorphism in DNA repair genes and oral squamous cell carcinoma in Thailand. *Int J Hyg Environ Health.* 209: 21-29, 2006.

Kim ES, Lee JJ, He G, Chow CW, Fujimoto J, Kalhor N, Swisher SG, Wistuba II, Stewart DJ and Siddik ZH, Tissue platinum concentration and tumor response in non-small-cell lung cancer. *J Clin Oncol.* 30(27):3345–3352, 2012.

Kim JW, Tchernyshyov I, Semenza GL, and Dang CV. HIF-1-mediated expression of pyruvate dehydrogenase kinase: a metabolic switch required for cellular adaptation to hypoxia. *Cell Metab.* 3:177–85, 2006.

Klimova T and Chandel NS. Mitochondrial complex III regulates hypoxic activation of HIF. *Cell Death Differ.* 15:660–666, 2008.

Koch CJ, Evans SM, and Lord EM. Oxygen dependence of cellular uptake of EF5 [2-(2-nitro-1H-imidazol-1-yl)-N-(2,2,3,3,3-pentafluoropropyl)acetamide]: analysis of drug adducts by fluorescent antibodies vs bound radioactivity. *Br J Cancer.* 72(4):869-74, 1995.

Koch U, Hohne K, von Neubeck C, Thames HD, Yaromina A, Dahm-Daphi J, Baumann M, and Krause M. Residual gamma H2AX foci predict local tumour control after radiotherapy. *Radiother Oncol.* 108:434–9, 2013.

Koukourakis MI, Bentzen SM, Giatromanolaki A, Wilson GD, Daley FM, Saunders MI, Dische S, Sivridis E and Harris AL. Endogenous markers of two separate hypoxia response pathways (hypoxia inducible factor 2 alpha and carbonic anhydrase 9) are associated with radiotherapy failure in head and neck cancer patients recruited in the CHART randomized trial. *J Clin Oncol.* 24:727–35, 2006.

Kumar B, Cordell KG, Lee JS, Worden FP, Prince ME, Tran HH, Wolf GT, Urba SG, Chepeha DB, Teknos TN, Eisbruch A, Tsien CI, Taylor JM, D’Silva NJ, Yang K, Kurnit DM, Bauer JA, Bradford CR, and Carey TE. EGFR, p16, HPV Titer, Bcl-xL and p53, sex, and smoking as indicators of response to therapy and survival in oropharyngeal cancer. *J Clin Oncol.* 26(19): 3128–3137, 2008.

LaFramboise T. Single nucleotide polymorphism arrays: a decade of biological, computational and technological advances. *Nucleic Acids Res.* 37(13):4181–4193, 2009.

Landi MT, Bertazzi PA, Shields PG, Clark G, Lucier GW, Garte SJ, Cosma G, and Caporaso NE. Association between CYP1A1 genotype, mRNA expression and enzymatic activity in humans. *Pharmacogenetics.* 4: 242-246, 1994.

Lassen P, Eriksen JG, Hamilton–Dutoit S, Tramm T, Alsner J, and Overgaard J. Effect of HPV-associated p16INK4A expression on response to radiotherapy and survival in squamous cell carcinoma of the head and neck. *J Clin Oncol.* 27:1992–1998, 2009.

Lavantiadou SN, Chan C, Ravid T, Tsaba A, van der Vliet A, Rasooly R, and Goldkorn T. Ceramide-mediated apoptosis in lung epithelial cells is regulated by GSH. *Am J Respir Cell Mol Biol.* 25: 676–684, 2001.

Lawrence T and Rosenberg S. Cancer: Principles and Practice of Oncology. Philadelphia, PA: Lippincott Williams and Wilkins, 2008.

Ledford H. US cancer institute to overhaul tumour cell lines. *Nature.* 539(7591):391, 2016.

Lee J, Cuddihy MJ, and Kotov NA. Three-dimensional cell culture matrices: state of the art. *Tissue Eng Part B Rev.* 14:61–86, 2008.

Lee K, Zhang H, Qian DZ, Rey S, Liu JO and Semenza GL. Acriflavine inhibits HIF-1 dimerization, tumor growth, and vascularization. *Proc Natl Acad Sci U S A.* 106:17910–5, 2009.

Leslie NR, Bennett D, Lindsay YE, Stewart H, Gray A, and Downes CP. Redox regulation of PI 3-kinase signalling via inactivation of PTEN. *EMBO J.* 22: 5501– 5510, 2003.

Li J and Holbrook NJ. Common mechanisms for declines in oxidative stress tolerance and proliferation with aging. *Free Radic Biol Med.* 35:292–9, 2003.

Li Q, Yu JJ, Mu C, Yunmbam MK, Slavsky D, Cross CL, Bostick-Bruton F and Reed E. Association between the level of ERCC-1 expression and the repair of cisplatin-induced DNA damage in human ovarian cancer cells, *Anticancer Res.* 20 (2A) 645–652, 2000.

Li ZH, Qiu MZ, Zheng ZL, Luo HY, Wu WJ, Wang F, Wang ZQ, Zhang DS, Li YH and Xu RH. Copper-transporting P-type adenosine triphosphatase (ATP7A) is associated with platinum-resistance in non-small cell lung cancer(NSCLC). *J Transl Med.* 10:21, 2012.

Linsley PS, Brady W, Urnes M, Grosmaire LS, Damle NK, and Ledbetter JA. CTLA-4 is a second receptor for the B-cell activation antigen B7. *J Exp Med.* 174:561–9, 1991.

Liu K, Chyr J, Zhao W and Zhou X. Immune signaling-based Cascade Propagation approach restratifies HNSCC patients. *Methods.* 111:72-79, 2016.

Liu R, Oberley TD and Overley LW. Transfection and expression of MnSOD cDNA decreases tumor malignancy of human oral squamous carcinoma SCC-25 cells. *Hum Gene Ther.* 8(5):585-95, 1997.

Lo Muzio L, Leonardi R, Mignogna MD, Pannone G, Rubini C, Pieramici T, Trevisiol L, Ferrari F, Serpico R, Testa N, D Rosa G, and Staibano S. Scatter factor receptor (c-Met) as possible prognostic factor in patients with oral squamous cell carcinoma. *Anticancer Res.* 24:1063–9, 2004.

Loft S and Oulsen HE. Cancer risk and oxidative DNA damage in man. *J Mol Med (Berl).* 74(6):297-312, 1996.

Lorch JH, Goloubeva Q, Haddad RI, Cullen K, Sarlis N, Tishler R, Tan M, Fasciano J, Sammartino DE, Psner MR and TAX 324 Study Group. Induction chemotherapy with cisplatin and fluorouracil alone or in combination with docetaxel in locally advanced squamous-cell cancer of the head and neck: long-term results of the TAX 324 randomized phase 3 trial. *Lancet Oncol.* 12(2):153–9, 2011.

Lu J, Wang LE, Xiong P, Sturgis E, Spitz MR and Wei Q. 172G>T variant in the 5' untranslated region of DNA repair gene *RAD51* reduces risk of squamous cell carcinoma of the head and neck and interacts with a *P53* codon 72 variant. *Carcinogenesis.* 28: 988-994, 2007.

Lu M, Wang X, Shen L, Jia J, Gong J, Li J, Li H, Li Y, Zhang X, Lu Z, hou J and Zhang X. Nimotuzumab plus paclitaxel and cisplatin as the first line treatment from advanced esophageal squamous cell cancer: a single centre prospective phase II trial. *Cancer Sci.* 107(4):486-90, 2016.

Lund EL, Bastholm L, and Kristjansen PE. Therapeutic synergy of TNP-470 and ionizing radiation: effects on tumor growth, vessel morphology, and angiogenesis in human glioblastoma multiforme xenografts. *Clin Cancer Res.* 6:971–8, 2000.

Machiels JP, Specenier P, Kraub J, Dietz A, Kaminsky MC, Lalami Y, Henke M, Keilholz U, Knecht R, Skartved NJ, Horak ID, Pamperin P, Braun S and Gauler TC. *Cancer Chemother Pharmacol.* 76:13-20, 2015.

Maddika S, Ande SR, Panigrahi S, Paranjothy T, Weglarczyk K, Zuse A, Eshraghi M, Manda KD, Wiechec E and Los M. Cell survival, cell death and cell cycle pathways are interconnected: implications for cancer therapy. *Drug Resist Updat.* 10:13–29, 2007.

Madian AG and Regnier FE. Proteomic identification of carbonylated proteins and their oxidation sites. *J Proteome Res.* 9: 3766–3780, 2010.

Mager DL, Haffajee AD, Devlin PM, Norris CM, Posner MR and Goodson JM. The salivary microbiota as a diagnostic indicator of oral cancer: a descriptive, non-randomized study of cancer-free and oral squamous cell carcinoma subjects. *J Transl Med.* 3:27, 2005.

Mahaney BL, Meek K and Lees-Miller SP. Repair of ionizing radiation-induced DNA double-strand breaks by non-homologous end-joining. *Biochem J.* 417:639- 650, 2009.

Majumder M, Sikdar N, Ghosh S and Roy B. Polymorphisms at *XPD* and *XRCC1* DNA repair loci and increased risk of oral leukoplakia and cancer among *NAT2* slow acetylators. *Int J Cancer.* 120: 2148-2156, 2007.

Malik UU, Zarina S, and Pennington SR. Oral squamous cell carcinoma: key clinical questions, biomarker discovery and the role of proteomics. *Archives of Oral Bio.*3:53-65, 2016.

Marino G, Salvador-Montoliu N, Fueyo A, Knecht E, Mizushima N, and Lopez-Otin C. Tissue-specific autophagy alterations and increased tumorigenesis in mice deficient in ATG4C/autophagin-3. *J Biol Chem.* 282:18573–83, 2007.

Masella R, Di Benedetto R, Vari R, Filesi C, and Giovannini C. Novel mechanisms of natural antioxidant compounds in biological systems: Involvement of glutathione and glutathione related enzymes. *J. Nutr. Biochem.* 16:577–586, 2005.

Matthias C, Bockmuhl U, Jahnke V, Harries LW, Wolf CR, Jones PW, Alldersea J, Worrall SF, Hand P, Fryer AA and Strange RC. The glutathione Stransferase *GSTP1* polymorphism: effects on susceptibility to oral/pharyngeal and laryngeal carcinomas. *Pharmacogenetics* 8:1-6, 1998.

McCord JM. The evolution of free radicals and oxidative stress. *Am J Med.* 108:652– 9, 2000.

Menegakis, A, Eicheler W, Yaromina A, Thames HD, Krause M, and Baumann M. Residual DNA double strand breaks in perfused but not in unperfused areas determine different radiosensitivity of tumours. *Radiother Oncol.* 100(1):137-44, 2011.

Metzger R, Leichman CG, Danenberg KD, Danenberg PV, Lenz HJ, Hayashi K, Groshen S, Salonga D, Cohen H, Laine L, Crookes P, Silberman H, Baranda J, Konda B, and Leichman L. ERCC1 mRNA levels complement thymidylate synthase mRNA levels in predicting response and survival for gastric cancer patients receiving combination cisplatin and fluorouracil chemotherapy. *J Clin Oncol.* 16(1) 309–316, 1998.

Miller VA, Hirsh V, Cadranel J, Chen YM, Park K, Kim SW, Zhou C, Su WC, Wang M, Sun Y, Heo DS, Crino L, Tan EH, Chao TY, Shahidi M, Cong XJ, Lorence RM, Yang JC. Afatinib versus placebo for patients with advanced, metastatic non-small-cell lung cancer after failure of erlotinib, gefitinib or both, and one or two lines of chemotherapy (LUX-Lung 1): a phase 2b/3 randomized trial. *Lancet Oncol.* 13:528-38, 2012

Mo N, Lu YK, Xie WM, Liu Y, Zhou WX, Nong L, Jia YX, Tan AH, Chen Y, Li SS and Luo BH. Inhibition of autophagy enhances the radiosensitivity of nasopharyngeal carcinoma expression. *Oncol Rep.* 32(5):1905-12, 2014.

Moeller BJ, Cao Y, Li CY, and Dewhirst MW. Radiation activates HIF-1 to regulate vascular radiosensitivity in tumors: role of reoxygenation, free radicals, and stress granules. *Cancer Cell.* 5:429–41, 2004.

Monsma DJ, Monks NR, Cherba DM, Dylewski D, Eugster E, Jahn H, Srikanth S, Morad SA and Cabot MC. Ceramide-orchestrated signaling in cancer cells. *Nat Rev Cancer.* 13(1):51e65, 2013.

Morita KI, Takeda K, Minowa O, Miyazono K, Noda T and Ichijo H. ASK1 is required for sustained activations of JNK/p38 MAP kinases and apoptosis. *EMBO Rep.* 2:222-228, 2001.

Munger K, Werness BA, Dyson N, Phelps WC, Harlow E, and Howley PM. Complex formation of human papillomavirus E7 proteins with the retinoblastoma tumor suppressor gene product. *EMBO J.* 8:4099–105, 1989.

Nagpal JK, Patnaik S and Das BR. Prevalence of high-risk human papilloma virus types and its association with p53 codon 72 polymorphism in tobacco addicted oral squamous cell carcinoma (OSCC) patients of Eastern India. *Int J Cancer.* 97:649-653, 2002.

Nakanishi T and Ross DD. Breast cancer resistance protein (BCRP/ABCG2): its role in multidrug resistance and regulation of its gene expression. *Chin J Cancer.* 31:73–99, 2012.

Neilson KA, Ali NA, Muralidharan S, Mirzaei M, Mariani M, Assadourian G, Lee A, van Sluyter SC and Haynes PA. Less label, more free: approaches in label-free quantitative mass spectrometry. *Proteomics.* 11(4):535-53, 2011.

Nelson KJ, Knutson ST, Soito L, Klomsiri C, Poole LB and Fetrow JS. Analysis of the peroxiredoxin family: using active-site structure and sequence information for global classification and residue analysis. *Proteins.* 79(3):947-64, 2011.

Nishimura T, Newkirk K, Sessions RB, Andrews PA, Trock BJ, Rasmussen AA, Montgomery EA, Bischoff EK and Cullen KJ. Immunohistochemical staining for glutathione-S-transferase predicts response to platinum-based chemotherapy in head and neck cancer. *Clin. Cancer Res.* 2(11):1859–1865, 1996.

Noh YH, Baek JY, Jeong W, Rhee SG, and Chang TS. Sulfiredoxin translocation into mitochondria plays a crucial role in reducing hyperoxidized peroxiredoxin III. *J Biol Chem.* 284:8470–8477, 2009.

Nonn L, Berggren M and Powis G. Increased expression of mitochondrial peroxiredoxin-3 (thioredoxin peroxidase-2) protects cancer cells against hypoxia and drug-induced hydrogen peroxide-dependent apoptosis. *Mol Cancer Res.* 1:682-689, 2003.

Ongkeko WM, Altuna X, Weisman RA, and Wang-Rodriguez J. Expression of protein tyrosine kinases in head and neck squamous cell carcinomas. *Am J Clin Pathol* 124:71–6, 2005.

Overgaard J. Hypoxic modification of radiotherapy in squamous cell carcinoma of the head and neck--a systematic review and meta-analysis. *Radiother Oncol.* 100:22–32, 2011.

Pardoll DM. The blockade of immune checkpoints in cancer immunotherapy. *Nat Rev Cancer.* 12:252-64, 2012.

Park JY, Schantz SP, Stern JC, Kaur T and Lazarus P. Association between glutathione S-transferase π genetic polymorphisms and oral cancer risk. *Pharmacogenetics.* 9: 497-504, 1999.

Park SH, Chung YM, Lee YS, Kim HJ, Chae HZ, and Yoo YD. Antisense of human peroxiredoxin II enhances radiation-induced cell death. *Clin Cancer Res.* 6(12):4915-20, 2000.

Pedersen MW, Jacobsen HJ, Koefoed K, Hey A, Pyke C, Haurum JS and Kragh M. Sym004: a novel synergistic anti-epidermal growth factor receptor antibody mixture with superior anticancer efficacy. *Cancer Res.* 70:588–597, 2010.

Pedicini P, Nappi A, Strigari L, Jerezek-Fossa BA, Alterio D, Cremonesi M, Botta F, Vischioni B, Caivano R, Fiorentino A, Improta G, Storto G, Benassi M, Orecchia R and Salvatore M. Correlation between EGFR expression and accelerated proliferation during radiotherapy of head and neck squamous cell carcinoma. *Radiat Oncol.* 7:143, 2012.

Peña-Rico MA, Calvo-Vidal MN, Villalonga-Planells R, Martinez-Soler F, Gimenez-Bonafe P, Navarro-Sabate A, Tortosa A, Bartrons R and Manzano A. TP53 induced glycolysis and apoptosis regulator (TIGAR) knockdown results in radiosensitization of glioma cells. *Radiother Oncol.* 101:132–9, 2011.

Perkins A, Nelson KJ, Parsonage D, Poole LB, and Karplus PA. Peroxiredoxins: guardians against oxidative stress and modulators of peroxide signaling. *Trends Biochem Sci.* 40:435–45, 2015.

Perri F, Pacelli R, Scarpati GDV, Cella L, Giuliano M, Caponigro F and Pepe S. Radioresistance in head and neck squamous cell carcinoma: biological bases and therapeutic implications. *Head Neck.* 37(5):763-70, 2015.

Petersen DR and Doorn JA. Reactions of 4-hydroxynonenal with proteins and cellular targets. *Free Radic Biol Med.* 37: 937–945, 2004.

Peysner ND, Pendleton K, Gooding WE, Lui VW, Johnson DE, and Grandis JR. Genomic and transcriptomic alterations associated with STAT3 activation in head and neck cancer. *PLoS One.* 11(11):166-185, 2016.

Philips GK and Atkins M. Therapeutic uses of anti-PD-1 and anti-PD-L1 antibodies. *Int Immunol.* 27:39–46, 2015.

Poetsch M, Lorenz G, and Kleist B. Detection of new PTEN/ MDM2 mutations in head and neck squamous cell carcinomas with loss of chromosome 10. *Cancer Genet Cytogenet.* 132:20–24, 2002.

Qiao Y, Spitz MR, Shen H, Guo Z, Shete S, Hedayati M, Grossman L, Mohrenweiser H and Wei Q. Modulation of repair of ultraviolet damage in the host-cell reactivation assay by polymorphic XPC and XPD/ERCC2 genotypes. *Carcinogenesis.* 23: 295-299, 2002.

Raleigh JA, Calkins-Adams DP, Rinker LH, Ballenger CA, Weissler MC, Fowler WC Jr., Novotny DB and Varia MA. Hypoxia and vascular endothelial growth factor expression in human squamous cell carcinomas using pimonidazole as a hypoxia marker. *Cancer Res.* 58(17):3765-8, 1998.

Ramachandran S, Ramadas K, Hariharan R, Kumar RR and Pillai MR. Single nucleotide polymorphisms of DNA repair genes XRCC1 and XPD and its molecular mapping in Indian oral cancer. *Oral Oncol.* 42: 350-362, 2006.

Rampias T, Sasaki C, and Psyrrri A. Molecular mechanisms of HPV induced carcinogenesis in head and neck. *Oral Onc.* 50:356-363. 2014.

Reisz JA, Bansal N, Qian J, Weiling Z and Furdui CM. Effects of ionizing radiation on biological molecules – mechanisms of damage and emerging methods of detection. *Antioxid Redox Signal.* 21(2):261-292, 2014.

Ribeiro KC, Kowalski LP, and Latorre MR. Impact of comorbidity, symptoms, and patients' characteristics on the prognosis of oral carcinomas. *Arch Otolaryngol Head Neck Surg.* 126:1079-1085, 2001.

Schmidt-Ullrich RK. Molecular targets in radiation oncology. *Oncogene.* 22:5730-5733, 2003.

Schoenfeld JD. Immunity in head and neck cancer. *Cancer Immunol Res.* 3:12-7, 2015.

Seitz HK and Stickel F. Molecular mechanisms of alcohol mediated carcinogenesis. *Nat Rev Cancer.* 7:599-612, 2007.

Seiwert TY, Fayette J, Cupissol D, del Campo JM, Clement PM, Hitt R, Degardin M, Zhang W, Blackman A, Ehrnrooth E, and Cohen EEW. A randomized, phase II study of afatinib versus cetuximab in metastatic or recurrent squamous cell carcinoma of the head and neck. *Annals of Oncology.* 25:1813-1820, 2014.

Seiwert TY, Burtneß B, Mehra R, Weiss J, Berger R, Eder JP, Heath K, McClanahan T, Lunceford J, Gause C, Cheng JD, and Chow LQ. Safety and clinical activity of pembrolizumab for treatment of recurrent or metastatic squamous cell carcinoma of the head and neck (KEYNOTE-012): an open-label, multicenter, phase 1b trial. *Lancet Oncol.* 17:956-65, 2016.

Selak MA, Armour SM, MacKenzie ED, Boulahbel H, Watson DG, Mansfield KD, Pan Y, Simon MC, Thompson CB and Gottlieb E. Succinate links TCA cycle dysfunction to oncogenesis by inhibiting HIF- α prolyl hydroxylase. *Cancer Cell.* 7:77–85, 2005.

Semenza GL. Oxygen-dependent regulation of mitochondrial respiration by hypoxia-inducible factor 1. *Biochem J.* 405:1–9, 2007.

Semenza GL. Regulation of cancer cell metabolism by hypoxia inducible factor 1. *Semin Cancer Biol.* 19:12–16, 2009.

Semenza GL. Targeting HIF-1 for cancer therapy. *Nat Rev Cancer.* 3:721–32, 2003.

Seo YH and Carroll KS. Profiling protein thiol oxidation in tumor cells using sulfenic acid-specific antibodies. *Proc Natl Acad Sci USA.* 106:16163–16168, 2009.

Serbagi-Vernat S, Differding S, Sterpin E, Hanin FX, Labar D, Bol A, Lee JA and Gregoire V. Hypoxia-guided adaptive radiation dose escalation in head and neck carcinoma: a planning study. *Acta Oncol.* 54(7):1008-16, 2015.

Sharma PK, Varshney R. 2-Deoxy-D-glucose and 6-aminonicotin-amide-mediated Nrf2 down regulation leads to radiosensitization of malignant cells via abrogation of GSH-mediated defense. *Free Radic Res.* 46:1446–57, 2012.

She Q, Solit D, Basso A, and Moasser MM. Resistance to gefitinib (ZD1839, Iressa) in PTEN null HER overexpressing tumor cells can be overcome through restoration of PETN function or pharmacologic modulation of constitutive PI3k/Akt pathway signaling. *Clin Cancer Res.* 9:4340–6, 2003.

Shin DM and Khuri FR. Advances in the management of recurrent or metastatic squamous cell carcinoma of the head and neck. *Head and Neck.* 35(3):443-53, 2013.

Siegel RL, Miller KD, and Jemal A. Cancer Statistics, 2017. *Ca Cancer J Clin.* 00:00-00, 2017.

Silva P, Homer JJ, Slevin NJ, Musgrove BT, Sloan P, Price P and West CM. Clinical and biological factors affecting response to radiotherapy in patients with head and neck cancer. *Clin Otolaryngol.* 32(5):337-45, 2007.

Silverman S Jr. Demographics and occurrence of oral and pharyngeal cancers. The outcomes, the trends, the challenge. *J Am Dent Assoc.* 132:7–11S, 2001.

Singh A and Singh H. Time-scale and nature of radiation biological damage: approaches to radiation protection and post-irradiation therapy. *Prog Biophys Mol Biol.* 39: 69–107, 1983.

Siu LL, Soulieres D, Chen EX, Pond GR, Chin SF, Francis P, Harvey L, Klein M, Zhang W, Dancey J, Eisenhauer EA, Winquist E, Princess Margaret Hospital Phase II Consortium, and National Cancer Institute of Canada Clinical Trials Group Study. Phase I/II trial of erlotinib and cisplatin in patients with recurrent or metastatic squamous cell carcinoma of the head and neck: a Princess Margaret Hospital phase II consortium and National Cancer Institute of Canada Clinical Trials Group Study. *J Clin Oncol.* 25:2178–2183, 2007.

Skartved NJ, Jacobsen HJ, Pedersen MW, Jensen PF, Sen JW, Jorgensen TK, Hey A and Kragh M. Preclinical pharmacokinetics and safety of Sym004: a synergistic antibody mixture directed against epidermal growth factor receptor. *Clin Cancer Res.* 17:5962–5972, 2011.

Smith L, Welham KJ, Watson MB, Drew PJ, Lind MJ and Cawkwell L. The proteomic analysis of cisplatin resistance in breast cancer cells. *Oncol. Res.* 16(11)497–506, 2007.

Smith LP and Thomas GR. Animal models for the study of squamous cell carcinoma of the upper aerodigestive tract: A historical perspective with review of their utility and limitations. Part A. chemically-induced *de novo* cancer, syngeneic animal models of HNSCC, animal models of transplanted xenogeneic human tumors. *Int J Cancer.* 118:2111-2122, 2006.

Sobotta MC, Liou W, Stocker S, Talwar D, Oehler M, Ruppert T, Scharf AND, and Dick TP. Peroxiredoxin-2 and STAT3 form a redox relay for H₂O₂ signaling. *Nat Chem Biol.* 11:64-70, 2015.

Sohal RS and Weindruch R. Oxidative stress, caloric restriction, and aging. *Science.* 273:59–63, 1996.

Sok JC, Coppelli FM, Thomas SM, et al. Mutant epidermal growth factor receptor (EGFRvIII) contributes to head and neck cancer growth and resistance to EGFR targeting. *Clin Cancer Res.* 12:5064–5073, 2006.

Solier S, Sordet O, Kohn KW and Pommier Y. Death receptor-induced activation of the Chk2- and histone H2AX-associated DNA damage response pathways. *Mol Cell Biol.* 29:68-82, 2009.

Soltoff SP, Carraway III KL, Prigent SA, Gullick WG and Cantley LC. ErbB3 is involved in activation of phosphatidylinositol 3-kinase by epidermal growth factor. *Mol Cell Biol.* 14:3550–8, 1994.

Somers KD, Merrick MA, Lopez ME, Incognito LS, Schechter GL, and Casey G. Frequent p53 mutations in head and neck cancer. *Cancer Res.* 52:5997–6000, 1992.

Soulieres D, Senzer NN, Vokes EE, Hidalgo M, Agarwala SS, and Siu LL. Multicenter phase II study of erlotinib and oral epidermal growth factor receptor tyrosine kinase inhibitor, in patients with recurrent or metastatic squamous cell cancer of the head and neck. *J Clin Oncol.* 22:77–85, 2004.

Stokvis E, Rosing H, and Beijnen JH. Liquid chromatography-mass spectrometry for the quantitative bioanalysis of anticancer drugs. *Mass Spectrom Rev.* 24(6):887-917, 2005.

Sturgis EM, Zheng R, Li L, Castillo EJ, Elcher SA, Chen M, Strom SS, Spitz MR, and Wei Q. XPD/ERCC2 polymorphisms and risk of head and neck cancer: a case-control analysis. *Carcinogenesis.* 21: 2219-2223, 2000.

Taylor RJ, Chan SL, Wood A, Voskens CJ, Wofl JS, Lin W, Chapoval A, Schulze DH, Tian G, and Strome SE. FccRIIIa polymorphisms and cetuximab induced cytotoxicity in squamous cell carcinoma of the head and neck. *Cancer Immunol Immunother.* 58:997–100, 2009.

Thompson LH. Recognition, signaling, and repair of DNA double-strand breaks produced by ionizing radiation in mammalian cells: the molecular choreography. *Mutat Res.* 751: 158–246, 2012.

Tibbitt MW and Anseth KS. Hydrogels as extracellular matrix mimics for 3D cell culture. *Biotechnol Bioeng.* 103:655–663, 2009.

Tomkiewicz C, Hans S, Mucchielli MH, Agier N, Delacroix H, Marisa L, Brasnu D, Aggerbeck LP, Badoual C, Barouki R and Aggerbeck M. . A head and neck cancer tumor response-specific gene signature for cisplatin, 5-fluorouracil induction chemotherapy fails with added taxanes. *PLoS One.* 7: e47170, 2012.

Travis LB, Ng AK, Allan JM, Pui CH, Kennedy AR, Xu XG, Purdy JA, Applegate K, Yahalom J, Constine LS, Gilbert ES, and Boice JD Jr. Second malignant neoplasms and cardiovascular disease following radiotherapy. *J Natl Cancer Inst.* 104(5):357–370, 2012.

Ueda S, Nakamura H, Masutani H, Sasada T, Yonehara S Takabayashi A, Yamaoka Y, and Yodoi J. Redox regulation of caspase-3(-like) protease activity: regulatory roles of thioredoxin and cytochrome c. *J Immunol.* 161:6689-6695, 1998.

Unger K. Integrative radiation systems biology. *Radiat Onc.*9:21, 2014.

Ursini F and Bindoli A. The role of selenium peroxidases in the protection against oxidative damage of membranes. *Chem Phys Lipids.* 44: 255–276, 1987.

Valko M, Leibfritz D, Moncol J, Cronin MT, Mazur M and Tesler J. Free radicals and antioxidants in normal physiological functions and human disease. *Int J Biochem Cell Biol.* 39(1):44-84, 2007.

Valko M, Rhodes CJ, Moncol J, Izakovic M and Mazur M. Free radicals, metals and antioxidants in oxidative stress-induced cancer. *Chem Biol Interact.* 160(1):1-40, 2006.

Vander Heiden MG .Targeting cancer metabolism: a therapeutic window opens. *Nat Rev Drug Discov.* 10:671–684, 2011.

Van Tonder A, Joubert AM and Cromarty AD. Limitations of the 3-(4,5-dimethylthiazol-2-yl)-2,5-diphenyl-2H-tetrazolium bromide (MTT) assay when compared to three commonly used cell enumeration assays. *BMC Res Notes.* 8:47, 2015.

Varilla V, Atienza J, and Dasanu CA. Immune alterations and immunotherapy prospects in head and neck cancer. *Expert Opin Biol Ther.* 13:1241-56, 2013.

Vaupel P, Kallinowski F and Okunieff P. Blood flow, oxygen and nutrient supply, and metabolic microenvironment of human tumors: a review. *Cancer Res.* 49(23):6449-65, 1989.

Veldman T, Horikawa I, Barrett JC, and Schlegel R. Transcriptional activation of the telomerase hTERT gene by human papillomavirus type 16 E6 oncoprotein. *J Virol.* 75:4467–72, 2001.

Venuti A, Curzio G, Mariani L, and Paolini F. Immunotherapy of HPV-associated cancer: DNA/plant-derived vaccines and new orthotopic mouse models. *Cancer Immunol Immunother.* 64:1329-38, 2015.

Vermorken JB, Remenar E, van Herpen, Gorlia T, Mesia R, Degardin M, Stewart JS, Jelic S, Betka J, Preiss JH, van den Weyngaert D, Awada A, Cupissol D, Kienzer HR, Rey A, Desauois I, Bernier J, Lefebvre JL, and EORTC 24971/TAX 323 Study Group. Cisplatin, fluorouracil, and docetaxel in unresectable head and neck cancer. *N Engl J Med.* 357(17): 1695–704, 2007.

Vousden KH and Lu X. Live or let die: the cell's response to p53. *Nat Rev Cancer.* 2:594–604, 2002.

Wang X, Hu C, and Eisbruch A. Organ-sparing radiation therapy for head and neck cancer. *Nat Rev Clin Oncol.* 8(11):639–648, 2011.

Wanka C, Steinbach JP, and Rieger J. Tp53-induced glycolysis and apoptosis regulator (TIGAR) protects glioma cells from starvation-induced cell death by up-regulating respiration and improving cellular redox homeostasis. *J Biol Chem.* 287:33436–46, 2012.

Watson WH, Yang X, Choi YE, Jones DP, and Kehrer JP. Thioredoxin and its role in toxicology. *Toxicolog Sci.* 78:3-14, 2004.

Wenk J, Brenneisen P, Wlaschek M, Pswig A, Briviba K, Overley TD and Scharffetter-Kochanek K. Stable overexpression of manganese superoxide dismutase in mitochondria identifies hydrogen peroxide as a major oxidant in AP-1 mediated induction of matrix-degrading metalloprotease-1. *J Biol Chem.* 274(36):25869-76, 1999.

Woo HA, Yim SH, Shin DH, Kang D, Yu DY, and Rhee SG. Inactivation of peroxiredoxin I by phosphorylation allows localized H₂O₂ accumulation for cell signaling. *Cell.* 140:517–28, 2010.

Wood ZA, Schroder E, Robin Harris J, and Poole LB. Structure, mechanism and regulation of peroxiredoxins. *Trends Biochem Sci.* 28:32–40, 2003.

Wood ZA, Poole LB, and Karplus PA. Peroxiredoxin evolution and the regulation of hydrogen peroxide signaling. *Science.* 300:650-653, 2003.

Wu PY, Frit P, Malivert L, Revy P, Biard D, Salles B and Calsou P. Interplay between Cernunnos-XLF and nonhomologous end-joining proteins at DNA ends in the cell. *J Bio Chem.* 282:31937- 31943, 2007.

Xuelei M, Jingwen H, Wei D, Hongyu Z, Jing Z, Changle S and Lei L. ERCC1 plays an important role in predicting survival outcomes and treatment response for patients with HNSCC: a meta-analysis. *Oral Oncol.* 51(5)483–492, 2015.

Yaromina A, Krause M, and Baumann M. Individualization of cancer treatment from radiotherapy perspective. *Mol Oncol.* 6: 211–21, 2012.

Yu J and Zhang L. PUMA, a potent killer with or without p53. *Oncogene.* 27 Suppl 1:S71–S83, 2008.

Zeng L, Morinibu A, Kobayashi M, Zhu Y, Wang X, Goto Y, Yeom CJ, Zhao T, Hirota K, Shinomiya K, Itasaka S, Yoshimura M, Guo G, Hammond EM, Hiraoka M and Harada H. Aberrant IDH3alpha expression promotes malignant tumor growth by inducing HIF-1-mediated metabolic reprogramming and angiogenesis. *Oncogene.* 34:4758–66, 2015.

Zhang H, Bosch-Marce M, Shimoda LA, Tan YS, Baek JH, Wesley JB, Gonzalez FJ and Semenza GL. Mitochondrial autophagy is an HIF-1-dependent adaptive metabolic response to hypoxia. *J Biol Chem.*283:10892–903, 2008.

Zhang M, Qureshi AA, Geller AC, Frazier L, Hunter DJ, and Han J. Use of tanning beds and incidence of skin cancer. *J Clin Oncol.* 30: 1588–1593, 2012.

Zhao M, Sano D, Pickering CR, Jasser SA, Henderson YC, Clayman GL, Sturgis EM, Ow TJ, Lotan R, Carey TE, Sacks PG, Grandis JR, Sidransky D, Heldin NE and Myers JN. Assembly and initial characterization of a panel of 85 genomically validated cell lines from diverse head and neck tumor sites. *Clin Cancer Res.* 17(23):7248-64, 2011.

Zhu W, Smith JW, and Huang CM. Mass spectrometry-based label-free quantitative proteomics. *J Biomed Biotechnol.* 2010:840518, 2010.

Zietarska M, Maugard CM, Filali-Mouhim A, Alam-Fahmy M, Tonin PN, Provencher DM and Mes-Masson AM. Molecular description of a 3D in vitro model for the study of epithelial ovarian cancer (EOC). *Mol Carcinog.* 46:872–885, 2007.

CHAPTER 2

Broad Phenotypic Changes Associated With Gain of Radiation Resistance in Head and Neck Squamous Cell Cancer

Jade Mims*¹, Nidhi Bansal*¹, Jeffrey G. Kuremsky², Amy L. Olex³, Weiling Zhao¹, Leimiao Yin¹, Revati Wani¹, Jiang Qian¹, Brian Center¹, Glen S. Marrs⁴, Mercedes Porosnicu⁵, Jacquelyn S. Fetrow³, Allen W. Tsang¹, Cristina M. Furdui¹

¹Section on Molecular Medicine, Department of Internal Medicine, Wake Forest School of Medicine, Winston-Salem, NC

²Department of Radiation Oncology, Wake Forest School of Medicine, Winston-Salem, NC

³Department of Computer Science, Wake Forest University, Winston-Salem, NC

⁴Department of Biology, Winston-Salem, NC

⁵Section of Hematology and Oncology, Department of Internal Medicine, Wake Forest School of Medicine, Winston-Salem, NC

*authors contributed equally

The following manuscript was published in the *Antioxidant Redox Signaling*, volume 21, pages 221 – 236, March 2014 and is reprinted with permission. The stylistic variations are due to the requirements of the journal.

ABSTRACT

Aims: The central issue of resistance to radiation remains a significant challenge in the treatment of cancer despite improvements in treatment modality and emergence of new therapies. To facilitate the identification of molecular factors that elicit protection against ionizing radiation, we developed a matched model of radiation resistance for head and neck squamous cell cancer (HNSCC) and characterized its properties using quantitative mass spectrometry and complementary assays. **Results:** Functional network analysis of proteomics data identified DNA replication and base excision repair, extracellular matrix-receptor interaction, cell cycle, focal adhesion, and regulation of actin cytoskeleton as significantly up- or downregulated networks in resistant (rSCC-61) HNSCC cells. Upregulated proteins in rSCC-61 included a number of cytokeratin's, fatty acid synthase, and antioxidant proteins. In addition, the rSCC-61 cells displayed two unexpected features compared with parental radiation-sensitive SCC-61 cells: (i) rSCC-61 had increased sensitivity to Erlotinib, a small molecule inhibitor of epidermal growth factor receptor; and (ii) there was evidence of mesenchymal-to epithelial transition in rSCC-61, confirmed by the expression of protein markers and functional assays (e.g. Vimentin, migration). **Innovation:** The matched model of radiation resistance presented here shows that multiple signaling and metabolic pathways converge to produce the rSCC-61 phenotype, and this point to the function of the antioxidant system as a major regulator of resistance to ionizing radiation in rSCC-61, a phenomenon further confirmed by analysis of HNSCC tumor samples. **Conclusion:** The rSCC-61/SCC-61 model provides the opportunity for future investigations of the redox-regulated mechanisms of response to combined radiation and Erlotinib in a preclinical setting.

INTRODUCTION

Head and neck squamous cell cancer (HNSCC) is the eighth most common cause of cancer death worldwide, and it accounts for 3% to 4% of cancers in the United States (26). The treatment options available for HNSCC patients rely primarily on various combinations of surgery, radiation, and chemotherapy, depending on the stage and resectability of the disease. Many patients are, however, medically unfit for surgery or have unresectable tumors because of the disease extent or involvement of critical structures. To alleviate the substantial toxicity associated with the combined radiation and chemotherapy regimens that are often prescribed for these patients, the focus has shifted recently toward the use of targeted agents alone or in combination with surgery, radiation, or chemotherapy. Epidermal growth factor receptor (EGFR) constitutes an attractive target for the treatment of HNSCC for a number of reasons: (i) EGFR protein is increased in > 80% of HNSCC tumors (8); (ii) Cetuximab, a monoclonal antibody against EGFR, was shown to improve the response to radiation in patients with locally advanced HNSCC and is currently approved for clinical use (9); and (iii) there are a number of small-molecule inhibitors against EGFR that have shown clinical success for the treatment of a number of cancers. Erlotinib (Tarceva) is one such small-molecule EGFR inhibitor currently in clinical trials for the treatment of HNSCC and non-small cell lung cancer. The goal of the studies presented here was to establish a clinically relevant *in vitro* model of resistance to radiation that would enable us to investigate the mechanisms contributing to radiation resistance, the response to Erlotinib, and the interconnecting networks which may regulate the response to radiation with the use of targeted agents.

Most reported studies investigating the resistance to radiation involve a comparative analysis of cancer cell lines established from patients with distinct genetic backgrounds and complex medical and treatment histories (32). A better understanding of resistance to radiation can be achieved by investigating the molecular and cellular features that characterize a clonal population which is resistant to radiation in matched cell lines. In this study, we generated a radiation resistant head

and neck cancer cell line (rSCC-61) from the radiation-sensitive SCC-61 cell line by fractionated radiation. We characterized the two cell lines in terms of their proteomic composition, survival in response to radiation and Erlotinib treatment, metabolic features, and a number of other parameters to unveil the mechanisms of resistance to radiation and response to Erlotinib in HNSCC. The most unexpected findings of our studies were the increased sensitivity to Erlotinib and the emergence of epithelial phenotype in rSCC-61 cells relative to the parental SCC-61 cells, which were Erlotinib resistant and had mesenchymal properties. This is significant in the context of recent studies showing the presence of both mesenchymal and epithelial cells in tumors of advanced-stage HNSCC (5, 39). Thus, the findings presented here have profound clinical implications for identifying molecular markers of radiation resistance that are associated with epithelial cell types in HNSCC and may offer selective avenues for drug targeting of epithelial radiation-resistant HNSCC cells in tumors.

Results

Generation of a matched model of radiation resistance for HNSCC and its primary characterization

The radiation-sensitive SCC-61 cells previously derived from an HNSCC tumor located at the base of the tongue (52) were treated in vitro with fractionated radiation (2 Gy) for a cumulative total of 16 Gy. The resulting cell population was plated at a low density on soft agar, and eight single-cell derived colonies were picked and expanded in culture. The clone R8E, hereafter called rSCC-61, was randomly selected for further investigation.

Cell morphology. The first noted difference between the SCC-61 and the rSCC-61 cells was their morphology. The SCC-61 cells were round and larger in size, while the rSCC-61 was spindle shaped and smaller. To quantify the change in morphology, we calculated the nucleus-to-cytoplasm ratio (NCR) using imaging analysis (**Fig. 1A**). The results show an approximately twofold higher NCR in rSCC-61 (1.1 – 0.05) compared with SCC-61 (0.5 – 0.01) (**Fig. 1B**). A potential explanation for the increased NCR in rSCC-61 is provided by the quantitative

proteomics analysis below, indicating the down regulation of proteins involved in cytoskeletal organization in rSCC-61.

Response to radiation treatment. Clonogenic assays were performed to determine the radiation response parameters for the SCC-61 and rSCC-61 cells (**Fig. 1C and Appendix S2 Table S1**). The D₀ values for rSCC-61 and SCC-61 were 2.04 and 1.3, respectively, confirming the acquisition of a radiation-resistant phenotype in rSCC-61. The results for rSCC-61 are comparable with other HNSCC cell lines that are isolated from radiation-resistant tumors (46, 51).

Cell cycle analysis. Cell cycle analysis was performed at 24 h after treatment with ionizing radiation. In the absence of radiation, the SCC-61 and rSCC-61 cells showed a similar distribution of cells in the G₁, S, and G₂/M phases of the cell cycle (e.g., rSCC-61 51.0% – 5.2%, 34.1% – 0.1%, and 14.9% – 5.3%, respectively) (**Fig. 1D**). Treatment with 2 Gy radiation induced increased G₂/M arrest in SCC-61 cells (45% – 15.4%) compared with rSCC-61 (22.9% – 8.9%).

Response to Erlotinib treatment. The resistance to Erlotinib treatment of SCC-61 cells has been previously reported (30, 45). To determine whether the acquired resistance to radiation in rSCC-61 has affected the response to Erlotinib, cell viability assays were performed at increasing concentrations of Erlotinib (0.5 to 100 μ M). The IC₅₀ for rSCC-61 was 4.5 – 0.4 μ M compared with > 50 μ M for SCC-61 suggesting a more than 10-fold increase in sensitivity to Erlotinib in rSCC-61 (**Fig. 1E**). Tumors become resistant to targeted inhibitors of EGFR through diverse mechanisms, which include acquisition of oncogenic mutations (e.g., mutations that inhibit the binding of inhibitors to EGFR but do not decrease its kinase activity), activation of bypass pathways, epithelial-to-mesenchymal transformation (EMT), and others [reviewed in Ref. (13)]. Here, we first explored the status of EGFR and Akt expression and activation, as reports have correlated increased activation of EGFR/Akt with resistance to EGFR inhibitors (11, 19). The phosphorylation status of EGFR and its downstream signaling molecule Akt in SCC-61 and

rSCC-61 cells was monitored using Western blot analysis. The results show a decrease in EGFR signaling in rSCC-61 cells by 50% despite an overall increase in tyrosine phosphorylation in rSCC-61 (**Fig. 1F**). The difference in EGFR phosphorylation is consistent with the response to Erlotinib and literature cited earlier. In addition to EGFR phosphorylation, the response to Erlotinib has also been linked to the regulation of integrin expression (27), lipid rafts content (25), and EMT (16). The results described next for the SCC-61/rSCC-61 system are consistent with all these independent studies. The finding of acquired sensitivity to Erlotinib further increases the value of the SCC-61/rSCC-61 cell model that now enables the investigation of the mechanisms of response to Erlotinib in the background of a matched radiation-resistant and radiation-sensitive cell model. It also points to the importance of pursuing clinical trials to investigate the treatment of head and neck tumors with Erlotinib, as tumors that are resistant to radiation may respond to Erlotinib treatment.

Quantitative proteomic analysis of SCC-61 and rSCC-61

To identify the underlying molecular mechanisms of the acquired resistance to radiation in rSCC-61, a quantitative proteomics analysis of SCC-61 and rSCC-61 was performed using stable isotope labeling with amino acids in cell culture (SILAC) and mass spectrometry. The experimental design is summarized in **Figure 2A**. The SCC-61 and rSCC-61 cells were cultured in medium containing light (SCC-61) and heavy (rSCC-61) isotopes of lysine and arginine. The SCC-61 and rSCC-61 lysates were then normalized with regard to their protein concentration, combined in a 1:1 ratio, and analyzed using a Thermo LTQ Orbitrap mass spectrometer. The data were processed using the Proteome Discoverer 1.2 (Thermo Fisher Scientific) and searched against the UniProtKB human database. The results were filtered using a false discovery rate of 1%, which yielded quantitative data for 965 proteins. Data in **Figure 2B** show the distribution of protein ratios in rSCC-61 versus SCC-61 (heavy/light) for 920 proteins whose ratios range from 0.017 to 50.5. The remaining 45 proteins listed in **Appendix S2 Table 2** had a ratio of less than

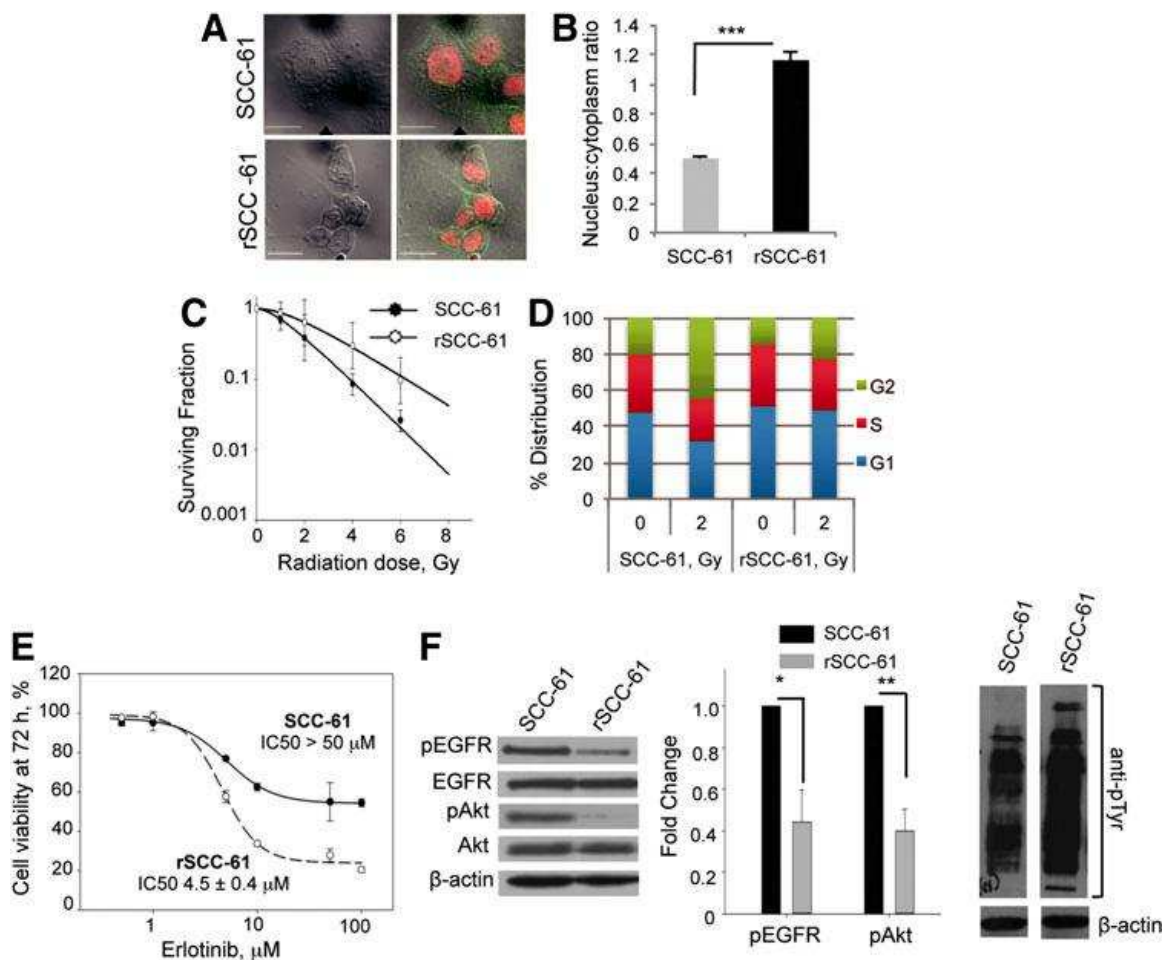


FIG. 1. rSCC-61 exhibits increased resistance to radiation and increased sensitivity to Erlotinib in comparison to SCC-61. (A) Cell morphology. The SCC-61 and rSCC-61 cells were immunostained with anti-EGFR antibodies, and the nucleus was stained with Topro-3-iodide to mark the cell and nuclear boundaries, respectively. Images were acquired using the Zeiss LSM510 confocal microscope. The scale bars represent a distance of 20 μm. (B) Quantification of nucleus-to-cytoplasm ratio (NCR). The NCR was quantitated using ImageJ software from confocal images shown in panel A (***) $p < 0.001$, $n = 50$ cells). (C) Clonogenic assay to determine the response to radiation. The survival curves of SCC-61 and rSCC-61 cells are shown in response to increasing doses of radiation. Data were fit to multi-target and linear-quadratic models. The values of D_0 , a and b parameters are listed in Appendix Table 1. (D) Cell-cycle analysis. The percent distribution of SCC-61 and rSCC-61 cells in the G1, S, and G2 phases of the cell cycle was determined at 24 h after treatment with the 0 and 2 Gy radiation doses. (E) Cell viability in response to Erlotinib treatment. MTT assay was used to measure cell viability at 72 h post-treatment with Erlotinib (0, 0.5, 1.0, 10.0, 25.0, 50.0, and 100.0 μM). The percentage of viable cells was calculated relative to the untreated control. (F) Western blot analysis of EGFR and Akt phosphorylation. SCC-61 and rSCC-61 cell lysates were immunoblotted with antibodies against pEGFR, total EGFR, pAkt, total Akt, total pTyr, and β-actin and quantified using ImageJ (pEGFR: * $p = 0.022$, $n = 3$; pAkt: ** $p = 0.004$, $n = 3$). EGFR, epidermal growth factor receptor; MTT, 3-(4,5-dimethylthiazol-2-yl)-2,5-diphenyltetrazolium bromide.

than 0.01, with the lower limit set in our quantitation algorithm. These are proteins that are more than 100-fold downregulated in rSCC-61 and were considered separately in an effort to avoid bias in the downstream computational analysis. Ingenuity Pathway Analysis (IPA) was used to analyze the 920 and 45 proteins datasets (i) to determine the distribution of subcellular locations and protein functions, and (ii) to identify biological networks and molecular functions that are enriched in proteins significantly which are up- or downregulated in rSCC-61. Overall, the most upregulated proteins in rSCC-61 were keratins (> 8-fold upregulation) followed by a 6.8-fold increase in the fatty acid synthase (FASN) (**Fig. 2C**) and a number of other proteins such as the deoxyuridine 5'-triphosphate nucleotidohydrolase (DUT), peroxiredoxins (PRX), and GSK3 β with a potential function in mediating the resistance to radiation in rSCC-61 (an extended list is included in **Appendix S2 Table 3**) [e.g., GSK3 β (33); FASN (29); PRX (41)]. The distribution of subcellular locations and functions of the 920 proteins is shown in **Figure 2D**. The IPA core analysis of this dataset identified that among proteins which were downregulated in rSCC-61 cells, there was significant enrichment of proteins involved in cell death ($p < 0.001$; z score: -1.174) and apoptosis ($p < 0.001$; z score: -2.016) (**Appendix S2 Table 4**). Similarly, the IPA analysis of the 45 protein dataset indicated a decrease in cell death ($p < 0.001$), a decrease in cell migration ($p < 0.001$; Z-score: -2.354), and downregulation of EGF signaling in rSCC-61 ($p < 0.001$; z score: -2.574). These results are consistent with the increased survival of rSCC-61 in response to radiation and the anti-proliferative effect of Erlotinib in rSCC-61. Interestingly, 36% (16 proteins) of the 45 downregulated proteins are localized in the extracellular space (**Appendix S2 Fig. 1**). Among these, integrin alpha 6, thrombospondin 1, and vitronectin are required for the regulation of focal adhesion and extracellular matrix (ECM)-receptor interactions.

Mapping of proteomics data to KEGG and HPRD human interaction networks and functional analysis

Cytoscape version 2.8.2 (47) was used to mine and visualize interactions present in the 920-protein dataset as described in the “Materials and Methods” section. Two interaction

databases—the Kyoto Encyclopedia of Genes and Genomes (KEGG) (28) and the Human Protein Reference Database (HPRD) (43)—were used in the analysis. The KEGG database contains known canonical pathway interactions, while HPRD comprises known protein–protein interactions derived from experimental data, thus providing overlapping as well as distinct information. In order to identify which parts of these networks contained significantly altered proteins in rSCC-61 cells, all proteins with an absolute fold change of 2.0 or greater were extracted, along with first neighbors and all associated interactions, to create the KEGG interaction subnetwork containing 130 nodes and 264 interactions (**Appendix S2 Fig. 2**) and the HPRD interaction subnetwork containing 184 nodes and 141 interactions (**Fig. 3**). Annotation analysis was performed on the lists of UniProt accessions representing the proteins present in the KEGG (130 proteins) and HPRD (184 proteins) networks using the tools provided by the Database for Annotation, Visualization, and Integrated Discovery (DAVID) (23, 24). A number of significantly regulated canonical pathways ($p < 0.05$) in rSCC-61 cells were identified by these analyses: DNA replication and base excision repair, ECM-receptor interaction, cell cycle, focal adhesion, and regulation of actin cytoskeleton (**Fig. 3 and Appendix S2 Table 5A–E**). Complementary data to support these results and the significance of the findings to the radiation-resistant phenotype of rSCC-61 are presented in the next few sections.

Mesenchymal-to-epithelial transition in rSCC-61

Functional annotation of the KEGG and HPRD networks identified proteins involved in the regulation of actin cytoskeleton, focal adhesion, and ECM-receptor interaction ($p < 0.05$) in rSCC-61 to be significantly downregulated. Combined with the noted morphological differences between SCC-61 and rSCC-61 cells, and the observation that proteins such as keratins (KRT8, KRT18) and periplakin are upregulated in rSCC-61, these events point to a mesenchymal-to-epithelial transition in rSCC-61. To further confirm the epithelial phenotype in rSCC-61, we performed semi-quantitative PCR and Western blot analysis to evaluate the expression of traditional markers of mesenchymal-to-epithelial transition: E-cadherin and vimentin. In

comparison to SCC-61, the rSCC-61 cells displayed a higher expression of E-cadherin and a lower expression of vimentin, which was further confirmed by Western blot analysis (**Fig. 4A**). Another hallmark that differentiates between mesenchymal and epithelial cells is their migration properties. From the proteomics analysis, it was evident that rSCC-61 exhibits reduced ECM-receptor interaction and focal adhesion, which are known mediators of migration (relative change of integrins and other proteins mapping to the ECM receptor interaction and focal adhesion networks is shown in **Fig. 4B and Appendix S2 Tables 5D and 5E**) (48, 49). A trans-well migration assay was performed and confirmed the significantly lower migration of rSCC-61 relative to the SCC-61 cells ($p < 0.001$; **Fig. 4C**). Cumulatively, these results point to a transition from mesenchymal phenotype in SCC-61 toward an epithelial phenotype in rSCC-61.

Measurement of intracellular and extracellular lactic acid

Lactic acid has been reported as one of the metabolic factors affecting migration (21). The proteomics data showed downregulation of lactate dehydrogenase A (LDH-A, threefold) and upregulation of lactate dehydrogenase-B (LDH-B, threefold) in rSCC-61, suggesting a shift from glucose routing into lactic acid synthesis in SCC-61 to pyruvate in rSCC-61 (**Fig. 5A**). To determine the intracellular and extracellular lactic acid in rSCC-61 and SCC-61 cells during cell growth, the lactic acid assay was performed as described in the “Appendix S2 Materials and Methods” section. Significantly higher levels of both intracellular and extracellular lactate were observed in SCC-61 cells at 48 and 72 h of cell growth (**Fig. 5B, C**). Extracellular pH of the two cell lines was also monitored at 4, 8, 24, 48, and 72 h after cell seeding, and the results show increased acidification of the extracellular environment in SCC-61 culture compared with rSCC-61 (**Fig. 5D**). Both the efflux of lactate and H^+ ions from inside the cell to the extracellular medium are likely contributing to the pH change (42). The mechanism of this dynamic process is not completely understood, and we will be investigating other potential sources that could lead to the observed differences in media acidification between the SCC-61 and rSCC-61 cells.

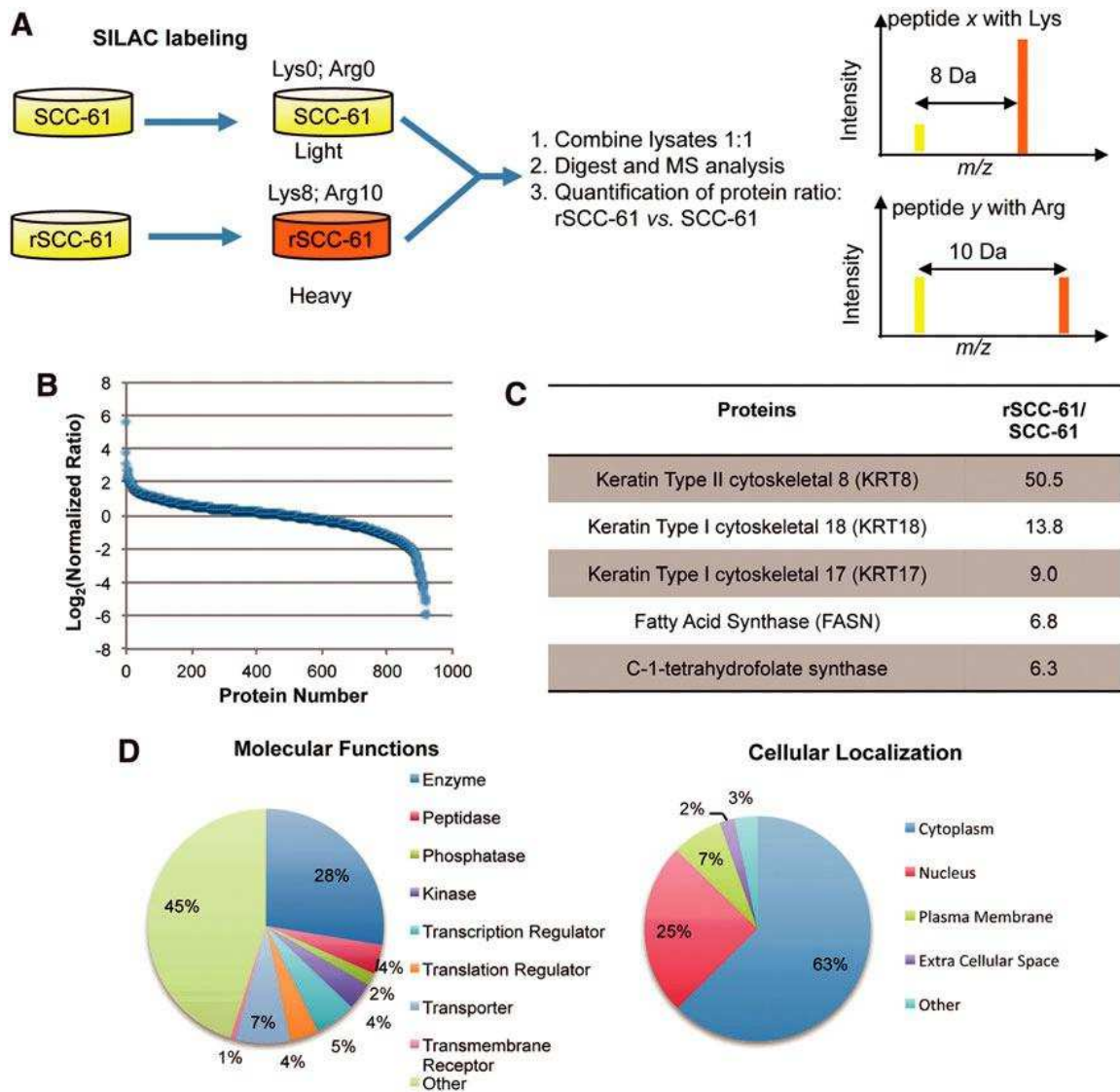


FIG. 2. Summary of quantitative proteomic analysis of SCC-61 and rSCC-61. (A) Schematic representation of mass spectrometry-based comparative proteomics approach. SCC-61 and rSCC-61 were cultured in media containing light and heavy isotopes of Lys and Arg as described in the “Materials and Methods” section. The normalized mixture of SCC-61 and rSCC-61 proteins lysates was analyzed by mass spectrometry. (B) Protein ratios in rSCC-61 versus SCC-61 (heavy/ light). The data were normalized to the median protein ratio. Approximately 30% of the proteins identified had altered protein status in rSCC-61 relative to SCC-61. (C) List of the top upregulated proteins in rSCC-61. The protein ratios generated by the SILAC proteomics analysis were arranged in descending order. An extended list is included in **Appendix Table 3**. (D) Cellular localization and functions of the proteins identified in the proteomic analysis. The list of 920 proteins with ratios between 0.017 and 50.5 was input into the IPA. The pie charts represent the classification of the proteins based on their cellular localization or functions. The pie charts corresponding to the entire 965 proteins dataset is included in Appendix Figure 1. IPA, Ingenuity Pathway Analysis; SILAC, stable isotope labeling with amino acids in cell culture.

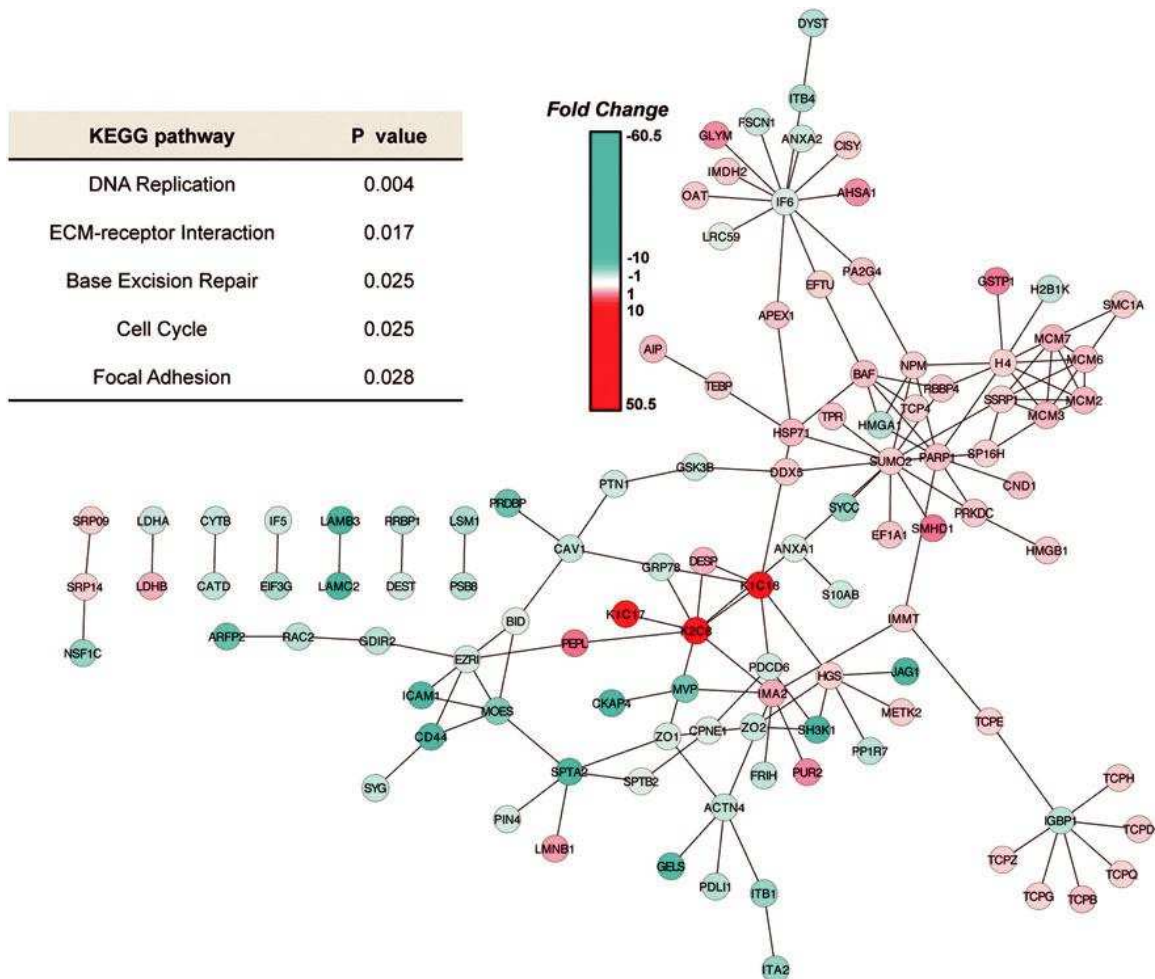


FIG. 3. Functional network analysis—Human Protein Reference Database (HPRD) interactions subnetwork. HPRD was used in Cytoscape version 2.8.2 to create a subnetwork consisting of significantly regulated nodes (≥ 2.0 or ≤ -2.0 -fold change). Node colors represent fold change, where red is upregulation and blue is downregulation as indicated by the color bar. DAVID analysis of the Uniprot IDs of these significantly regulated nodes identified 5 significantly over-represented ($p < 0.05$) pathways in this network, which are listed in the table on the left. DAVID, Database for Annotation, Visualization and Integrated Discovery.

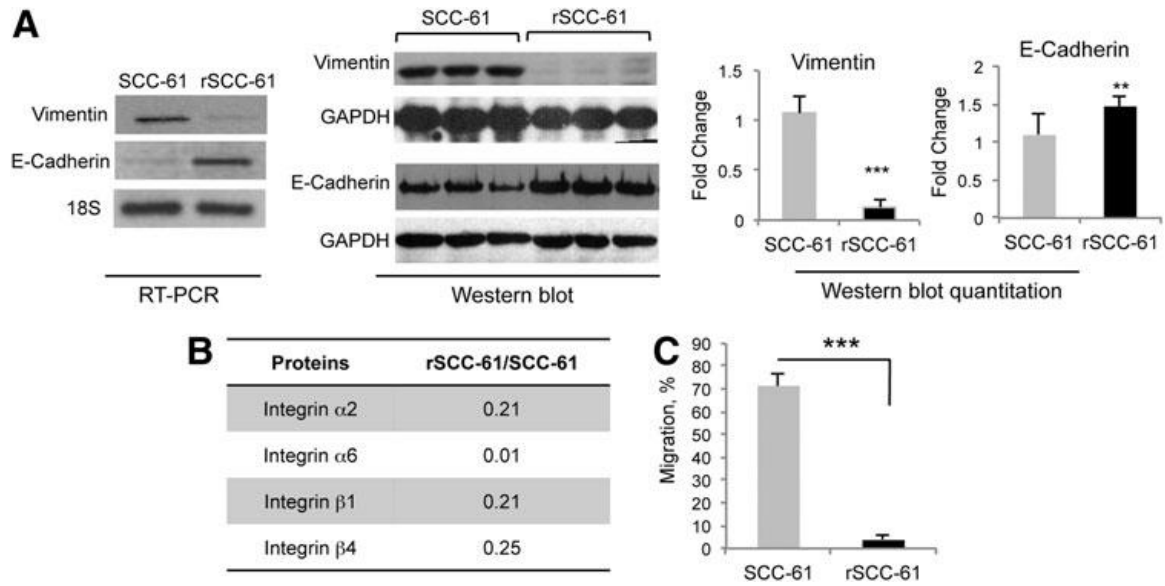


FIG. 4. rSCC-61 cells are associated with mesenchymal-to-epithelial transition (MET). (A) Semi-quantitative PCR and Western blot analysis of Vimentin and E-cadherin. The relative expression of vimentin and E-cadherin in SCC-61 and rSCC-61 was determined using semi-quantitative PCR ($n = 1$). 18S RNA amplification was used as endogenous control. Three out of five biological replicates are shown for the Western blot analysis; quantification is based on all five replicates and taking into account the differences in GAPDH (Vimentin: $***p < 0.001$, $n = 5$; E-cadherin: $**p = 0.01$, $n = 5$). (B) Table showing the protein ratio of integrin isoforms identified by the SILAC proteomics analysis. (C) Trans-well migration assay. The migration properties of SCC-61 and rSCC-61 cells were quantified using the trans-well migration assay described in the “Appendix Materials and Methods” section ($*** p < 0.001$, $n = 3$).

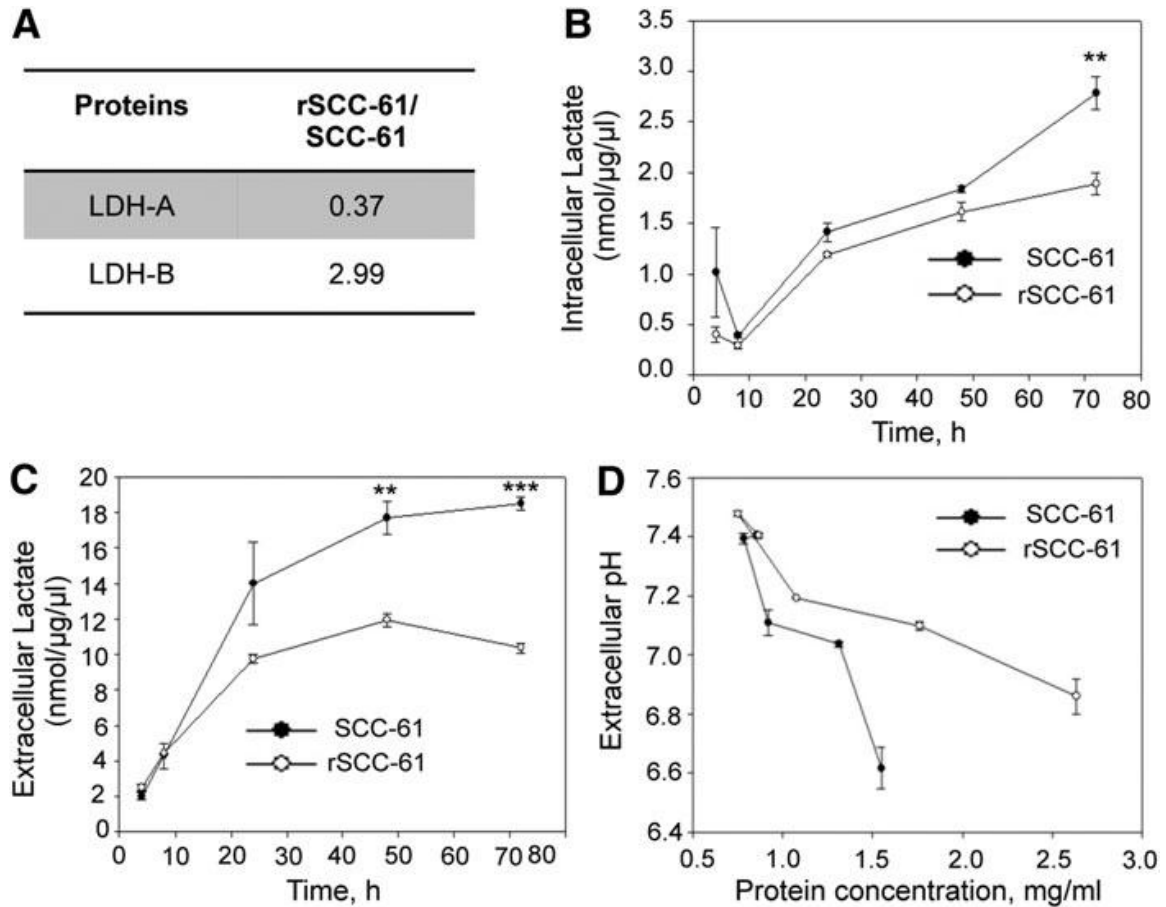


FIG. 5. The stoichiometry of LDH-A and LDH-B determines the pyruvate/lactate equilibrium. (A) Table showing the ratios of LDH-A and LDH-B in rSCC-61 and SCC-61 determined by the SILAC proteomic analysis. **(B, C)** Intracellular and extracellular lactate measurements. SCC-61 and rSCC-61 were harvested at different time intervals after seeding (4, 8, 24, 48, and 72 h). Total protein concentrations were estimated for each time point. The intracellular lactate levels were estimated and plotted against the respective time points **(B)** (72 h: ** $p = 0.01$, $n = 3$). Similarly, the extracellular lactate levels were estimated from the culture medium collected at each of the respective time points **(C)** (48 h: ** $p = 0.005$, $n = 3$; 72 h: *** $p = 0.001$, $n = 3$). **(D)** A decrease in extracellular pH with cell growth. The extracellular pH of the SCC-61 and rSCC-61 cells in culture was measured at 4, 8, 24, 48, and 72 h after seeding the cells. Protein concentration at each time point was measured and plotted on the x-axis. LDH-A, lactate dehydrogenase A.

Reactive oxygen species, the antioxidant system, and DNA damage in SCC-61 and rSCC-61 cells

Under normal conditions, physiological levels of reactive oxygen species (ROS) are under the tight control of the cellular antioxidant system, which is considered responsible for maintaining ROS below the threshold at which DNA damage can occur while enabling temporal and localized accumulation of these species when needed during cell growth. Cancer cells, however, are known to accumulate intracellular ROS, and numerous studies have linked ROS in cancer cells to processes such as DNA damage, response to therapies, cellular plasticity, and others (18). The proteomics analysis described here revealed the upregulation of a number of antioxidant proteins in rSCC-61 (**Appendix S2 Table 6**). The upregulation of proteins such as glutathione S-transferase pi (GSTpi) and PRX was also previously reported in a comparison study of the radiation-resistant AMC-HN9 and the radiation-sensitive AMC-HN3 head and neck cancer cell lines (32). Thus, one of our first goals was to assess the intracellular ROS in the SCC-61 and rSCC-61 cells and to validate the upregulation of antioxidant proteins. The dichlorofluorescein (DCF) staining and imaging analysis showed lower ROS in rSCC-61 compared with SCC-61 (**Fig. 6A**). Western blot analysis showed increased levels of antioxidant proteins such as Prx1, Prx 2, and GSTpi, thus further corroborating the proteomic findings (**Fig. 6B**). In addition, the higher ratio of superoxide dismutase (SOD) to catalase in SCC-61 offered reasoning for the higher ROS accumulation in SCC-61. We have further monitored the hyperoxidation of Prx proteins (Prx-SO₂/3, markers of oxidative stress) and PTEN expression and oxidation. PTEN is a known negative regulator of Akt and to be consistent with the pAkt results in **Figure 1F**, we posed that PTEN oxidation would be lower in rSCC-61 as a result of lower ROS and/or there would be increased expression of PTEN in rSCC-61. The analysis in **Figure 6B** shows a higher expression of PTEN in rSCC-61, thus confirming a part of our hypothesis. Due to the difference in protein expression, we could not reliably conclude whether there is a shift in protein migration (oxidized PTEN migrates slightly lower than the reduced protein). However, given the lower ROS in rSCC-61, it is unreasonable to hypothesize higher PTEN oxidation in this cell line.

Taking this together with increased expression of PTEN in rSCC-61, the results clearly point to combined EGFR and PTEN-mediated downregulation of Akt activity. The contribution of ROS to EGFR/Akt signaling will be further investigated in future using complementary approaches. Glutathione is another component of the antioxidant system that is implicated in the response to radiation (10, 37). We quantified total, oxidized, and reduced glutathione using the glutathione assay kit as described in the “Appendix Materials and Methods” section. While the total glutathione was significantly less in rSCC-61 than in SCC-61, the endogenous reduced glutathione was significantly higher in rSCC-61 (**Fig. 6C**). Nevertheless, the majority of glutathione resided in oxidized state in both cell lines, suggesting a lesser redox buffering capacity by this system in response to an ROS challenge. To determine whether the combined effects of increased ROS scavenging capacity in rSCC-61, and the upregulation of proteins involved in DNA replication and base-excision repair result in lesser radiation-induced DNA damage, we monitored the γ H2AX protein, a known marker of DNA damage. As shown in Figure 7, there was a lower number of γ H2AX foci formation in rSCC-61 compared with SCC-61 in response to radiation treatment, indicating decreased DNA damage in rSCC-61 compared with SCC-61 [Western blot analysis (**Fig. 7A**); Immunofluorescence analysis of γ H2AX foci (**Fig. 7B, C**)]. This was further supported by the IPA analysis of the proteomic data using the function prediction tool, in which the fold change of a number of proteins listed in **Appendix S2 Table S7** pointed toward reduced DNA damage in rSCC-61.

Relationship between ROS, lipid rafts, and the response to radiation and Erlotinib treatment

Another significant consequence of radiation-induced ROS is triggering the coalescence of lipid microdomains in the plasma membrane to form enlarged lipid rafts. Both resistance to radiation and increased sensitivity to EGFR inhibitors have been independently correlated to decreased lipid rafts and decreased localization of EGFR within these structures. The decreased basal and radiation-induced ROS in rSCC-61 coupled with the sevenfold upregulation of FASN in this cell line (**Appendix S2 Table 3**) led us to explore the potential differences in the lipid raft

arrangements in SCC-61 and rSCC-61 cells. The cells were stained for lipid rafts and EGFR. Unlike rSCC-61, the SCC-61 cells showed increased lipid raft formation and EGFR co-localization within these structures in both control and irradiated cells (**Fig. 8A**).

We then asked whether a decrease in the intracellular ROS in SCC-61 would influence the formation of lipid rafts and whether the disruption of lipid rafts would affect the response to Erlotinib or radiation. The SCC-61 cells were treated with polyethylene glycol-catalase, and the lipid rafts were stained with cholera toxin subunit B (**Fig. 8B**). A gradual disruption of lipid raft structures was observed on increasing catalase activity (2 and 20 U, respectively). The results were comparable with those obtained by the treatment of cells with a cholesterol extracting cyclodextrin M β CD and/ or Lovastatin, an inhibitor of cholesterol biosynthesis (**Fig. 8C**) (14). Further experiments were performed to investigate the impact of lipid rafts in SCC-61 on the response to Erlotinib and radiation. As shown in **Figure 8D and E**, the disruption of lipid rafts increased the sensitivity of SCC-61 to Erlotinib and rendered the cells more resistant to radiation, a phenotype characteristic of rSCC-61.

Evaluation of redox balance in HNSCC clinical samples

Given the in vitro data showing a mechanistic connection between the control of ROS and resistance to radiation, we next investigated whether this has relevance in vivo. We have used the redox biotin-tagged probe BP1 [**Fig. 9A**, (44)] to investigate the protein oxidation as a marker of ROS in a set of HNSCC tumor samples. The criteria for tumor selection and grouping into the treatment “responsive” and “resistant” groups are presented in the “Materials and Methods” section. The control experiments showing the selectivity of BP1 for oxidized proteins and the lack of signal in the absence of BP1 are presented in **Figure 9B**. The quantification of BP1 staining in the radiation and chemoradiation-resistant and -responsive HNSCC groups shows statistically significant differences in protein oxidation, providing initial validation of the in vitro findings (**Fig. 9C**).

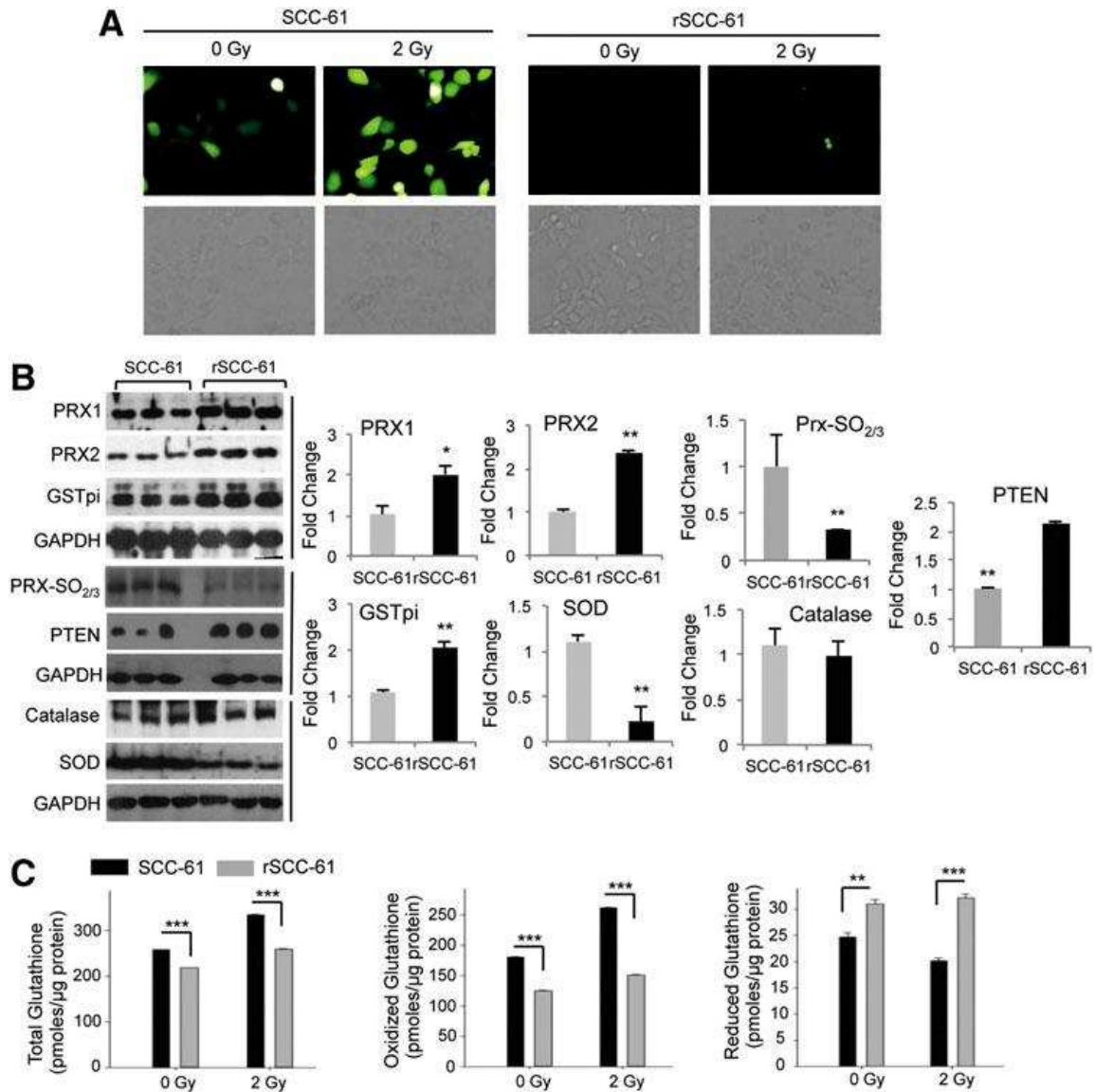


FIG. 6. rSCC-61 have decreased ROS and reduced DNA damage. (A) ROS imaging analysis. DCF fluorescence images of ROS in SCC-61 and rSCC-61 cells before and after treatment with radiation (control - 0 Gy and 2 Gy). Images were captured using the Arcturus PixCell II laser capture microscope under 20 \times objective. (B) Western blot analysis of proteins involved in the antioxidant system in rSCC-61 and SCC-61. Three out of five biological replicates are shown here for Prx1 and 2, Prx-SO_{2/3}, PTEN, GSTpi, SOD, and catalase. Quantification is based on all five replicates (n = 5) and taking into account the differences in GAPDH (Prx1: *p = 0.03; Prx2: **p = 0.003; Prx-SO_{2/3}: **p = 0.0012; GSTpi: **p = 0.0014; SOD: **p = 0.004; Catalase: p > 0.05; PTEN: **p = 0.009). (C) Quantification of glutathione. Glutathione (total, oxidized and reduced) in SCC-61 and rSCC-61 cells was measured at 1 h after treatment with 2 Gy of ionizing radiation. Quantification is based on three biological replicates, and the respective p-values are ***p < 0.001 for total and oxidized glutathione (0 Gy and 2 Gy) and reduced glutathione (2 Gy); **p = 0.005 for reduced glutathione (0 Gy). DCF, dichlorofluorescein; GSTpi, glutathione S-transferase pi; ROS, reactive oxygen species; SOD, superoxide dismutase.

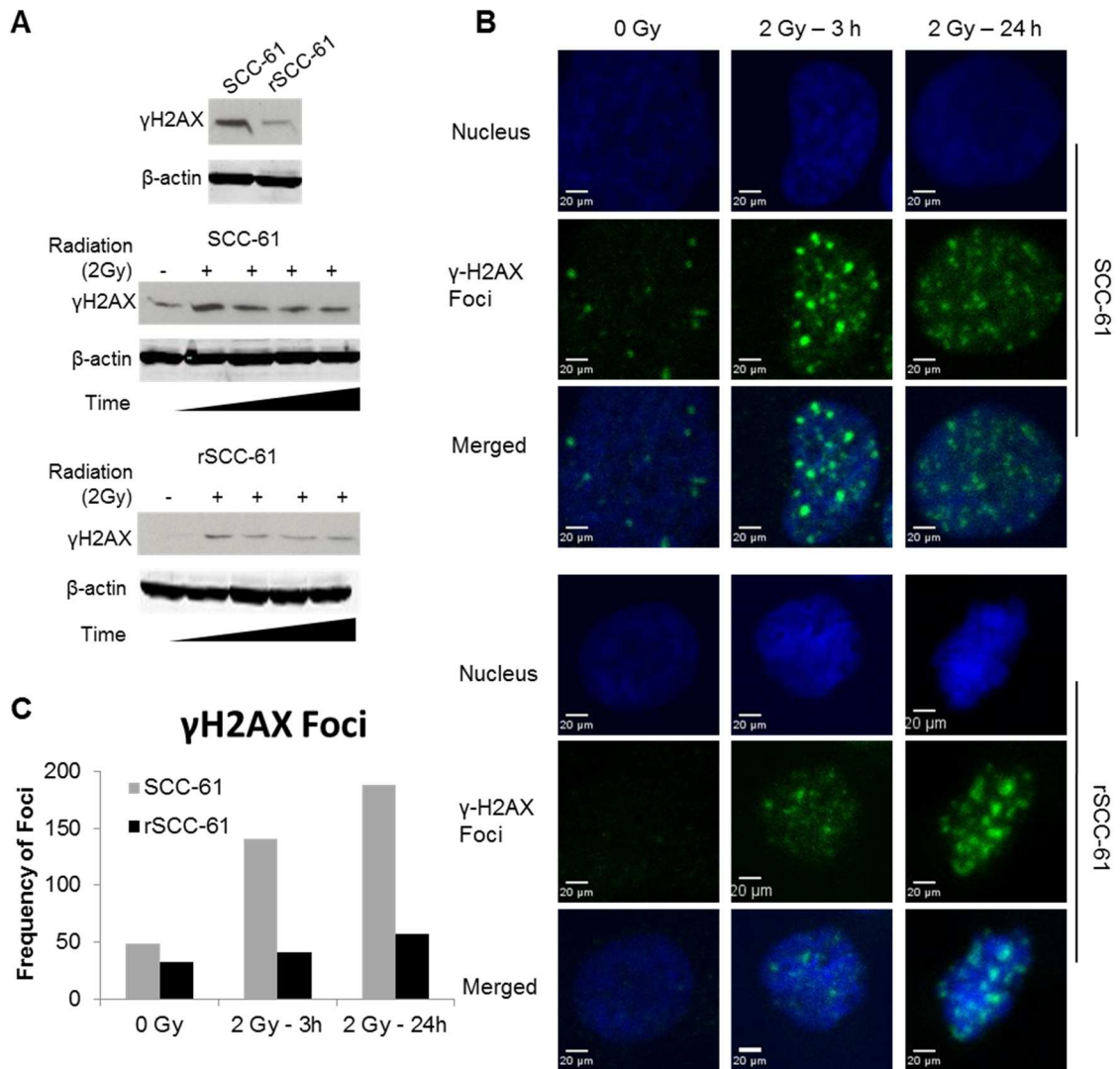


FIG. 7. Western blot and immunofluorescence analysis of γ H2AX. (A) SCC-61 and rSCC-61 cells were irradiated with 2 Gy and lysed at different time intervals (0.5, 2, 6, and 24 h) followed by immunoblotting with γ H2AX antibody. β -actin is used as a loading control. (Note: the SCC-61 and rSCC-61 samples were processed in a single 10-well SDS-PAGE gel. The image was separated to accommodate space available in the figure.) (B) and (C) Quantification of γ H2AX foci in SCC-61 and rSCC-61 using immunofluorescence staining. Untreated cells and cells irradiated with 2 Gy were imaged using anti- γ H2AX antibody (green) and Topro-3-iodide for nucleus (red). Frequency of foci was based on the monitoring of an average of 50 cells per experimental condition.

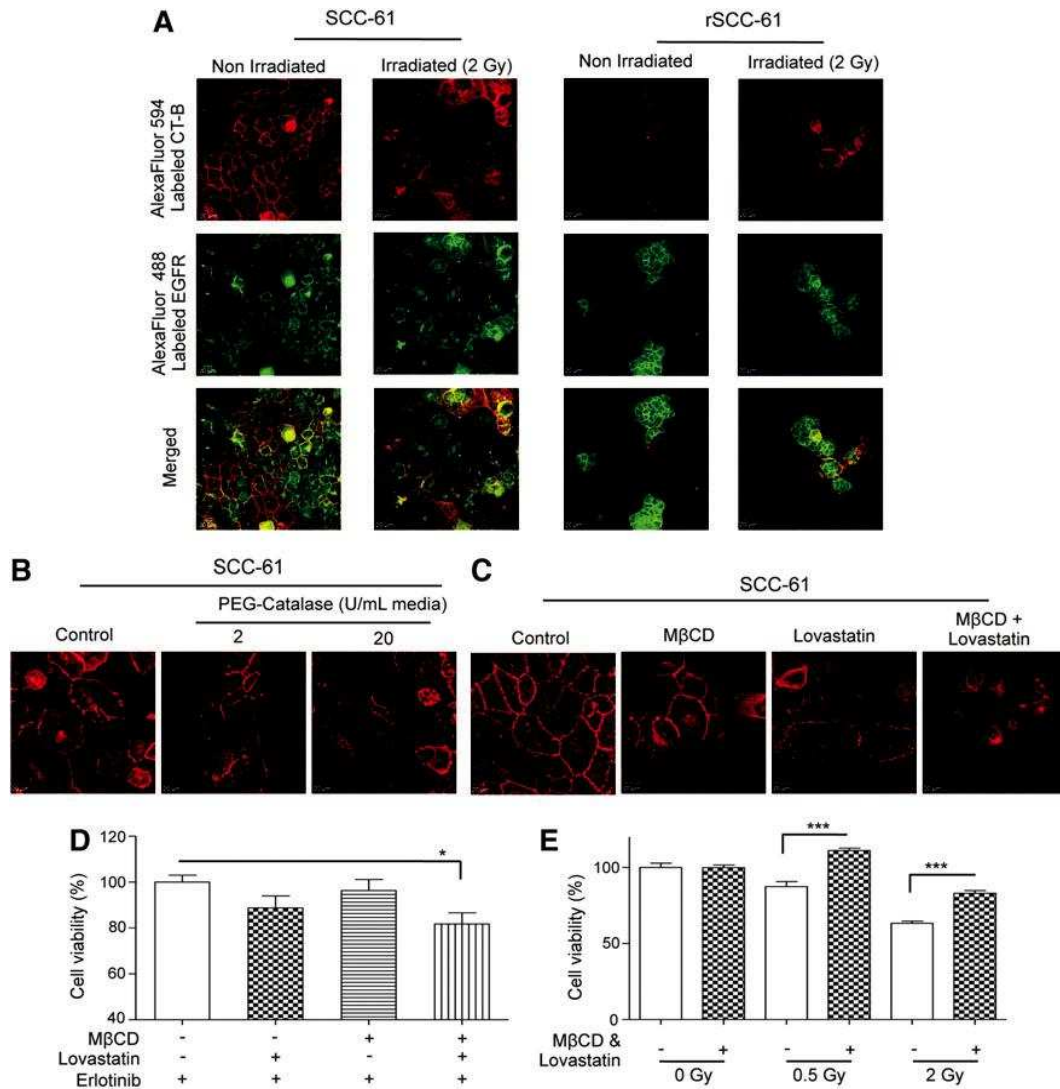


FIG. 8. Lipid rafts and response to radiation and EGFR inhibition. (A) Imaging of lipid rafts in SCC-61 and rSCC-61 cells. SCC-61 and rSCC-61 cells were either untreated or irradiated with 2 Gy followed by staining for confocal microscopy with cholera toxin subunit B (CT-B) conjugated to AlexaFluor594 (red) and EGFR antibody conjugated to AlexaFluor488 (green). The scale bars represent a distance of 20 μ m. (B) The role of ROS in lipid raft formation in SCC-61. The SCC-61 cells were treated with 2 and 20 U of catalase and for 24 h followed by staining with AlexaFluor594 conjugated CT-B. A gradual decrease in the structural integrity of lipid rafts is observed. The scale bars represent a distance of 20 μ m. (C) Inhibition of lipid rafts by M β CD and Lovastatin in SCC-61. The SCC-61 cells were treated for 24 h with 1 mM M β CD, 2 μ M Lovastatin or 1 mM M β CD plus 2 μ M Lovastatin and imaged using AlexaFluor594 conjugated CT-B. A decrease in the lipid rafts formation is observed under all treatment conditions. The scale bars represent a distance of 20 μ m. (D) Inhibition of lipid rafts results in improved response to Erlotinib in SCC-61. After 24 h pretreatment of SCC-61 with M β CD, Lovastatin, or M β CD plus Lovastatin, the cells were treated with 2 μ M Erlotinib for 48 h. The cell viability was determined using the MTT assay. An increased response to Erlotinib was observed under all treatment conditions and achieved statistical significance under combined M β CD and Lovastatin treatment (* p = 0.0189, n = 4). (E) Inhibition of lipid rafts results in decreased response to radiation in SCC-61. After 24 h pretreatment of SCC-61 with M β CD plus Lovastatin, the cells were treated with 0.5 and 2 Gy radiation. After 48 h, the cell viability was determined using the MTT assay. A statistically significant increase in resistance to radiation was noted at both radiation doses in the M β CD and Lovastatin-treated cells relative to the untreated control (0.5 Gy: *** p < 0.001; 2 Gy, n = 4: *** p < 0.001, n = 4).

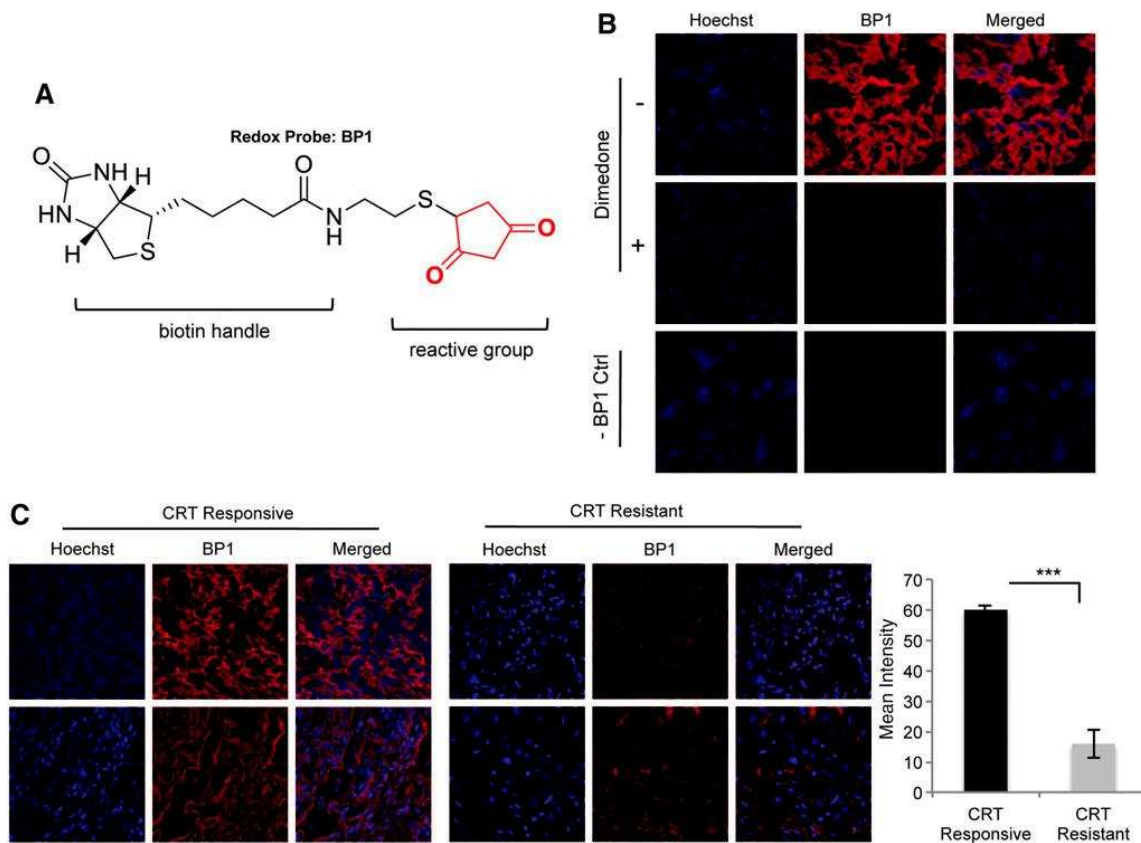


FIG. 9. Increased protein oxidation in clinical samples of radiation and chemoradiation-responsive HNSCC. (A) The chemical structure of the redox probe BP1. The structure highlights the 1,3- cyclopentanedione reactive group and the biotin tag that is used to detect labeled proteins. (B) Control experiments. The control experiments address the specificity of the probe toward oxidized proteins and the lack of signal in the absence of probes. (C) Representative staining of two tissue samples from the treatment-responsive and treatment-resistant groups. The tissues were treated with BP1 and visualized using Streptavidin-linked AlexaFluor594. Hoechst was used as a counterstain for the nuclei. The quantification of BP1 staining in the five samples/group was performed using ImageJ (**p < 0.001, n = 5). CRT, radiation or chemoradiation treatment; HNSCC, head and neck squamous cell cancer.

Discussion

Surgery, radiation, and chemotherapy are the major modes of treatment for HNSCC, and resistance to radiation or chemotherapy poses significant problems in disease management. While the newer EGFR therapies show significant promise, only ~10% of HNSCC tumors respond to Cetuximab; for example, despite the fact that more than 80% of these tumors have increased EGFR (9, 20). It is, therefore, highly important to identify the critical molecular features involved in response to radiation, chemotherapy, and targeted therapies. These would facilitate the discovery and validation of clinical biomarkers to predict the response to a particular treatment in HNSCC patients; to date, such biomarkers are not available in clinics.

Our studies show a complex mechanistic connection between cellular phenotype (epithelial/mesenchymal), extracellular environment (pH, ROS), and the response to radiation or Erlotinib in HNSCC cells. A summary of the results is presented in **Figure 10A and B**, and the mechanistic connections are further discussed next.

Reversible epithelial-to-mesenchymal transition and response to radiation and Erlotinib

The epithelial-to-mesenchymal transition (EMT) has gained attention because of its role in the acquisition of cancer stem cell properties. In this process, the cells undergo cytoskeletal remodeling, loss of E-cadherin, and switch from keratin to vimentin-type intermediate filaments. The HNSCC tumors have been traditionally classified as mesenchymal characterized by loss of keratin and a substantial increase in vimentin (31). More recent studies, however, demonstrate the presence of both mesenchymal and epithelial cells in advanced-stage HNSCC tumors (5). There is extensive evidence that connects the epithelial or mesenchymal phenotype to the response to radiation, chemotherapy, or EGFR inhibitors. Examples include (i) the EMT transition was proposed to be responsible for the modest response of HNSCC tumors to small-molecule EGFR inhibitors such as Gefitinib (Iressa) and Erlotinib (Tarceva) (16); (ii) the increased keratin—a hallmark of epithelial phenotype—was correlated to resistance to DNA-damaging drugs (2, 12); (iii) in a study involving patients with advanced HNSCC, the non-keratinizing HNSCC responded

better to combined radiation and chemotherapy than the tumors that expressed keratin (15, 36). These observations are consistent with the properties of the rSCC-61 cells described here. The upregulation of keratins, periplakin, and E-cadherin in rSCC-61, the decrease in vimentin, and the decreased migration in rSCC-61 are the main results that support the transition from a mesenchymal phenotype in SCC-61 to an epithelial phenotype in rSCC-61. This conclusion is also supported mechanistically by the quantitative proteomics analysis that showed downregulation of functional pathways involved in migration and cell morphology in rSCC-61 such as the ECM-receptor interaction, actin cytoskeleton regulation, and focal adhesion signaling. While the response of SCC-61 and rSCC-61 to radiation and Erlotinib is in accordance with the studies described earlier, the mechanisms involved are complex. We discuss next a potential network that may connect the cellular phenotype to the observed response to radiation and Erlotinib.

EGFR phosphorylation, ROS, lipid rafts, and response to radiation and Erlotinib

Observations from Figure 1F show that despite increased total phosphoprotein content in rSCC-61, there is significant downregulation of EGFR signaling in rSCC-61. The decreased phosphorylation of EGFR in rSCC-61 cells has two major consequences: (i) It results in reduced phosphorylation of downstream signaling proteins such as Akt, and the inhibition of Akt was previously shown to induce mesenchymal-to-epithelial transition in HNSCC cells (22); downregulation of Akt in rSCC-61 is further enforced by upregulation of PTEN, a negative regulator of Akt, in this cell line (**Fig. 6B**). (ii) Decreased phosphorylation of EGFR, along with the upregulation of antioxidant proteins, contributes to lower intracellular ROS through mechanisms that may involve decreased activation of NADPH oxidase and decreased glycolysis/mitochondrial electron transport chain, two major sources of ROS. The regulation of redox microenvironment in rSCC-61 is important to explain both the resistance to radiation and the sensitivity to Erlotinib in rSCC-61. The Western blot analysis of γ H2AX indicates reduced DNA damage in rSCC-61, and the cell cycle analysis shows reduced G2/M arrest with 2 Gy

radiation in rSCC-61. Another contributing factor to reduced DNA damage with radiation results from upregulation of proteins involved in base-excision repair and DNA replication pathways shown by the proteomics data. In addition, both resistance to radiation and increased sensitivity to EGFR-inhibitors have been independently correlated to impaired structural rearrangement and formation of lipid rafts. Lipid rafts are a hub for the amplification of receptor signaling, including death receptor signaling, and are regulated by ROS—increased ROS have been linked to increased lipid raft formation (35, 38, 50). Our data show decreased ROS in rSCC-61 and increased FASN in these cells. FASN is the main enzyme for synthesis of palmitate and lipogenesis, and its upregulation has been linked to resistance to chemotherapy and radiation (34, 53). FASN inhibition was also proposed to contribute to increased levels of ceramide, a major component of lipid rafts (4). The studies described here show lower lipid staining at the cell membrane in rSCC-61, which may contribute to the increased cell survival and sensitivity to EGFR inhibitors. Indeed, the disruption of lipid rafts in SCC-61 resulted in gain of resistance to radiation and improved sensitivity to Erlotinib. The increased sensitivity of rSCC-61 to Erlotinib is contrary to previous studies which show that cells resistant to EGFR-targeted inhibitors are cross-resistant to ionizing radiation (6, 17). Our results show that the connection between the resistance to radiation and EGFR inhibitors is not bidirectional and emphasizes the significance of adding targeted therapies to radiation or chemotherapy for improving clinical response to treatment. The analysis of protein redox status in clinical samples shows a clear difference between tumors that responded well to radiation and chemoradiation treatment and tumors which did not respond to treatment. This provides the necessary justification for further exploring protein oxidation as a potential biomarker of response to radiation and chemoradiation treatment. In conclusion, we generated a matched model of radiation resistance in HNSCC that shows increased sensitivity to EGFR inhibition by Erlotinib. Cumulatively, quantitative proteomics, computational, and mechanistic investigations of this system show a convergence of signaling and metabolism networks to elicit protection against ionizing radiation. In some cases, such as the

system described here, the acquired resistance to radiation can be accompanied by phenotypic changes or altered sensitivity to other treatments (e.g., targeted inhibitors). The preliminary analysis of clinical samples using newly developed chemical probes for protein oxidation is consistent with the in vitro findings. Prospective clinical studies are ongoing and will address the predictive value of the potential biomarkers of response identified by the studies described here. These include global protein redox status, FASN level, EGFR phosphorylation, and tumor epithelial–mesenchymal composition.

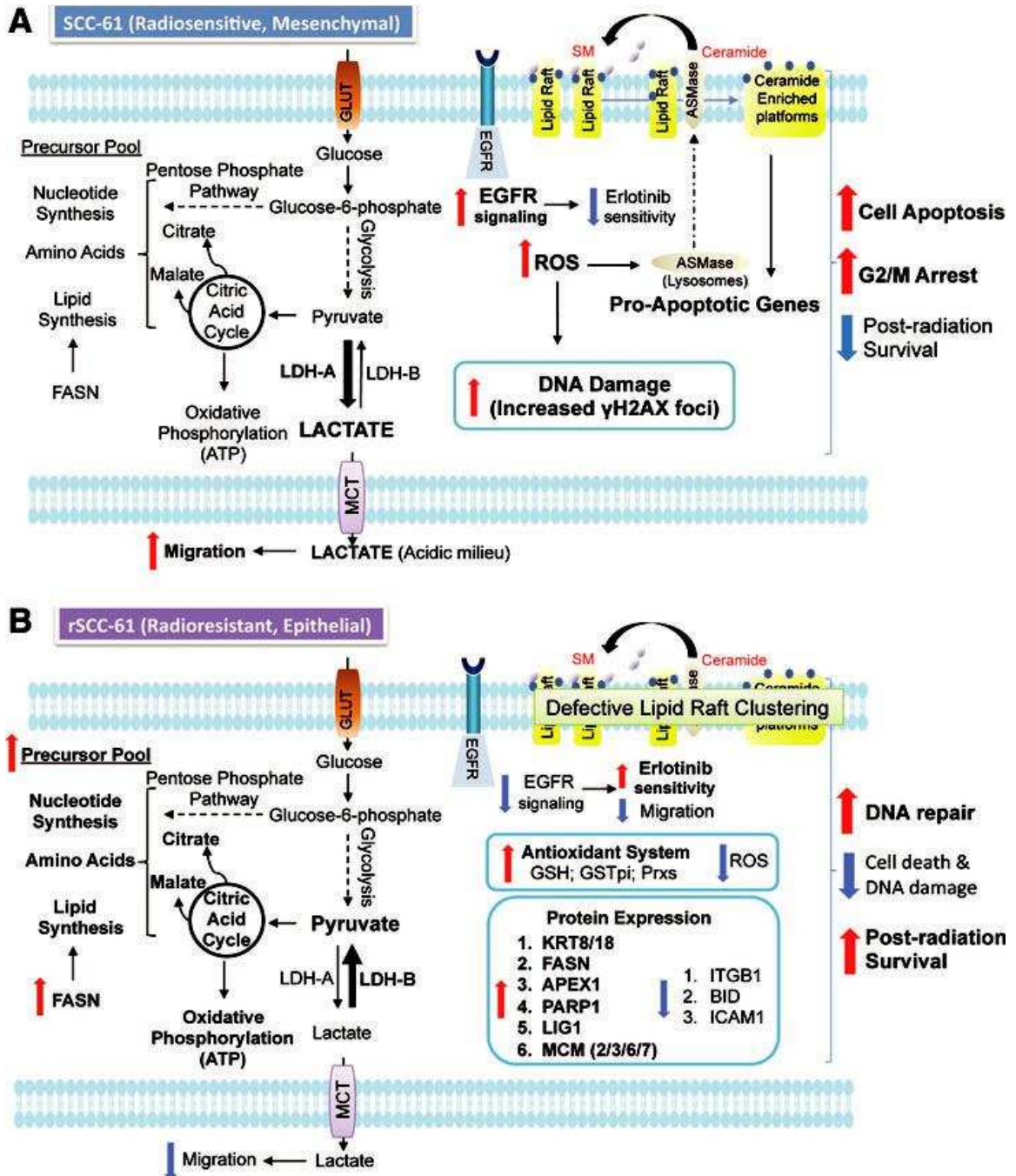


FIG. 10. Mechanistic model of radiation response in head and neck cancer. (A) Radiation-sensitive SCC-61 and **(B)** Radiation-resistant rSCC-61. SM, sphingomyelin; GLUT, glucose transporter; FASN, fatty acid synthase; LDH, lactate dehydrogenase (A or B); MCT, monocarboxylate transporter.

Materials and Methods

Reagents and details of standard methods used in the study are included in the “Appendix Materials and Methods” section

Cell culture and radiation treatment All cells used in this study were cultured in the DMEM/ F12 medium that was supplemented with 10% fetal bovine serum (FBS; Invitrogen) at 37 °C and 5% CO₂. The head and neck cancer cell line SCC-61 was kindly provided by Ezra Cohen, Department of Medicine, University of Chicago. Fresh medium was added to cultured cells every 2 days. Subconfluent cells (~60%–80% confluence) were subjected to radiation with different doses as indicated for each experiment. Radiation was performed using a 444 TBq 12,000 Ci self-shielded ¹³⁷Cesium (Cs) irradiator. Culture dishes were placed on a Styrofoam insert within the chamber of the irradiator, such that the distance from the Cs source results in a homogenous dose distribution over the desired field with a dose rate of 392 rad/min. From the dose rate, the exposure time required to deliver the desired dose was calculated and input into the irradiator.

Establishment of the radiation-resistant rSCC-61 clone The radiation-sensitive SCC-61 cells were irradiated using a 2 Gy radiation dose. After the radiation treatment, the cells were cultured, split 1:2, allowed to achieve 60% confluence, and then exposed to another cycle of 2 Gy radiation. This process was repeated for a cumulative total of 16 Gy. The resulting cell population was plated at a low density on soft agar, and single cell colonies were picked and expanded in culture. The studies here were focused on the clone R8E, called rSCC-61.

Stable isotope labeling of amino acids in cell culture The SCC-61 and rSCC-61 cells were cultured in DMEM/ F12 media containing the light and heavy isotopes of Lys and Arg, respectively, and supplemented with 10% dialyzed FBS and 200 mg/L proline to prevent the conversion of isotope coded arginine to proline in cells (7, 40). The cells were passed in their respective media to achieve a minimum of 97% incorporation of the isotope labeled Lys and Arg. The cells were then lysed in modified RIPA buffer (50 mM TrisHCl, pH 7.4; 1% NP40; 0.25% Sodium deoxycholate; 15 mM NaCl; 1 mM EDTA; 1 mM NaF; supplemented with Roche

protease and phosphatase inhibitor tablets). Protein concentration was determined using the bicinchoninic acid (BCA) assay (Thermo Scientific). The SCC-61 and rSCC-61 lysates were then mixed in a 1:1 ratio, precipitated using chloroform/ methanol to concentrate the sample, and resuspended in 0.1% SDS. The mixed lysates were resolved on 12% SDS-PAGE and stained with Coomassie Brilliant Blue (R-250). The entire lane was divided into 15 gel bands, which were then digested with trypsin following standard in-gel digestion protocols (1). The resulting tryptic peptides were analyzed on a nanoLC system that was coupled with a LTQ Orbitrap mass spectrometer. Peptide separation was performed on a Thermo Scientific Acclaim PepMap RSLC column (15 cm, 2 μ m particle sizes, 100 \AA pore sizes) with a flow rate of 300 nL/ min and using a 65 min gradient of solutions A (0.05% formic acid in water) and B (80% acetonitrile, 20% water, 0.05% formic acid). The mass spectrometer was operated in the data-dependent mode. The first MS scan was acquired in the Orbitrap at 60,000 resolutions (m/z 300–2000). The following MS/MS scans were collected in the ion trap for the top five most intense ions using collision-induced dissociation. The raw MS files were analyzed by Proteome Discoverer 1.2 software (Thermo Fisher Scientific) using MASCOT search engine and the UniProtKB human database. The results were filtered using a false discovery rate of 1%.

Pathway and network analysis IPA software (www.ingenuity.com) was used to identify significantly over-represented pathways and cellular functions in the list of identified proteins. The rSCC-61/SCC-61 proteomics data were imported into IPA and filtered on 2-fold change before a core analysis was performed to identify the most significantly regulated proteins and associated cellular functions. Additional network associations were generated with Cytoscape version 2.8.2 (47) using KEGG and HPRD databases. The Cytoscape plug-in BioNetBuilder version 2.0 (3) was used to obtain all KEGG interactions available for humans on December 16, 2011 using default settings, while the plug-in BisoGenet was used to mine all available human interactions present in the list from the HPRD database on January 10, 2012. Network annotation analysis was performed on the lists of UniProt accessions by representing the proteins present in

the KEGG and HPRD networks. Both lists were independently analyzed in the tools provided by the DAVID (23, 24). To determine what types of biological functions were over-represented in each network, the Annotation Clustering tool was used to analyze each list of proteins where only GO_FAT terms were selected for analysis and all other options remained at their default setting. Results were filtered for annotation clusters that had an Enrichment Score of 1.3 or greater (equivalent to a p-value of 0.05 or less).

Analysis of clinical samples Tissue samples. Previously collected and deidentified tumor samples (n = 10, flash frozen) were obtained from the Tumor Tissue Core Laboratory at Wake Forest School of Medicine (IRB # 00022263). All patients signed consent forms to permit the use of tumor specimens for scientific, developmental technology, research, and education purposes. Each of these 10 samples was squamous cell carcinomas of the base of tongue. Each patient had radiation as a component of upfront definitive treatment, whether it was radiation, chemoradiation, or surgery followed by radiation or chemoradiation. Treatment-responsive samples (n = 5) were classified as those patients who had no evidence of any local or distant failure, or residual or persistent disease (such as noted in a neck dissection) within 1 year after completion of radiation. Of these five radiation sensitive samples, one patient underwent definitive chemoradiation, two patients underwent surgery with immediate adjuvant chemoradiation, and two patients underwent surgery with immediate adjuvant radiation alone. Treatment resistant samples (n = 5) were those who were found to have biopsy proven residual or persistent disease within 1 year of completion of radiation. Of these five radiation-resistant samples, one patient underwent definitive radiation and the remaining four patients underwent definitive chemoradiation. The biotin-tagged redox probe BP1 was synthesized in our laboratory following the procedure previously published (44).

Cryosectioning of frozen tissue samples. The flash frozen tissue blocks were stored at – 80 °C until the time of sectioning. Before sectioning the frozen tissue, blocks were transferred to a

cryotome cryostat (e.g., - 20C) and allowed to equilibrate to the temperature of the instrument. The tissue sections (8 μ m thickness) were placed on poly-L-lysine-coated glass slides.

BP1 staining for protein oxidation. The tissue sections were fixed by immersing the slides of 4% paraformaldehyde in 0.1 M phosphate-buffered saline (PBS) for 20 min at room temperature followed by washing 5X – 5 min with 0.1 M PBS. After fixation, the samples were permeabilized and stained with BP1 (500 μ M) in 0.01 M, pH 7.4 PBS containing 0.2% Triton X-100 (PBT) for a total of 80 min. After this incubation, the slides were washed 5X – 5 min with PBS and then incubated with Streptavidin-AlexaFluor594 (Red) (2 mg/ml; 1:100 dilution in PBT). The slides were washed with PBS followed by nuclear staining with Hoechst (1:10,000 in 0.01 M, pH 7.4 PBS). Two control experiments were performed: 1. Dimedone, a nontagged reagent for protein oxidation (1 mM, 1 h) was added as blocking reagent before the addition of BP1; and, 2: the same staining procedure was followed as described earlier but in the absence of BP1.

Image collection, processing, and data analysis. A Zeiss 510 or 710 confocal microscope was used for the collection of images as indicated for each study. For each tissue sample, the 40X images were taken at a laser intensity setting of 1% for all samples. All fluorescent excitation and emitted light collection settings were carefully held constant between samples to facilitate equivalence for intensity comparisons. LSM image browser was used for processing the confocal images. The mean fluorescence intensity in sections stained for BP1 was quantified using ImageJ.

Statistical analysis

Statistical analysis (t-test, one-way analysis of variance) was based on a minimum of three biological replicates using SigmaPlot v. 12.0. Asterisks indicate statistically significant changes compared with untreated controls ($\alpha = 0.05$, p-values of 0.01–0.05 [*], 0.001–0.01 [**], or < 0.001 [***]).

Acknowledgments

Research reported in this article was supported by the National Cancer Institute of the National Institutes of Health under award number R01 CA136810 to C.M.F. The authors also acknowledge financial support from the Wake Forest School of Medicine (development funds to C.M.F. and TRADONC fellowship to B.C.). An NSF Major Research Instrumentation award supported purchase of the LSCM used to generate images for the clinical samples included in this article (MRI-0722926) within the WFU Microscopic Imaging Core Facility. The clinical samples were obtained from the Tumor Tissue Core Laboratory of the Wake Forest University Comprehensive Cancer Center (grant number P30 CA12197).

Author Disclosure Statement

The redox probe BP1 is manufactured in the laboratory of C.M.F. and distributed by KeraFast. No competing financial interests exist for any of the other authors.

Literature Cited

1. **Aitken A and Learmonth M.** Protein identification by in-gel digestion and mass spectrometric analysis. *Mol Biotechnol* 20: 95–97, 2002.
2. **Anderson JM, Heindl LM, Bauman PA, Ludi CW, Dalton WS, and Cress AE.** Cytokeratin expression results in a drug-resistant phenotype to six different chemotherapeutic agents. *Clin Cancer Res* 2: 97–105, 1996.
3. **Avila-Campillo I, Drew K, Lin J, Reiss DJ, and Bonneau R.** BioNetBuilder: automatic integration of biological networks. *Bioinformatics* 23: 392–393, 2007.
4. **Bandyopadhyay S, Zhan R, Wang Y, Pai SK, Hirota S, Hosobe S, Takano Y, Saito K, Furuta E, Iizumi M, Mohinta S, Watabe M, Chalfant C, and Watabe K.** Mechanism of apoptosis induced by the inhibition of fatty acid synthase in breast cancer cells. *Cancer Res* 66: 5934–5940, 2006.
5. **Basu D, Montone KT, Wang LP, Gimotty PA, Hammond R, Diehl JA, Rustgi AK, Lee JT, Rasanen K, Weinstein GS, and Herlyn M.** Detecting and targeting mesenchymal-like subpopulations within squamous cell carcinomas. *Cell Cycle* 10: 2008–2016, 2011.
6. **Benavente S, Huang S, Armstrong EA, Chi A, Hsu KT, Wheeler DL, and Harari PM.** Establishment and characterization of a model of acquired resistance to epidermal growth factor receptor targeting agents in human cancer cells. *Clin Cancer Res* 15: 1585–1592, 2009.
7. **Bendall SC, Hughes C, Stewart MH, Doble B, Bhatia M, and Lajoie GA.** Prevention of amino acid conversion in SILAC experiments with embryonic stem cells. *Mol Cell Proteomics* 7: 1587–1597, 2008.
8. **Bentzen SM, Atasoy BM, Daley FM, Dische S, Richman PI, Saunders MI, Trott KR, and Wilson GD.** Epidermal growth factor receptor expression in pretreatment biopsies from head and neck squamous cell carcinoma as a predictive factor for a benefit from accelerated radiation therapy in a randomized controlled trial. *J Clin Oncol* 23: 5560–5567, 2005.
9. **Bonner JA, Harari PM, Giralt J, Azarnia N, Shin DM, Cohen RB, Jones CU, Sur R, Raben D, Jassem J, Ove R, Kies MS, Baselga J, Yousoufian H, Amellal N, Rowinsky EK, and Ang KK.** Radiotherapy plus cetuximab for squamous-cell carcinoma of the head and neck. *N Engl J Med* 354: 567–578, 2006.

10. **Bump EA and Brown JM.** Role of glutathione in the radiation response of mammalian cells in vitro and in vivo. *Pharmacol Ther* 47: 117–136, 1990.
11. **Cappuzzo F.** Erlotinib in gliomas: should selection be based on EGFR and Akt analyses? *J Natl Cancer Institute* 97: 868–869, 2005.
12. **Caulin C, Ware CF, Magin TM, and Oshima RG.** Keratin dependent, epithelial resistance to tumor necrosis factor induced apoptosis. *J Cell Biol* 149: 17–22, 2000.
13. **Chong CR and Janne PA.** The quest to overcome resistance to EGFR-targeted therapies in cancer. *Nat Med* 19: 1389– 1400, 2013.
14. **Christian AE, Haynes MP, Phillips MC, and Rothblat GH.** Use of cyclodextrins for manipulating cellular cholesterol content. *J Lipid Res* 38: 2264–2272, 1997.
15. **Crissman JD, Pajak TF, Zarbo RJ, Marcial VA, and AlSarraf M.** Improved response and survival to combined cisplatin and radiation in non-keratinizing squamous cell carcinomas of the head and neck. An RTOG study of 114 advanced stage tumors. *Cancer* 59: 1391–1397, 1987.
16. **Frederick BA, Helfrich BA, Coldren CD, Zheng D, Chan D, Bunn PA, Jr., and Raben D.** Epithelial to mesenchymal transition predicts gefitinib resistance in cell lines of head and neck squamous cell carcinoma and non-small cell lung carcinoma. *Mol Cancer Ther* 6: 1683–1691, 2007.
17. **Gee JM and Nicholson RI.** Expanding the therapeutic repertoire of epidermal growth factor receptor blockade: radiosensitization. *Breast Cancer Res* 5: 126–129, 2003.
18. **Gupta SC, Hevia D, Patchva S, Park B, Koh W, and Aggarwal BB.** Upsides and downsides of reactive oxygen species for cancer: the roles of reactive oxygen species in tumorigenesis, prevention, and therapy. *Antioxid Redox Signal* 16: 1295–1322, 2012.
19. **Haas-Kogan DA, Prados MD, Tihan T, Eberhard DA, Jelluma N, Arvold ND, Baumber R, Lamborn KR, Kapadia A, Malec M, Berger MS, and Stokoe D.** Epidermal growth factor receptor, protein kinase B/Akt, and glioma response to erlotinib. *J Natl Cancer Inst* 97: 880–887, 2005.
20. **Harari PM and Huang S.** Radiation combined with EGFR signal inhibitors: head and neck cancer focus. *Semin Radiat Oncol* 16: 38–44, 2006.

21. **Hirschhaeuser F, Sattler UG, and Mueller-Klieser W.** Lactate: a metabolic key player in cancer. *Cancer Res* 71: 6921–6925, 2011.
22. **Hong KO, Kim JH, Hong JS, Yoon HJ, Lee JI, Hong SP, and Hong SD.** Inhibition of Akt activity induces the mesenchymal-to-epithelial reverting transition with restoring E-cadherin expression in KB and KOSCC-25B oral squamous cell carcinoma cells. *J Exp Clin Cancer Res* 28: 28, 2009.
23. **Huang da W, Sherman BT, and Lempicki RA.** Bioinformatics enrichment tools: paths toward the comprehensive functional analysis of large gene lists. *Nucleic Acids Res* 37: 1–13, 2009.
24. **Huang da W, Sherman BT, and Lempicki RA.** Systematic and integrative analysis of large gene lists using DAVID bioinformatics resources. *Nat Protoc* 4: 44–57, 2009.
25. **Irwin ME, Mueller KL, Bohin N, Ge Y, and Boerner JL.** Lipid raft localization of EGFR alters the response of cancer cells to the EGFR tyrosine kinase inhibitor gefitinib. *J Cell Physiol* 226: 2316–2328, 2011.
26. **Jemal A, Siegel R, Ward E, Murray T, Xu J, and Thun MJ.** Cancer statistics, 2007. *CA Cancer J Clin* 57: 43–66, 2007.
27. **Kanda R, Kawahara A, Watari K, Murakami Y, Sonoda K, Maeda M, Fujita H, Kage M, Uramoto H, Costa C, Kuwano M, and Ono M.** Erlotinib resistance in lung cancer cells mediated by integrin beta1/Src/Akt-driven bypass signaling. *Cancer Res* 73: 6243–6253, 2013.
28. **Kanehisa M and Goto S.** KEGG: Kyoto encyclopedia of genes and genomes. *Nucleic Acids Res* 28: 27–30, 2000.
29. **Kao YC, Lee SW, Lin LC, Chen LT, Hsing CH, Hsu HP, Huang HY, Shiue YL, Chen TJ, and Li CF.** Fatty acid synthase overexpression confers an independent prognosticator and associates with radiation resistance in nasopharyngeal carcinoma. *Tumour Biol* 34: 759–768, 2013.
30. **Khodarev NN, Beckett M, Labay E, Darga T, Roizman B, and Weichselbaum RR.** STAT1 is overexpressed in tumors selected for radioresistance and confers protection from radiation in transduced sensitive cells. *Proc Natl Acad Sci USA* 101: 1714–1719, 2004.

31. **Klymkowsky MW and Savagner P.** Epithelial-mesenchymal transition: a cancer researcher's conceptual friend and foe. *Am J Pathol* 174: 1588–1593, 2009.
32. **Lee YS, Chang HW, Jeong JE, Lee SW, and Kim SY.** Proteomic analysis of two head and neck cancer cell lines presenting different radiation sensitivity. *Acta Otolaryngol* 128: 86–92, 2008.
33. **Li B, Zhang C, He F, Liu W, Yang Y, Liu H, Liu X, Wang J, Zhang L, Deng B, Gao F, Cui J, Liu C, and Cai J.** GSK-3 β Inhibition Attenuates LPS-Induced Death but Aggravates Radiation-Induced Death via Down-Regulation of IL-6. *Cell Physiol Biochem* 32: 1720–1728, 2013.
34. **Liu H, Liu Y, and Zhang JT.** A new mechanism of drug resistance in breast cancer cells: fatty acid synthase overexpression-mediated palmitate overproduction. *Mol Cancer Ther* 7: 263–270, 2008.
35. **Lu SP, Lin Feng MH, Huang HL, Huang YC, Tsou WI, and Lai MZ.** Reactive oxygen species promote raft formation in T lymphocytes. *Free Radic Biol Med* 42: 936–944, 2007.
36. **Marcial VA, Pajak TF, Mohiuddin M, Cooper JS, al Sarraf M, Mowry PA, Curran W, Crissman J, Rodriguez M, and Velez-Garcia E.** Concomitant cisplatin chemotherapy and radiotherapy in advanced mucosal squamous cell carcinoma of the head and neck. Long-term results of the Radiation Therapy Oncology Group study 81-17. *Cancer* 66: 1861–1868, 1990.
37. **Mitchell JB and Russo A.** The role of glutathione in radiation and drug induced cytotoxicity. *Br J Cancer Suppl* 8: 96–104, 1987.
38. **Morgan MJ, Kim YS, and Liu Z.** Lipid rafts and oxidative stress-induced cell death. *Antioxid Redox Signal* 9: 1471–1483, 2007.
39. **Nijkamp MM, Span PN, Hoogsteen IJ, van der Kogel AJ, Kaanders JH, and Bussink J.** Expression of E-cadherin and vimentin correlates with metastasis formation in head and neck squamous cell carcinoma patients. *Radiother Oncol* 99: 344–348, 2011.
40. **Ong SE and Mann M.** A practical recipe for stable isotope labeling by amino acids in cell culture (SILAC). *Nat Protoc* 1: 2650–2660, 2006.

41. **Park SH, Chung YM, Lee YS, Kim HJ, Kim JS, Chae HZ, and Yoo YD.** Antisense of human peroxiredoxin II enhances radiation-induced cell death. *Clin Cancer Res* 6: 4915–4920, 2000.
42. **Parkins CS, Stratford MR, Dennis MF, Stubbs M, and Chaplin DJ.** The relationship between extracellular lactate and tumour pH in a murine tumour model of ischaemiareperfusion. *Br J Cancer* 75: 319–323, 1997.
43. **Prasad TS, Kandasamy K, and Pandey A.** Human Protein Reference Database and Human Proteinpedia as discovery tools for systems biology. *Methods Mol Biol* 577: 67–79, 2009.
44. **Qian J, Klomsiri C, Wright MW, King SB, Tsang AW, Poole LB, and Furdai CM.** Simple synthesis of 1,3-cyclopentanedione derived probes for labeling sulfenic acid proteins. *Chem Commun* 47: 9203–9205, 2011.
45. **Quiet CA, Weichselbaum RR, and Grdina DJ.** Variation in radiation sensitivity during the cell cycle of two human squamous cell carcinomas. *Int J Radiat Oncol Biol Phys* 20: 733–738, 1991.
46. **Ramsamooj P, Kasid U, and Dritschilo A.** Differential expression of proteins in radioresistant and radiosensitive human squamous carcinoma cells. *J Natl Cancer Inst* 84: 622–628, 1992.
47. **Smoot ME, Ono K, Ruscheinski J, Wang PL, and Ideker T.** Cytoscape 2.8: new features for data integration and network visualization. *Bioinformatics* 27: 431–432, 2011.
48. **Thomas GJ, Lewis MP, Whawell SA, Russell A, Sheppard D, Hart IR, Speight PM, and Marshall JF.** Expression of the alphavbeta6 integrin promotes migration and invasion in squamous carcinoma cells. *J Invest Dermatol* 117: 67–73, 2001.
49. **Tilghman RW, Slack-Davis JK, Sergina N, Martin KH, Iwanicki M, Hershey ED, Beggs HE, Reichardt LF, and Parsons JT.** Focal adhesion kinase is required for the spatial organization of the leading edge in migrating cells. *J Cell Sci* 118: 2613–2623, 2005.
50. **Ushio-Fukai M.** Localizing NADPH oxidase-derived ROS. *Sci STKE* 2006: re8, 2006.
51. **Weichselbaum RR, Beckett MA, Vijayakumar S, Simon MA, Awan AM, Nachman J, Panje WR, Goldman ME, Tybor AG, Moran WJ, Vokes EE, Ahmed-Swan S, and**

- Farhangi E.** Radiobiological characterization of head and neck and sarcoma cells derived from patients prior to radiotherapy. *Int J Radiat Oncol Biol Phys* 19: 313–319, 1990.
52. **Weichselbaum RR, Dahlberg W, Beckett M, Karrison T, Miller D, Clark J, and Ervin TJ.** Radiation-resistant and repair-proficient human tumor cells may be associated with radiotherapy failure in head- and neck-cancer patients. *Proc Natl Acad Sci U S A* 83: 2684–2688, 1986.
53. **Yang Y, Liu H, Li Z, Zhao Z, Yip-Schneider M, Fan Q, Schmidt CM, Chiorean EG, Xie J, Cheng L, Chen JH, and Zhang JT.** Role of fatty acid synthase in gemcitabine and radiation resistance of pancreatic cancers. *Int J Biochem Mol Biol* 2: 89–98, 2011.
54. **Zou L, Cao S, Kang N, Huebert RC, and Shah VH.** Fibronectin induces endothelial cell migration through beta1 integrin and Src-dependent phosphorylation of fibroblast growth factor receptor-1 at tyrosines 653/654 and 766. *J. Biol. Chem* 287, 7190-7202, 2012.

CHAPTER 3

Energy Metabolism in a Matched Model of Radiation Resistance for Head and Neck Squamous Cell Cancer

Jade Mims¹, Nidhi Bansal¹, Manish S. Bharadwaj², Xiaofei Chen¹, Anthony J. Molina², Allen W. Tsang¹, Cristina M. Furdul¹

¹Section on Molecular Medicine, Department of Internal Medicine, Wake Forest School of Medicine, Winston-Salem, NC

²Section on Gerontology and Geriatric Medicine, Department of Internal Medicine, Wake Forest School of Medicine, Winston-Salem, NC

The following manuscript was published in *Radiation Research*, volume 183, pages 291 – 304, March 2015 and is reprinted with permission. The stylistic variations are due to the requirements of the journal.

ABSTRACT

While radiation therapy is commonly used for treating cancer, radiation resistance can limit long-term control of the disease. In this study, we investigated the reprogramming of the energy metabolism in radiosensitive and radioresistant head and neck squamous cell carcinomas (HNSCC) using a preclinical matched model of radiation resistance. Our investigation found that radioresistant rSCC-61 cells: 1. They display increased glucose uptake and decreased fatty acid uptake; 2. They deviate from the classical Warburg effect by diverting the glycolytic flux into the pentose phosphate pathway; 3. They are more dependent on glucose than glutamine metabolism to support growth; 4. They have decreased mitochondrial oxidative phosphorylation; 5. They have enhanced fatty acid biosynthesis by increasing the expression of fatty acid synthase; and 6. They utilize endogenous fatty acids to meet the energy demands for proliferation. Inhibition of fatty acid synthase with orlistat or FASN siRNA resulted in increased cytotoxicity and sensitivity to radiation in rSCC-61 cells. These results demonstrate the potential of combination therapy using radiation and orlistat or other inhibitors of lipid and energy metabolism for treating radiation resistance in HNSCC.

INTRODUCTION

Head and neck squamous cell carcinomas (HNSCC) accounts for nearly 3% of all new cancers in the U.S. and has an annual incidence of 500,000 new cases worldwide (1). The treatment options available for HNSCC patients utilize various combinations of surgery, radiation therapy and chemotherapy, depending on the stage and resectability of the disease. Radiation therapy alone or combined with chemotherapy can be a primary curative treatment prescribed for these patients either as definitive or as adjuvant post-surgical therapy. Significant acute and long-term side effects (e.g., oral mucositis, dysphagia) as well as the development of therapy resistant tumor cells can limit the effective use of radiation therapy. For these reasons, there is an increased focus on the use of targeted radiosensitizing agents used in combination with radiation therapy to treat radiation-resistant tumors, and potentially reduce normal tissue toxicity. Because of the increased expression of epidermal growth factor receptor (EGFR) found in >80% of HNSCC cases (2), this protein is considered as an attractive target for HNSCC treatment. In 2007, the FDA approved the first targeted therapy against EGFR (Cetuximab, a monoclonal antibody against EGFR), to be used in conjunction with radiation therapy in patients with locally advanced HNSCC based on the clinical studies reported by Bonner *et al.* (3). However, despite the wide overexpression of EGFR in HNSCC, only 10–15% of patients respond to this treatment, suggesting a need for additional targets (4).

The reprogramming of cancer cell metabolism has gained recent attention as one of the major hallmarks of cancer (5, 6). The rewiring of tumor cell metabolism is recognized as a dynamic process adopted by cancer cells to ensure a steady supply of metabolites for generation of both biomass and energy (7, 8). A seminal finding for this metabolic diversion is the Warburg effect (9), which allows for conversion of glucose into lactate instead of pyruvate even when sufficient oxygen is available to support mitochondrial oxidative phosphorylation (OXPHOS). The advantage of this process for energy production is the buildup of glycolytic intermediates, which

can provide for the biosynthetic needs of daughter cells after cell division (10). The Warburg effect is often misinterpreted as an indicator of damaged mitochondrial function in tumor cells (11). However, more recent reports show that mitochondrial function in cancer cells is intact and although these cells may not maximize their ATP production through mitochondrial OXPHOS, a significant fraction of the ATP might still be derived from it (12). In addition, cancer cells are known to utilize mitochondrial enzymes to meet their challenge of macro-molecular biosynthesis and ensure effective cellular proliferation (12). Over the past years, a number of studies have addressed the diversity of tumor energy metabolism and identified the mechanistic connections between metabolism, signaling and cancer cell proliferation (13). It is now recognized that tumor cells demonstrate metabolic heterogeneity with capacity to utilize alternative oxidizable substrates such as glutamine and fatty acids (14–16). Therefore, interference with tumor cell metabolism is emerging as a novel treatment strategy in many types of malignancies including HNSCC (17–23).

Previous investigations of HNSCC metabolism have revealed dysregulation of multiple metabolic pathways such as OXPHOS, TCA cycle and glutaminolysis (19), as well as a general reliance on glucose as the dominant energy source for survival and proliferation (17). However, to our knowledge, the metabolic changes associated with radiation-resistant tumor cells in HNSCC have not been investigated. Thus, a better understanding of the underlying molecular and metabolic regulation that leads to radiation-resistant cells in HNSCC could significantly aid in the introduction of more effective and novel therapeutics. In an effort to underpin the molecular reprogramming associated with the acquisition of radiation resistance in HNSCC, we developed a matched model of radiation-resistant cells for this disease, the SCC-61/rSCC-61 system, which we reported on previously (24). Quantitative proteomic profiling showed broad changes in protein expression in the radioresistant cells (rSCC-61) that were associated with cellular

metabolism, in addition to the expected upregulation of proteins involved in protection against DNA damage (24).

In this study, we followed up on the findings from the proteomics analysis and investigated the reprogramming of energy metabolism in the SCC-61/rSCC-61 matched model of radioresistant cells. We found that radioresistant rSCC-61 cells deviate from the classical Warburg effect by diverting the glycolytic flux into the pentose phosphate pathway (PPP). Additionally, these cells have decreased mitochondrial OXPHOS, and increased expression of fatty acid synthase (FASN), which is related to increased reliance on the utilization of endogenous fatty acids for energy production. Inhibition of FASN with orlistat or FASN siRNA resulted in increased cytotoxicity and sensitivity to radiation treatment in rSCC-61 cells. Bioenergy studies showed decreased ATP synthesis and lower spare respiratory capacity as potential mechanisms of increased sensitivity to radiation in orlistat-treated rSCC-61 cells.

MATERIALS AND METHODS

Reagents

Antibodies and reagents were obtained from the following sources: rabbit anti-COXIV, rabbit anti-glucose 6-phosphate dehydrogenase, rabbit anti- β actin and goat anti-rabbit IgG HRP (Cell Signaling Technology®, Danvers, MA); mouse anti-FASN (BD Biosciences, San Jose, CA); rabbit anti-GAPDH (Millipore, Billerica, MA); mouse anti-TIGAR and rabbit anti-mouse IgG HRP (Santa Cruz Biotechnology, Dallas, TX); Dulbecco's modified Eagle medium (DMEM)/F12 and fetal bovine serum (FBS) (Gibco/Invitrogen™, Carlsbad, CA); phosphate buffered saline (PBS) (Lonza Group Ltd., Basel, Switzerland); sulforhodamine B (SRB) for measuring cell proliferation (Sigma-Aldrich® LLC, St. Louis, MO); bicinchoninic acid (BCA) protein estimation kit and Western Lightning® Plus-ECL (Thermo Fisher Scientific Inc., Boston, MA). Orlistat was kindly provided by the laboratory of Prof. Steven Kridel, Department of Cancer

Biology, Wake Forest University Health Sciences, Winston-Salem, NC. FASN siRNA was purchased from Dharmacon™ (Thermo Fisher Scientific Inc.), and ¹⁴C-palmitate and 2-deoxy-D-[3H] glucose were purchased from PerkinElmer® Inc. (Waltham, MA).

Cell Culture and Radiation Treatment

The generation of the SCC-61/rSCC-61 matched model of response to radiation was described earlier (24). Briefly, the radiation-sensitive SCC-61 cells were irradiated *in vitro* with fractionated ionizing radiation (8×2 Gy), the resulting cell population was plated on soft agar and a single colony (rSCC-61) was picked for in-depth analysis of the mechanisms driving the response to radiation treatment in HNSCC. Both SCC-61 and rSCC-61 cells used in this study were cultured in the DMEM/F12 medium supplemented with 10% FBS (Invitrogen) at 37°C and 5% CO₂. Cell medium was replaced every two days with fresh medium. Where applicable, a 444 TBq 12,000 Ci self-shielded ¹³⁷Cs (Cesium) irradiator was used for radiation treatment. Culture dishes were placed on a Styrofoam insert within the chamber of the irradiator, such that the distance from the cesium source would result in a homogenous dose distribution over the desired field with a dose rate of 392 rad/min. From the dose rate, the exposure time required to deliver the desired dose was calculated and entered into the irradiator.

Glucose Uptake

SCC-61 and rSCC-61 cells were grown in six-well plates to 70% confluence. Medium was then removed and cells were washed two times with PBS at room temperature. The assay was initiated by the addition of 0.1 mM 2-deoxyglucose and 0.5 μCi/mL 2-deoxy-D-[3H] glucose (PerkinElmer) and terminated after 30 min by washing cells two times in ice-cold PBS and quenching with 0.05 M NaOH. Uptake of 2-deoxy-D-[3H] glucose was detected in ScintiVerse™ BD scintillation mixture (Thermo Fisher Scientific) using a Beckman LS 6000 SC scintillation counter and was normalized by protein concentration.

Cell Proliferation Using SRB Assay

The proliferation of SCC-61 and rSCC-61 cells in response to glucose or glutamine deprivation, 6-aminonicotinamide (6-AN) (Sigma-Aldrich® LLC, St. Louis, MO) or 2-deoxy-D-glucose (2-DG) (Sigma-Aldrich) or orlistat treatment was determined using the SRB colorimetric assay. The cells were seeded in 24-well plates at a density of 50,000/well in 1 mL. After overnight incubation at 37°C, the cells were either incubated in glucose-free or glutamine-free medium, or treated with either 5 μ M 6-AN, 20 mM 2-DG or 0.1–100 μ M orlistat and then given 0 Gy or 2 Gy irradiation and incubated for an additional 48 h at 37°C. For experiments involving glutamine deprivation the treated cells were incubated for 72 h at 37°C. After incubation, cells were fixed with 500 μ L cold 10% trichloroacetic acid (TCA) and incubated at 4°C for 1 h. After fixing, cells were washed 4 \times with water and dried completely before the addition of 100 μ L of 0.057 % (wt/vol) SRB solution to each well for 30 min at room temperature. Plates were quickly rinsed 4 \times with 1% (vol/vol) acetic acid to remove unbound dye and dried completely. Next, 200 μ L of 10 mM Tris base solution (pH 10.5) was added to each well and then shaken for 30 min to solubilize protein-bound dye. The absorbance was measured at 510 nm using a microplate reader.

GLUT1 Imaging Analysis

SCC-61 and rSCC-61 cells were seeded in 1 mL Microtek chambers at a density of 2×10^4 cells/mL and incubated overnight at 37°C and 5% CO₂. After overnight incubation, cells were washed with cold PBS, fixed in 4% formaldehyde for 15 min and permeabilized with 0.1% Triton X-100 followed by blocking with 5% BSA for 1 h at room temperature. The cells were incubated with 1:200 dilution of rabbit anti-GLUT1 (Millipore) overnight at 4°C followed by washing 3 \times with PBS, incubation with 1:1,000 dilution of secondary anti-rabbit Alexa Fluor® 488 conjugate for 1 h at room temperature and 10 min incubation with 1:1,000 Hoechst before mounting with Fluoromount™ (Sigma-Aldrich). Imaging was performed using a Zeiss LSM710 confocal

microscope and a 40× objective. LSM image browser was used for processing the confocal images.

Mitochondrial Stress Assays Using the Seahorse XFA 24-3 System

Measurement of OCR under normal growth conditions

O₂ consumption was determined using a Seahorse XFA 24-3 system. SCC-61 and rSCC-61 (4×10^4 cells) were seeded in the 24-well XF24 cell culture plate in DMEM/F12 (+10% FBS) and allowed to grow for 24 h. One hour prior to analysis, culture media was replaced by XF assay medium supplemented with glucose (17.5 mM) and sodium pyruvate (0.5 mM) and incubated at 37°C for 1 h to allow pH and temperature stabilization in a non-CO₂ incubator. The OCR was repeatedly measured for a total of 5 measurements followed by sequential injection of oligomycin (0.75 μM), FCCP (1 μM) and antimycin A/rotenone (1 μM each), after measurements 5, 9 and 15, respectively. After all measurements were completed, cells were lysed and protein estimation was performed by BCA assay to confirm equal distribution of cells per well and to correct the OCR readings by protein concentration if needed. All data were analyzed using XF software and displayed as average OCR (pM/min). The data is the average of replicate wells ($n = 3-5$) ± SEM.

Fatty acid oxidation (FAO) assay using cells treated with exogenous palmitate

Similarly to above, 4×10^4 cells were seeded in the 24-well XF24 cell culture plate in DMEM/F12 (+10% FBS) and allowed to grow for 24 h. At 24 h prior to analysis, culture media was replaced by substrate limited media supplemented with glucose (0.5 mM), GlutaMAX (1 mM), carnitine (0.5 mM) and 1% FBS and incubated at 37°C to prime the cells to oxidize exogenous fatty acids. Culture media was replaced by FAO assay medium (111 mM NaCl, 4.7 mM KCl, 1.25 mM CaCl₂, 2 mM MgSO₄, 1.2 mM NaH₂PO₄) supplemented with 2.5 mM glucose, 0.5 mM carnitine and 5 mM HEPES, and preheated at 37°C for 1 h in a non-CO₂ incubator. A final concentration of 1.2 mM BSA or XF Palmitate-BSA substrate was added to the appropriate

wells immediately before the start of assay. The OCR was measured repeatedly 4 times and after the sequential injection of oligomycin (0.75 μM), FCCP (1 μM) and antimycin A/rotenone (1 μM each), added after measurements 4, 7, and 10, respectively. After all measurements were completed, cells were lysed, protein concentration was measured by the BCA assay and data was processed as described above.

Measuring orlistat effects on OCR

The same procedure was followed as described for the assays under normal growth conditions with the only difference being pretreatment of cells with 10 μM orlistat for 2.5 h before the start of the experiment. After all measurements were completed, cells were lysed, protein concentration was measured by the BCA assay and data was processed as described above.

Detection of mitochondrial reactive oxygen species

Subconfluent SCC-61 and rSCC-61 cells were treated with 20 mM 2-DG for 24 h, stained with 0.5 μM MitoSOX™ Red (Ex/Em 500/580, designated red) and imaged. Imaging was performed using a Zeiss LSM 710 confocal microscope and a 10 \times objective. All images were collected under the same confocal settings. LSM image browser was used for processing the confocal images.

NADPH/NADP⁺ Quantification

Cells were seeded at 1×10^5 , allowed to attach, and then washed with cold PBS immediately after attachment. Cells were extracted with 200 μL of NADP⁺/NADPH extraction buffer by homogenization, then vortexed for 10 s, followed by centrifugation at 13,000g for 10 min to remove insoluble material. Samples were deproteinized before use in assay by filtering through a 10 kDa cutoff spin filter. To detect NADPH, NADP⁺ was decomposed by centrifuging tubes and heating to 60°C for 30 min in a water bath followed by cooling on ice. Samples were quickly

spun to remove any precipitates, leaving only NADPH. NADP⁺ and NADPH samples were incubated with Master Reaction mixture for 2 h before absorbance was measured at 450 nm according to the manufacturer's (cat. no. MAK038; Sigma-Aldrich) protocol.

Clonogenic Cell Survival Assay

Radiation-resistant rSCC-61 cells and the parental SCC-61 cells were trypsinized, resuspended in complete medium (DMEM/F12 + 10% FBS) and plated (250 cells/well) into the 6-well culture dishes. After overnight incubation at 37°C, the cells were treated with a range of concentrations of orlistat in triplicates (0.5–100 μ M) and allowed to incubate for 16 h. Fresh media was then added and the cells were incubated for additional 7–8 days for the colony formation. Once formed, the colonies were fixed in methanol and acetic acid (1:1) solution and stained with 0.5% crystal violet. The colonies containing more than 50 cells were scored as clonogenic survivors. The surviving fraction of the drug-treated cells was normalized using the plating efficiencies of their corresponding untreated control.

Fatty Acid Synthase Activity (FASN) Assay

Cells were harvested by treatment with trypsin-EDTA solution, pelleted by centrifugation, washed twice, and resuspended in cold PBS. Cells were sonicated for 30 min at 4°C and centrifuged for 15 min at 4°C to obtain particle-free supernatants. A supernatant sample was taken to measure protein content by BCA assay. One μ g/ μ L of total protein was used for the assay and 120 μ L of this particle-free supernatant were pre-incubated for 15 min at 37°C for temperature equilibration. The sample was then added to 150 μ L of the reaction buffer [200 mM potassium phosphate buffer (pH 7.0), 1 mM EDTA, 1 mM DTT, 30 μ M acetyl-CoA, 0.24 mM NADPH], followed by 30 μ L of 500 μ M malonyl-CoA (FASN substrate), and the final volume of 0.3 mL of reaction mixture was assayed for 20 min to determine FASN-dependent

oxidation of NADPH. Before the addition of malonyl-CoA, the background rate of NADPH oxidation in the presence of acetyl-CoA was monitored at 340 nm for 10 min.

siRNA Transfections and Clonogenic Assays

Cells were grown to 60% confluence followed by transfection with FASN siRNA (60 and 100 nM) or control siRNA (100 nM) (Dharmacon) according to manufacturer's protocol. After 36 h, transfected cells were trypsinized and resuspended in the complete medium and plated (500 cells/well) into the six-well culture dishes. After 4 h, the cells were irradiated with 2 Gy and incubated for an additional 7–8 days for the colony formation. Once formed, the colonies were fixed in methanol and acetic acid (1:1) solution and stained with 0.5% crystal violet. The colonies containing more than 50 cells were scored as clonogenic survivors. The surviving fraction of the irradiated cells was normalized using the plating efficiencies of their corresponding untreated control. SCC-61 cells were also included in the clonogenic assays. Western blot analysis was performed to confirm the depletion of FASN upon treatment of rSCC-61 cells with respective siRNAs.

¹⁴C-Palmitate Uptake Assay

SCC-61 and rSCC-61 cells (2×10^5 cells) were seeded per well in a six-well plate and grown overnight at 37°C and 5% CO₂. On the following day, cells were washed, then starved in HBSS for 30 min and subsequently washed twice with HBSS. The cells were then incubated with ¹⁴C-labeled palmitate (1 μCi) for 30 min followed by three washes with PBS. The cells were collected in 0.5 N NaOH (500 μL) and transferred to scintillation vials containing 1 mL of scintillation fluid. The ¹⁴C-palmitate uptake was expressed as nM/mg of total protein.

Western Blot Analysis

SCC-61 or rSCC-61 cells (8×10^5 cells) were seeded in 100 mm culture dishes. Cells were lysed after 48 h and the fresh media was replenished 24 h before lysis. Cells were lysed using RIPA buffer [20 mM Tris-Cl (pH 7.4); 150 mM NaCl (1% sodium deoxycholate); 1% Triton X-100 (0.1% SDS); supplemented with protease and phosphatase inhibitor tablets (Roche Diagnostics, Indianapolis, IN)]. The lysates were incubated on ice for 1 h followed by centrifugation at 10,000g for 10 min. The lysates were then normalized for their protein concentration across different treatment conditions and subjected to SDS-PAGE. The separated proteins were then transferred to a nitrocellulose membrane (0.45 μ m; Bio-Rad Laboratories Inc., Hercules, CA) and probed for the indicated proteins using the corresponding primary and HRP-linked secondary antibodies. Proteins were visualized by treating the blots with the Western Lightning Plus-ECL reagents followed by exposure to autoradiography film (GeneMate Blue Ultra Autorad film; BioExpress, Kaysville, UT). Quantification of Western blot results was performed using ImageJ (National Institutes of Health, Bethesda, MD).

Statistical Analysis

Statistical analysis (*t* test) was based on a minimum of three biological replicates using SigmaPlot™ (Systat® Software Inc., San Jose, CA), version 12.0 or Microsoft Excel 2010. Asterisks indicate statistically significant changes compared with untreated controls ($\alpha = 0.05$, **P* = 0.01–0.05, ***P* = 0.001–0.01 and ****P* = <0.001).

RESULTS

Contribution of Glycolysis to SCC-61 and rSCC-61 Proliferation

We examined the glucose uptake and utilization in radiosensitive SCC-61 and radioresistant rSCC-61 cells. The total glucose uptake of rSCC-61 cells was significantly higher than the SCC-61 cells ($P < 0.001$; **Fig. 1A**) consistent with the increased expression and membrane localization of glucose transporter GLUT1 in rSCC-61 determined by imaging and Western blot ($P < 0.001$; **Fig. 1B**). To further determine the requirement for glucose metabolism in rSCC-61 cells, we examined cell viability under glucose deprivation with 0 and 2 Gy irradiation. Cells were grown using regular media, media depleted of glucose or regular media supplemented with 2-DG, a glycolysis inhibitor, followed by radiation treatment. Cell proliferation was measured using the SRB assay (25). Regardless of radiation treatment, both glucose starvation and 2-DG treatment significantly reduced cell proliferation in both rSCC-61 and SCC-61 cells, although the effect was more pronounced in rSCC-61 (e.g., ~twofold vs. ~fourfold decrease in cell proliferation in glucose-deprived SCC-61 and rSCC-61 cells, respectively, in the absence of radiation treatment; $P < 0.001$; **Fig. 1C**).

Contribution of PPP to SCC-61 and rSCC-61 Proliferation

Multiple levels of regulation on glycolysis have been identified that can divert glucose towards the synthesis of molecular building blocks that are fundamental to cancer cell proliferation. For example, TP53-inducible glycolysis and apoptosis regulator (TIGAR) has fructose-2,6-bisphosphatase activity and is an established regulator of glycolysis and PPP (26). Increased expression of TIGAR inhibits glycolysis and promotes PPP by lowering fructose-2,6-bisphosphate and increasing fructose-6-phosphate in cells. One of the mechanisms underlying glycolysis/PPP regulation is the conversion of fructose-6-phosphate into glucose-6-phosphate, the substrate for the rate-limiting reaction in the PPP catalyzed by glucose-6-phosphate

dehydrogenase (G6PD). The parallel decrease in fructose-2,6-biphosphate results in downregulation of phosphofructokinase 1 activity, a glycolytic enzyme catalyzing the conversion of fructose-6-phosphate to form fructose-1,6-bisphosphate. Western blot analysis showed increased expression of TIGAR ($P = 0.004$) and G6PD ($P < 0.001$) in rSCC-61, suggesting an increased routing of glucose into the PPP (**Fig. 2A**). In addition, quantitative proteomics analysis reported earlier showed a 3.5-fold increased expression in rSCC-61 of the enzyme 6-phosphogluconate dehydrogenase (6PGD) catalyzing the second NADPH producing step in the oxidative phase of PPP (24). Based on these results, we hypothesized that rSCC-61 would be more dependent on PPP than SCC-61. Indeed, treatment of SCC-61 and rSCC-61 cells with the 6-phosphogluconate dehydrogenase inhibitor, 6-aminonicotinamide, resulted in decreased cell proliferation in rSCC-61 compared with SCC-61 in both irradiated and control cells ($P = 0.005$ and $P = 0.008$, respectively; **Fig. 2B**). The expected consequence of upregulated PPP is increased production of NADPH and ribose-5-phosphate for subsequent biosynthesis of nucleic acids and defense against radiation-induced oxidative damage (27). Indeed, quantification of NADPH/NADP⁺ ratio showed NADPH to be increased 1.5-fold in rSCC-61 compared to SCC-61 cells ($P = 0.04$; **Fig. 2C**). These results are also consistent with the functional analysis of our previously published quantitative proteomic data for SCC-61 and rSCC-61 cells, which showed significantly increased nucleotide metabolism, DNA replication and base excision repair in rSCC-61 (24).

Glutamine Utilization in SCC-61 and rSCC-61 Cells

Metabolic rewiring to satisfy rapid proliferation often includes utilization of secondary nutrient glutamine as a source for energy and biomass generation (8, 28, 29). Previously published data from a panel of 15 HNSCC cell lines indicated that glucose, not glutamine, is the dominant energy source for proliferation and survival of HNSCC cells (17). To demonstrate the preference

of glucose and glutamine utilization in radiosensitive and radioresistant HNSCC, we investigated the effect of glutamine depletion without and with radiation treatment on rSCC-61 and SCC-61 proliferation. SCC-61 and rSCC-61 cells were cultured in the medium containing various concentrations of glutamine (0–2.5 mM) and cell proliferation was determined using the SRB assay. As shown in Fig. 3, glutamine starvation resulted in significantly decreased proliferation of SCC-61 cells compared with rSCC-61 (e.g., $P < 0.001$ for 0 mM glutamine) indicating that the radioresistant rSCC-61 cells are largely dependent on glucose for meeting their energy and growth requirements and less dependent on glutamine compared with the SCC-61 cells. Interestingly, the effects of glutamine depletion on cell proliferation seem to be much stronger than those induced by irradiation, as indicated by lack of a significant difference in cell proliferation between irradiated and control cells in the absence of glutamine as substrate. This result is consistent with the data presented in Figs. 1C and 2B, which suggested a dependence of radiation-induced cell death on cellular energy metabolism.

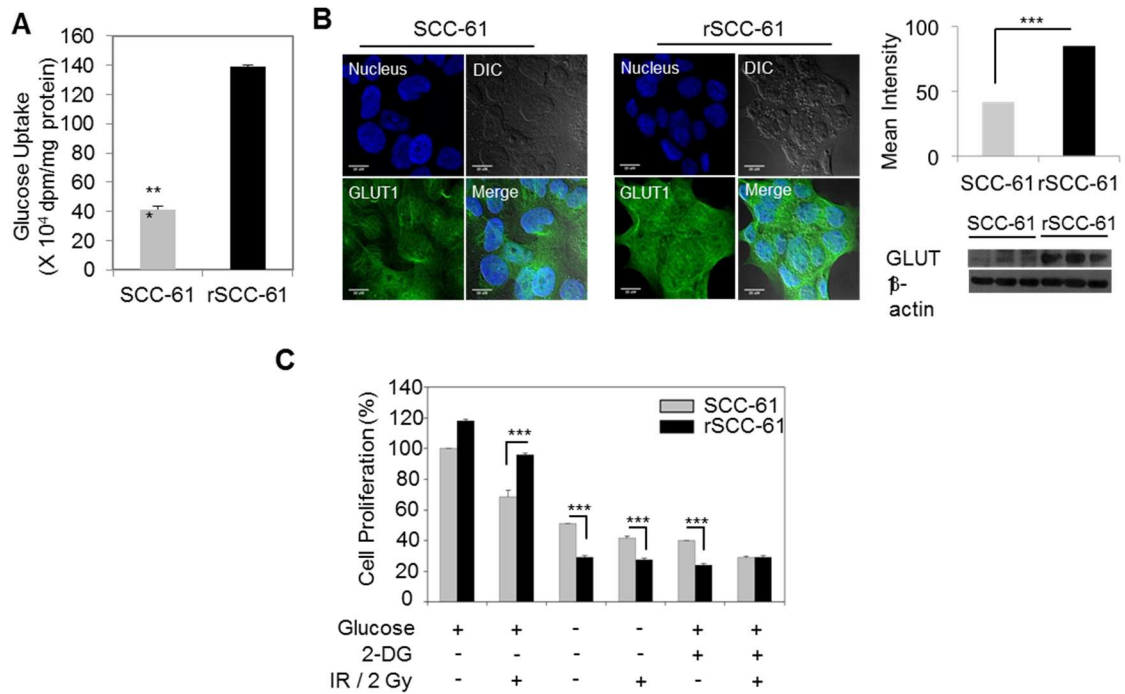


FIG. 1. Glucose uptake and dependence of cell growth on glucose metabolism in SCC-61 and rSCC-61 cells. Panel A: Assay showing increased glucose uptake in rSCC-61 compared to SCC-61 cells (** $P < 0.001$). **Panel B:** Imaging analysis of GLUT1 (green) in SCC-61 and rSCC-61 cells, quantification of imaging data and validation by Western blot. Blue: Hoechst nucleus staining. The differential contrast images (DIC) and merge panels are also shown. Increased GLUT1 staining and expression by Western blot was observed in rSCC-61 consistent with the glucose uptake data. The scale bars represent a distance of 20 μm (** $P < 0.001$). **Panel C:** Glucose deprivation (–) or 2-DG treatment (+) effects on cell proliferation with or without irradiation (–/+). Cell proliferation is expressed as percentage relative to the untreated SCC-61 cells in the absence of radiation exposure. Compared to SCC-61, the rSCC-61 cells have increased requirement of glucose for survival and enhanced sensitivity to the metabolic inhibitor 2-DG regardless of radiation treatment. The statistical analysis is based on three biological replicates (** $P < 0.001$).

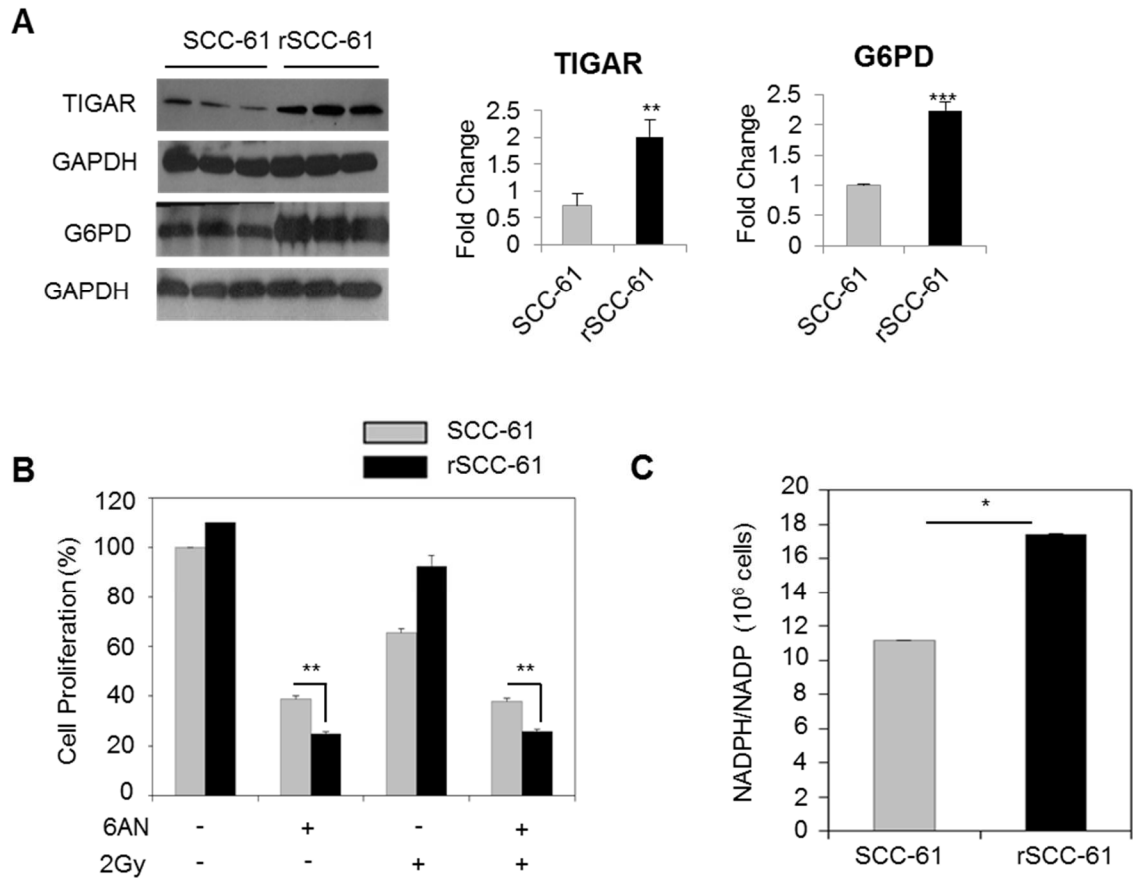


FIG. 2. Contribution of PPP to cellular proliferation in SCC-61 and rSCC-61 cells. Panel A: Western blot analysis showing increased expression of TIGAR (** $P = 0.004$) and glucose 6-phosphate dehydrogenase (G6PD) (** $P < 0.001$) in rSCC-61 compared with SCC-61. **Panel B:** Cell proliferation with or without 6-AN treatment, a PPP inhibitor targeting 6-phosphogluconate dehydrogenase (** $P = 0.008$) and 2 Gy irradiation (** $P = 0.005$). Cell proliferation was measured using the sulforhodamine B (SRB) assay and expressed as percentage relative to the untreated control. Three biological replicates were used in this analysis. The results show increased dependence on PPP in rSCC-61 cells compared with SCC-61 cells before and after irradiation. **Panel C:** NADPH/NADP⁺ quantification showing increased NADPH in rSCC-61 cells compared to SCC-61 cells (** $P=0.04$).

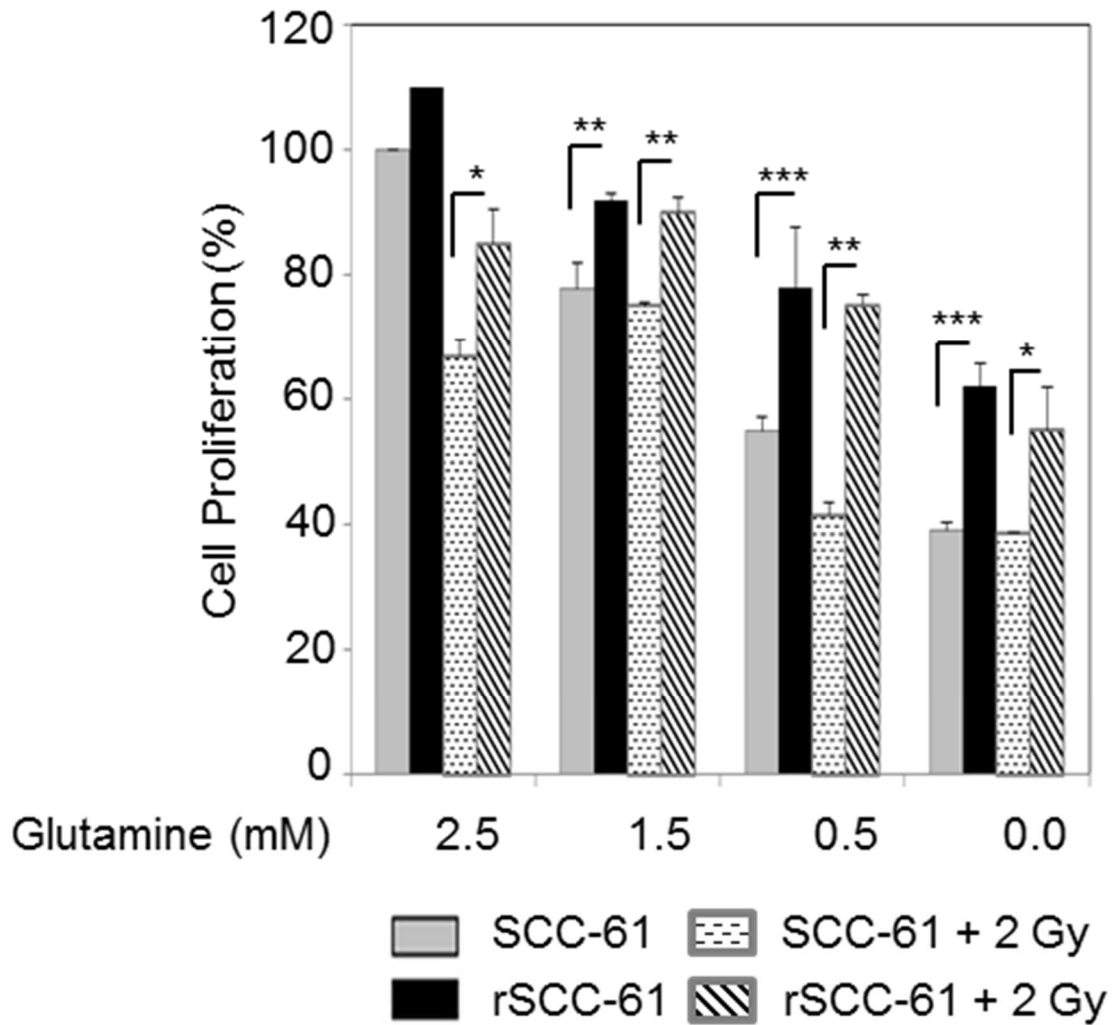


FIG. 3. Glutamine utilization in SCC-61 and rSCC-61 cells. Cell proliferation using media supplemented with decreasing concentrations of glutamine and either without or with irradiation (e.g., *** $P < 0.001$ and * $P = 0.04$ for 0.0 mM glutamine, without irradiation and with 2 Gy irradiation, respectively). SRB assay for cell proliferation was performed using three biological replicates for each treatment condition. The results show an overall increased reliance on glutamine metabolism in SCC-61 compared with rSCC-61 cells.

rSCC-61 Cells Have Reduced Mitochondrial OXPHOS

The results presented in **Figs. 1 and 2** demonstrate an increased dependence on overall glucose metabolism in rSCC-61 cells and increased flux through PPP in these cells. We have reported previously that rSCC-61 cells have increased expression of lactate dehydrogenase B enzyme (favoring conversion of lactate to pyruvate) and decreased expression of lactate dehydrogenase A (favoring conversion of pyruvate to lactate) (24), which also pointed to a possible diversion from the conventional Warburg metabolism. Taken together, the data indicated that a significant proportion of glycolytic flux was diverted into lactic acid synthesis in SCC-61 while in rSCC-61 the upstream glycolytic intermediates were funneled into the PPP but also possibly into the TCA and mitochondrial electron transfer chain (ETC) to support OXPHOS. To investigate the relative proportion of glycolytic flux entering the TCA cycle and mitochondrial ETC in SCC-61 and rSCC-61 cells, we measured the oxygen consumption rate (OCR) at basal and in response to modulators of ETC function using the Seahorse XF24 extracellular flux analyzer. Inhibition of ATP synthase with oligomycin was used to determine the proportion of OCR utilized for ATP production at basal conditions. Trifluorocarbonyl cyanide phenylhydrazone (FCCP) was added to assess maximal uncoupled respiration and finally, rotenone/antimycin A was used to assess any residual nonmitochondrial OCR (**Fig. 4A**). Western blot analysis of the mitochondrial enzyme COXIV showed comparable mitochondrial content in SCC-61 and rSCC-61 cells (**Fig. 4A**). Six primary parameters were extracted using this methodology: basal respiration, ATP production, maximal respiration, spare respiratory capacity, proton leak and nonmitochondrial respiration ($***P < 0.001$, $**P < 0.01$; **Fig. 4B**). These parameters were calculated as shown by the highlighted areas under the SCC-61 data shown in Fig. 4A. There was a slight decrease in the proton leak in rSCC-61, however, this was not statistically significant. On the other hand, basal respiration, ATP production, maximal respiration, spare respiratory capacity, as well as the nonmitochondrial respiration were all statistically higher in SCC-61. Thus, we conclude that

compared to SCC-61, the radiation-resistant rSCC-61 cells have decreased overall OXPHOS activity and ATP generation. These experiments also allow for detection and quantification of proton production or extracellular acidification rate (ECAR). The results show higher rates of proton production in SCC-61 cells compared with rSCC-61 cells (**Fig. 4C**). Overall, the results are consistent with the increased channeling of glycolysis intermediates into the PPP in rSCC-61 shown in **Fig. 2**, and with the increased proton secretion in SCC-61 (24). Thus, although there is more glucose uptake in rSCC-61 a greater proportion of this is funneled through the PPP and less through the mitochondrial ETC.

We then investigated whether the higher ROS content in SCC-61 compared with rSCC-61 reported earlier (24) could also be partly explained by the increased routing of glucose into the TCA and mitochondrial ETC in SCC-61 identified here. We used MitoSOX to determine differences in mitochondrial ROS between the two cell lines and the consequence of 2-DG treatment on mitochondrial ROS generation. The results showed higher mitochondrial ROS in SCC-61 compared with rSCC-61 and decreased ROS with 2-DG treatment in SCC-61 consistent with the mitochondrial energy findings presented above. These results also show that the increased cytotoxicity of 2-DG in rSCC-61 is not due to an increase in mitochondrial ROS but more likely to decreased flux through PPP or possibly through other mechanisms, since 2-DG effects on cells extend well beyond blockage of glycolysis and PPP (30).

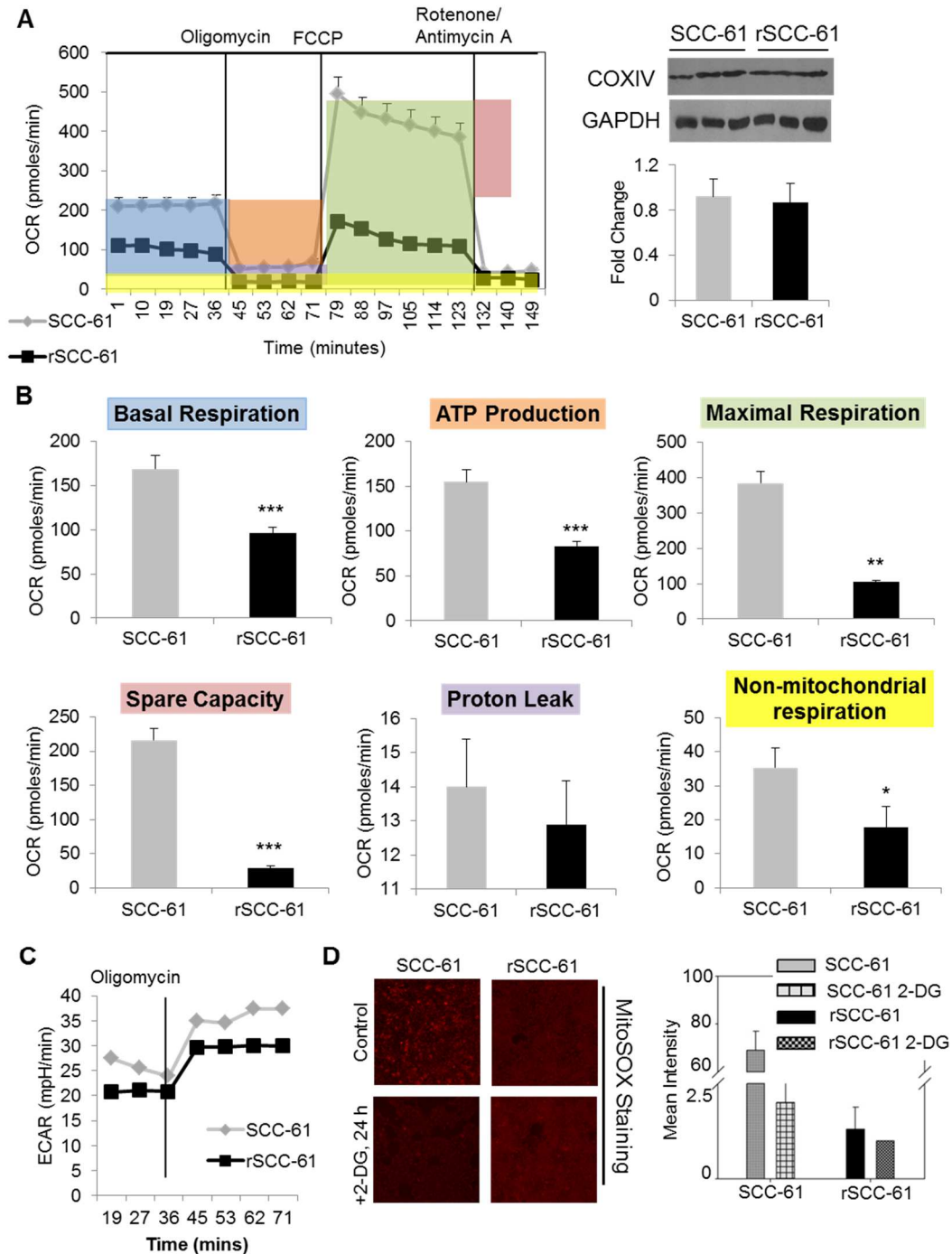


FIG. 4. rSCC-61 has decreased OXPHOS capabilities. **Panel A:** Oxygen consumption rate (OCR) for SCC-61 and rSCC-61 cells using Seahorse XFA 24-3. As shown in the OCR profile plot, the first five measurements represent OCR of untreated cells followed by sequential addition of three mitochondrial inhibitors (after measurements 5, 9 and 15, respectively). Right panel shows the CoxIV Western blot demonstrating equal mitochondrial content in the two cells lines. **Panel B:** Statistical analysis and representative plots extracted from the study in panel A. The P values are as follows: basal respiration ***P < 0.001; ATP production ***P < 0.001; maximal respiration **P = 0.006; spare capacity ***P < 0.001; and nonmitochondrial respiration *P $\frac{1}{4}$ 0.03. **Panel C:** Extracellular acidification rate (ECAR) data showing increased ECAR in SCC-61 (n = 5). **Panel D:** Imaging analysis of mitochondrial ROS using MitoSOX staining for superoxide in SCC-61 and rSCC-61 cells untreated and treated with 20 mM 2-DG for 24 h.

Contribution of Fatty Acid Metabolism to Energy Balance and Radiation Resistance in rSCC-61

Lipid metabolism is a major contributor to energy balance in cells, and while it is known to be upregulated in cancers (31), it has been less studied in relationship to radiation resistance. Since our previous quantitative proteomics studies identified a sevenfold increase in the expression of FASN in rSCC-61 relative to SCC-61 cells, we wanted to investigate the functional contribution of fatty acid metabolism (uptake, biosynthesis and oxidation) to energy balance and radiation response in these cells.

Fatty acid synthase (FASN) activity and uptake of exogenous fatty acids. First, we followed up on the proteomics findings with Western blot analysis showing a threefold increased expression of FASN ($P < 0.001$; **Fig. 5A**). The inconsistency in fold-change values is due to the limited linear dynamic range enabled by Western blot detection compared with the mass spectrometry-based quantitative analysis. Nevertheless, both analyses show a significant >3-fold increase of FASN in rSCC-61 cells. Next, we measured the FASN activity and detected a fivefold increased activity in rSCC-61 relative to SCC-61 ($P < 0.01$, **Fig. 5B**), which was consistent with the increased expression of FASN in these cells. We then hypothesized that the increased biosynthesis of fatty acids in rSCC-61 is associated with a decreased dependence on exogenous fatty acids. To address this, we quantified the uptake of fatty acids in SCC-61 and rSCC-61 cells using ^{14}C -palmitate and found a significant twofold decrease in both the amount and rate of palmitic acid uptake in rSCC-61 (**Fig. 5C**).

Fatty acid oxidation (FAO) assay shows decreased utilization of exogenous fatty acids to support mitochondrial OXPHOS in rSCC-61. SCC-61 and rSCC-61 FAO was determined using BSA conjugated palmitate as exogenous substrate. As shown in the OCR profile plots (**Fig. 5D**), the basal respiration in the presence of BSA:palmitate (purple box) was significantly higher than the BSA control (310 pM/min) in SCC-61 cells. The basal respiration under palmitate and BSA control treatment was calculated by subtracting the nonmitochondrial respiration (average of last

three readings in each plot) from the average of the first four readings. The addition of BSA:palmitate to the rSCC-61 cells also resulted in an increase in basal respiration (85 pM/min) but this was lower than in SCC-61. The expected uncoupling of mitochondria by palmitate (blue box) was observed in both cell lines contributing to the basal respiration with 298 pM/min in SCC-61 and 228 pM/min in rSCC-61. The uncoupling of mitochondria by palmitate or BSA was calculated as the difference between the average of readings 5, 6 and 7 and the average of readings 11, 12 and 13 (nonmitochondrial respiration). Maximal respiration (green box) of SCC-61 due to utilization of exogenous palmitate was increased by 195 pM/min compared to 75 pM/min in rSCC-61. Maximal respiration was calculated as the difference between the average of readings 8, 9 and 10 and the average of readings 11, 12 and 13 (nonmitochondrial respiration). The results demonstrate significant reliance on utilization of endogenous fatty acids in radioresistant rSCC-61. While we do not currently understand the shift in basal OCR in rSCC-61 treated with BSA alone (control experiment), the significantly increased basal OCR in SCC-61 compared with rSCC-61 cells after the addition of palmitate correlates with the higher palmitate uptake seen in **Fig. 5C**.

Inhibition of FASN decreases rSCC-61 survival. Since tumor cells utilize fatty acids for multiple purposes (e.g., membrane synthesis, signaling, antioxidants) and the data in the FAO assay pointed to the need for endogenous fatty acid synthesis to support mitochondrial OXPHOS in rSCC-61, we next investigated the requirement for FASN activity in radiation resistance in rSCC-61. The rSCC-61 and SCC-61 cells were treated with orlistat, a pharmacological inhibitor of FASN, and cell survival was monitored using both clonogenic and cell proliferation assays. The results showed that compared to SCC-61 cells, rSCC-61 had decreased survival upon treatment with orlistat [rSCC-61 IC₅₀ 16.5 μ M, SCC-61 IC₅₀ > 100 μ M (**Fig. 6A**)] and increased sensitivity to radiation [$P = 0.009$, $P = 0.005$, $P = 0.007$ for orlistat concentrations 0.1, 1.0 and 10.0 μ M, respectively (**Fig. 6B**)]. Next, we decreased the expression of FASN in rSCC-61 using a siRNA approach and quantified the consequence on the response to radiation. Overall, down-

regulation of FASN with orlistat or siRNA treatment resulted in increased sensitivity to radiation in rSCC-61 cells ($P = 0.001-0.05$, **Fig. 6C, left side**) matching the response to radiation in SCC-61 cells, which were used as control in this experiment. The depletion of FASN protein upon transfection with FASN siRNA was confirmed by Western blot analysis (**Fig. 6C, right side**). To determine the role of endogenous fatty acids in mitochondrial OXPHOS activity in rSCC-61 cells, we inhibited FASN using 10 μM orlistat and measured OCR as shown in **Fig. 4B**. The results showed inhibition of FASN by orlistat significantly decreased five out of six parameters extracted from the OCR data in rSCC-61 cells. In SCC-61, the orlistat treatment decreased only nonmitochondrial respiration while not affecting or slightly increasing some of the other OCR parameters (**Fig. 6D**). This data further supports the necessary role of fatty acid synthesis in OXPHOS activity and ATP generation in the radiation-resistant rSCC-61 cells and a potential contribution of fatty acid metabolism to nonmitochondrial respiration in both SCC-61 and rSCC-61 cells.

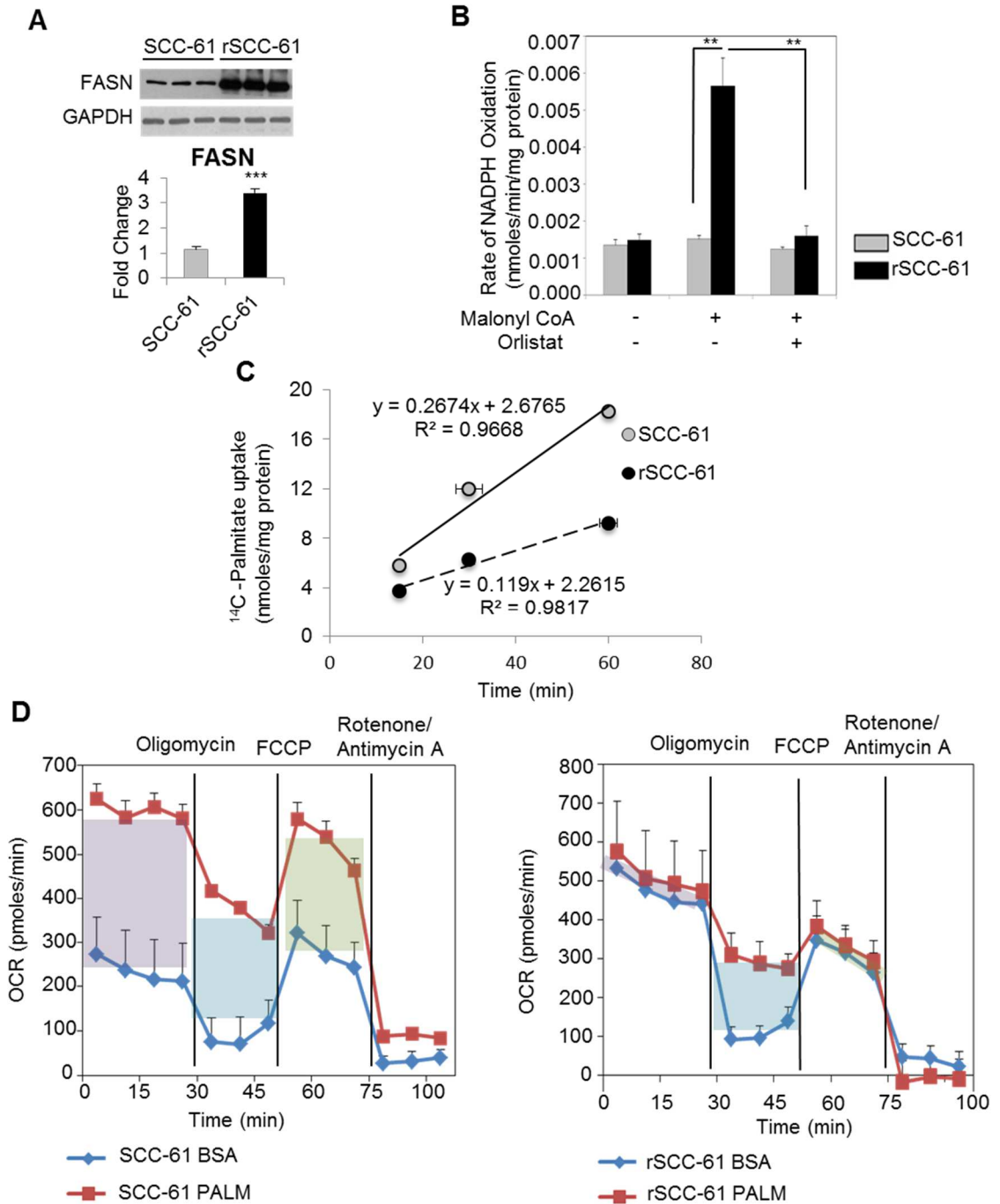


FIG. 5. Fatty acid synthase is overexpressed and correlated to radioresistance in rSCC-61. **Panel A:** Western blot analysis of FASN and quantification ($P < 0.001$) showing increased expression in rSCC-61 cells. GAPDH staining was performed to show equal protein loading. **Panel B:** Fatty acid synthase activity assay. FASN-dependent oxidation of NADPH with or without orlistat treatment was measured as described in the Materials and Methods section. rSCC-61 have significantly higher ($P < 0.01$) FASN activity that is reduced upon the addition of the FASN inhibitor orlistat. **Panel C:** ¹⁴C-Palmitate uptake. SCC-61 and rSCC-61 were cultured and incubating with ¹⁴C-palmitate for 15, 30 and 60 min. Exogenous palmitate uptake in rSCC-61 cells was twofold lower than in SCC-61. **Panel D:** Fatty acid oxidation assay. SCC-61 cells demonstrate a significant reliance on utilization of exogenous palmitate to respond to energy demand compared to rSCC-61. Purple box: basal respiration; blue box: uncoupling of mitochondria; green box: maximal respiration.

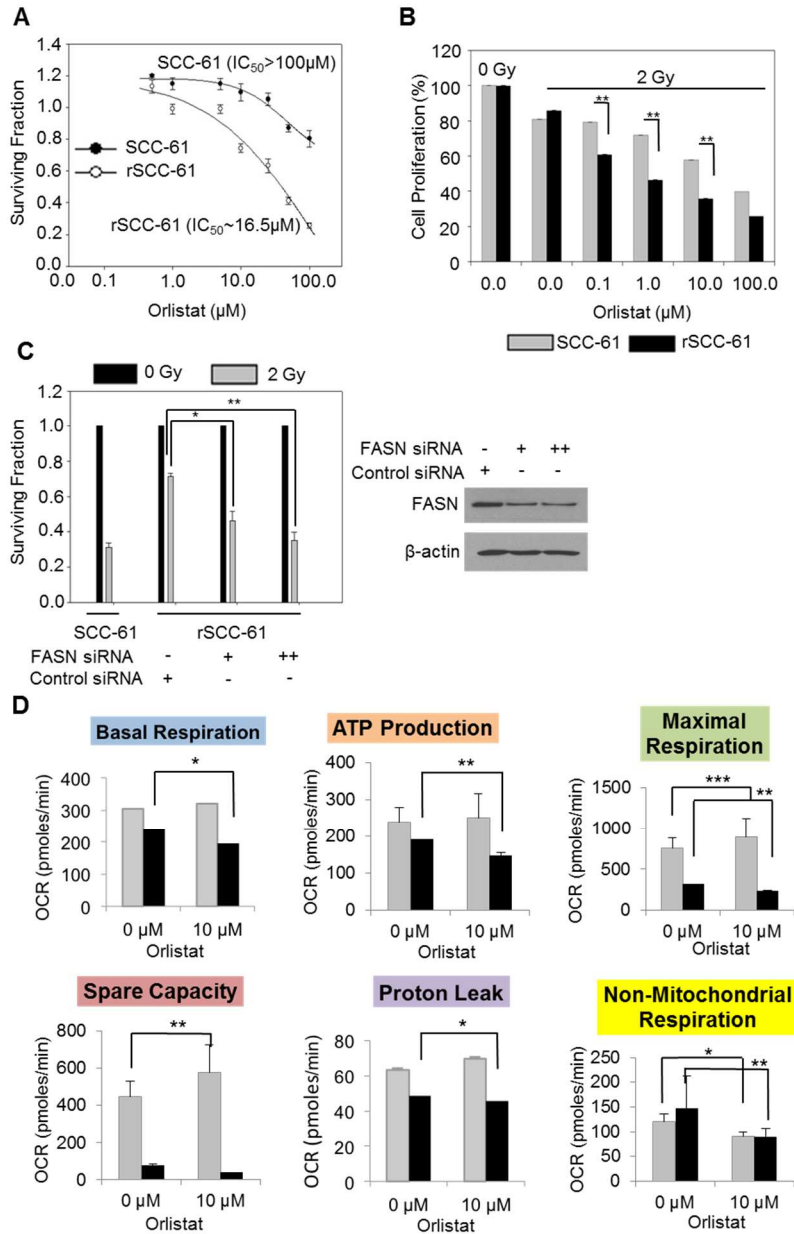


FIG. 6. Panel A: Clonogenic assay to determine the response to orlistat treatment. The survival plots for the SCC-61 and rSCC-61 cells are shown in response to increasing doses of orlistat. The calculated IC_{50} for orlistat in each cell line is indicated and show enhanced sensitivity to orlistat treatment in rSCC-61. **Panel B:** Cell proliferation in the presence of increasing concentrations of orlistat and 2 Gy irradiation was determined using the SRB assay (** $P = 0.009$, ** $P = 0.005$, ** $P = 0.007$ for 0.1, 1 and 10.0 μM orlistat, respectively). Three biological replicates were used for each study. The results show increased sensitivity to radiation after treatment with orlistat in rSCC-61 compared with SCC-61 cells. **Panel C:** Clonogenic assay to determine the radiosensitizing effect of FASN depletion. rSCC-61 cells transfected with control or FASN siRNA were set up for clonogenic assays and their survival was calculated with 2 Gy irradiation or without irradiation. siRNA-mediated depletion of FASN protein significantly radiosensitized rSCC-61 cells (** $P = 0.001-0.01$). SCC-61 cells were also set up alongside for the assay for a comparative overview of radiosensitivity. **Panel D:** OCR for SCC-61 and rSCC-61 cells using Seahorse XFA 24-3 after treatment with 10 μM orlistat. Inhibition of FASN by orlistat significantly decreased mitochondrial OCR in rSCC-61 cells and impacted the nonmitochondrial OCR in both SCC-61 and rSCC-61 cells (* $P = 0.01-0.05$, ** $P = 0.001-0.01$ and *** $P < 0.001$).

DISCUSSION

Despite significant advances in the understanding of HNSCC tumor biology, the management of HNSCC remains complicated and a multimodality approach is often employed to treat HNSCC patients. Radiation therapy is a common treatment for HNSCC and used in nearly all disease stages in combination with surgery or chemotherapy (32). However, despite recent progress on the use of targeted therapies (e.g., Cetuximab targeting epidermal growth factor receptor) in combination with radiation therapy to treat HNSCC, resistance to radiation treatment remains a serious concern (33 – 35). Ongoing efforts to sensitize tumors to radiation treatment include improvements in radiation regimens and delivery, identification of molecular markers of radiation response, discovery of new therapeutic targets as sensitizers of radiation response and their optimization with existing radiation treatment options. Towards this goal, we had previously established a preclinical matched model of radiation resistance in HNSCC and performed comprehensive proteomics analysis to identify molecular networks that can contribute to the radiation-resistant phenotype in HNSCC (24). The study has now been extended to understand the nutrient and energy signatures of SCC-61 and the matched radiation-resistant rSCC-61.

Normal untransformed eukaryotic cells have evolved for optimal utilization of biochemical pathways (e.g., glycolysis, TCA, mitochondrial OXPHOS, PPP) to convert glucose into CO₂ and H₂O while maximizing the production of ATP, NADPH and various biosynthetic intermediates. In contrast, tumor cells have been traditionally classified as “addicted to glucose” where they employ aerobic glycolysis for energy generation and divert mitochondrial activity into biosynthetic pathways for biomass generation to support cell proliferation (12). In addition, studies have increasingly shown that tumor cells demonstrate utilization of alternative oxidizable substrates like glutamine and fatty acids to potentiate their survival (14–16). Despite the increased recognition of the need to understand tumor metabolism for improved disease management, few studies have focused on presenting a clear picture of the metabolic phenotype of HNSCC (17, 19,

36). Two earlier published studies showed NMR-based metabolic profiling of HNSCC tumor specimens and varied levels of metabolites that revealed dysregulation in multiple metabolic events, including the Warburg effect, TCA, glutaminolysis and antioxidant mechanisms, among others (19, 36). In another study by Sandulache *et al.* (17), a panel of 15 HNSCC cell lines was evaluated for metabolic phenotype and the potential for targeting key energy metabolism pathways for inhibiting cell proliferation in head and neck cancer. The majority of cell lines tested in this study relied on glucose and not glutamine for their survival. However, there remains a lack of coherent understanding of the metabolic perturbations that exist in the development of radioresistance in HNSCC. In the current study we show that radiation resistance is associated with increased glucose uptake consistent with the increased reliance of these cells on glycolysis and PPP. We identified increased expression of GLUT1, a clinically useful marker for HNSCC disease (37) and increased localization to the membrane in rSCC-61 cells compared to SCC-61 cells. While both SCC-61 and rSCC-61 cells were sensitive to metabolic inhibitors of glycolysis (2-DG) and PPP (6-AN), the effects of 2-DG and 6-AN in rSCC-61 were stronger than in SCC-61. Further analyses support the increased routing of glucose into the PPP pathway due to increased expression of TIGAR, G6PD and increased production of NADPH in rSCC-61 for synthesis of lipids and nucleic acids. These observations are in accordance with previous reports showing combinatorial treatment with 2-DG and 6-AN to radiosensitize head and neck cancer cells through mechanisms that involved redox-mediated alteration of ASK1-JNK/p38MAPK apoptosis signaling pathway (38). With respect to glutaminolysis, the rSCC-61 cells were less reliant on this pathway for proliferation compared with SCC-61, which had significantly decreased cell proliferation with glutamine deprivation. Glutamine is a nonessential versatile amino acid with multiple functions in nucleotide, protein, lipid and ATP biosynthesis (39). It should also be noted that cancer cells show systemic differences in their glutamine dependence and that not all cancer cells require exogenous supply of glutamine (40). Resistance to glutamine metabolism has also been associated with *de novo* biosynthesis of glutamine or utilization of

alternate anaplerotic pathways (40). Whether rSCC-61 bypasses glutamine metabolism or redirects glutamine biosynthesis along with its functional consequence to resistance to radiation remains to be explored. Radiation treatment significantly impaired cell proliferation when used alone. However, an additive or synergistic effect, when used in combination with inhibitors of cellular energy metabolism, was not evident from the studies reported here suggesting either: 1. masking of the radiation-induced cell death due to the much stronger effects of energy deprivation; or 2. dependence of radiation effects on energy metabolism. We favor the second scenario based on the known mechanisms of radiation-induced ROS and ROS amplification in time (41) and data showing an inhibition of the radiation-induced bystander effects and cell death in G6PD null cells (42).

Recent research has identified mitochondrial respiration as an important contributor to tumor cell survival and proliferation (12). Previous observations, such as reduced intracellular and extracellular lactate in rSCC-61 cells (24), have suggested potential deviation of rSCC-61 from the classical Warburg phenotype and channeling of pyruvate into the TCA cycle to support mitochondrial OXPHOS or into PPP to promote NADPH and nucleotide synthesis. To investigate this metabolic restructuring in rSCC-61, we measured the mitochondrial activity (OCR) in SCC-61 and rSCC-61 cells using the Seahorse XF analyzer. rSCC-61 cells had significantly lower basal OCR, indicating that these cells generate less ATP via mitochondrial respiration. Another significant observation was the lower spare capacity in rSCC-61 compared with SCC-61 ($P < 0.001$). It has been demonstrated that under stress mitochondria can draw on the spare capacity to meet the additional energy demands for detoxification and repair of stress-induced damage (43). Thus, intuitively we expected the spare capacity in rSCC-61 to be higher than SCC-61, a hypothesis that was proven incorrect by the analysis shown in Fig. 4. However, despite the lower spare capacity in rSCC-61, the rSCC-61 cells maintain a significant level of ATP production that could potentially be used to repair radiation-associated damage. Interestingly, the

nonmitochondrial respiration was also decreased in rSCC-61 (though the statistical significance was lower compared to other OCR parameters) and was inhibited by orlistat treatment in both SCC-61 and rSCC-61 cells. A full investigation of the ROS sources and metabolism in SCC-61 and rSCC-61 cells is underway, but these results raise the possibility that other cellular oxygen-consuming reactions such as those catalyzed by cell membrane-associated NAD(P)H oxidases or oxidoreductases may contribute to both ROS content and energy metabolism by regenerating, for example, NAD⁺ needed for glycolysis (44). Fatty acid metabolism may well contribute to these processes since there is an established regulatory relationship between plasma membrane lipid composition and activity of the enzymes embedded or associated with cellular plasma membrane (45). We plan to study these mechanisms as we further investigate this model of radiation resistance.

Fatty acids are also key contributors to energy metabolism, and key enzymes in the lipid synthesis pathway such as FASN have been shown to be upregulated in cancer cells (31). While a number of studies implicate the role of FASN in tumorigenesis and appreciate its diagnostic and prognostic value, studies focusing on the association of FASN overexpression with response to therapy are limited. In head and neck cancer, overexpression of FASN has been previously reported and associated with lung metastasis of HNSCC and radiation resistance in nasopharyngeal cancer (46–49). Consistent with these observations, we found increased expression and activity of FASN in radiation-resistant rSCC-61 cells. Moreover, we demonstrate that inhibition of FASN by orlistat reduces rSCC-61 cell proliferation, and depletion of FASN with orlistat or siRNA renders the rSCC-61 cells sensitive to the cytotoxic effects of radiation. Depletion of FASN with orlistat significantly decreased ATP production in rSCC-61, thereby potentially reducing its ability to repair radiation-induced damage. We are particularly intrigued by a recent study showing the induction of epithelial-to-mesenchymal transition by decreasing the expression of FASN (50). These results match nicely with our previously reported analysis of the

mesenchymal-to-epithelial change in phenotype in SCC-61/rSCC-61 system, which was associated with increased FASN expression in rSCC-61 (24). Together these studies point not only to the potential value of exploring FASN inhibitors for treatment of radiation-resistant HNSCC, but also to lipid metabolism as a major driver of radiation response and cellular epithelial or mesenchymal phenotype.

To summarize, we present an analysis of the nutrient and energy metabolism in a matched model of radiation resistance for HNSCC (**Fig. 7**). The radioresistant rSCC-61 cells were distinctly characterized by increased dependency on glucose and enhanced sensitivity to glycolysis and PPP inhibitors. The radiation-resistant phenotype was associated with a deviation from the Warburg effect and utilization of endogenous fatty acids for energy production. One of the significant findings of our study was the increased sensitivity to radiation upon inhibition of FASN, which opens new directions for research focused on development and optimization of inhibitors targeting lipid metabolism pathways that are enhanced in radiation-resistant HNSCC.

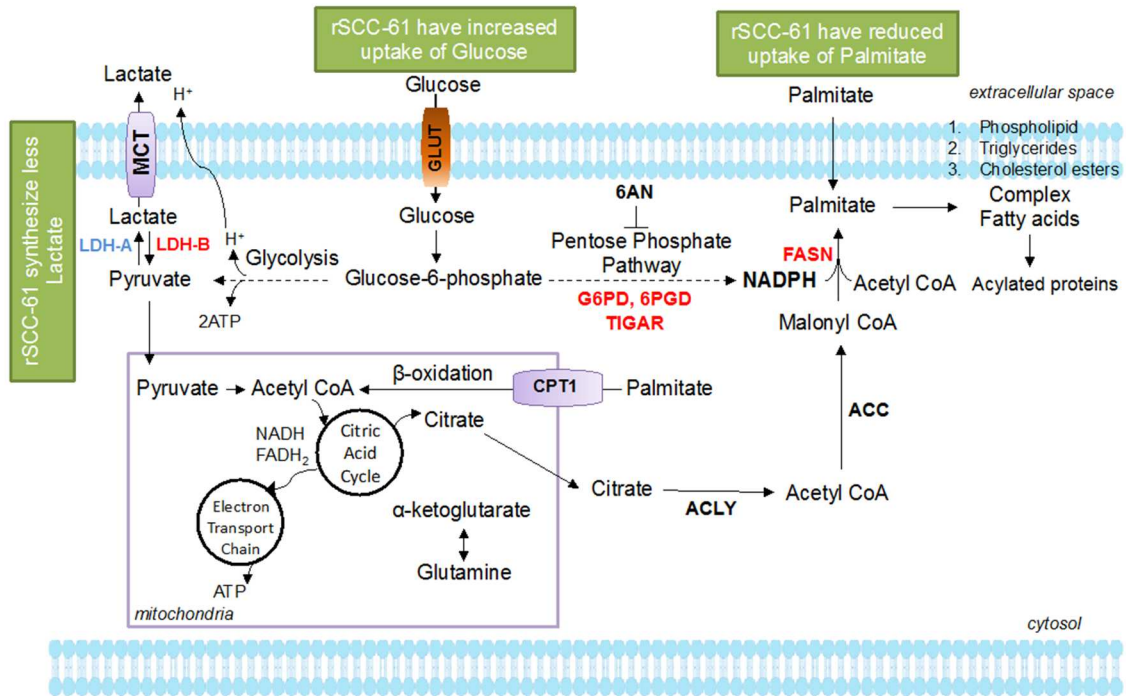


FIG. 7. Summary overview of the differential carbohydrate and lipid metabolism in SCC-61 and rSCC-61 cells. 6-AN = 6-aminonicotinamide; G6PD = glucose 6-phosphate dehydrogenase; 6PGD = 6-phosphogluconate dehydrogenase; ACC = acetyl-CoA carboxylase; ACLY = ATP:citrate lyase; CPT1 = carnitine palmitoyl-transferase I; FASN = fatty acid synthase; GLUT = glucose transporter; LDHA/B = lactate dehydrogenase A/B; MCT = monocarboxylate transporter; TIGAR = TP53-inducible glycolysis and apoptosis regulator.

Acknowledgments

Research reported in this article was supported by the National Cancer Institute of the National Institutes of Health [R01 CA136810 (CMF)]. The authors acknowledge financial support from Wake Forest School of Medicine (development funds to CMF) and the Wake Forest University Structural and Computational Biophysics training program [T32GM095440 (predoctoral fellowship to JM)]. A National Science Foundation Major Research Instrumentation award supported the purchase of the LSCM used to generate GLUT1 images included in this article (MRI-0722926) within the WFU Microscopic Imaging Core Facility. The authors would also like to thank Dr. Glen Marrs (WFU) for advice on the imaging studies, Dr. Tiefu Liu in Dr. Charles McCall's laboratory (WFSM) for technical support with the palmitate uptake assay, Drs. Achche Patel and Weiling Zhao for technical assistance with some of the studies included here and Dr. Steven Kridel (WFSM) for advice on the FASN/orlistat studies.

Literature Cited

1. **Bernstein JM, Bernstein CR, West CM, Homer JJ.** Molecular and cellular processes underlying the hallmarks of head and neck cancer. *Eur Arch Otorhinolaryngol.* 2012; 270:2585–93. [PubMed: 23263268]
2. **Bentzen SM, Atasoy BM, Daley FM, Dische S, Richman PI, Saunders MI, Trott KR, Wilson GD.** Epidermal growth factor receptor expression in pretreatment biopsies from head and neck squamous cell carcinoma as a predictive factor for a benefit from accelerated radiation therapy in a randomized controlled trial. *J Clin Oncol.* 2005; 26:5560–7. [PubMed: 16110017]
3. **Bonner JA, Harari PM, Giralt J, Azarnia N, Shin DM, Cohen RB, Jones CU, Sur R, Raben D, Jassem J, Ove R, Kies MS, Baselga J, Yousoufian H, Amellal N, Rowinsky EK, Ang KK.** Radiotherapy plus cetuximab for squamous-cell carcinoma of the head and neck. *N Engl J Med.* 2006; 354:567–78. [PubMed: 16467544]
4. **Harari PM, Huang S.** Radiation combined with EGFR signal inhibitors: head and neck cancer focus. *Semin Radiat Oncol.* 2006; 16:38–44. [PubMed: 16378905]
5. **Hanahan D, Weinberg RA.** Hallmarks of cancer: the next generation. *Cell.* 2011; 144:646–74. [PubMed: 21376230]
6. **Hanahan D, Weinberg RA.** The hallmarks of cancer. *Cell.* 2000; 100:57–70. [PubMed: 10647931]
7. **Barger JF, Plas DR.** Balancing biosynthesis and bioenergetics: metabolic programs in oncogenesis. *Endocr Relat Cancer.* 2010; 17:R287–304. [PubMed: 20699334]
8. **Wise DR, DeBerardinis RJ, Mancuso A, Sayed N, Zhang XY, Pfeiffer HK, Nissim I, Daikhin E, Yudkoff M, McMahon SB, Thompson CB.** Myc regulates a transcriptional program that stimulates mitochondrial glutaminolysis and leads to glutamine addiction. *Proc Natl Acad Sci U S A.* 2008; 105:18782–7. [PubMed: 19033189]
9. **Warburg O.** On the origin of cancer cells. *Science.* 1956; 123:309–14. [PubMed: 13298683]
10. **Vander Heiden MG, Cantley LC, Thompson CB.** Understanding the Warburg effect: the metabolic requirements of cell proliferation. *Science.* 2009; 324:1029–33. [PubMed: 19460998]

11. **Koppenol WH, Bounds PL, Dang CV.** Otto Warburg's contributions to current concepts of cancer metabolism. *Nat Rev Cancer*. 2011; 11:325–37. [PubMed: 21508971]
12. **Ward PS, Thompson CB.** Metabolic reprogramming: a cancer hallmark even Warburg did not anticipate. *Cancer Cell*. 2012; 21:297–308. [PubMed: 22439925]
13. **Cairns RA, Harris IS, Mak TW.** Regulation of cancer cell metabolism. *Nat Rev Cancer*. 2011; 11:85–95. [PubMed: 21258394]
14. **Weinberg F, Hamanaka R, Wheaton WW, Weinberg S, Joseph J, Lopez M, Kalyanaraman B, Mutlu GM, Budinger GR, Chandel NS.** Mitochondrial metabolism and ROS generation are essential for Kras-mediated tumorigenicity. *Proc Natl Acad Sci U S A*. 2010; 107:8788–93. [PubMed: 20421486]
15. **Pike LS, Smift AL, Croteau NJ, Ferrick DA, Wu M.** Inhibition of fatty acid oxidation by etomoxir impairs NADPH production and increases reactive oxygen species resulting in ATP depletion and cell death in human glioblastoma cells. *Biochim Biophys Acta*. 2011; 1807:726–34. [PubMed: 21692241]
16. **Diers AR, Broniowska KA, Chang CF, Hogg N.** Pyruvate fuels mitochondrial respiration and proliferation of breast cancer cells: effect of monocarboxylate transporter inhibition. *Biochem J*. 2012; 444:561–71. [PubMed: 22458763]
17. **Sandulache VC, Ow TJ, Pickering CR, Frederick MJ, Zhou G, Fokt I, Davis-Malesevich M, Priebe W, Myers JN.** Glucose, not glutamine, is the dominant energy source required for proliferation and survival of head and neck squamous carcinoma cells. *Cancer*. 2011; 117:2926–38. [PubMed: 21692052]
18. **Simons AL, Parsons AD, Foster KA, Orcutt KP, Fath MA, Spitz DR.** Inhibition of glutathione and thioredoxin metabolism enhances sensitivity to perifosine in head and neck cancer cells. *J Oncol*. 2009; 2009:519563. [PubMed: 19746172]
19. **Tripathi P, Kamarajan P, Somashekar BS, MacKinnon N, Chinnaiyan AM, Kapila YL, Rajendiran TM, Ramamoorthy A.** Delineating metabolic signatures of head and neck squamous cell carcinoma: phospho-lipase A2, a potential therapeutic target. *Int J Biochem Cell Biol*. 2012; 44:1852–61. [PubMed: 22743333]
20. **Yang C, Sudderth J, Dang T, Bachoo RM, McDonald JG, DeBerardinis RJ.** Glioblastoma cells require glutamate dehydrogenase to survive impairments of glucose metabolism or Akt signaling. *Cancer Res*. 2009; 69:7986–93. [PubMed: 19826036]

21. **Maschek G, Savaraj N, Priebe W, Braunschweiger P, Hamilton K, Tidmarsh GF, De Young LR, Lampidis TJ.** 2-deoxy-D-glucose increases the efficacy of adriamycin and paclitaxel in human osteosarcoma and non-small cell lung cancers in vivo. *Cancer Res.* 2004; 64:31–4. [PubMed: 14729604]
22. **Mohanti BK, Rath GK, Anantha N, Kannan V, Das BS, Chandramouli BA, Banerjee AK, Das S, Jena A, Ravichandran R, Sahi UP, Kumar R, Kapoor N, Kalia VK, Dwarakanath BS, Jain V.** Improving cancer radiotherapy with 2-deoxy-D-glucose: phase I/II clinical trials on human cerebral gliomas. *Int J Radiat Oncol Biol Phys.* 1996; 35:103–11. [PubMed: 8641905]
23. **Dwarakanath BS, Singh D, Banerji AK, Sarin R, Venkataramana NK, Jalali R, Vishwanath PN, Mohanti BK, Tripathi RP, Kalia VK, Jain V.** Clinical studies for improving radiotherapy with 2-deoxy-D-glucose: present status and future prospects. *J Cancer Res Ther.* 2009; 5(Suppl 1):S21–6. [PubMed: 20009289]
24. **Bansal N, Mims J, Kuremsky JG, Olex AL, Zhao W, Yin L, Wani R, Qian J, Center B, Marrs GS, Porosnicu M, Fetrow JS, Tsang AW, Furdul CM.** Broad phenotypic changes associated with gain of radiation resistance in head and neck squamous cell cancer. *Antioxid Redox Signal.* 2014; 21:221–36. [PubMed: 24597745]
25. **Vichai V, Kirtikara K.** Sulforhodamine B colorimetric assay for cytotoxicity screening. *Nat Protoc.* 2006; 1:1112–6. [PubMed: 17406391]
26. **Bensaad K, Tsuruta A, Selak MA, Vidal MN, Nakano K, Bartrons R, Gottlieb E, Vousden KH.** TIGAR, a p53- inducible regulator of glycolysis and apoptosis. *Cell.* 2006; 126:107–20. [PubMed: 16839880]
27. **Robey RB, Hay N.** Mitochondrial hexokinases, novel mediators of the antiapoptotic effects of growth factors and Akt. *Oncogene.* 2006; 25:4683–96. [PubMed: 16892082]
28. **DeBerardinis RJ, Lum JJ, Hatzivassiliou G, Thompson CB.** The biology of cancer: metabolic reprogramming fuels cell growth and proliferation. *Cell Metab.* 2008; 7:11–20. [PubMed: 18177721]
29. **Yuneva M, Zamboni N, Oefner P, Sachidanandam R, Lazebnik Y.** Deficiency in glutamine but not glucose induces MYC-dependent apoptosis in human cells. *J Cell Biol.* 2007; 178:93–105. [PubMed: 17606868]
30. **Ralser M, Wamelink MM, Struys EA, Joppich C, Krobitsch S, Jakobs C, Lehrach H.** A catabolic block does not sufficiently explain how 2-deoxy-D-glucose inhibits cell growth. *Proc Natl Acad Sci U S A.* 2008; 105:17807–11. [PubMed: 19004802]

31. **Menendez JA, Lupu R.** Fatty acid synthase and the lipogenic phenotype in cancer pathogenesis. *Nat Rev Cancer.* 2007; 7:763–77. [PubMed: 17882277]
32. **Corvo R.** Evidence-based radiation oncology in head and neck squamous cell carcinoma. *Radiother Oncol.* 2007; 85:156–70. [PubMed: 17482300]
33. **Nutting CM, Bhide SA, Harrington KJ.** Treatment of head and neck cancer. *N Engl J Med.* 2008; 358:1076–7. author reply 77–8. [PubMed: 18326077]
34. **Forastiere AA, Trotti A, Pfister DG, Grandis JR.** Head and neck cancer: recent advances and new standards of care. *J Clin Oncol.* 2006; 24:2603–5. [PubMed: 16763271]
35. **Sandulache VC, Myers JN.** Altered metabolism in head and neck squamous cell carcinoma: an opportunity for identification of novel biomarkers and drug targets. *Head Neck.* 2012; 34:282–90. [PubMed: 21322078]
36. **Somashekar BS, Kamarajan P, Danciu T, Kapila YL, Chinnaiyan AM, Rajendiran TM, Ramamoorthy A.** Magic angle spinning NMR-based metabolic profiling of head and neck squamous cell carcinoma tissues. *J Proteome Res.* 2011; 10:5232–41. [PubMed: 21961579]
37. **Kunkel M, Reichert TE, Benz P, Lehr HA, Jeong JH, Wieand S, Bartenstein P, Wagner W, Whiteside TL.** Overexpression of Glut-1 and increased glucose metabolism in tumors are associated with a poor prognosis in patients with oral squamous cell carcinoma. *Cancer.* 2003; 97:1015–24. [PubMed: 12569601]
38. **Sharma PK, Varshney R.** 2-Deoxy-D-glucose and 6-aminonicotin-amide-mediated Nrf2 down regulation leads to radiosensitization of malignant cells via abrogation of GSH-mediated defense. *Free Radic Res.* 2012; 46:1446–57. [PubMed: 22946929]
39. **Daye D, Wellen KE.** Metabolic reprogramming in cancer: unraveling the role of glutamine in tumorigenesis. *Semin Cell Dev Biol.* 2012; 23:362–9. [PubMed: 22349059]
40. **Hensley CTWA, DeBerardinis RJ.** Glutamine and cancer: cell biology, physiology, and clinical opportunities. *J Clin Invest.* 2013; 123:3678–84. [PubMed: 23999442]
41. **Reisz JA, Bansal N, Qian J, Zhao W, Furdul CM.** Effects of ionizing radiation on biological molecules-mechanisms of damage and emerging methods of detection. *Antioxid Redox Signal.* 2014; 21:260–92. [PubMed: 24382094]

42. **Mothersill C, Stamato TD, Perez ML, Cummins R, Mooney R, Seymour CB.** Involvement of energy metabolism in the production of ‘bystander effects’ by radiation. *Br J Cancer*. 2000; 82:1740–6. [PubMed: 10817512]
43. **Hill BG, Dranka BP, Zou L, Chatham JC, Darley-Usmar VM.** Importance of the bioenergetic reserve capacity in response to cardiomyocyte stress induced by 4-hydroxynonenal. *Biochem J*. 2009; 424:99–107. [PubMed: 19740075]
44. **Herst PM, Berridge MV.** Plasma membrane electron transport: a new target for cancer drug development. *Curr Mol Med*. 2006; 6:895–904. [PubMed: 17168740]
45. **Jin S, Zhou F, Katirai F, Li PL.** In health and disease. *Antioxid Redox Signal*. 2011; 15:1043–83. [PubMed: 21294649]
46. **Benevenuto de Andrade BA, Pina AR, Leon JE, Paes de Almeida O, Altemani A.** Primary nasal mucosal melanoma in Brazil: clinicopathologic and immunohistochemical study of 12 patients. *Ann Diagn Pathol*. 2012;16:344–9.
47. **De Vincentiis M, Di Cello P, Censi F, Leopizzi M, Natalizi S, Sardella B, et al.** Immunohistochemical expression of fatty acid synthase, Ki-67 and p53 in squamous cell carcinomas of the larynx. *Int J Biol Markers*. 2008;23:176–81.
48. **Kao YC, Lee SW, Lin LC, Chen LT, Hsing CH, Hsu HP, et al.** Fatty acid synthase overexpression confers an independent prognosticator and associates with radiation resistance in naso-pharyngeal carcinoma. *Tumour Biol*. 2012;34:759–68.
49. **Silva SD, Cunha IW, Younes RN, Soares FA, Kowalski LP, Graner E.** ErbB receptors and fatty acid synthase expression in aggressive head and neck squamous cell carcinomas. *Oral Dis*. 2010;16:774–80.
50. **Jiang L, Xiao L, Sugiura H, Huang X, Ali A, Kuro OM, et al.** Metabolic reprogramming during TGFbeta1-induced epithelial-to-mesenchymal transition. *Oncogene*. 2014 doi: 10.1038/onc.2014.321.

CHAPTER 4

Integration of Signaling and Metabolism in a Head and Neck Cancer Cell Model of Radiation Resistance using COSM^{RO}

Zhiwei Ji^{1,2}, Jade Mims³, Nelmi O. Devarie-Baez³, Hanzhi Wu³, Elsa I. Silva Lopez³, Joshua Lewis⁵, Victor Vitvitsky⁵, Jing Su², Melissa L. Kemp⁴, Ruma Banerjee⁵, Allen W. Tsang³, Xiaobo Zhou^{2,*}, Cristina M. Furdai^{3,*}

¹School of Electronics and Information Engineering, Tongji University, 4800 Cao'an Road, Shanghai, P.R. China 201804

²Division of Radiologic Sciences – Center for Bioinformatics and Systems Biology, Wake Forest School of Medicine, Medical Center Boulevard, Winston-Salem, NC, USA 27157

³Section on Molecular Medicine, Department of Internal Medicine, Wake Forest School of Medicine, Medical Center Boulevard, Winston-Salem, NC, USA 27157

⁴The Parker H. Petit Institute of Bioengineering and Bioscience, Georgia Institute of Technology, 315 Ferst Dr NW, Atlanta GA 30332-0363 and The Wallace H. Coulter Department of Biomedical Engineering, Georgia Institute of Technology and Emory School of Medicine, 950 Atlantic Dr NW, Atlanta GA 30332-2000

⁵Department of Biological Chemistry, University of Michigan Medical Center, Ann Arbor, MI 48109-0600

The following manuscript is in preparation to be submitted to *Cell*. The stylistic variations are due to the requirements of the journal.

Abstract

Radiation therapy alone or combined with systemic chemotherapy is widely used for treatment of solid cancers. Resistance to radiation therapy significantly impacts the ability to achieve remission or local control of cancer. To systematically study the molecular mechanisms that elicit protection against radiation treatment, we have developed a matched model of resistance to radiation in Head and Neck Squamous Cell Cancer (HNSCC). The primary analysis of this model system revealed broad redox changes associated with the acquisition of resistance to radiation including suppression of reactive oxygen species (ROS). The work presented here models the role of endogenous antioxidant system in integration of signaling and metabolism in HNSCC. A constraint-based computational method (COSM^{ro}) was developed for this purpose, which combines multiple omics data and takes into consideration the relationships among signaling proteins, metabolic flux distribution, and the thermodynamic and stoichiometric characteristics of metabolites in the network. The analysis provides insight into the redox-dependent changes that are fundamental to the response to radiation in HNSCC. The discovered relationship between intracellular redox state, cholesterol metabolism, and response to radiation is validated.

Keywords Radiation Resistance; Head and Neck Cancer; Redox; Mixed Integer Programming

Introduction

Ionizing radiation is widely used to treat cancer and more than 50% of cancer patients receive either definitive or adjuvant radiation therapy during the course of their treatment (Vatner et al., 2014). The therapeutic outcome of radiation therapy is, however, difficult to predict and is often undermined by the fraction of tumor cells that resist radiation damage. Ionizing radiation exerts its effects through direct interaction with biological molecules such as nucleic acids and through the action of reactive species generated by the radiolysis of water, which include reactive oxygen species (ROS) such as hydroxyl radicals (HO \cdot). These primary events quickly give rise to secondary ROS, superoxide and hydrogen peroxide, which are then further propagated in cells by endogenous ROS-producing systems such as NADPH oxidases and mitochondrial electron transport chain (Singh and Singh, 1982). The chemistry of interaction between ROS and nucleic acids, lipids and proteins has been discussed thoroughly in a review article (Reisz et al, 2014). In recent years, many proteins with critical functions have been shown to respond to oxidants through a variety of mechanisms including oxidation of critical cysteine residues to form Cys-SOH, Cys-SO $_2$ H and intra or intermolecular -SS- species (Devarie-Baez, 2016). For example, ROS regulates phosphorylation cascades both through the oxidative inactivation of protein tyrosine phosphatases (PTPs) (Lou, 2008; Rhee, 2006), and the activation or inactivation of kinases [e.g., PKA, MEKK1, MKK6 and ATM] (Pace & Weerapana, 2013). In the case of ATM, radiation-induced ROS activates this DNA damage response protein by inducing intermolecular disulfides (Guo, 2010). Thus, as with phosphorylation, it is clear that oxidation events across the proteome exert regulatory effects on signaling proteins. Similarly, there are a number of studies reporting direct and indirect metabolic (small or large-scale) changes by ROS (Cano, 2010; Cheema, 2011; Varghese, 2010). The ATM described above was found to regulate purine, pyrimidine, and urea cycle metabolism through the activation of AMP-activated protein kinase, a crucial sensing enzyme in the regulation of cellular energy pathways (Cheema, 2011; Varghese,

2010). Another example is the PKM2 inhibition by ROS. PKM2 is a metabolic enzyme that also acts as a phospho- and redox-regulated protein kinase when transferred to nucleus (Anastasiou, 2011; Hitosugi, 2009; Israelsen, 2013; Yang, 2012).

The focus of the work presented here is the interaction of ROS with proteins and the consequence of this interaction on cellular signaling and metabolism that is relevant for the radiation response in head and neck cancer, a disease for which development of resistance frequently limits the use of radiation therapy. Understanding the redox-regulated mechanisms by which radiation resistant tumor cells avoid and repair the damage induced by radiation is key to identifying the targets that will sensitize these tumors to radiation therapy. To facilitate these investigations we reported the development of a matched model of response to radiation in HNSCC (radiation sensitive SCC-61 and its radiation resistant derivative rSCC-61) and performed the primary characterization of this system using proteomics and a series of complementary assays. A critical and exciting finding emerging from these studies was the identification of common radiation resistance “themes” in rSCC-61 such as the up-regulation of DNA-damage repair, up-regulation of the antioxidant system, and an overall suppression of intracellular ROS (Bansal, 2014).

In this study, we sought to first develop a mathematical approach to integrate ROS-mediated effects on signaling and metabolism contributing to the radiation resistance in HNSCC (**Figure 1**) and then validate some of the discoveries emerging from this analysis. We describe constraint-based systemic modeling of redox regulation (COSM^{ro}) in SCC-61/rSCC-61 system using multiple experimental data from proteomics, metabolomics, redox and phosphoproteomics studies. The results were consistent with our earlier findings showing routing of glycolysis into the pentose phosphate pathway to provide the reducing equivalents and nucleotide building blocks to suppress radiation-induced ROS and repair the DNA damage induced by radiation. Follow-up studies to better understand the coordination of signaling and metabolism in this matched model system of radiation response led to the discovery of a mechanistic triad

connecting cellular redox state, cholesterol metabolism, and DNA damage. A significant decrease in the survival of radiation resistant rSCC-61 cells of up to 90% was achieved either by targeting the NAD(P)H reserve or by increasing intracellular cholesterol. The implications of these findings are profound, as it would suggest opportunities for manipulating the tumor redox state and cholesterol metabolism to synergistically increase response to radiation therapies in radiation-resistant tumors.

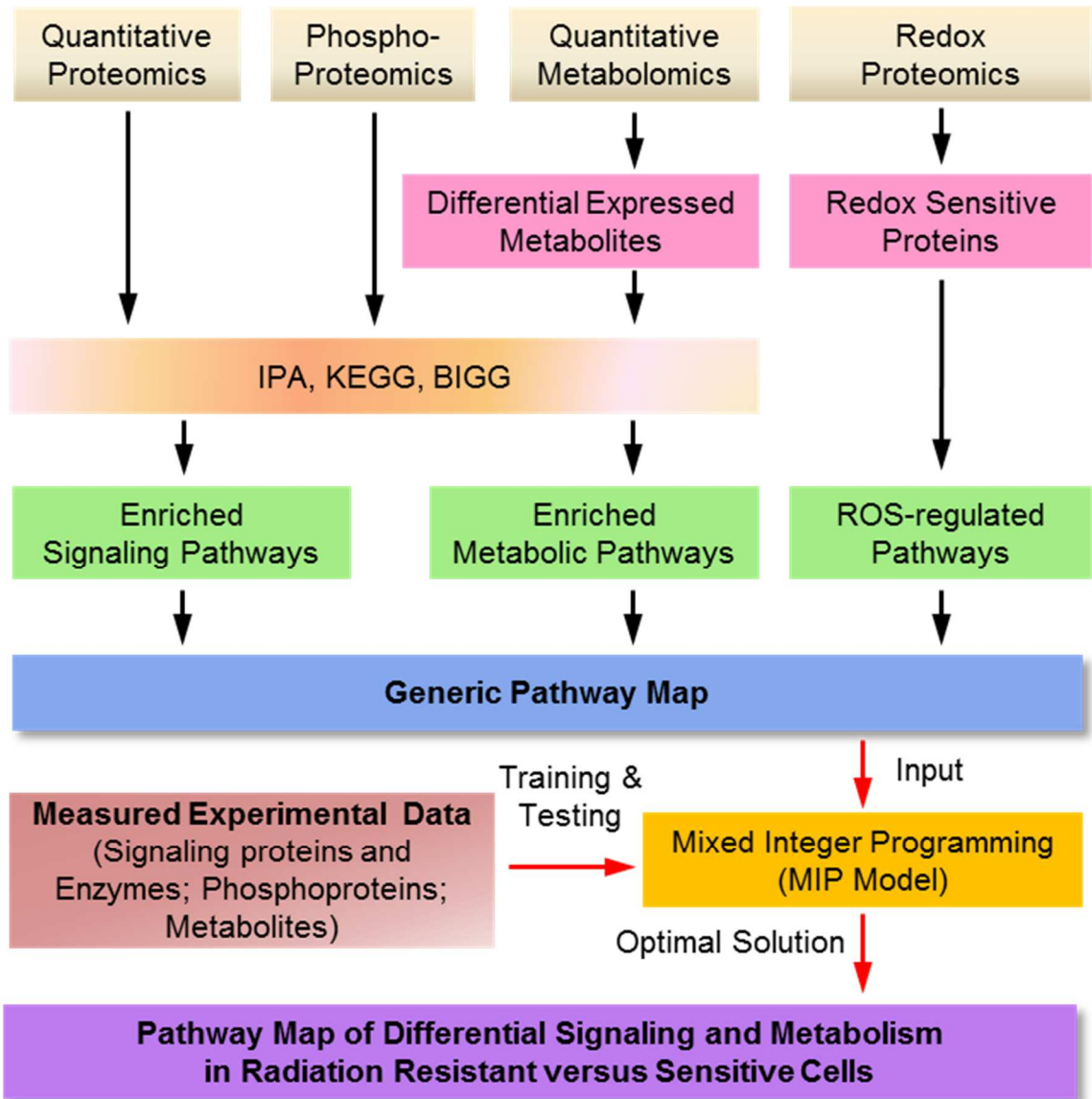


Figure 1. Mathematical approach to integrate ROS-mediated effects on signaling and metabolism contributing to radiation resistance in HNSCC.

Results

Experimental data employed for development and validation of the network model

In our study, we considered four types of data obtained from a diverse set of assays to infer redox-regulated cell-specific network. The proteomics data includes the total expression of 965 proteins, which are applied to screen enriched signaling pathways and metabolic enzymes (Bansal, 2014). The metabolomics, redox proteomics and protein phosphorylation data employed here are described next.

Metabolomics analysis. The metabolic profiles of SCC-61 and rSCC-61 cells were compared to identify the metabolites that are significantly up- or down-regulated in rSCC-61. Data analysis using the ChemTOF software identified 195 peaks after applying the metabolite extraction, chemical derivatization and alignment procedures described in **Materials and Methods**. Principal component analysis (PCA) was first performed on all samples to check the outliers. The results (**Appendix S4 1A**) showed no obvious outlier was found for this dataset (2 components with $R^2X=0.713$, $Q^2=0.518$). This was followed by supervised partial least square discriminant analysis (PLS-DA), which was employed to analyze the difference between SCC-61 and rSCC-61 groups. Three components PLS-DA models were obtained with $R^2X=0.783$, $R^2Y=0.992$ and $Q^2=0.97$. The scores plot is shown in **Appendix S4 Fig 1B**. The statistically different metabolites were selected according to the variable importance in the projection (VIP) ($VIP > 1$) and p values from the student t test ($p < 0.05$). The 61 identified differential metabolites from SCC-61 and rSCC-61 groups are listed in **Appendix S4 Dataset S4**. Additional metabolites were added from our previously published data (Bansal, 2014).

ROS and identification of redox-regulated proteins in SCC-61 and rSCC-61 cells. Previous imaging analysis has shown decreased intracellular ROS in rSCC-61 compared with SCC-61 (Bansal et al, 2014). To quantify the consequence on protein oxidation, the analysis of redox-regulated proteins in SCC-61 and rSCC-61 was performed here using labeling of protein sulfenic

acids (Cys-SOH) with the biotin-tagged BP1 probe (Qian, 2011) (**Appendix S4 Fig. 2A**) following the workflow in **Appendix S4 Fig. 2B**. Briefly, the SCC-61 and rSCC-61 were grown in SILAC media (SILAC - stable isotope labeling by amino acids in cell culture; SCC-61 - light isotopes of Lys and Arg; rSCC-61 heavy isotopes of Lys and Arg), lysed in the presence of BP1, precipitated to remove unreacted BP1, followed by enrichment in BP1-labeled proteins and analysis by mass spectrometry (MS). The complete list of proteins quantified by this analysis is included in **Appendix S4 Dataset 1** and the plot of $\log_2(\text{Normalized Ratios})$ in **Appendix S4 Figure 2C**. The Ingenuity Pathway Analysis was used to analyze the protein dataset: **a)** to determine the distribution of proteins subcellular locations (**Appendix S4 Fig. 2D**, upper chart); and **b)** to identify biological networks and molecular functions that are enriched in redox-regulated proteins in rSCC-61 versus SCC-61 (**Appendix S4 Fig. 2D**, lower chart).

Protein Phosphorylation. The phosphorylation status of 12 proteins of interest was monitored by Western blot (**Appendix S4 Fig. 3B**). These proteins were selected based on their key function in HNSCC signaling and metabolism. The measured ratios of protein phosphorylation, the phosphorylation site monitored and the consequence on protein activity in rSCC-61 and SCC-61 cells are summarized in **Appendix Dataset 2**.

Construction of the generic redox-regulated pathway map of rSCC-61 cells

The information obtained from the four types of analysis (proteomics, redox proteomics, metabolomics, and protein phosphorylation) was used first to build a generic network composed of integrated signaling and metabolic sub-networks (**Appendix S4 Fig. 4**). For building the signaling pathways sub-network, we started by selecting enriched signaling pathways generated from Ingenuity Pathway Analysis of proteomics data. Other signaling pathways of interest to radiation resistance in HNSCC were added based on existing literature, such as the EGFR signaling pathway (De Carvalho, 2013; Psyrris, 2013), IGF1R pathway (Papaconstantinou, 2009), TNFR pathway (Toyozumi, 2004), JNK/p53 pathway (De Carvalho, 2013; Toyozumi, 2004), and

NF- κ B pathway (Farshadpour, 2012). The metabolic sub-network was built based on the Ingenuity Pathway Analysis of combined proteomics and metabolomics data and also contains the metabolism of superoxide (O_2^-) and hydrogen peroxide (H_2O_2) as key reactive oxygen species. The BIGG database was used to annotate each metabolic reaction as reversible or irreversible (Schellenberger, 2010). The last steps in building the generic network involved the identification of proteins connecting signaling and metabolic sub-networks and the annotation of the effects of oxidation and/or phosphorylation on the activity of the proteins based on our own data and literature information. The proteins connecting the signaling and metabolic sub-networks were: SOD2, G6PD, PGM1, PGM2, CTP, TK1, PKM2, HMGCR, SQS and SHMT2. Four of the proteins in the generic network were identified as being under redox-regulation in SCC-61 and rSCC-61 based on the redox proteomics data: STAT3, EGFR, HSP90, EEF2, GCLC, and PKM (Table 1). We also considered the redox-sensitive targets AKT2, NF- κ B, PKM2, and SHMT2 in our study, which were validated in literature (Feng, 2013; Wani, 2011). The eight redox-regulated signaling proteins and metabolic enzymes were connected to a node “ROS” in the network according to the information in Table 2.

Next we represented the signaling pathway map as a Boolean network (Mitsos, 2009; Ji, 2014). The Boolean network consists of a set of nodes and a set of directed edges. Nodes in the signaling pathway sub-network represent signaling proteins (including some metabolic enzymes) and they have associated logical values (1 or 0) illustrating the change in the respective protein activity in rSCC-61 cells relative to SCC-61 cells (1 and 0 denote “up-regulation” and “down-regulation”, respectively). In the model presented here, protein activity is determined by the combined changes in *phosphorylation*, *oxidation*, and *total expression* between the two cell lines. There are two types of edges in the signaling sub-network: activation reaction and inhibition reaction. The state of each reaction is encoded by Boolean operations on the protein nodes, which also have logical values (“occurred” (1) or “not occurred” (0)). In our analysis, activation reactions indicate that the change in activity of upstream and downstream proteins is positively related. For

example, we can assume that up-regulation of AMPK will be activated by its increased upstream protein CAMMK because there is an activation edge between them in the generic pathway network (**Appendix S4 Fig. 5A**). On the contrary, inhibitory edges represent the negatively related relationships. For example, we can assume down-regulation of AKT2 was induced by the increase in ROS (**Appendix S4 Fig. 5B**). All the edges linked to the same protein are considered as independent. These relationships are exemplified in **Appendix S4 Figure 5C**.

The metabolic sub-network was processed using flux balance analysis (Orth, 2010). Similar to the signaling sub-network, the metabolic sub-network topology consists of a set of nodes and a set of edges. The nodes denote the metabolites in biochemical reactions and their measurements as ratios of concentrations in rSCC-61 relative to SCC-61. The edges indicate the metabolic reactions that are controlled by corresponding metabolic enzymes. The edges with duplex arrows denote reversible metabolic reactions, while unidirectional arrows show the irreversible reactions. The states of enzymes are encoded by logical values (“activation” (1) or “inactivation” (0)). If an enzyme is activated, the corresponding reaction might occur and there is non-zero net flux (or energy) passing through this reaction; otherwise, the corresponding reaction is blocked. In addition, our developed constraints described in *Materials and Methods/Computational Procedures* ensure the consensus rule that the direction of net flux is opposite to the change in Gibb’s free energy of reaction (Hopper, 2007). The net flux and the Gibb’s free energy of reaction are represented as continuous variables.

The resulting topology of the generic integral network built using the combined methods described above is shown in **Appendix S4 Figure 4**. The upper portion of **Appendix S4 Figure 4** is the Boolean topology of signaling sub-network. There are 54 signaling proteins (23 measured) and 9 metabolic enzymes (5 measured) connected through 87 regulatory signaling events: blue lines represent signaling events and black dash lines delineate potential ROS-regulated events (see details in **Appendix S4 Dataset 3**). The metabolic sub-network is represented in the lower part of **Appendix S4 Figure 4**. This sub-network contains 74 metabolic reactions (37 metabolic

enzymes measured) and 107 metabolites (38 metabolites measured). The list of all metabolic sub-network components is included in **Appendix S4 Dataset 4**. Based on BIGG database, we determined the directions of each metabolic reaction: 16 reversible and 60 irreversible reactions. The thermodynamic parameters for each metabolic reaction were extracted from NIST Standard Reference Database (Goldberg, 2004), BIGG (Schellenberger, 2010), KEGG (Kotera, 2012), and literature. The thermodynamic parameters for each metabolic reaction are included in **Appendix S4 Dataset 5**. The states of all the nodes and edges were assigned based on the developed constraints described next.

Network analysis using Mixed Integer Programming (MIP)

We first defined the rules governing the activity of signaling and metabolic proteins by taking into account the measured changes in *phosphorylation*, *oxidation*, and *total expression* in rSCC-61 relative to SCC-61 cells. (1) For the redox-regulated proteins in the generic network, we considered the combined oxidation, phosphorylation, and/or total expression ratios to fix the protein activities, such as in the case of EGFR. (2) For all other proteins, we combined the phosphorylation ratio and/or total expression to determine whether the respective protein activity is upregulated or downregulated in rSCC-61 relative to SCC-61 cells. These rules are exemplified here using EGFR and JNK1 as case studies. It is known that EGFR can be activated by both oxidation and phosphorylation (Paulsen CE1, 2011). In our experimental data, the rSCC-61/SCC-61 pEGFR ratio was 0.4, which indicated a lower EGFR activity in rSCC-61. Considering that the concentration of ROS in rSCC-61 is much lower than that in SCC-61, it follows that the oxidation state of EGFR in rSCC-61 should also be lower than in SCC-61. The rSCC-61/SCC-61 BP1-labeled EGFR ratio of 0.64 determined by the redox proteomics studies confirmed this expected results. Therefore, lower oxidation in rSCC-61 also contributes to lower EGFR activity in these cells. Combining the effects of phosphorylation and oxidation, we inferred EGFR activity is down-regulated in rSCC-61 relative to SCC-61 cells. JNK1, on the other hand, was not identified

as redox regulated in the rSCC-61/SCC-61 system. The total JNK1 expression ratio in rSCC-61 versus SCC-61 is 0.79 and phosphorylation ratio is 0.2. Based on literature, phosphorylation at xxx residue activates JNK1 activity (LIN, 2005). Thus, we considered JNK1 activity is down-regulated in rSCC-61 cell line. For cases where oxidation and phosphorylation induced opposite effects, we used the following priority: oxidation > phosphorylation > total expression (oxidation overriding the effects of phosphorylation) to determine whether a protein is activated or inhibited. For some proteins, the activities were not assigned so our computational model could predict these. The detailed information and analysis for all measured proteins are described in **Appendix S4 Dataset 2**.

To infer the rSCC-61 pathway network based on the generic pathway map constructed above, we minimized the differences between the measurements and the simulated values, as well as the complexity of network's topology structure. To simplify this optimization problem, we developed a Mixed Integer Programming (MIP) approach to optimize such multi-objective functions (Lee, 2000; Nollenburg & Wolff, 2010). The concept behind MIP was that the states of the signaling proteins were normalized to binary variables, which indicated up-regulation or down-regulation of protein's activities in rSCC-61 relative to SCC-61 cells; the states of edges in signaling sub-network were also represented as binary numbers ("occurred" or "not occurred"). The metabolic enzymes were also normalized to binary variables ("down-regulation" or "up-regulation"), which denotes the corresponding metabolic reactions are blocked or un-blocked. The changes of concentrations of metabolites, Gibb's free energy, and the net flux through reactions were represented as continuous variables. Our developed mathematical constraints in the MIP model were applied to describe: (1) the states of all the species (nodes) in this integral network; (2) the relationships between upstream and downstream proteins in the network topology; (3) the flux balance analysis for ensuring the total amount of any compound being produced must be equal to the total amount being consumed at steady state; (4) the direction of net flux of each metabolic reaction is opposite to the change of Gibb's free energy; (5) the concentration of products in a

single metabolic reaction is restricted by enzyme's state. The detailed information can be found in *Materials and Methods*.

The MIP formulation was solved with the MATLAB optimization toolbox Gurobi 5.1 (Werbos, 2012) which guarantees minimal differences between measurements and predicted data, as well as the complexity of inferred network topology. To optimize the multi-objective function in formula (1), the rSCC-61 specific network was inferred with MIP to best fit the measurements.

Figure 2 shows the inferred rSCC-61 network. IGF1R/PI3K/AKT2 and INSR (insulin receptor)/PI3K/AKT2 pathway were activated in rSCC-61 cells; however, other receptors are all down-regulated. In the signaling sub-network, the fitting precision of the optimized topology on 28 measured proteins is 96.43% (only the 14-3-3 prediction is inconsistent). There are 15 signaling reactions (grey lines) removed from the generic pathways after optimization (such as Myc→p53) because the inferred states of these reaction indicated that they did not occur. In the metabolic sub-network, 11 metabolic reactions are marked “×”, which indicates there is decreased net flux passing through these biochemical reactions. The direction of unblocked reversible reactions was inferred with our model and marked with purple arrows. The predicting error of metabolic concentration of 33 differential metabolites was zero. According to the cell images, the concentration of intracellular ROS in rSCC-61 cell line is obviously lower than that in SCC-61, so that the state of node “ROS” was inferred as zero (down-regulated) (Bansal, 2014).

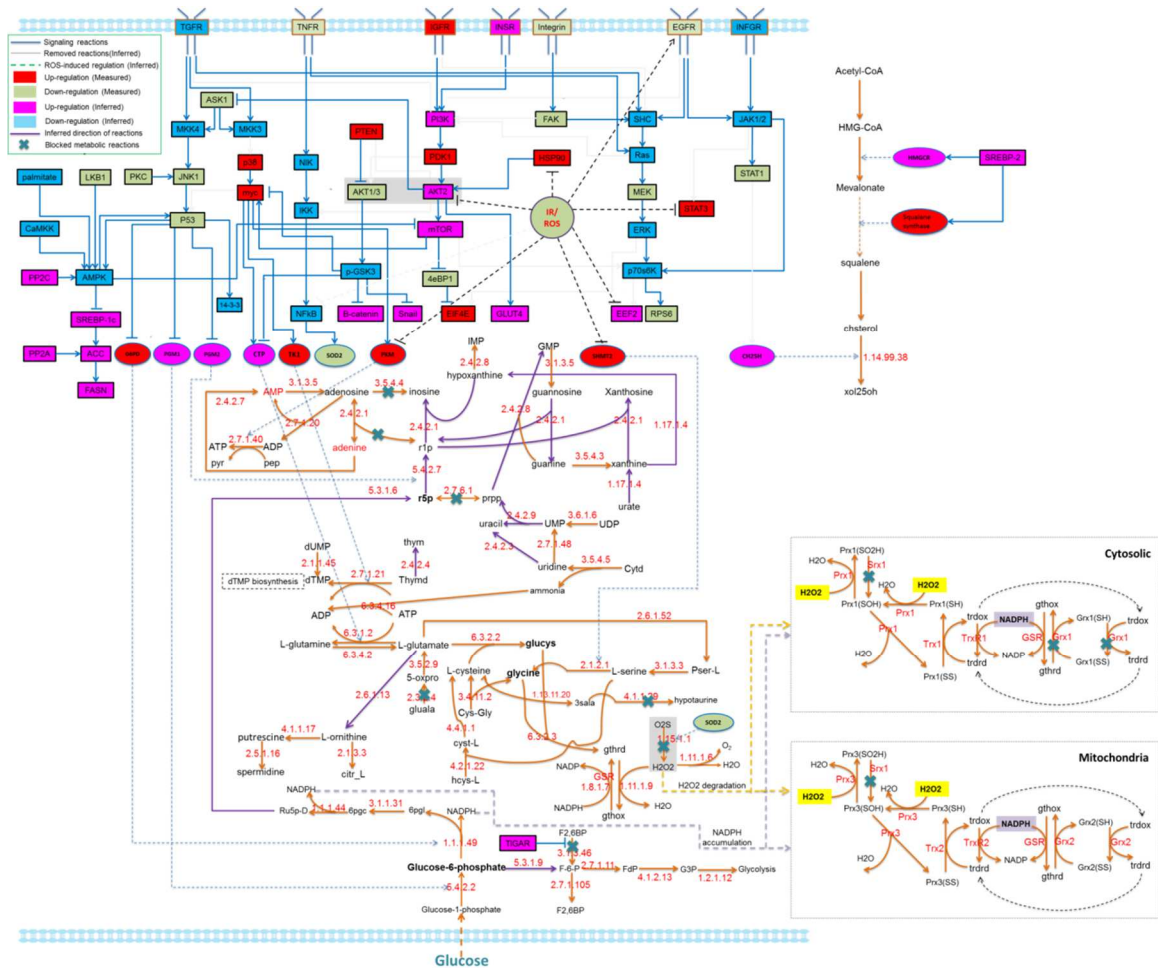


Figure 2. Inferred Network. Measured and inferred regulation of signaling proteins and inferred direction and inferred block of metabolic reactions. --- = inferred ROS-induced regulation. Red box = measured upregulated protein. Green box = measured downregulated protein. Pink = inferred downregulated protein. Blue = inferred downregulated protein. Purple line = inferred direction of reaction. X = blocked metabolic reaction.

Validation of inferred pathways generated by MIP network analysis

The network highlighted potentially interlinked pathways contributing to radiation resistance in HNSCC including (1) increased Akt2 and decreased Akt1/3 activities driving glucose uptake and activation of GSK3 α/β signaling, (2), glycolytic flux diverted into pentose phosphate pathway (PPP) leading to an increase in precursors for nucleic acid biosynthesis and increased NADPH production and (3) suppression of H₂O₂ in rSCC-61 through the enzymatic activities of cytosolic and mitochondrial peroxiredoxins, the NADPH-dependent Trx/TrxR and the GR (GSH/GSSG) system. The predicted outcomes were further investigated as described next.

Differential regulation of AKT2 and AKT1/3 drive increased glucose uptake and GSK3 β activities in rSCC-61. The phosphorylation of all Akt isoforms was downregulated in rSCC-61. However, given the increased H₂O₂ in SCC-61 and the isoform-selective inhibition of Akt2 activity by H₂O₂ (Wani et al, 2011), the Akt2 activity was predicted to be upregulated in rSCC-61 (**Fig. 3A**). Akt2 is a known regulator of glucose uptake by promoting GLUT1 localization at the cell surface (Ng et al, 2008). Our published data showed both increased membrane localization of GLUT1 in rSCC-61 and increased glucose uptake consistent with the predictions of the model (Mims, 2015). Since GSK3 β can be phosphorylated by all Akt isoforms, the prediction was that overall GSK3 β phosphorylation would be decreased in rSCC-61 driven primarily by the decreased activity of AKT1 and AKT3. Western blot analysis confirmed ~50% decreased GSK3 β phosphorylation in rSCC-61 compared with SCC-61 (**Fig. 3B**). In addition, GSK3 α/β mediated phosphorylation functions as a switch in regulation of β -catenin stability and activation (Wu, 2010). The network modeling predicted up-regulation of β -catenin due to decreased GSK3 β phosphorylation. This was confirmed by semi-quantitative PCR and analysis of mRNA expression data from microarray analysis showing increased expression of β -catenin in rSCC-61 cells (**Fig. 3C**). This is consistent with the epithelial phenotype of rSCC-61 and the mesenchymal phenotype of SCC-61 reported earlier.

Contribution of PPP to the NADPH reserve. Our previously published studies on energy metabolism have demonstrated the routing of glycolysis into the PPP resulting in lower flux through the mitochondrial ETC overall contributing to increased NADPH and low mitochondrial ROS generation in rSCC-61, respectively (Mims, 2015). These results were consistent with the predictions from the network modeling (**Fig. 4**). Here we sought to build on these findings and quantify the relative contribution of PPP to NADPH reserve in SCC-61 and rSCC-61 cells using flux balance analysis (FBA). First, we generated genome-scale metabolic models predictive of flux contributions to NADPH production and consumption from the framework of the Human Metabolic Reaction (HMR) 2.0 model (Mardinoglu, 2014), which contains 5546 metabolites, 8181 reactions, and 3765 reaction-associated genes, encompassing all possible human metabolic reactions that could occur in any cell type. Boolean gene rules were used to determine the on/off status of the reactions in a context-specific manner. The three models were generated by further trimming HMR 2.0 by the following methods: the HNC model was generated by the Human Protein Atlas (HPA) data directly; SCC-61/rSCC-61 specific models were generated by Illumina transcriptomics by using a 1 standard deviation cutoff to determine the gene expression status compared to a catalog of 196 HPV-negative HNSCC samples (Wichmann, 2015) and the resulting cell line models contained 6,789 (SCC-61) and 6,596 (rSCC-61) reactions. DMEM/F-12 media conditions used by the SCC-61/rSCC-61 cells were modeled by setting the upper bound for each metabolite exchange reaction from the environment in proportion to its concentration in the actual media. Optimization was performed independently for maximal cytosolic NAD(P)H and maximal mitochondrial NAD(P)H production. Collectively from this analysis, we have identified a subset of 7 genes (G6PD, PGD, MTHFD2, IDH1, IDH2, DHFR, and DFHRL1) that are responsible for 84-90% of the cellular NAD(P)H production in both the rSCC-61 and SCC-61 cells and thus will have the most significant impact on the suppression of ROS and response to radiation. Out of this, the PPP enzymes G6PD and PGD contributed 44% and 46% to the NADPH reserve in SCC-61 and rSCC-61 cells, respectively (**Fig. 4A**).

1-C metabolism and NAD(P)H reserve. The FBA also revealed the 1-C metabolism enzymes MTHFD2 (mitochondrial) as the second most important contributors to NAD(P)H reserve with MTHFD2 contributing 34% and 24% in rSCC-61 and SCC-61, respectively (**Fig. 4A**). The increased MTHFD2 protein in rSCC-61 was confirmed by Western blot analysis (**Fig. 4B**). Clonogenic survival assays comparing the response to radiation in SCC-61, rSCC-61 and rSCC-61 with depleted MTHFD2 further confirmed the function of this enzyme in the radiation resistance phenotype of rSCC-61 (**Fig. 4C**). Together with our previously reported proteomics studies showing increased cytosolic MTHFD1 and mitochondrial serine hydroxymethyltransferase 2 (SHMT2) in rSCC-61 by 6.3- and 4.0-fold, these studies brought into focus the critical contribution of 1-C metabolism to the NAD(P)H reserve and response to radiation treatment. In mitochondria, SHMT2 catalyzes the reversible reaction of serine and tetrahydrofolate to glycine and 5, 10-methylene tetrahydrofolate, which is then converted to 10-formyl-tetrahydrofolate by the NAD(P)⁺ dependent MTHFD2 generating NAD(P)H (**Fig. 4D**). In cytosol, the NADP⁺ dependent MTHFD1 catalyzes the conversion of formate transported from the mitochondria and cytosolic tetrahydrofolate into 10-formyl-THF routed for purine biosynthesis or further metabolized to 5, 10-methylene tetrahydrofolate in an NADPH consuming reaction. 5, 10-methylene tetrahydrofolate is utilized for cytosolic methionine synthesis (after conversion to 5-methyl THF in another NADPH consuming reaction) and nuclear/mitochondrial dTMP synthesis (thymidylate synthase). DHFR/DHFRL1 catalyzes the recycling of DHF byproduct of dTMP synthesis to THF in an NADPH-consuming reaction. Inhibition of DHFR by methotrexate resulted in decreased survival of rSCC-61 compared with SCC-61 (**Fig. 4E**). While on one hand, DHFR inhibition is expected to result in accumulation of cytosolic NADPH, it would also deplete the THF pool and the flux through mitochondrial SHMT2 and MTHFD2. This infers coordinated maintenance of cellular NAD(P)H reserve between cytosolic and mitochondrial compartments. To further test this hypothesis we performed clonogenic survival assays in rSCC-61 with combined MTHFD2 knockdown, methotrexate and CB83, an irreversible

inhibitor of the PPP rate-limiting enzyme glucose-6-phosphate dehydrogenase (G6PD) (Bielitza, 2015). While each treatment condition decreased cell survival, the combined targeting of MTHFD2, DHFR and G6PD produced the strongest effect (<10% cell survival) (**Fig. 4F**).

Cysteine and glutathione biosynthesis. The 1-C metabolism and PPP pathways contributing to the NAD(P)H/NAD(P)⁺ ratio are intrinsically connected to both the levels and the balance of reduced and oxidized glutathione in cells (**Fig. 5A**). GSH biosynthesis starts with the ATP dependent rate-limiting catalysis of L-glutamate and L-cysteine to γ -glutamylcysteine by glutamate-cysteine ligase (GCL) followed by the condensation of γ -glutamylcysteine and glycine to form glutathione by glutathione synthase (GSS). Cysteine availability is derived from the diet, protein breakdown and in the liver from methionine via transsulfuration. Other determinants include import of disulfide form of cysteine or cystine via the X_c⁻ cystine / glutamate antiporter system and methionine pools via the L-methionine transport system. During transsulfuration, homocysteine condenses with serine in a reaction catalyzed by cystathionine β -synthase (CBS) to produce cystathionine which is then cleaved by cystathionine γ -lyase (CSE) to release free cysteine for GSH synthesis. Transsulfuration pathway is closely linked to the methionine metabolic pathway. Homocysteine also participates in *de novo* methionine biosynthesis as it can combine with the 1-C metabolism intermediate 5-methyl tetrahydrofolate to produce methionine, a critical intermediate in SAM biosynthesis. Thus, in the absence of extracellular cysteine or methionine, the GSH biosynthesis is determined by the partitioning of homocysteine into the biosynthesis of methionine/SAM and cysteine/GSH driven by 1-C metabolism. NADPH contributed by 1-C and PPP pathways is critical for the activity of glutathione reductase, the enzyme converting oxidized GSSG to reduced GSH and responsible for maintaining the GSH/GSSG redox balance in cells. We have previously measured GSH/GSSG ratios in the SCC-61 and rSCC-61 cells and found increased GSH/GSSG ratio in rSCC-61 consistent with increased NADPH/NADP⁺ ratio and decreased ROS in these cells. Interestingly, two critical enzymes in GSH biosynthesis, CBS and

CSE, were inversely regulated in SCC-61 and rSCC-61 cells. CBS was downregulated in SCC-61 while CSE was downregulated in rSCC-61 cells (**Fig. 5D**), suggesting impaired GSH biosynthesis in both cell lines. Downregulation of CSE in rSCC-61 cells was consistent with the cystathionine accumulation (**Fig. 5C**) and increased H₂S production in these cells (**Fig. 5D**). We have then measured the oxidized and reduced glutathione to confirm the earlier results but using a different method of analysis based on thiol blocking, chemical labeling of primary amines, and HPLC separation as described in the *Materials and Methods* section. The results showed increased levels of both GSH and GSSG in rSCC-61 but slightly decreased GSH/GSSG ratio in rSCC-61 cells compared to SCC-61 cells (**Fig. 5B**). The overall GSH content and the GSH/GSSG ratios in both SCC-61 and rSCC-61 cells were comparable with the values found in most cell lines (~50 nmoles/mg protein (Gamcsik 2012)). These findings have led to the alternative hypothesis that both SCC-61 and rSCC-61 bypass the requirement for de novo cysteine biosynthesis by importing cystine from the extracellular media. To test this hypothesis, we performed clonogenic assay to determine cell survival after inhibition of cystine transporter Slc7A11 or xCT with sulfasalazine (SAS) or growing cells in Cys or Cys/Met depleted media (**Fig. 5E**). Indeed, inhibition of cystine transporter Slc7A11/xCT with SAS or growing of cells in Cys or Cys/Met depleted media led to a significant 1.5-fold decrease in cell survival of both SCC-61 and rSCC-61 cell lines. Depletion of Cys or Cys/Met depletion led to a 50% reduction in overall survival in SCC-61 and rSCC-61 cells with the effect driven primarily by depletion of cysteine/cystine.

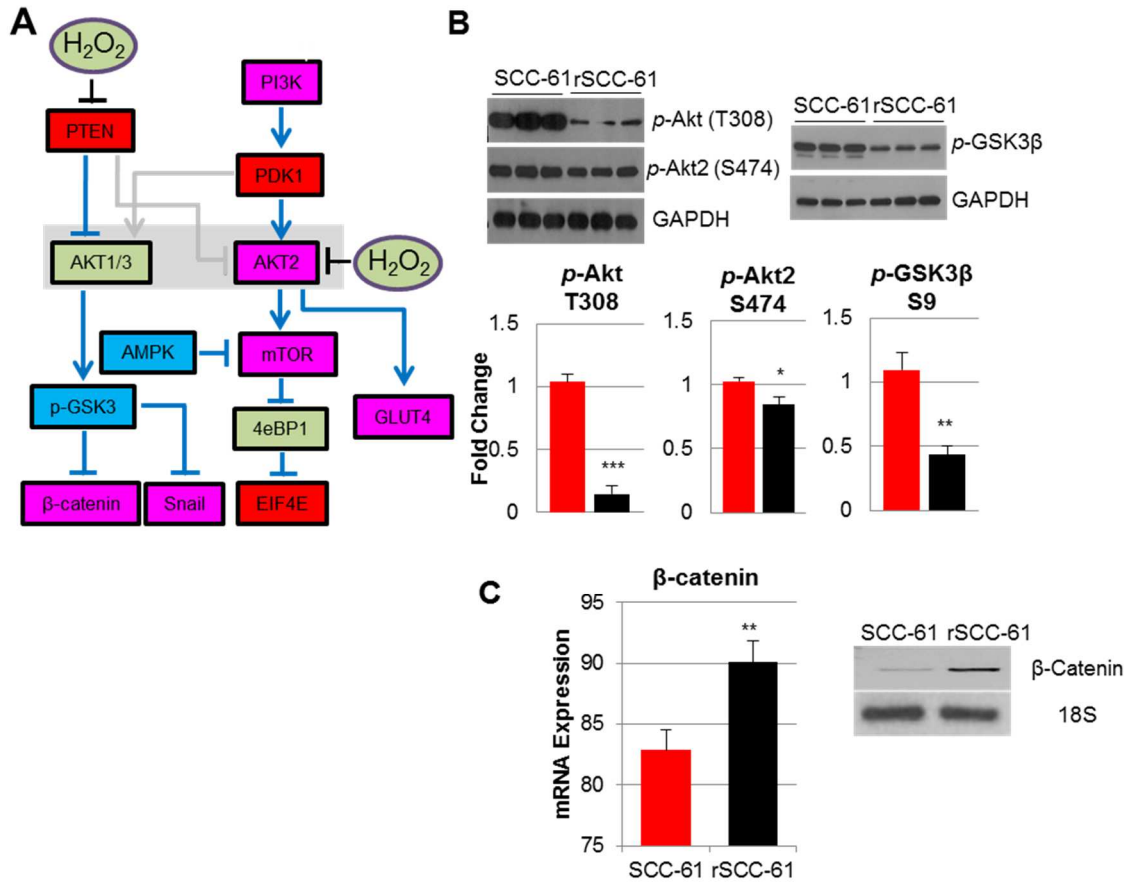


Figure 3. Inferred Pathway Predicts Differential Regulation of AKT2 and AKT1/3 in Radiation Resistant Cells. **A.** Inferred network predicting upregulated Akt2 and β -catenin and downregulated p-GSK3 β in rSCC-61 cells. **B.** SCC-61 and rSCC-61 lysates immunoblotted with antibodies against pAkt (T308), pAkt2 (S474), pGSK3 β , and GAPDH used as a loading control validating network prediction. **C.** mRNA expression and RT-PCR analysis showing β -catenin significantly increased expression in rSCC-61 compared to SCC-61. *0.05, **0.01-0.001, ***<0.001

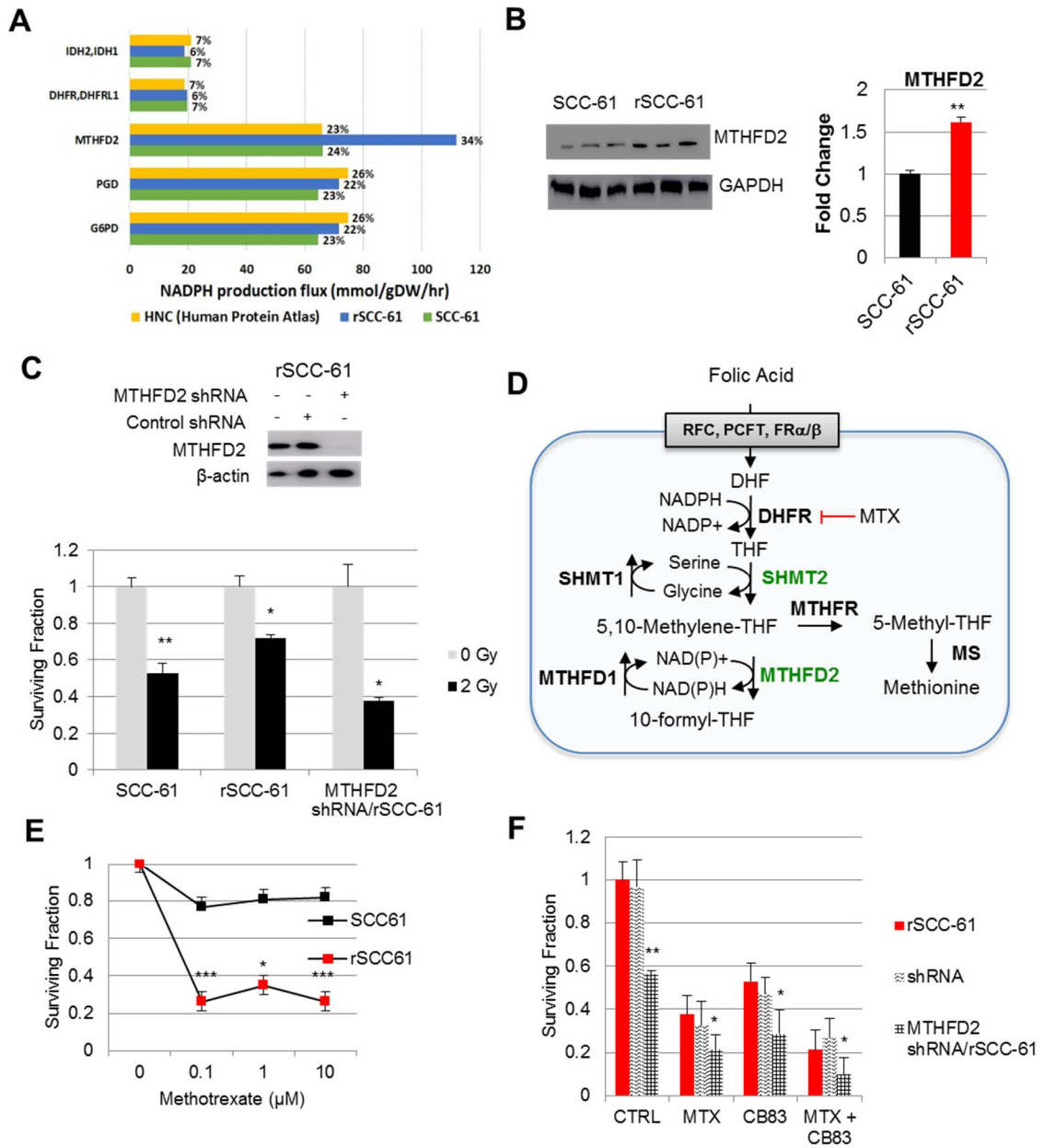


Figure 4. Network Predicts Flux through Pentose Phosphate Pathway to Increase NADPH in Radiation Resistant Cells. **A.** Flux balance analysis of rSCC-61 and SCC-61 cells and HPV-negative HNSCC samples identifying 7 genes: MTHFD2, PGD, G6PD, DHFR/DHFRL1 and IDH2/3 as contributing 84-90% of cellular NAD(P)H production. **B.** Immunoblotting against MTHFD2 confirming increased MTHFD2 expression in rSCC-61 cells compared to SCC-61 cells. **C. (upper)** Immunoblot with antibody against MTHFD2 in rSCC-61, rSCC-61 control shRNA and MTHFD2 shRNA lysates confirming selective knockdown of MTHFD2 in MTHFD2 shRNA/rSCC-61 cells; **(lower)** Clonogenic assay after 2 Gy irradiation in SCC-61, rSCC-61 and MTHFD2 shRNA/ rSCC-61 cells showing MTHFD2 knock-out sensitizes radiation resistant cells to irradiation. **D.** Schematic of 1-carbon metabolism contribution to NAD(P)H reserve. **E.** Clonogenic assay showing treatment with 0 – 10 μ M methotrexate decreases rSCC-61 cell survival more significantly than SCC-61 cells. **F.** Clonogenic assay in rSCC-61, rSCC-61 control shRNA and MTHFD2 shRNA/rSCC-61 demonstrating cell survival decreased by treatment with 0.1 μ M MTX and 10 μ M CB83 and MTX and CB83 combined. *0.05, **0.01-0.001, ***<0.001

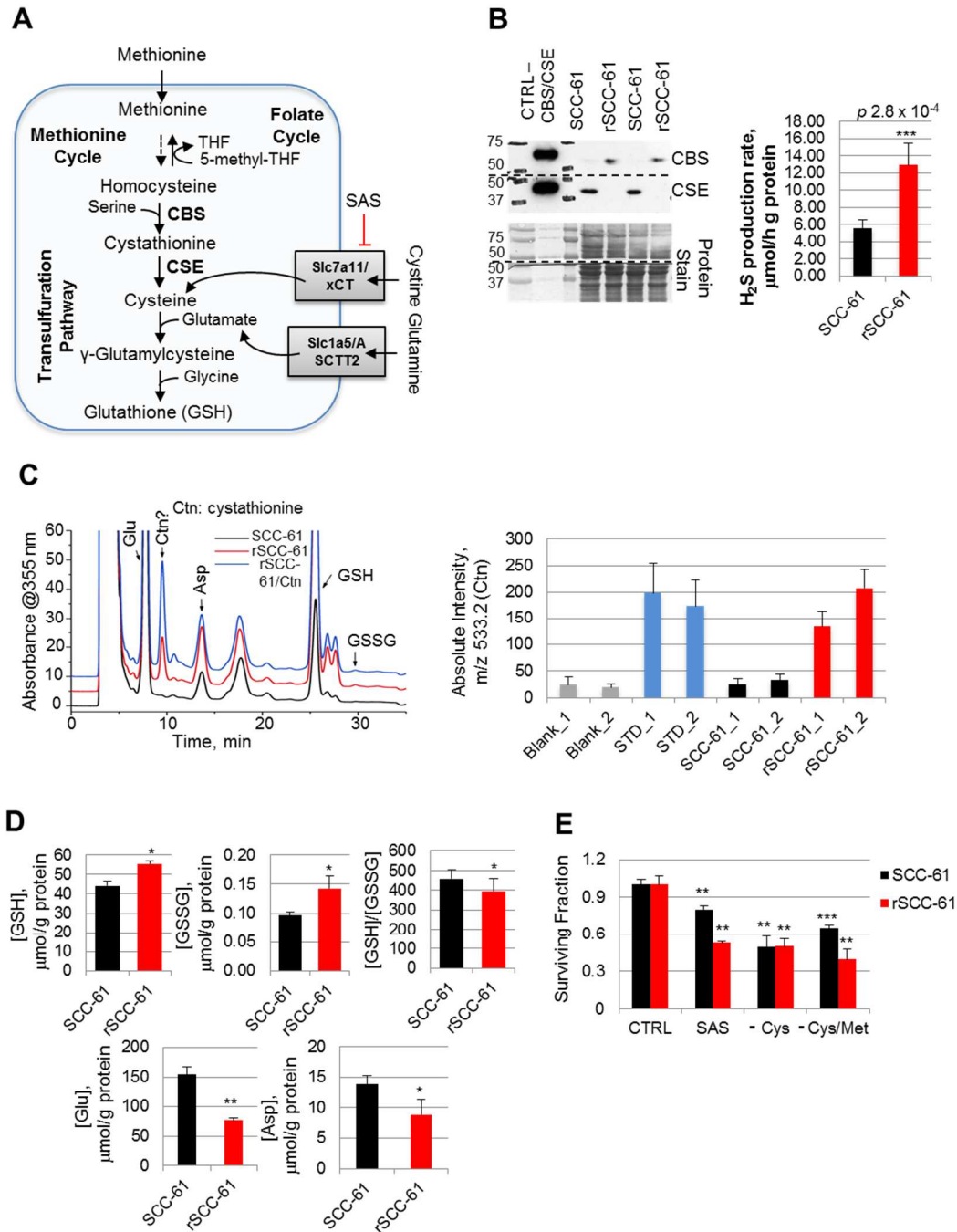


Figure 5. Cysteine and Glutathione Biosynthesis Critical for Cell Survival in Radiation Resistant Cells. A. Schematic of glutathione biosynthesis and cysteine/glutamate transport in cells. **B. (left)** Immunoblot with antibody against CSE and CBS showing increased CSE in SCC-61 cells and increased CBS in rSCC-61 and protein stain as loading control; **(right)** Measurement of H₂S production rate showing increased H₂S production in rSCC-61 cells. **C.** MS measurement of cystathionine accumulation in rSCC-61 cells compared to SCC-61 cells. **D.** Analysis of GSH and GSSG showing significantly increased GSH and GSSG but decreased GSH/GSSG, glutamate and aspartate in rSCC-61 cells compared to SCC-61 cells. **E. (upper)** Immunoblot against xCT/Slc7A11 transporter showing no differences in xCT protein expression; **(lower)** Clonogenic assay showing SCC-61 and rSCC-61 cells treated with 0.5 mM SAS or media depleted of cysteine/methionine resulting in significantly decreased cell survival in rSCC-61 cells after SAS inhibition compared to SCC-61 cells. *0.05, **0.01-0.001, ***<0.001 with 0.1 μM MTX and 10 μM CB83 and MTX and CB83 combined. *0.05, **0.01-0.001, ***<0.001

AMPK connects fatty acids and cholesterol metabolism. Overcoming metabolic stress requires coordination between metabolism and signaling pathways to maintain supply of metabolites for generation of biomass and energy. AMPK is a signaling enzyme with critical function in regulating lipid, cholesterol and glucose metabolism (Hardie & Alessi, 2013). AMPK was predicted to be downregulated in the rSCC-61 cells based on network modeling (**Fig. 6A**). The AMPK-deficient cells would be expected to exhibit enhanced rates of lipid and cholesterol synthesis through mechanisms involving metabolic enzymes ACC and HMGR (Shackelford & Shaw, 2009), the expression of which is controlled by SREBP-1c and SREBP-2, respectively. Validation studies confirmed decreased phosphorylation of AMPK in rSCC-61 (**Fig. 6B**) resulting in decreased suppression of SREBP-1c/2 and activation of gene expression for critical enzymes involved in fatty acids and cholesterol biosynthesis. We have previously reported data showing increased fatty acid synthase (FASN) and reliance on endogenous fatty acids for energy production in rSCC-61 cells (Mims, 2015). Here we focused on the regulation of cholesterol metabolism as analysis of cholesterol levels by LC-MS/MS to validate the modeling prediction showed significantly decreased cholesterol and oxysterols in rSCC-61 cells compared to SCC-61 cells. These results were inconsistent with the predicted upregulation of this pathway by AMPK and measured 1.8-fold increase in squalene synthase and 15.14-fold increase in squalene levels in rSCC-61 cells compared to SCC-61 cells (**7A**). However, when we measured cholesterol and oxysterols by LC-MS/MS we found decreased cholesterol and oxysterols in rSCC-61 cells compared to SCC-61 cells (**Fig. 7B**). We hypothesized two potential causes for decreased cholesterol levels in rSCC-61 cells: 1) decreased influx and/or increased efflux of cholesterol, and 2) defective metabolic enzyme(s) connecting squalene and cholesterol controlled by gene expression and/or post-translational regulation (**Fig. 7C**). When we measured efflux and influx using [3H]-cholesterol, we found SCC-61 cells had a maximal efflux of 7.5% after treatment with 30 mM cAMP and 20 μ g human APOA1 compared to no change in rSCC-61 cells. SCC-61 cells were also able to import cholesterol into the cell 1.5-fold faster than rSCC-61 cells (**Fig.**

7D). We further confirmed by western blot that ABCA1 expression is equal between SCC-61 cells and rSCC-61 cells (**Appendix S4 Fig. 6B**). This data suggest there is no impairment in cholesterol import or export in the two cell lines but cholesterol dysregulation may be caused by transcriptional or post-translational regulation. HumanHT-12 v3 expression BeadChip mRNA expression data showed downregulation of SREBP2 and LXR target genes (i.e. LDLR, HMGCR, LXR, APOE, ABCA1, ABCG1) in rSCC-61 cells compared to SCC-61 cells (**Appendix S4 Fig. 6A**). Despite decreased cholesterol biosynthesis activity and cholesterol levels in rSCC-61 cells, there is increased mRNA expression of INSIG1, INSIG2 and AMFR as well as oxysterol, 24-OH, which lead to inhibition of SREBP2 translocation (**Appendix S4 Fig. 6C**). We have previously reported the interdependence of H₂O₂ and lipid rafts in SCC-61 cells. Treatment of these cells with polyethylene-glycol (PEG) catalase led to reduction of lipid rafts and decreased response to radiation. Here we extended these studies and in addition to decreasing H₂O₂ in SCC-61, we have also inhibited cholesterol biosynthesis with Lovastatin and monitored changes in intracellular H₂O₂ and nuclear DNA damage (**Fig. 7E**). In rSCC-61 cells, we performed the complementary treatments by treating with tBuOOH to increase intracellular H₂O₂ and with cholesterol to promote lipid rafts formation. Lipid rafts, H₂O₂ accumulation, and DNA damage were measured across conditions (**Fig. 7D**). We found increased lipid rafts led to more H₂O₂ in cytosol and mitochondria and resulted in increased DNA double strand breaks as indicated by imaging with γ H2AX. This change in redox status mitigated by lipid raft formation led to the sensitization of rSCC-61 to 2 Gy radiation (**Fig. 7F**).

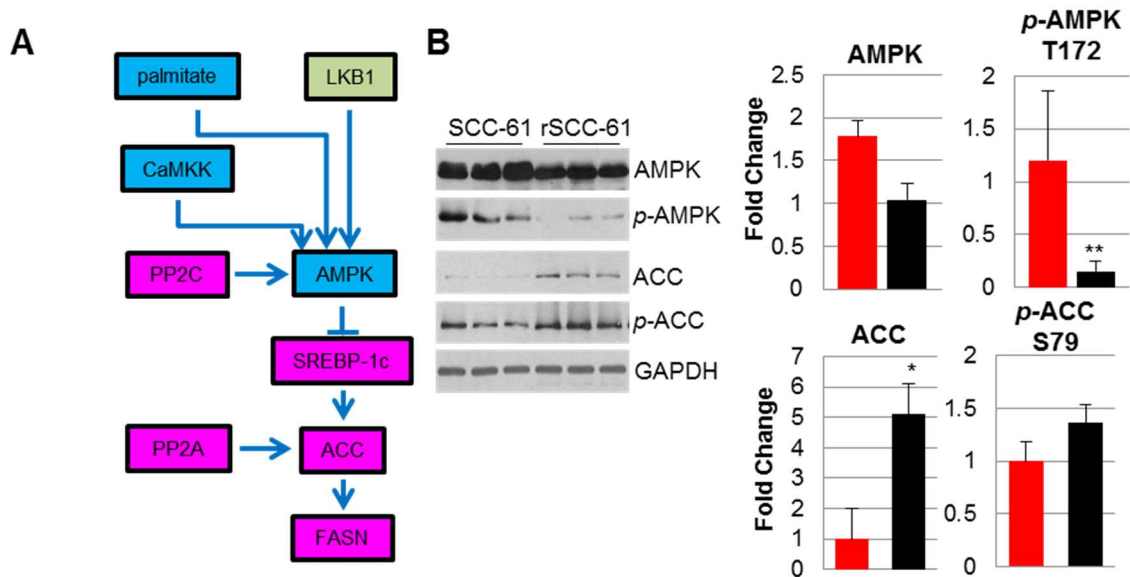


Figure 6. Inferred Pathway Connects AMPK Activity to Fatty Acids and Cholesterol Metabolism. **A.** Inferred network predicting downregulated AMPK and upregulated ACC in rSCC-61 cells. **B.** SCC-61 and rSCC-61 lysates immunoblotted with antibodies against AMPK, pAMPK (T172), ACC and pACC (S79) and GAPDH used as a loading control validating network prediction. *0.05, **0.001 with 0.1 μ M MTX and 10 μ M CB83 and MTX and CB83 combined. *0.05, **0.01-0.001, ***<0.001

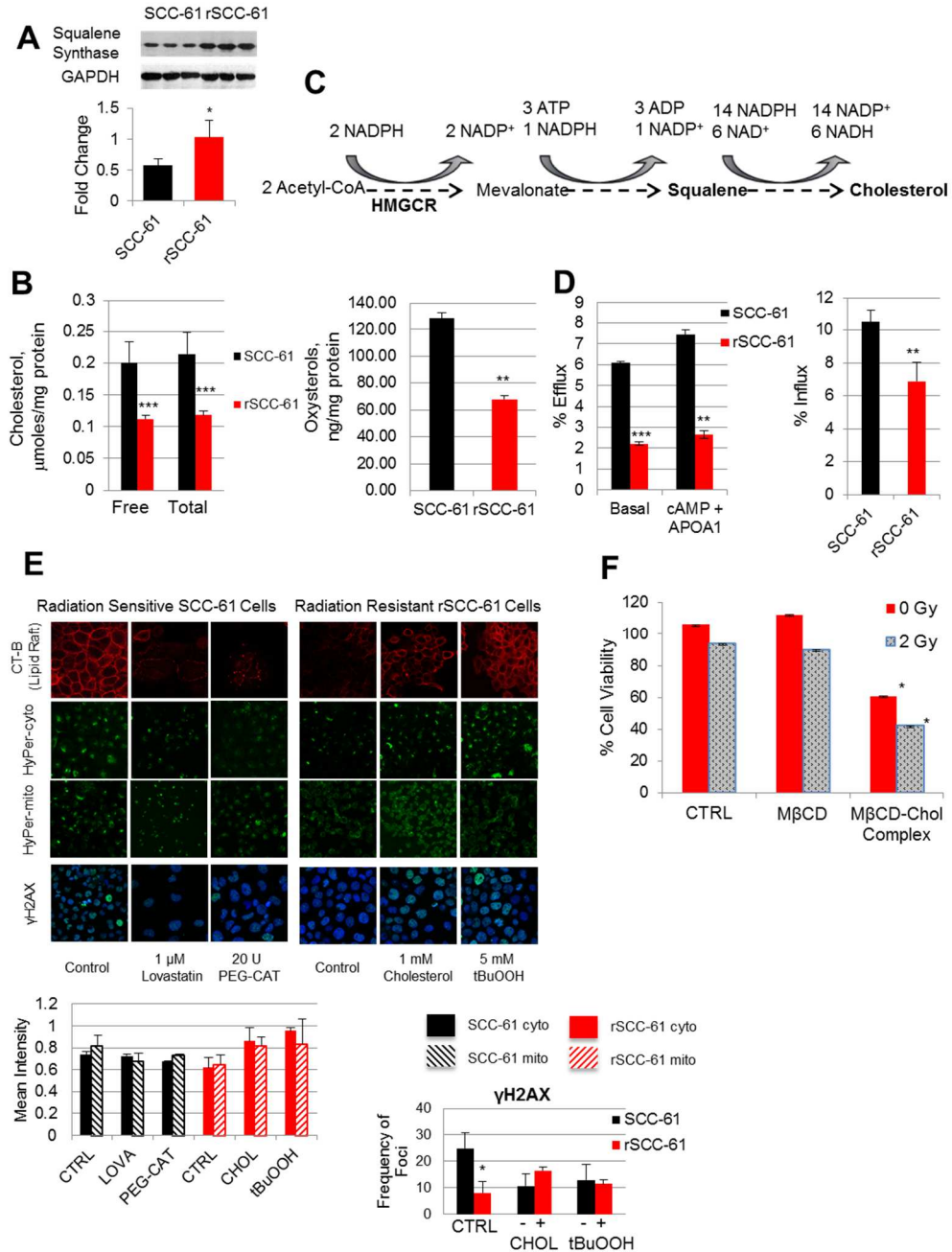


Figure 7. Cholesterol regulation in lipid raft formation and response to radiation. **A.** Western blot of squalene synthase in SCC-61 cells and rSCC-61 cells. **B.** LC-MS/MS analysis of cholesterol and oxysterols showing significantly decreased cholesterol and oxysterol in rSCC-61 cells. **C.** Abbreviated schematic of cholesterol biosynthesis. **D.** Cholesterol efflux and influx showing (**left**) maximal efflux of 7.5% in SCC-61 cells after treatment with 30 mM cAMP and 20 µg human APOA1 compared to no change in rSCC-61 cells and (**right**) SCC-61 cells influx cholesterol 1.5-fold faster than rSCC-61 cells. **E.** Fluorescence imaging of lipid rafts with CT-B, cytosolic and mitochondrial H₂O₂ production with HyPer and DNA damage with γH2AX (**left**) in SCC-61 cells after treatment with 1 µM Lovastatin and 20 U PEG-CAT showing reduction in lipid rafts, H₂O₂, and γH2AX foci formation compared to (**right**) rSCC-61 cells after treatment with 1 mM cholesterol and 5 mM tBuOOH showing increased lipid rafts, H₂O₂, and γH2AX foci formation. **F.** MTT Assay of cell viability of rSCC-61 cells after treatment 1 mM cholesterol and 2 Gy irradiation demonstrating increased sensitivity to radiation. *0.05, **0.01-0.001, ***<0.001

Discussion

In this paper, we present first a constraint-based systemic modeling of integrated signaling and metabolic networks using multi-omics data. We combined enriched signaling and metabolic pathways to obtain a generic pathway map. This generic pathway map included 54 signaling proteins, 87 regulatory signaling reactions, 107 metabolites, and 74 metabolic reactions. We then applied a mixed integer programming (MIP) approach for joint optimization of signaling and metabolism to infer signaling and metabolic networks that define the rSCC-61 phenotype. The MIP approach generated 457 constraints (160 quadratic constraints and 297 linear constraints) and 397 variables in the optimization process of the pathways map. The analysis took into consideration the relationships among signaling protein activity by combining changes in oxidation, phosphorylation and total expression between the two cell lines. The nodes are represented as activating or inhibitory reactions thereby allowing the prediction of signaling reactions as up- or downregulated. The metabolic subnetwork took into consideration the relationships among metabolic flux distribution, and metabolite thermodynamic and stoichiometric characteristics. This analysis combines enzyme concentration with metabolite flux allowing the prediction of flux direction as blocked and the ability to predict unknown enzyme concentrations. After optimization with MIP (Eq. 1), 11 metabolic reactions were predicted as being “blocked” and 14 signaling reactions were identified as inconsistent with the experimental data on connected proteins. The optimized network topology in **Figure 2** fits the measured data very well. The optimal solution of Eq. 1 ensured the fitting accuracy between the measurements and predicted values, and also obtained a maximal sub-graph of the generic network. Compared to other systems modeling approaches (such as ODE-based methods) (Komarova & Wodarz, 2010), our approach, which is based on constraints, can simplify the optimization process and quickly search an optimal solution in an allowable subspace. Given the details of the system

analyzed here (large scale of generic pathways, a single measured data point – ratio of rSCC-61 to SCC-61), an ODE-based method could not have been suitable for analysis (Lu et al, 2011).

The network predicted a critical interlink between three pathways necessary to support radiation resistance in HNSCC: 1) AKT signaling: differential redox regulation of AKT isoforms resulting in increased glucose uptake, 2) NADPH reserve: routing of glycolytic intermediates into the PPP leading to increased NADPH production to maintain suppression of H₂O₂ in the cytosol and mitochondria, and 3) Cholesterol metabolism. We therefore sought to validate these predictions and better understand how these key signatures are involved in development of radiation resistance in HNSCC. We validated the predicted differential regulation of AKT isoforms and its downstream targets by western blot and semi-quantitative PCR (**Fig. 3**). The network predicted increased AKT2 activity due to decreased ROS causing increased GLUT1 membrane localization and glucose uptake in rSCC-61 cells compared to SCC-61 cells. These predictions were supported by previously published studies on energy metabolism demonstrating increased uptake of glucose and flux of glycolytic intermediates into PPP resulting in increased NADPH reducing equivalents (Mims 2015). The MIP analysis also predicted decreased activity of AKT isoforms 1 and 3 in rSCC-61 cells and decreased phosphorylation of downstream target GSK3 β causing upregulation of β -catenin. These predictions were validated experimentally and shown in **Figure 3**. This differential regulation highlights the critical role redox regulation plays in signaling and facilitates radiation resistant cells ability to proliferate and evade cell death.

As NADPH is the ultimate provider of reducing equivalents in cells, we wanted to determine whether pathways other than PPP contribute to the increased NADPH reserve in rSCC-61 cells. Flux balance analysis (FBA) indicated that in addition to the PPP enzymes G6PD and PGD, which contributed ~45% of the NADPH, the increased NADPH/NADP⁺ ratio in rSCC-61 was also supported by the mitochondrial 1-C metabolism enzyme MTHFD2 (**Fig 4**). These results aligned with previously published proteomics data, which showed an increase in 1-C metabolism enzymes, MTHFD1 and SHMT2, in rSCC-61 cells compared to SCC-61 cells. Knockdown of

MTHFD2 in rSCC-61 cells resulted in 40% reduction in cell survival after treatment with irradiation. MTHFD2 knockdown in combination with DHFR inhibition by methotrexate and PPP inhibitor, CB83, significantly decreased cell survival of rSCC-61 cells to < 10% compared to SCC-61 cells (**Fig. 4F**). Taken together, these data demonstrate the coordinated PPP and 1-C metabolism is critical to maintain cellular NADPH reserve in cytosolic and mitochondrial compartments of rSCC-61 cells. Lack of coordination, as evident by singular inhibition of PPP or 1-C enzymes, leads to lesser inhibitory effects on cell survival and proliferation with or without irradiation.

NADPH also provides the reducing equivalents necessary for regeneration of GSH by GR and breakdown of H₂O₂ by PRXs, ultimately through the activity of NADPH-dependent TRX system. Therefore, the NADPH reserve maintained by 1-C metabolism and PPP is intrinsically connected to the levels of ROS in the cell. HPLC separation of GSH and GSSG confirmed increased GSH and GSSG in rSCC-61 cells compared to SCC-61 cells despite defects in glutathione biosynthesis as evidenced by downregulation of CBS and CSE proteins in SCC-61 cells and rSCC-61 cells, respectively (**Fig. 5B, D**). Studies completed in colon and ovarian cancer demonstrated overexpression of CBS causes increased H₂S production and increases the rate of proliferation, bioenergetics and angiogenesis (Bhattacharyya 2013, Modis 2014, Szabo 2013). The study in colon cancer also demonstrated silencing or inhibition of CBS attenuated ATP production, reduced glycolytic functions, and enhanced ROS generation (Bhattacharyya 2013). This data suggest CBS may play a protective role in cancer cells leading to radiation resistance and could be a potential therapeutic target for radiation resistant HNSCC. Clonogenic assay further confirmed an increased dependence of rSCC-61 cells on cystine import to maintain GSH/GSSG ratio in the cell (**Fig. 5E**). Overall, these studies revealed the critical function of GSH/GSSG and NADPH/NADP⁺ as key drivers of redox homeostasis in radiation resistant cells

pointing to the opportunity to radiosensitize HNSCC by targeting MTHFD2 and CBS metabolic enzymes.

To help overcome metabolic stress, a steady supply of metabolites is necessary for generation of biomass and energy. Our previously published energy metabolism work identified rSCC-61 cells divert from classical Warburg effect by fluxing the majority of glycolytic intermediates into the PPP resulting in low ETC activity and reduced mitochondrial ROS. However, there was an increase in FASN protein expression and reliance on endogenous fatty acids for energy production and biomass (Mims, 2015). Consistent with these findings, the network analysis predicted downregulation of AMPK causing uninhibited SREBP activity and upregulation of *FASN* transcription along with cholesterol biosynthesis genes (**Fig. 6**). Interestingly, LC-MS/MS analysis showed decreased cholesterol and oxysterols but increased squalene and squalene synthase in rSCC-61 cells compared to SCC-61 cells (**Fig. 7A,B**). While squalene is a known antioxidant and could be upregulated to provide defense against oxidative stress, its role in rSCC-61 cells remains unclear. The data presented here suggest cholesterol downregulation could be due to alterations in SREBP2 leading to downregulation of gene expression of cholesterol biosynthesis components. Gene expression of key SREBP2 genes (e.g. LDLR, HMGCR) are downregulated while gene expression of SREBP2 inhibitory genes (e.g. INSIG1, AMFR) are upregulated in rSCC-61 cells compared to SCC-61 cells (**Fig. S6B**). Taken together, it is possible there is a defect in the cholesterol feedback loop that signals to increase cholesterol synthesis, and/or SREBP2 translocation is inhibited by posttranslational modifications. Cholesterol influx and efflux data were able to rule out deficiency in cholesterol transport as ABCA1 expression was equal between the two cell lines and SCC-61 cells imported and exported cholesterol better than rSCC-61 cells (**Fig. 7D**). This increased import and export could simply be due to there being less cholesterol to transport in rSCC-61 cells than in SCC-61 cells rather than point to significant changes. However, due to significant lower cholesterol levels

in rSCC-61 cells and our previous data showing gain of resistance to radiation with inhibition of cholesterol biosynthesis in SCC-61 cells, we explored further the role of cholesterol and ROS in modulating response phenotype in rSCC-61 cells. Indeed increasing cholesterol or ROS in rSCC-61 cells resulted in increased sensitivity to radiation, decreased sensitivity to EGFR drug targeted therapy, and increased DNA double strand breaks as evidenced by γ H2AX foci formation (**Fig. 7E**). Further investigation into the potential redox regulation of cholesterol biosynthesis and its contribution to the response to radiation and targeted therapeutic is necessary to discover potential drug targets with radiosensitizing potential in the future.

Overall, combining multi-omics data with network and flux balance analysis allowed identification of clinically relevant radiation resistance signatures for HNSCC such as those driven by the pathways connecting cholesterol, ROS and NADPH metabolism.

Materials and Methods

EXPERIMENTAL STUDIES

Reagents. Antibodies were obtained from the following sources: Rabbit anti-pIGFR (Y1135/1136), anti-pAsk1 (S83), anti-pPDK1 (S241), anti-pPKD-PKC μ (S744/748), anti-pJNK1/2 (T183/Y185), anti-p-LKB1 (S428), anti-TP53, anti-pSTAT1 (Y701), anti-pSTAT3 (Y705), anti-pRSP6 (S235/236), anti-pMyc (T58/T62), anti-p4EBP1 (T37/46), anti-pAkt (S473/T308), anti-pAkt2 (S474), anti-pGSK3 β (S9), anti-AMPK, anti-pAMPK (T172), anti-ACC, anti-pACC (S79), anti-peEF2 (S366), anti- γ H2AX, anti-GAPDH, and anti-rabbit IgG HRP-linked from Cell Signaling. AlexaFluor594 conjugated cholera toxin subunit B (CT-B) and DMEM/F12 purchased from Gibco (Invitrogen) and fetal bovine serum purchased from Atlanta Biologicals. PBS was purchased from Lonza. BCA protein estimation kit and Western Lightning Plus ECL were purchased from Thermo Scientific.

Generation of SCC-61/rSCC-61 matched model system of radiation resistance in HNSCC.

We have reported the establishment of the radiation resistant rSCC-61 cell line in a previous publication (Bansal, 2014). Briefly, the radiation sensitive SCC-61 cells were irradiated using a 2 Gy radiation dose. After the radiation treatment the cells were cultured, split, allowed to achieve 60 % confluence and then exposed to another cycle of 2 Gy radiation. This process was repeated for cumulative total of 16 Gy. The resulting cell population was plated at low density on soft agar. rSCC-61 was picked as a single colony and expanded in culture.

Quantitative proteomics and redox proteomics. SCC-61 cells and rSCC-61 cells were cultured in DMEM/F12 media containing the light and heavy isotopes of Lys (8) and Arg (10), respectively, and supplemented with 10 % dialyzed FBS and 200 mg/L proline to prevent the conversion of isotope-coded arginine to proline in cells (Bendall, 2008). The cells were passed in their respective media to achieve a minimum of 97% incorporation of the isotope labeled Lys and

Arg. For proteomics studies the cells were lysed, processed and analyzed by mass spectrometry as described previously (Bansal, 2014). For the redox proteomics, the SCC-61 and rSCC-61 cells were cultured in DMEM/F12 under SILAC conditions as described above. The cells were then lysed in 0.5 mL with modified RIPA buffer (50 mM Tris-HCl, pH 7.4; 1 % NP40; 15 mM NaCl; 1 mM EDTA; 1 mM NaF; Roche protease and phosphatase inhibitor tablets) supplemented with 1 mM 1,3-cyclopentanedione (BP1) (Qian, 2011) and 200 U/ml Catalase. Protein concentration was determined using BCA assay (Thermo Scientific). Samples were normalized, combined 1:1, precipitated by cold acetone and pellets were resuspended in minimum volume (approx. 100 μ L) of 1 % SDS in PBS. Samples were diluted 10-fold prior to enrichment with 50 mM ammonium bicarbonate. Approximately 250 μ L of suspended streptavidin agarose beads (Cat. # 20361, Thermo/Invitrogen) were used for each 1 mg of lysate. The beads were equilibrated 3 times with 4 bed volumes of 0.1% SDS in PBS for 10 min each. Biotinylated lysates were added to the beads and incubated on rotator (end-over-end) overnight at 4 °C. The non-specifically bound proteins were removed by washing the beads sequentially with 2 M urea, 1 M NaCl; 0.1% SDS, 10 mM DTT; and 50 mM ammonium bicarbonate. The proteins on beads were digested overnight at 37 °C on a shaker with trypsin using a 1:50 enzyme-to-substrate ratio. The resulting peptides were acidified with 1% formic acid, centrifuged at 2,000 g for 5 min, and desalted using a tC18 SepPak column (cat #WAT036820) following the manufacturer's protocol. The dried samples were used in HPLC fraction immediately or stored in -20 °C. **HPLC fractionation.** Basic high pH reversed-phase chromatography was conducted on a Waters 2695 instrument using a Xbridge C18, 3.5 μ m, 4.6 x 150 mm chromatography column. Desalted peptides were reconstituted in 20 mM ammonium formate, pH 10, injected and separated using a flow rate of 0.5 mL/min and the following gradient: [Solvent A (2% acetonitrile, 5 mM ammonium formate, pH 10), Solvent B (90% acetonitrile, 5 mM ammonium formate, pH 10); 0% B for 2 min; 0- 10% B in 5 min; 10- 27% B in 34 min; 27- 31% B in 4 min; 31- 39% B in 4 min; 39-60% in 7 min; 60% B for 8 min; 60- 100% B in 2 min; 100% B for 4 min; 100- 0% B in 1 min; 0% B for 1 min]. Eluted peptides

fractions (1 mL/tube) were collected using Water Fraction Collector III. The 36 eluted fractions were combined from the beginning, middle, and end of the run to generate 12 fractions (1,13,25; 2,14,26; etc) and then dried using a SpeedVac SavantTM SPD1010 (Thermo). ***NanoLC MS/MS and database searching.*** Dried peptide extracts were dissolved in 0.1% formic acid, 5% ACN, and separated by nanoLC (Dionex Ultimate 3000) equipped with a Nano Trap Column, Acclaim PepMap100 (C18, 5 μm , 100 \AA , 100 μm i.d. x 2 cm nanoViper) and an Acclaim PepMap RSLC nanocolumn (C18, 2 μm , 100 \AA , 75 μm i.d. x 15 cm, nanoViper) (Thermo Scientific). The samples (10 μL) were injected and separated on the nanocolumn at a flow rate of 300 nL/min using the following gradient: [Solvent A: 95% water, 5% ACN, 0.1% formic acid; Solvent B: 20% water, 80% ACN, 0.1% formic acid); 2–10 min: 2–7% B; 10– 130 min: 7–50% B; 130–132 min: 50–85% B; 132–147 min: 85% B; 147-150 min: 85-2% B; 150–160 min, 2% B]. LTQ Orbitrap Velos Pro (Thermo Scientific) was used for MS/MS analysis. The sample was ionized in the nanospray source equipped with stainless steel emitter (Thermo Scientific). The spray voltage was set to 1.5 kV and the temperature of the heated capillary was set to 200 °C. Full scan MS survey spectra in profile mode were acquired in the Orbitrap. In positive ion mode by alternating full-scan MS 10 most intense peaks in the ion trap with dynamic exclusion enabled. These most intense peptide ions were fragmented by collision-induced dissociation (CID) using a normalized collision energy of 35.0. The resolution was 60,000. The lock mass (371.101240) option was enabled for survey scans to improve mass accuracy. Data were acquired using the XCalibur v.2.1 software. Protein identification and quantitation was performed using Proteome Discoverer v 1.4 and human protein database downloaded in FASTA format from UniProt (<http://www.uniprot.org/>). Data files (.raw format) were searched against the downloaded database using the following parameters: Enzyme: trypsin; Max. Missed Cleavage Sites: 2; Search Mode: MS/MS ion search with decoy database search included; Precursor Mass Tolerance: 10 ppm, Fragment Mass Tolerance: 0.6 Da; Target False Discovery Rate (FDR): 0.01.

Western blot analysis for protein expression and protein phosphorylation. Cells were lysed with the modified RIPA buffer as described above. The lysates were incubated on ice for 1 h followed by centrifugation at 10,000 x g for 10 min. The lysates were then normalized for their protein concentration across different treatment conditions and subjected to SDS-PAGE. The separated proteins were then transferred to a nitrocellulose membrane (0.45 μ m, BioRad) and probed for the indicated proteins after overnight incubation with the corresponding primary antibodies (Cell Signaling) diluted in 5 % BSA in Tris Buffered Saline (TBS)-Tween20 buffer followed by incubation with respective HRP-conjugated secondary antibodies. The Western blots were developed using Western Lightning Plus-ECL reagents followed by exposure to autoradiography film (Blue Ultra Autorad Film from GeneMate). The ratio (rSCC-61/SCC-61) was determined using ImageJ.

Metabolomics studies. Cells (10^8 /sample) were first extracted with 500 μ L of mixture solvent (methanol: chloroform: water= 2.5:1:1), followed by addition of 500 μ L of methanol. The supernatant was transferred to GC sampling vials and vacuum dried at room temperature. The residue was then derivatized using a two-step procedure. First, 80 μ L methoxyamine (15 mg/mL in pyridine) was added to each vial and incubated for 90 min at 30°C. This was followed by addition of 80 μ L BSTFA (N,O-bis(trimethylsilyl)trifluoroacetamide) (1% TMCS, trimethylchlorosilane) to initiate the derivatization reaction. The samples were heated for 60 min at 70°C and 1- μ L aliquot of the derivatized solution was injected in splitless mode into an Agilent 7890N gas chromatograph coupled with a Pegasus HT time-of-flight mass spectrometer (Leco Corporation, St Joseph, USA). Separation was achieved on a Rxi-5MS capillary column (30 m \times 250 μ m I.D., 0.25- μ m film thickness, Restek), with helium as carrier gas at a constant flow rate of 1.0 mL/min. The temperature of injection, transfer interface, and ion source was set to 260°C, 260°C, and 210°C, respectively. The GC temperature programming was set to 80°C for 2 min, followed by 10°C/min oven temperature ramps to 140°C, 4°C/min to 210°C, 10 °C/min to 240°C, and 25°C/min to 290 °C, and a final 4.5 min maintenance at 290°C. Electron impact ionization

(70 eV) at full scan mode (m/z 40-600) was used, with an acquisition rate of 20 spectra/second in the TOFMS setting. The acquired MS files from GC/TOFMS analysis were analyzed by ChromaTOF software (v4.22, Leco Co., CA, USA). Statistic component analysis provided the aligned data sheet containing sample information, unique mass, and the area of unique mass of each sample. Internal standards and any known artificial peaks, such as peaks caused by noise, column bleed and BSTFA derivatization procedure, were removed from the data set. The resulting data was normalized to sum of all peaks prior to statistical analysis (and multiplied by 10,000). The normalized data was mean centered and unit variance scaled during chemometric data analysis in the SIMCA-p 12.0 Software package (Umetrics, Umeå, Sweden). Compound identification was performed by comparing the mass fragments with NIST 11 Standard mass spectral databases in NIST MS search 2.0 (NIST, Gaithersburg, MD) software with a similarity of more than 70%.

COMPUTATIONAL PROCEDURES: Mixed Integer Programming (MIP)

Here, we describe the methods to infer the rSCC-61-specific network using joint optimization of signaling and metabolism via MIP. Linear programming is a novel approach for systemic modeling and network optimization. Mitsos proposed a integer linear programming (ILP) approach to infer cell-specific signaling pathways and identify the drug effects (Mitsos et al, 2009). Mixed Integer Programming (MIP) was also widely applied to metabolic networks for flux balance analysis (Orth et al, 2010). However, there are limited studies on how to joint optimize an integral network which includes both signaling and metabolic reactions. Besides, none of the methods that are currently available account for redox effects on the activity of proteins on a network scale comparable with the one described here.

In the integral network topology, the signaling subnetwork is defined as a set of signaling proteins $PP = \{1, 2, \dots, j, \dots, n_s\}$ and reactions $Z = \{1, 2, \dots, i, \dots, n_r\}$. The signaling proteins are receptors, kinases, phosphatases and transcription factors. In our study, a subset (EP) of enzymes bridging

the signaling and metabolic subnetworks were also considered as components of the signaling subnetwork. The i -th signaling reaction is defined as $j \rightarrow p$ ($j, p \in PP$), which connects two proteins: the upstream protein j , and the downstream protein p . If several signaling reactions connect with the same protein p , the relationship between these reactions were logic “OR” which indicate that the state (x_p) of protein p might be regulated by several upstream proteins, simultaneously.

In our MIP approach, a binary variable $x_j \in \{0,1\}$ indicates if the protein j is up-regulated ($x_j = 1$) or down-regulated ($x_j = 0$) in rSCC-61 relative to SCC-61. The variable z_i denotes if the reaction i takes place ($z_i = 1$) or not ($z_i = 0$). In the signaling pathway topology, there are two types of reactions: activation and inhibition. When activation takes place, which means the changes in the activity of protein p are positively related to that of its upstream protein j , the state of z_i can be represented with a logic operation (the reverse “exclusive OR”) between x_{ij} and x_{ip} (Eq. (2)). Similarly, the increased upstream protein x_{ij} might lead to down-regulation of downstream protein x_{ip} via inhibition. Thus, the state of z_i equal’s logic “exclusive OR” between x_{ij} and x_{ip} (Eq. (3)).

The metabolic sub-network is defined as a set of metabolites $M = \{1,2, \dots, k, \dots, m_s\}$ and a set of metabolic reactions $I_M = \{1,2, \dots, l, \dots, m_r\}$. The concentration of metabolite k is represented with a continuous variable C_k , in which $k \in \{1,2, \dots, m_s\}$. Each metabolic reaction l has two corresponding index sets, substrates S_l and products P_l , which are subsets of the metabolites index set ($S_l, P_l \subset M$). In our study, each metabolic reaction was simply related to an enzyme; hence, we applied the enzyme states to represent the states of corresponding reactions in our MIP model. The set (E) of binary variables is defined to denote all the metabolic enzymes in our network, where $E = \{e_1, e_2, \dots, e_l, \dots, e_{m_r}\}$. A subset (EP) of set E denotes the enzymes connecting signaling and metabolic subnetworks. Thus, the enzymes in EP belong to both subnetworks ($EP \subset E$). With regard to the metabolic reaction $l \in I_M$, the binary variable $e_l \in$

$\{0,1\}$ indicates if the state of l -th enzyme is up-regulated ($e_l = 1$) or down-regulated ($e_l = 0$) in rSCC-61. In our proposed model, down-regulated enzymes potentially block the corresponding metabolic reactions. The flux value and the change in Gibb's free energy of reaction l are denoted with continuous variables v_l , and ΔG_l , respectively. We first performed flux balance analysis (FBA) to ensure the mass or energy balance in the whole network (Orth et al, 2010; Tepper et al, 2013). Thermodynamic constraints were then applied to restrict the consensus rule that the net flux of a chemical reaction and the change of Gibb's free energy are related to each other: $sgn(v) = -sgn(\Delta G)$ (Hoppe et al, 2007).

For inferring the rSCC-61 network, we used the MIP approach to find an optimal solution for the integral pathway network. We considered two types of elements in our optimization: The first was to minimize the difference between predicted values and measurements of species, which includes signaling proteins, metabolic concentrations, and the states of enzymes. The second objective is to obtain a maximal sub-graph of the generic network. The objective function is defined as:

$$MIN \left\{ a_1 \sum_{j \in PP} (x_j^m - x_j^p)^2 + a_2 \sum_{k \in M} (C_k^m - C_k^p)^2 + a_3 \sum_{l \in E} (e_l^m - e_l^p)^2 - a_4 \sum_{l \in E} (e_l^p) - a_5 \sum_{i \in Z} (z_i^p) \right\} \quad (1)$$

The positive parameters (a_1, a_2, a_3, a_4, a_5) in Eq. (1) control the weight of corresponding objectives. x_j^m and x_j^p are the measured and predicted activities of j -th signaling protein, respectively. C_k^m and C_k^p are the measured and predicted concentrations of k -th metabolite. e_l^m and e_l^p are the measured and predicted activities of l -th metabolic enzyme. Therefore, the first three parameters (a_1, a_2, a_3) minimized the differences between measurements and predicted values, including the states of signaling proteins, concentrations of metabolites, and the

states of enzymes in the whole network. The last two parameters (a_4 and a_5) optimized the scale of inferred network topology aiding in removal of inconsistent reactions. The constraints in our MIP approach can be summarized as:

$$z_i = \overline{x_{ip} \oplus x_{ij}}, \quad i = 1, \dots, n_r, \quad j, p \in \{1, 2, \dots, j, \dots, n_s\} \quad (2)$$

$$z_i = x_{ip} \oplus x_{ij}, \quad i = 1, \dots, n_r, \quad j, p \in \{1, 2, \dots, j, \dots, n_s\} \quad (3)$$

$$z_i \geq x_{ij}, \quad i = 1, \dots, n_r, \quad j \in \{1, 2, \dots, j, \dots, n_s\} \quad (4)$$

$$S * V = 0 \quad (5)$$

$$\frac{\Delta G_l}{RT} = \left(\sum_{k1 \in P_l} \ln(C_{k1}) - \sum_{k2 \in S_l} \ln(C_{k2}) \right) - \ln[K_{eq}^l] \quad (6)$$

$$\begin{cases} C_{min} \leq C_{k1} \leq C_{max}, k1 \in P_l \\ C_{min} \leq C_{k2} \leq C_{max}, k2 \in S_l \end{cases} \quad (7)$$

$$0 \leq v_l \leq e_l v_{max}, \quad E \in \{1, 2, \dots, j, \dots, n_s\} \quad (8)$$

$$\Delta G_l \leq \varepsilon(1 - e_l), \quad E \in \{1, 2, \dots, j, \dots, n_s\} \quad (9)$$

$$e_l \cdot C_{min} \leq C_{k1} \leq e_l \cdot C_{max} \quad (10)$$

$$v_{min} \leq v_l \leq v_{max}, \quad E \in \{1, 2, \dots, j, \dots, n_s\} \quad (11)$$

$$-v_l + d^+(\varepsilon - v_{min}) \leq -v_{min} \quad (11)$$

$$\Delta G_l + d^+(\varepsilon - v_{min}) \leq -v_{min} \quad (13)$$

$$v_l + d^-(\varepsilon + v_{max}) \leq v_{max} \quad (14)$$

$$-\Delta G_l + d^-(\varepsilon + v_{max}) \leq v_{max} \quad (15)$$

$$e_l = d_l^+ + d_l^- \quad (16)$$

$$X \in \{0, 1\}^{n_s}, Z \in \{0, 1\}^{n_r}, E \in \{0, 1\}^{m_r}, d_l^+, d_l^- \in \{0, 1\} \quad (17)$$

According to these formulas, the constraints (2-3) are used to infer the states of all regulated reactions (Eq. (2) activation, Eq. (3) inhibition). The constraint (4) was used to restrict the states of a reaction when it uniquely promotes a terminal protein. The system of mass or energy balance equations at steady state is given in constraint (5). The metabolic reactions are represented as a

stoichiometric matrix (S) and the flux vector was represented as V . The constraint (6) indicates the changes in Gibb's free energy calculated from changes in standard Gibb's energy, where C_{k1} and C_{k2} are the active concentrations (activity) of the metabolites in reaction l . S_l and P_l denote the sets of substrates and products of the reaction l , respectively. R is universal gas constant and T is the absolute temperature. The values for all parameters were extracted from NIST Standard Reference Database (Goldberg et al, 2004), HMDB (Wishart et al, 2007) and Uniprot (Dimmer et al, 2012; O'Donovan & Apweiler, 2011). Constraint (7) is used to restrict the concentration values of all metabolites in the network. Thermodynamic constraint (8) ensures that the net flux v_l is restricted between 0 and v_{max} as lower and upper bounds if the irreversible reaction l is activated (the state of enzyme x_E is up-regulated); otherwise, the flux value is zero. Equations (8)-(9) ensure the opposite relationship between direction of the net flux and the change of Gibb's free energy when the reaction is un-blocked in a single metabolic reaction if the enzyme is blocked by an inhibitor, the products will be unchanged even though the substrates are significantly expressed (see constraint 10).. Constraint (11) is also used to restrict the flux values in the reversible reactions. Similarity, constraints (12)-(15) ensure the direction of net flux and Gibb's energy in reversible reactions. The constraint (16) restricts the flux of a reversible reaction to one direction if the corresponding enzyme is up-regulated. Because variables e_l , d_l^+ and d_l^- are all binary, it is possible to infer the unique direction of flux in a reversible reaction. The formula (17) restricts the values of three groups of binary variables X , Z and d_l^+ , d_l^- . Since our data reflects the changes in the activities of proteins between two cell lines, there is only one data point in the analysis. Different from the ODE-based approaches (Lu et al, 2011), the MIP model described here can quickly infer a cell-specific network by fitting the measurements to a network topology.

Identification of intracellular GSH and GSSG. To measure the concentration of intracellular thiols, GSH and GSSG, $2 - 4 \times 10^6$ cells grown at a density of 1×10^6 cells/ml in a 60 mm culture dish. Cells are washed 3X with ice-cold PBS, then 100 μ L of PBS is added to the culture plates

on ice. Cells are detached by scraping and collected in a 1.5 ml centrifuge tube. Nonadherent cells can be collected by centrifugation then washed with ice-cold PBS. An aliquot of the cell suspension in PBS is mixed with an equal volume of metaphosphoric acid solution (16.8 mg/ml HPO_3 , 2 mg/ml EDTA and 9 mg/ml NaCl) and vortexed gently. The precipitated proteins are sedimented by centrifugation at 13,000 x g for 10 min at 4 °C. The supernatant is transferred into a 1.5 ml centrifuge tube and thiols are alkylated with monoiodoacetic acid at a final concentration of 7 mM, then vortexed; the pH is adjusted to 7 – 8 with saturated K_2CO_3 . The reaction is allowed to proceed for 1 h in the dark at room temperature (RT). Finally, an equal volume of 2,4-dinitrofluorobenzene solution (1.5 % v/v in absolute ethanol) is added to the mixture, then vortexed, and the reaction is allowed to proceed for at least 4 h in the dark at RT. The N-dinitrophenyl derivatives of cysteine, GSH, and GSSG are separated by HPLC on a Waters μ Bondapak NH2 column (300 mm x 3.9 mm, 10 μM) at a flow rate of 1 ml/min. The mobile phase consists of solvent A (4:1 methanol/water mixture) and solvent B, which is prepared by mixing 14 g of ammonium acetate in 122 ml of water and 378 ml of glacial acetic acid and adding 500 ml of the resulting solution to 1,000 ml of solvent A. The following elution conditions are used: from 0 – 10 min isocratic 25 % solvent B; from 10 – 30 min linear gradient 25 – 100 % solvent B; from 30 – 34 min 100 % solvent B; from 34 – 36 min 100 – 25 % solvent B; and finally 36 – 45 min 25 % solvent B. Prior to injection, the column is equilibrated with 25 % solution B for 10 min. Elution of metabolites is monitored by their absorbance at 355 nm. Under these conditions, GSH and GSSG exhibit retention times of 18, 26, 29 min, respectively. The concentration of individual thiols is determined by comparing the integrated peak areas with independently generated calibration curves for each compound. Typically, the concentration of each metabolite is normalized to the protein concentration in the corresponding sample. The detection limit of this method is ~ 20 pmol.

Analysis of H₂S producing activity in the cells. Cells were grown in 10 cm Petri dishes until confluency of 80 %. Then the medium was aspirated, cells were washed two times with cold PBS and then trypsinized or scraped from the surface with small amount of PBS. Cell suspension was placed into preweighed sample tubes, centrifuged for 5 min at 2000 g to sediment cells, supernatant was aspirated and tubes were weighed again. The difference in initial tube weight and in tube weight with cell pellet gives cell pellet weight in the tube. Then 100 mM HEPES buffers, pH 7.4 was added to the tubes in a volume equal to 9 volumes of cell pellet assuming the cell density equal to 1 g/ml. Tubes were vortexed and freeze/thawed 3 times to lyse the cells. Protein levels in lysate were measured using Protein Assay Dye Reagent (Bio-Rad) as described elsewhere (Garg, 2010). To measure rate of H₂S production 400 μ L of cell lysate was mixed with L-cysteine (Sigma) (20 mM final concentration) plus D,L-homocysteine (Sigma) (40 mM final concentration) in a total volume of 500 μ L and incubated under anaerobic conditions for 20 min at 37 °C. Accumulation of H₂S was measured using gas chromatograph equipped with sulfur chemiluminescence detector (SCD 355) (Agilent) as described elsewhere (Vitvitsky, 2015). Cell lysate alone as well as mixture of cysteine and homocysteine in buffer were used as control samples. H₂S levels obtained in control samples were subtracted from H₂S levels obtained in experimental samples. The rates of H₂S production were normalized to protein levels in lysate.

Clonogenic assay. Radiation-resistant rSCC-61 and the parental SCC-61 cells were grown to 60 % confluence. Cells were then trypsinized and resuspended in complete medium (DMEM/F12 + 10 % FBS and 0.5 % PenStrep (Gibco), and plated (300 cells/well) into six well culture dishes. Following o/n incubation at 37°C, each 6-well plate were treated with either (i) 1 μ M sulfasalazine (SAS) in DMEM, (ii) DMEM without cysteine, (iii) DMEM without methionine and cysteine, or (iv) 0 – 10 μ M methotrexate (MTX) and allowed to incubate further for 12 days for the colony formation. For other clonogenic assays, radiation-resistant rSCC-61 cells were grown to 60 % confluence followed by transfection with MTHFD2 shRNA (50 nM) or control

shRNA (50 nM) (Santa Cruz Biotechnology) using Lipofectamine 2000 (ThermoFisher Scientific) according to manufacturer's protocol. After 48 h, transfected cells were trypsinized, resuspended in complete medium (DMEM/F12 + 10 % FBS and 0.5 % PenStrep (Gibco), and selected using puromycin. After selection, plated (300 cells/well) into six well culture dishes and incubated overnight. Cells were then subjected to (i) 2 Gy irradiation, (ii) 10 μ M Methotrexate, (iii) 1.7 μ M CB83 or (iv) 10 μ M Methotrexate combined with 1.7 μ M CB83 and incubated for an additional 12 days for the colony formation. Once formed, the colonies were fixed in methanol and acetic acid (7:1) solution and stained with 0.5 % crystal violet (Fisher Scientific). The colonies containing more than 50 cells were counted. The surviving fraction of the treated cells was normalized using the plating efficiencies of their corresponding untreated control. The data were fitted to the multi-target and linear quadratic formulae, where survival (S) was related to dose (D) by the expression $S = 1 - \left(1 - e^{-\frac{D}{D_0}}\right)^N$ and $S = e^{-\alpha D - \beta D^2}$ using SigmaPlot v.12 software (Harari, 2006).

Flux balance analysis Flux balance analysis was performed using the COBRApy software package (Ebrahim, 2013). We sought to maximize the conversion from cytoplasmic NADP⁺ to cytoplasmic NADPH, and see which NADPH-producing reactions in the solution carried the largest flux. This is equivalent to asking: if the cell is converting as much NADP⁺ to NADPH as possible, through which pathways will this occur? This objective function is implemented by adding the reaction $x: \text{nadph_c} \rightarrow \text{nadp_c}$ to the metabolic model, and then maximizing the flux through this reaction with the constraints of the following equations

$$\begin{aligned}
 &\text{max} && v_x, \text{ where } x: \text{nadph_c} \rightarrow \text{nadp_c} \\
 &\text{subject to} && \mathbf{Sv} = \mathbf{0} && (5) \\
 &\text{and} && \text{lb}_i \leq v_i \leq \text{ub}_i
 \end{aligned}$$

where S is the stoichiometric matrix of m metabolites and r reactions, \mathbf{v} is a $r \times 1$ vector of reaction fluxes, and lb_i and ub_i indicate the lower bound and upper bound of each given flux v_i .

The objective function will cause other reactions in the model that produce cytoplasmic NADPH from NADP⁺ to have very high flux (to balance out the consumption of cytoplasmic NADPH and production of NADP⁺ in the maximized reaction x).

Media constraints In HMR 2.0 (Mardinoglu, 2014), exchange reactions exist between the different compartments of the model (see Figure 1). Exchange reactions between C_x and C_e, and then between C_e and C_c, provide the cell with nutrients and metabolic precursors from its environment. The media within which the cell lives is often modeled as the upper bounds of metabolite exchange from C_x to C_e. For example, to model a low-glucose environment, a small upper bound for glucose exchange between C_x and C_e is set. Traditionally in flux balance analysis, media constraints imposed on the cell are limited to setting a small upper bound for a few “limiting metabolites” (usually including glucose), and making all other metabolites freely-available (by setting the upper bound to the maximum possible flux value). However, a more accurate representation of the media constraints on cellular metabolism can be modeled by setting upper bounds for all available metabolites in proportion to their concentration in the media. We modeled ThermoFisher’s DMEM/F-12 media by setting the upper bound for each metabolite exchange reaction from C_x to C_e in proportion to its concentration in the actual media; for C_x to C_e exchange reactions involving metabolites not in the media, we set the upper bound to zero. Each upper bound (in units of mmol/gDW/hr) is set equal to the numerical value of the metabolite’s media concentration in mmol/L.

Context-specific models (HNC) HMR 2.0 contains metabolites and reactions found within all cells of the human body; however, in order to study the redox metabolism of a particular cell type or cancer type, we must create context-specific models of these different cells. This can be accomplished by removing reactions in HMR 2.0 that do not normally occur within the particular cell type. To create context-specific models of HNC cancer, proteomic data from the Human Protein Atlas (HPA) was used (Uhlen, 2015). The expression status of a gene was set to “Expressed” if at least 50% of the biopsy results had a HPA expression level of High, Medium, or

Low. If at least 50% of the biopsy results had a HPA expression level of Not Detected, the expression status of the gene was set to “Not Expressed”. These gene expression statuses were used to determine which reactions from the original HMR 2.0 model would be removed or not removed in the context-specific model.

Each reaction in HMR 2.0 has an associated gene reaction rule, written as a Boolean function of the genes whose products execute the reaction (for example, the gene reaction rule can be a Boolean function of the genes representing different isoforms of the enzyme which catalyzes the reaction). To determine whether a particular reaction should be removed from HMR 2.0 to build the context-specific model, the expression status of each gene was placed in the gene reaction rules (Expressed = True, Not Expressed = False). If the resulting Boolean function came out to be True, then the genes necessary to execute the reaction are being expressed in the tissue, and the reaction is kept in the context-specific model. If the Boolean function came out to be False, then the necessary genes are not expressed, and the reaction was removed from the context-specific model.

Context-specific models (SCC-61, rSCC-61) Triplicate transcriptomic data from rSCC-61 and SCC-61 cells were log₂ transformed and normalized by robust spline normalization. We aggregated HNC transcriptomic data into a single Illumina dataset by performing batch correction between our data and the HPV- samples from (Wichmann, 2015) using ComBat (Kitchen 2010). Using the HNC model as the starting point for our cell line-specific models, we performed the following steps:

If the reaction is not associated with any gene, keep the reaction ON;

If the reaction is associated with a gene(s), but there are no Illumina probes in the aggregated data set associated with the gene(s), use the same reaction ON/OFF status as in the original head-neck cancer model;

If the reaction is associated with a gene(s), and there are Illumina probe(s) in the data sets associated with the gene(s): initialize a score for the gene for both SCC-61 and rSCC-61

For each gene:

a) Initialize a score for the gene for both SCC-61 and rSCC-61: $\text{score_SCC} = 0$, $\text{score_rSCC} = 0$

b) For each Illumina probe associated with the gene:

If ALL 3 of the SCC-61 values are > 1 standard deviation (of the 196 Wichmann samples) from the mean (of the 196 Wichmann samples), ADD 1 point to the gene's SCC-61 score.

If ALL 3 of the SCC-61 values is < 1 standard deviation from the mean, SUBTRACT 1 points to the gene's SCC-61 score. Otherwise, don't change the gene's SCC-61 score.

Repeat for the rSCC-61 values and gene's rSCC-61 score

c) If the gene's SCC-61 score is > 0 , make the gene's expression status ON.

d) If the gene's SCC-61 score is < 0 , make the gene's expression status OFF. Otherwise, use the same expression status as the original head-neck cancer model.

d) Repeat for rSCC-61

4) Use the reaction's Boolean gene reaction rule (e.g. gene 1 AND gene 2) to set the reaction ON/OFF status in the SCC-61 and rSCC-61 models.

Lipidomics. Cholesterol and oxysterols were extracted from 1×10^6 million SCC-61 or rSCC-61 cell pellet by adding 0.9 % saline followed by an addition of methanol, chloroform, and $1 \mu\text{g}/\mu\text{l}$ C13-cholesterol (Sigma Aldrich) and 20 ng oxysterol internal standard mix. Samples were vortexed, incubated at room temperature for 30 min followed by a 1:1 addition of water and chloroform and centrifuged at $4 \text{ }^\circ\text{C}$ at 2500 rpm for 5 min. The bottom layer was transferred to a new tube and repeated extraction steps above on monolayer before transferring the bottom layer to the previous sample collection. Samples were evaporated under nitrogen flow and dissolved in $500 \mu\text{l}$ chloroform. For **free cholesterol analysis**, approximately $100 \mu\text{l}$ of total sample was evaporated under nitrogen, re-dissolved in methanol and transferred 1:10 dilution of sample to an

auto sampler vial to run on LC-MS/MS. For **total cholesterol analysis**, approximately 100 μ l of total sample was evaporated under nitrogen, re-dissolved in ethanol, vortexed before adding 100 μ l of aqueous 50 % KOH (w/w). Samples were vortexed and incubated at 60 °C for 1 hour. Next a 3:1 addition of hexane and dH₂O were added to samples followed by vortex and 4000 rpm centrifugation for 3 min. The upper phase was evaporated under nitrogen and re-dissolved in methanol and transferred 1:10 dilution of sample to an auto sampler vial to run by LC-MS/MS. For **oxysterol analysis**, samples were evaporated under nitrogen and re-dissolved in methanol followed by vortex and addition of 100 μ l of aqueous 50 % KOH (w/w). Samples were vortexed and incubated at room temperature for 2 hours with vortexing every 30 min. Next a 3:1 addition of toluene and dH₂O were added to the sample followed by vortex and 4000 rpm centrifugation for 5 min. The upper phase was evaporated under nitrogen and re-dissolved in toluene and vortexed thoroughly. Isolute 100 mg silica SPE-cartridges (Isolute, Cat #460-0010-A) were preconditioned with hexane and samples were loaded onto column in toluene. Columns were washed with 1 ml hexane, 8 ml hexane: isopropanol (99.5:0.5) and then oxysterol fraction was eluted with 5 ml hexane: isopropanol (70:30). LC/MS Method

Cholesterol influx and efflux. SCC-61 and rSCC-61 cells were plated 2.0×10^5 cells in 0.5 mL complete media (DMEM/F12, 10% FBS, 0.5% penstrep) and allowed to adhere before labeling with 2 μ Ci/ml [3H]cholesterol (PerkinElmer) in DMEM/F12 (Gibco) containing 0.5 % penstrep and 2.5% FBS for 24 h. Cells were washed with 0.5 ml 1X DMEM (Gibco) containing 14 mM HEPES followed by 20 h equilibration in DMEM/F12 with or without 0.30 mM adenosine 3',5'-cyclic monophosphate (cAMP). Cells were washed again with 0.5 ml 1X DMEM containing 14 mM HEPES and subsequently incubated with 0.5 ml MEM-HEPES (Gibco) supplemented with or without 0.15 mM cAMP and with or without 30 μ g/ml apolipoprotein A1 (APOA1) for 4 h. Following 4 h incubation, 0.5 ml of media was removed and 0.1 ml of media combined with 5 ml Bio-Safe II scintillation fluid (Research Products Int.) to be counted. Each well is then washed 2X with 0.5 ml cold saline buffer followed by extracting lipids with 1 ml isopropanol o/n at room

temperature on rotator. The lipid extract is dried under N₂ and resuspended in 0.5 ml isopropanol. Then 0.1 ml of lipid extract is combined with 5 ml Bio-Safe II scintillation fluid (Research Products Int.) to be counted. 3H-activity is counted in medium and lipid extract. 3H-activity was counted in the medium and lipid extraction, and cholesterol efflux was calculated as the percentage of 3H-activity medium/(3H-activity medium plus 3H- activity lipid extract) * 100.

Immunostaining of lipid rafts and γ H2AX. SCC-61 and rSCC-61 cells were seeded in 1 ml microtek chambers (EMD Millipore) at a density of 2×10^4 cells/ml and incubated overnight at 37 °C and 5 % CO₂. After overnight incubation, SCC-61 cells were treated with (i) 1 μ M Lovastatin, (ii) 20 U polyethylene glycol (PEG)-catalase (Sigma-Aldrich) and rSCC-61 cells were treated with (iii) 1 mM M β CD-Cholesterol complex (REF), and (iv) 5 μ M tert-butyl hydroperoxide (Sigma-Aldrich) in 1 ml serum-free medium for 24 h. **CT-B Staining.** The cells were stained with 1 μ g/ml of AlexaFluor594 conjugated cholera toxin β (CT-B) for 15 min at 4 °C. Cells were fixed in 4% formaldehyde for 15 min and permeabilized with 0.1% TritonX-100. **γ H2AX.** Cells were washed with cold PBS and fixed in 4% formaldehyde for 15 min, washed with PBS 3X for 5 min, permeabilized with 0.1 % TritonX-100 followed by blocking with 8% BSA for 1 h at room temperature. The cells were incubated with 1:500 dilution of γ H2AX overnight at 4 °C followed by washing with PBS and incubation with 1:500 dilution secondary anti-rabbit Alexa Fluor 488 Conjugate antibody for 1 h at room temperature. Following lipid raft staining or γ H2AX immunostaining, the cells were mounted using UltraCruz® Mounting Medium (Santa Cruz Biotechnology). Imaging acquisition, processing and analysis was performed using a Zeiss LSM710 confocal microscope at a 63X objective.

Detection of H₂O₂ generation using HyPer proteins. To assess the level of reactive oxygen species (ROS) in SCC-61 and rSCC-61 cells, a plasmid encoding the cytoplasmic or mitochondrial form of HyPer (Evrogen) was introduced into cells with Lipofectamine 2000 (Invitrogen) and fluorescent cells were selected with Geneticin (ThermoScientific). Cells were seeded on 8-well chambered cover glass system (ThermoScientific) at a density of 2×10^4

cells/mL and incubated overnight at 37 °C and 5 % CO₂. After overnight incubation, SCC-61 cells were treated with (i) 1 μM Lovastatin, (ii) 20 U polyethylene glycol (PEG)-catalase (Sigma-Aldrich) and rSCC-61 cells were treated with (iii) 1 mM MβCD-Cholesterol complex, and (iv) 5 μM tBuOOH (Sigma-Aldrich) in 1 ml serum-free media for 24 h. HyPer protein was excited at wavelengths 405/30 nm and 488/25 nm light and emission was recorded at 550/40 nm, with the lamp intensity set at 0.5 %. Image acquisition, processing and analysis were conducted with Zeiss LSM710 confocal microscope on a 40X objective. The HyPer ratio for each field was calculated by dividing the mean pixel intensity at 488 nm by mean pixel intensity at 415 nm.

MTT Cell Viability Assay. To assess the effects of lipid raft activation on response to radiation in rSCC-61 cells, the cells were trypsinized, resuspended in complete DMEM/F12 medium and seeded in 24-well plates at a density of 5 x 10⁴ cells/ml. After overnight incubation at 37 °C, cells were treated with 1 mM MβCD and 1 mM MβCD-Cholesterol complex for 24 h followed by 2 Gy radiation for 48 h. After incubation, 0.125 ml MTT (5 mg/ml in PBS) was added to each well and plates were further incubated for 4 h at 37 °C. At the end of incubation, 0.5 ml solubilization solution was added to each well and the absorbance was recorded at 570 nm.

HumanHT-12 v4 Expression BeadChip. Total RNA was extracted and purified from SCC-61 and rSCC-61 cells using the RNeasy Plus Mini kit (Qiagen Cat. No. 74134). The quality of extracted total RNA was assessed by the 260/280 absorbance ratios and by RIN (RNA integrity number) measured using the Agilent BioAnalyzer System. The analysis was based on three biological replicates for each cell line. The 260/280 absorbance ratios varied between 2 and 2.1 and the RIN values between 9.4 and 10. All samples were assayed with the HumanHT-12 v4 Expression BeadChip (Illumina, Inc.) (Benjamini, 1995) and read on an iScan array reader (Illumina, Inc.). This microarray assays over 47,000 probes spanning approximately 30,000 genes. Sample intensities were determined and preliminary quality control analyses were performed with the GenomeStudio software (Illumina, Inc.). Probes with detection p-values less than 0.05 were kept for future analysis and annotated with human genome version hg19 of the

human genome. Gene expression comparisons between samples were calculated with Limma module of Bioconductor, using linear models and Bayes methods to assess differential expression. Genes were considered to be significantly expressed if the associated p-value was less than 0.05 and Log₂-based expression change was greater than 1.5 or less than -1.5. The *P*-values for gene expression changes were corrected for multiple tests using the Benjamini and Hochberg method.

Statistical Analysis.

Data are presented as mean \pm SEM. All statistical analyses were performed using SigmaPlot v.12. All data are from three independent experiments unless stated otherwise. Statistical significance of differences was evaluated with the Student's *t* test unless stated otherwise. Significance was accepted at the level of $p < 0.05$. * $p < 0.05$, ** $p < 0.01$, and *** $p < 0.001$ denote significant differences compared to control cells.

Acknowledgement

The authors would like to acknowledge valuable discussion with Dr. Hua Tan at the Center for Bioinformatics and Systems Biology at Wake Forest School of Medicine and support with metabolomics analysis by Drs. Wei Jia and Yunping Qiu at Center for Translational Biomedical Research at University of North Carolina at Greensboro. Research reported in this article was supported by the National Cancer Institute of the National Institutes of Health [R01 CA136810 (CMF), R01 U01 CA166886-03 (Zhou)]. The authors acknowledge financial support from Wake Forest School of Medicine (development funds to CMF) and the Wake Forest University Structural and Computational Biophysics training program [T32GM095440 (predoctoral fellowship to JM)]. This work was also partially supported by NSFC No.61373105 and No.61133010.

Author contributions

CF and AT designed and supervised the experimental studies. XZ supervised the computational work. JM collected the experimental data. XZ, ZJ, and JS designed the computational model. ZJ analyzed the experimental data, performed computational modeling work, and wrote the manuscript. CF, XZ, and ZJ edited the manuscript.

Conflict of interest

The authors declare that they no conflict of interest.

Literature Cited

Aitken A, Learmonth M (2002) Protein identification by in-gel digestion and mass spectrometric analysis. *Molecular biotechnology* **20**: 95-97

Anastasiou D, Poulogiannis G, Asara JM, Boxer MB, Jiang JK, Shen M, Bellinger G, Sasaki AT, Locasale JW, Auld DS, Thomas CJ, Vander Heiden MG, Cantley LC (2011) Inhibition of pyruvate kinase M2 by reactive oxygen species contributes to cellular antioxidant responses. *Science* **334**: 1278-1283

Anderson DD, Stover PJ (2009) SHMT1 and SHMT2 are functionally redundant in nuclear de novo thymidylate biosynthesis. *PloS one* **4**: e5839

Bansal N, Mims J, Kuremsky JG, Olex AL, Zhao W, Yin L, Wani R, Qian J, Center B, Marrs GS, Porosnicu M, Fetrow JS, Tsang AW, Furdul C (2014) Broad Phenotypic Changes Associated with Gain of Radiation Resistance in HNSCC. *Antioxid Redox Signal* **21**(2):221-36

Bendall SC, Hughes C, Stewart MH, Doble B, Bhatia M, Lajoie GA (2008) Prevention of amino acid conversion in SILAC experiments with embryonic stem cells. *Molecular & cellular proteomics : MCP* **7**: 1587-1597

Benjamini Y and Hochberg Y. (1995) Controlling the false discovery rate – a practical and powerful approach to multiple testing. *J Roy Stat Soc B Met.* **57**:289-300.

Bensaad K, Vousden KH (2007) p53: new roles in metabolism. *Trends in cell biology* **17**: 286-291

Bielitza M, Belorgey D, Ehrhardt K, Johann L, Lanfranchi DA, Gallo V, Schwarzer E, Mohring F, Jortzik E, Williams DL et al (2015) Antimalarial NADPH-consuming redox-cyclers as superior glucose-6-phosphate dehydrogease deficiency copycats. *Antioxid Redox Signal* **22**(15):1337-51

Cano KE, Li YJ, Chen Y (2010) NMR metabolomic profiling reveals new roles of SUMOylation in DNA damage response. *J Proteome Res* **9**: 5382-5388

Cheema AK, Timofeeva O, Varghese R, Dimtchev A, Shiekh K, Shulaev V, Suy S, Collins S, Resson H, Jung M, Dritschilo A (2011) Integrated analysis of ATM mediated gene and protein expression impacting cellular metabolism. *J Proteome Res* **10**: 2651-2657

- De Carvalho TG, De Carvalho AC, Maia DC, Ogawa JK, Carvalho AL, Vettore AL** (2013) Search for mutations in signaling pathways in head and neck squamous cell carcinoma. *Oncology reports* **30**: 334-340
- Devarie-Baez NO, Silva Lopez EI, Furdui CM.** (2016) Biological chemistry and functionality of protein sulfenic acids and related thiol modifications. *Free Radic Res.* **50**(2): 172-94
- Dimmer EC, Huntley RP, Alam-Faruque Y, Sawford T, O'Donovan C, Martin MJ, Bely B, Browne P, Mun Chan W, Eberhardt R, et al** (2012) The UniProt-GO Annotation database in 2011. *Nucleic acids research* **40**: D565-570
- Ebrahim A, Lerman JA, Palsson BO, Hyduke DR** (2013) COBRApy: COstraints-based reconstruction and analysis for python. *BMC Syst Biol.* **7**:74
- Farshadpour F, Roepman P, Hordijk GJ, Koole R, Slootweg PJ** (2012) A gene expression profile for non-smoking and non-drinking patients with head and neck cancer. *Oral diseases* **18**: 178-183
- Feng X, Sun T, Bei Y, Ding S, Zheng W, Lu Y, Shen P** (2013) S-nitrosylation of ERK inhibits ERK phosphorylation and induces apoptosis. *Scientific reports* **3**: 1814
- Filipp FV** (2013) Cancer metabolism meets systems biology: Pyruvate kinase isoform PKM2 is a metabolic master regulator. *Journal of carcinogenesis* **12**: 14
- Gamesik MP, Kasibhatla MS, Teeter SD, Colvin OM** (2012) Glutathione levels in human tumors. *Biomarkers* **17**(8): 671-691
- Garg SK, Yan Z, Vitvitsky V, Banerjee R.** (2010) Analysis of sulfur-containing metabolites involved in redox and methionine signaling. *Methods in Redox Signaling.* p. 7-11.
- Giannoni E, Buricchi F, Grimaldi G, Parri M, Cialdai F, Taddei ML, Raugei G, Ramponi G, Chiarugi P** (2008) Redox regulation of anoikis: reactive oxygen species as essential mediators of cell survival. *Cell Death Differ* **15**: 867-878
- Goldberg RN, Tewari YB, Bhat TN** (2004) Thermodynamics of enzyme-catalyzed reactions - a database for quantitative biochemistry. *Bioinformatics* **20**: 2874-2877
- Guo Z, Kozlov S, Lavin MF, Person MD, Paull TT** (2010) ATM activation by oxidative stress. *Science* **330**: 517-521

Harari PM and Huang S (2006) Radiation combined with EGFR signal inhibitors: head and neck cancer focus. *Semin Radiat Oncol* **16**:34-44

Hardie DG, Alessi DR (2013) LKB1 and AMPK and the cancer-metabolism link - ten years after. *BMC biology* **11**: 36

Hitosugi T, Kang S, Vander Heiden MG, Chung TW, Elf S, Lythgoe K, Dong S, Lonial S, Wang X, Chen GZ et al (2009) Tyrosine phosphorylation inhibits PKM2 to promote the Warburg effect and tumor growth. *Science signaling* **2**: ra73

Hoppe A, Hoffmann S, Holzhutter HG (2007) Including metabolite concentrations into flux balance analysis: Thermodynamic realizability as a constraint on flux distributions in metabolic networks. *Bmc Syst Biol* **1**

Israelsen WJ, Dayton TL, Davidson SM, Fiske BP, Hosios AM, Bellinger G, Li J, Yu Y, Sasaki M, Horner JW et al (2013) PKM2 isoform-specific deletion reveals a differential requirement for pyruvate kinase in tumor cells. *Cell* **155**: 397-409

Ji Z, Wu D, Zhao W, Peng H, Zhao S, Huang D, Zhou X (2015). Systemic modeling myeloma-osteoclast interactions under normoxic/hypoxic condition using a novel computational approach. *Sci Rep.* **5**:13291

Kitchen RR, Sabine VS, Sims AH, Macaskill EJ, Renshaw L, Thomas JS, van Hemert JI, Dixon JM and Bartlett JM (2010) Correcting for intra-experiment variation in Illumina BeadChip data is necessary to generate robust gene-expression profiles. *BMC Genomics.* **11**: 134

Komarova NL, Wodarz D (2010) ODE models for oncolytic virus dynamics. *Journal of theoretical biology* **263**: 530-543

Kotera M, Hirakawa M, Tokimatsu T, Goto S, Kanehisa M (2012) The KEGG databases and tools facilitating omics analysis: latest developments involving human diseases and pharmaceuticals. *Methods in molecular biology* **802**: 19-39

Lee EK, Fox T, Crocker I (2000) Optimization of radiosurgery treatment planning via mixed integer programming. *Medical physics* **27**: 995-1004

Liang Y, Liu J, Feng Z (2013) The regulation of cellular metabolism by tumor suppressor p53. *Cell & bioscience* **3**: 9

Liu J and Lin A (2005) Role of JNK activation in apoptosis: A double-edged sword. *Cell Research* **15**

Lou YW, Chen YY, Hsu SF, Chen RK, Lee CL, Khoo KH, Tonks NK, Meng TC (2008) Redox regulation of the protein tyrosine phosphatase PTP1B in cancer cells. *The FEBS journal* **275**: 69-88

Lu T, Liang H, Li H, Wu H (2011) High Dimensional ODEs Coupled with Mixed-Effects Modeling Techniques for Dynamic Gene Regulatory Network Identification. *Journal of the American Statistical Association* **106**: 1242-1258

Mardinoglu A, Agren R, Kampf C, Asplund A, Uhlen M and Nielsen J (2014) Genome-scale metabolic modelling of hepatocytes reveals serine deficiency in patients with non-alcoholic fatty liver disease. *Nat Commun.* **5**:3083

Mims J, Bansal N, Bharadqaj MS, Chen X, Molina AJ, Tsang AW, and Furdul CM (2015) Energy metabolism in a matched model of radiation resistance for head and neck squamous cell cancer. *Radiat Res* **183**(3):291-304

Mitsos A, Melas IN, Siminelakis P, Chairakaki AD, Saez-Rodriguez J, Alexopoulos LG (2009) Identifying Drug Effects via Pathway Alterations using an Integer Linear Programming Optimization Formulation on Phosphoproteomic Data. *Plos Comput Biol* **5**

Mougiakakos D, Okita R, Ando T, Durr C, Gadiot J, Ichikawa J, Zeiser R, Blank C, Johansson CC, Kiessling R (2012) High expression of GCLC is associated with malignant melanoma of low oxidative phenotype and predicts a better prognosis. *J Mol Med* **90**: 935-944

Ng Y, Ramm G, Lopez JA, James DE (2008) Rapid activation of Akt2 is sufficient to stimulate GLUT4 translocation in 3T3-L1 adipocytes. *Cell Metab* **7**: 348-356

Nollenburg M, Wolff A (2010) Drawing and Labeling High-Quality Metro Maps by Mixed-Integer Programming. *IEEE transactions on visualization and computer graphics*

O'Donovan C, Apweiler R (2011) A guide to UniProt for protein scientists. *Methods in molecular biology* **694**: 25-35

Oh SY, Park SK, Kim JW, Ahn YH, Park SW, Kim KS (2003) Acetyl-CoA carboxylase beta gene is regulated by sterol regulatory element-binding protein-1 in liver. *The Journal of biological chemistry* **278**: 28410-28417

Orth JD, Thiele I, Palsson BO (2010) What is flux balance analysis? *Nat Biotechnol* **28**: 245-248

Pace NJ, Weerapana E (2013) Diverse functional roles of reactive cysteines. *ACS chemical biology* **8**: 283-296

Papaconstantinou J (2009) Insulin/IGF-1 and ROS signaling pathway cross-talk in aging and longevity determination. *Mol Cell Endocrinol* **299**

Paulsen CE1 TT, Garcia FJ, Homann A, Gupta V, Leonard SE, Carroll KS (2011) Peroxide-dependent sulfenylation of the EGFR catalytic site enhances kinase activity. *Nat Chem Biol* **8**

Poole TH, Reisz JA, Zhao W, Poole LB, Furdui CM, King SB (2014) Strained cycloalkynes as new protein sulfenic acid traps. *Journal of the American Chemical Society* **136**: 6167-6170

Psyrrri A, Seiwert TY, Jimeno A (2013) Molecular pathways in head and neck cancer: EGFR, PI3K, and more. *American Society of Clinical Oncology educational book / ASCO American Society of Clinical Oncology Meeting*: 246-255

Qian J, Klomsiri C, Wright MW, King SB, Tsang AW, Poole LB, Furdui CM. (2011) Simple synthesis of 1,3-cyclopentanedione derived probes for labeling sulfenic acid proteins. *Chem Commun (Camb)*. 47(32):9203-5

Reisz JA, Bansal N, Qian J, Zhao W, Furdui CM (2014) Effects of Ionizing Radiation on Biological Molecules-Mechanisms of Damage and Emerging Methods of Detection. *Antioxid Redox Signal*. **21**(2):260-92

Rhee SG (2006) Cell signaling. H₂O₂, a necessary evil for cell signaling. *Science* **312**: 1882-1883

Schellenberger J, Park JO, Conrad TM, Palsson BO (2010) BiGG: a Biochemical Genetic and Genomic knowledgebase of large scale metabolic reconstructions. *BMC bioinformatics* **11**: 213

Shackelford DB, Shaw RJ (2009) The LKB1-AMPK pathway: metabolism and growth control in tumour suppression. *Nature Reviews Cancer* **9**: 563-575

Shao H, Peng T, Ji Z, Su J, Zhou X (2013). Systematically studying kinase inhibitor induced signaling network signatures by integrating both therapeutic and side effects. *PloS one* **8** (12), e80832

Shi X, Miller JS, Harper LJ, Poole RL, Gould TJ, Unterwald EM (2014) Reactivation of cocaine reward memory engages the Akt/GSK3/mTOR signaling pathway and can be disrupted by GSK3 inhibition. *Psychopharmacology (Berl)*. **231**(16):3109-18

Singh A, Singh H (1982) Time-scale and nature of radiation-biological damage: approaches to radiation protection and post-irradiation therapy. *Progress in biophysics and molecular biology* **39**: 69-107

Tepper N, Noor E, Amador-Noguez D, Haraldsdottir HS, Milo R, Rabinowitz J, Liebermeister W, Shlomi T (2013) Steady-State Metabolite Concentrations Reflect a Balance between Maximizing Enzyme Efficiency and Minimizing Total Metabolite Load. *PloS one* **8**

Toyozumi Y, Arima N, Izumaru S, Kato S, Morimatsu M, Nakashima T (2004) Loss of caspase-8 activation pathway is a possible mechanism for CDDP resistance in human laryngeal squamous cell carcinoma, HEP-2 cells. *Int J Oncol*. **25**: 721-728

Uhlen M, Fagerberg L, Hallstrom BM, Lindskog C, OKsvold P, Mardinoglu A, Sivertsson A, Kampf C, Sjostedt E, Asplund A, et al (2015) Proteomics. Tissue-based map of the human proteome. *Science*. **347**(6220):1260419

Varghese RS, Cheema A, Cheema P, Bourbeau M, Tuli L, Zhou B, Jung M, Dritschilo A, Ressom HW (2010) Analysis of LC-MS data for characterizing the metabolic changes in response to radiation. *J Proteome Res* **9**: 2786-2793

Vatner RE, Cooper BT, Vanpouille-Box C, Demaria S, Formenti SC (2014) Combinations of immunotherapy and radiation in cancer therapy. *Frontiers in oncology* **4**: 325

Vitvitsky V and Banerjee R (2015) H₂S analysis in biological samples using gas chromatography with sulfur chemiluminescence detection. *Methods in Enzymology*. **554**:111-123

Wani R, Qian J, Yin L, Bechtold E, King SB, Poole LB, Paek E, Tsang AW, Furdui CM (2011) Isoform-specific regulation of Akt by PDGF-induced reactive oxygen species. *PNAS USA* **108**: 10550-10555

Werbos L, Kozma R, Silva-Lugo R, Pazienza GE, Werbos PJ (2012) Metamodeling and the Critic-based approach to multi-level optimization. *Neural networks : the official journal of the International Neural Network Society* **32**: 179-185

Wichmann G, Rosolowski M, Krohn K, Kreuz M, Boehm A, Reiche A, Scharrer U, Halamma D, Bertolini J, Bauer U et al (2015) The role of HPV RNA transcription, immune response-related gene expression and disruptive TP53 mutations in diagnostic and prognostic profiling of head and neck cancer. *Int J Cancer* **132**(12): 2846-57

Wishart DS, Tzur D, Knox C, Eisner R, Guo AC, Young N, Cheng D, Jewell K, Arndt D, Sawhney S et al (2007) HMDB: the Human Metabolome Database. *Nucleic acids research* **35**: D521-526

Wu D and Pan W (2010) GSK3: a multifaceted kinase in Wnt signaling. *Trends Biochem Sci.* **35**(2): 161-168

Yan D, Avtanski D, Saxena NK, Sharma D (2012) Leptin-induced epithelial-mesenchymal transition in breast cancer cells requires beta-catenin activation via Akt/GSK3- and MTA1/Wnt1 protein-dependent pathways. *The Journal of biological chemistry* **287**: 8598-8612

Yang W, Zheng Y, Xia Y, Ji H, Chen X, Guo F, Lyssiotis CA, Aldape K, Cantley LC, Lu Z (2012) ERK1/2-dependent phosphorylation and nuclear translocation of PKM2 promotes the Warburg effect. *Nature cell biology* **14**: 1295-1304

Z Ji, J Su, C Liu, H Wang, D Huang, X Zhou (2014). Integrating genomics and proteomics data to predict drug effects using binary linear programming. *PloS one* **9** (7), e102798.

CHAPTER 5 – ADDITIONAL STUDIES

Investigation of Lipid Raft Signaling through Proteomics Analysis

Background: Lipid rafts are stable, detergent-resistant sphingolipid and cholesterol-enriched microdomains with signaling function in cancer cells (Pike 2003). They are believed to directly impact signaling pathways and modulate response to combination therapies in various cancers by compartmentalizing and recruiting specific signaling proteins. Major findings thus far including our data presented in Chapters 2 and 4 have shown that lipid rafts play a role in modulating redox signaling but also, redox molecules can alter or regulate lipid raft formation. For example, studies completed in breast cancer cells showed lipid raft formation can activate NOX isoforms (Raghu 2010), a major source of O_2^- in the membrane (Li 2007). Taken together, these results suggest ROS and lipid raft signaling platforms constitute a cyclic regulation resulting in amplification of signals in different biological membranes ensuring efficient signal transduction. However, the mechanisms and molecular factors determining protein targeting to rafts, physiological functions of rafts, and trafficking and signaling within rafts are not well understood. Unfortunately, direct characterization of rafts has been difficult because they cannot be isolated in pure form. We used quantitative high-resolution LC-MS/MS to specifically detect proteins in lipid rafts of SCC-61 cells and rSCC-61 cells. **Method:** *Raft Isolation-Triton X-100 Extraction:* SCC-61 cells and rSCC-61 cells were grown on 2-15 cm culture plates, washed with cold PBS 3X and scraped into ice-cold PBS followed by centrifugation at 1000 x g for 10 min at 4 °C. The cell pellets were resuspended in 1 ml of ice-cold MES lysis buffer with Triton X-100 (TMBS) lysis buffer, vortexed for 15 s on ice and allowed to sit on ice for 10 min for two repetitions. The pellets were then centrifuged at 1000 x g for 10 min at 4 °C to remove high density insoluble debris. Finally, the supernatant was mixed with an equal volume of 80% sucrose in MBS (25 mM MES, 150 mM NaCl) and mixed by gentle vortexing before loading samples on a 5-30% continuous sucrose gradient and ultracentrifuge at 37,000 rpm for 24 h at 4 °C using an SW41 rotor. Following

centrifugation, 12 x 1 mL fractions were harvested from top to bottom and protein concentrations were determined prior to Western blot analysis to identify the fractions enriched in flotillin-1, a lipid raft marker (**Fig. 1A**). *Proteomics analysis*: The lysates were resolved on 12% SDS-PAGE and stained with Coomassie Brilliant Blue (R-250). The entire lane was divided into 10 gel bands, which were then digested with trypsin following standard in-gel digestion protocols. The resulting tryptic peptides were analyzed on a nanoLC system as described in Chapter 2, *Methods*. The raw MS files were analyzed by Proteome Discoverer 1.2 software (Thermo Fisher Scientific) using MASCOT search engine and the UniProtKB human database. The results were filtered using a false discovery rate of 1%. IPA software (www.ingenuity.com) was used to identify significantly over-represented pathways and cellular functions in SCC-61 cells and rSCC-61 cells. **Results**: We detected a large portion of proteins representing glycolysis, cholesterol metabolism, and Wnt/ β -catenin signaling, as significantly associated with lipid rafts in rSCC-61 cells compared to SCC-61 cells (**Fig. 1B**). These signaling pathways were highlighted in Chapter 4 as critical to maintaining redox homeostasis and cell survival in radiation resistant cells. More importantly, redox signaling protein EEF2 discussed in Chapter 4 and phosphofructokinase 1 (PFK), a rate-limiting enzyme in glycolysis, were found in lipid rafts of both, SCC-61 cells and rSCC-61 cells. As the majority of glycolytic intermediates are fluxed through the PPP in rSCC-61, it is possible lipid raft sequestering of PFK in rSCC-61 cells inhibits the protein. Also, critical one carbon metabolism protein, SHMT2, which was significantly upregulated in rSCC-61 cells, was found exclusively in rSCC-61 lipid rafts suggesting lipid rafts association may play a role in either activating or inhibiting the activity of this protein (**Fig. 1C**). These preliminary data demonstrate potential regulation of key radiation response pathways by physical assembly in lipid rafts.

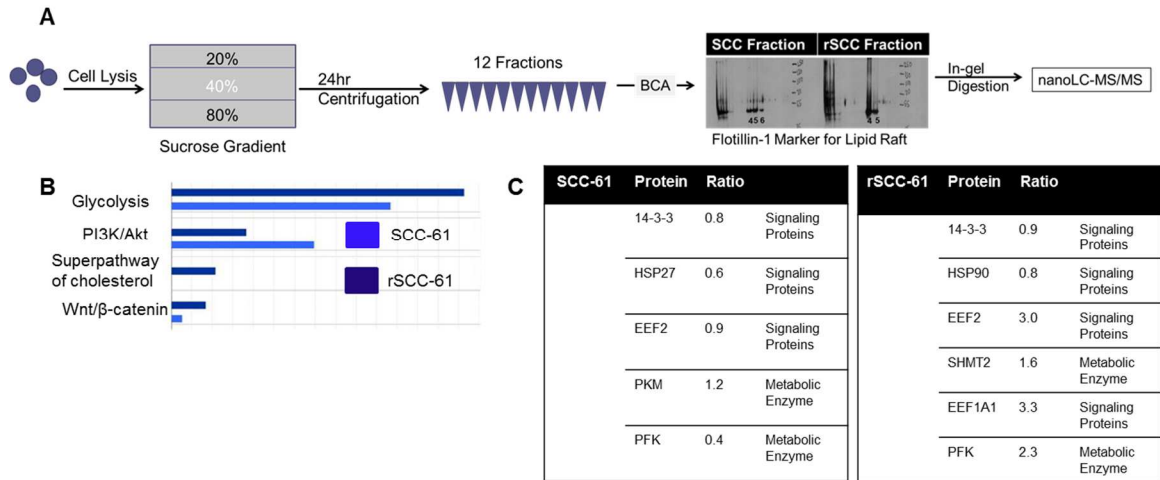


Figure 1 – Identifying lipid raft proteins. **A.** Lipid raft isolation and analysis by LC-MS/MS workflow. **B.** Ingenuity Pathway Analysis identifying four major pathways including glycolysis, super pathway of cholesterol and Wnt/β-catenin have more lipid raft proteins in rSCC-61 cells compared to SCC-61 cells while P3K/AKT pathway has less proteins targeted to lipid rafts. **C.** Significant proteins identified between lipid rafts in SCC-61 cells and rSCC-61 cells. HSP27 = heat shock protein 27; EEF2 = eukaryotic elongation factor 2; PKM = pyruvate kinase; PFK = phosphofructokinase 1; HSP90 = heat shock protein 90; SHMT2 = serine hydroxymethyltransferase 2; EEF1A1 = eukaryotic translation elongation factor 1 alpha 1;

Lipid Raft Modulation in other Radioresistant Head and Neck Cell Lines

Background: The studies presented in Chapters 2 and 4 have shown distinct lipid raft characteristics in SCC-61 and rSCC-61 HNSCC cells. The reduction of lipid rafts in rSCC-61 cells may be due to increased damage to the lipid bilayer during repeated insults with IR or cell survival adaptive mechanisms. The role of lipid rafts in cancer cells is still not well understood and whether or not this phenomena is critical or found in other HNSCC radiation resistant cell lines has yet to be determined. The preliminary data presented here sought to better characterize radiation resistant lipid raft content in several other HNSCC radiation resistant cell lines including SCC-4, SCC-9 and SQ20B. **Method:** *MTT Assay.* SCC-4, SCC-9 and SQ-20B cells were trypsinized, resuspended in complete medium, and seeded in 24-well plates at a density of 50,000/well in 1 mL. After overnight incubation at 37 °C, each plate was subjected to radiation with different doses (0 – 8 Gy) and allowed to incubate for further 72 h. After incubation 125 µl MTT (5 mg/ml in PBS) was added to each well, and the plates were further incubated for 4 h at 37 °C. At the end of the incubation, 0.5 ml solubilization solution was added to each well, and the absorbance was recorded at 570 nm. *Immunostaining of lipid rafts.* SCC-4, SCC-9 and SQ-20B cells were seeded in 1 ml microtek chambers at a density of 2×10^4 cells/ml and incubated overnight at 37 °C and 5% CO₂. After overnight incubation, cells were incubated with 1 µg/ml of AlexaFluor594 conjugated CT-B for 15 min at 4 °C before cell fixation. Cells were fixed in 4% paraformaldehyde for 15 min and permeabilized with 0.1 TritonX-100, washed, and mounted using Fluoromount (Sigma) for imaging. Imaging was performed using a Zeiss LSM710 confocal microscope and a 40X objective. The images were processed using the LSM image browser. **Results:** We found lipid raft content is directly correlated with levels of radiation resistance in the three cell lines. In **Figure 2A**, MTT assay, which is consistent with previously published MTT and clonogenic data in literature (Aravindan 2013, Bionda 2007), shows different levels of radiation resistance between the three cell lines with SQ-20B < SCC-9 < SCC-4 being the most

resistant. SQ-20B is the most sensitive to radiation in this series though it is still considered a radiation resistant cell line. SQ-20B has the most lipid raft formation compared to SCC-9 and SCC-4, which are more resistant to radiation and have lower levels of lipid rafts (**Figure 2B**). Taken together, radiation resistance and lipid raft content are directly correlated and can potentially be used to predict response to radiation. Future studies should explore the levels of ROS between the cell lines and other molecular signatures including increased GSH/GSSG and the role of PPP and 1-C metabolism in supporting NADPH/NADP⁺ levels. Better understanding the transient state of lipid rafts and their role in radioresistance would greatly improve knowledge around response to radiation in HNSCC.

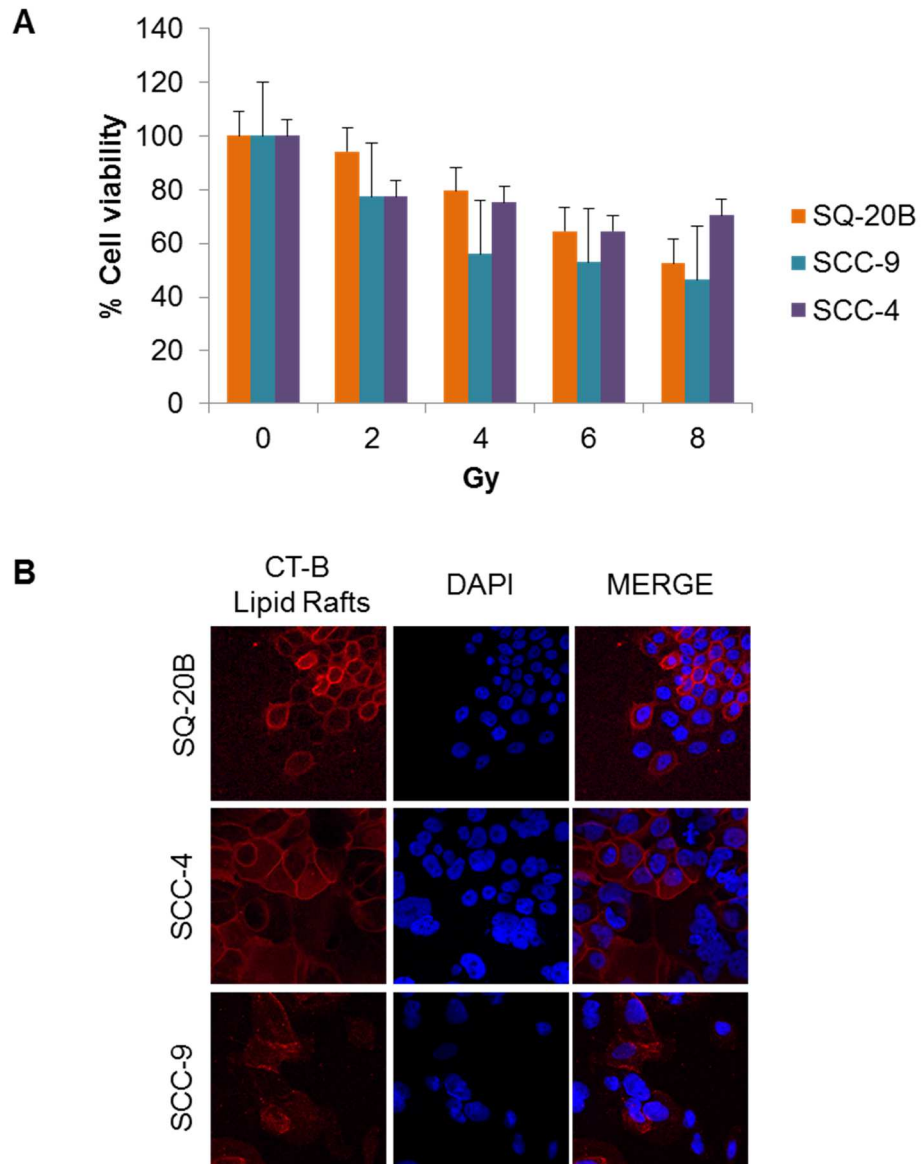


Figure 2 – Lipid Raft Formation and Response to Irradiation. A. MTT assay of SCC-4, SCC-9 and SQ-20B. **B.** CT-B staining of SCC-4, SCC-9 and SQ-20B showing increased lipid raft formation in SQ-20B compared to the more radioresistant SCC-4 and SCC-9.

Mitochondrial Reactive Oxygen Species Cycling

Background: Mitochondria house numerous biosynthetic pathways, facilitate energy production through the ETC and regulate cell death. More recently, production of ROS by mitochondria has garnered more attention because it contributes to retrograde redox signaling and underlies oxidative damage in many disease pathologies. ROS generated in the mitochondria is a tightly regulated process that when deregulated has the potential to cause mitochondrial damage as well as play a role in intracellular signaling. Mitochondrial antioxidant proteins (i.e. PRX3, MnSOD) can reduce cellular ROS levels following exposure to IR thereby protecting cancer cells from ROS mediated apoptosis (Clement 1999). As discussed in Chapter 3, rSCC-61 cells have decreased OXPHOS activity and decreased mitochondrial ROS levels suggesting this is a potential mechanism cells have adapted to resist apoptotic cell death. While high levels of ROS can be detrimental, small ROS exposures induce a pro-oxidant state resulting in oxidative inactivation of caspases at the catalytic cysteine residues, rendering them ineffective and cells resistant to apoptotic triggers (Pervaiz 1999). In the preliminary studies included here, we investigated whether increasing mitochondrial ROS with a series of Mn-porphyrin compounds would alter lipid raft formation and change radiation response phenotype in SCC-61 and rSCC-61 cells. **Method:** *Clonogenic assay.* SCC-61 cells and rSCC-61 cells were trypsinized, resuspended in complete medium, and plated into the six-well culture dishes at a low density. After 4 h of incubation at 37 °C, each 6-well plate was treated with 10 µM MnTE, MnTnBuOE, MnTnHex, or MnTnHex for 24 h followed by 4 Gy irradiation and allowed to incubate for further 14 days for the colony formation. Once formed, the colonies were fixed in methanol and acetic acid (7:1) solution and stained with 0.5% crystal violet. The colonies containing more than 50 cells were counted. The surviving fraction of the radiated cells was normalized using the plating efficiencies of their corresponding untreated control. The data were fitted to the multi-target and linear-quadratic formulae, where survival (S) was related to dose (D) by the expression $S = 1 - (1 - e^{-D/D_0})^N$ and $S = e^{-\alpha D - \beta D^2}$ using Sigma Plot v.12 software. The survival curves were obtained, and

the radiation-sensitivity parameters were calculated according to the published methods (12, 20).

Immunostaining of lipid rafts. SCC-61 cells and rSCC-61 cells were seeded in 1 ml microtek chambers at a density of 2×10^4 cells/ml and incubated overnight at 37 °C and 5% CO₂. After overnight incubation, SCC-61 cells were treated with 10 μM MitoQ and rSCC-61 cells were treated with 50 μM MitoPQ and incubated for 24 h (Kelso 2001). After treatment, cells were incubated with 1 μg/ml of AlexaFluor594 conjugated CT-B for 15 min at 4 °C before cell fixation. Cells were fixed in 4% paraformaldehyde for 15 min and permeabilized with 0.1 TritonX-100, washed, and mounted using Fluoromount (Sigma) for imaging. Imaging was performed using a Zeiss LSM710 confocal microscope and a 40X objective. The images were processed using the LSM image browser. **Results:** SCC-61 cells and rSCC-61 cells were treated with Mn-porphyrins, which mimic kinetics and thermodynamics of the catalysis of superoxide dismutation by SOD enzymes (Moeller 2005). This causes perturbation of the cellular redox environment. As shown in **Figure 3A**, treatment alone with either compound in both, SCC-61 cells or rSCC-61 cells resulted in 25–50% decrease in cell viability. Treatment with the Mn-porphyrin compound in combination with irradiation significantly inhibited cell survival in rSCC-61 cells more than in SCC-61 cells. These preliminary data support the data presented in Chapter 3 showing decreased OXPHOS activity to reduce superoxide and total ROS in rSCC-61 cells is critical to maintain cell survival and proliferation. While antioxidants are increased in rSCC-61 cells, there is a critical threshold that when overcome leads to significant cell death. It provides evidence that a redox cyler can perturb the redox environment in rSCC-61 cells and should be further explored as potential radiosensitizers in HNSCC treatment. **Figure 3B** further supports the trend that increasing cytosolic ROS as shown in Chapter 4 or mitochondrial ROS with MitoPQ in rSCC-61 cells leads to increased lipid raft formation. This data taken with proteomic investigation of lipid rafts necessitates exploration into how ROS triggers lipid raft formation and what signaling pathways are activated or inhibited when lipid rafts are formed.

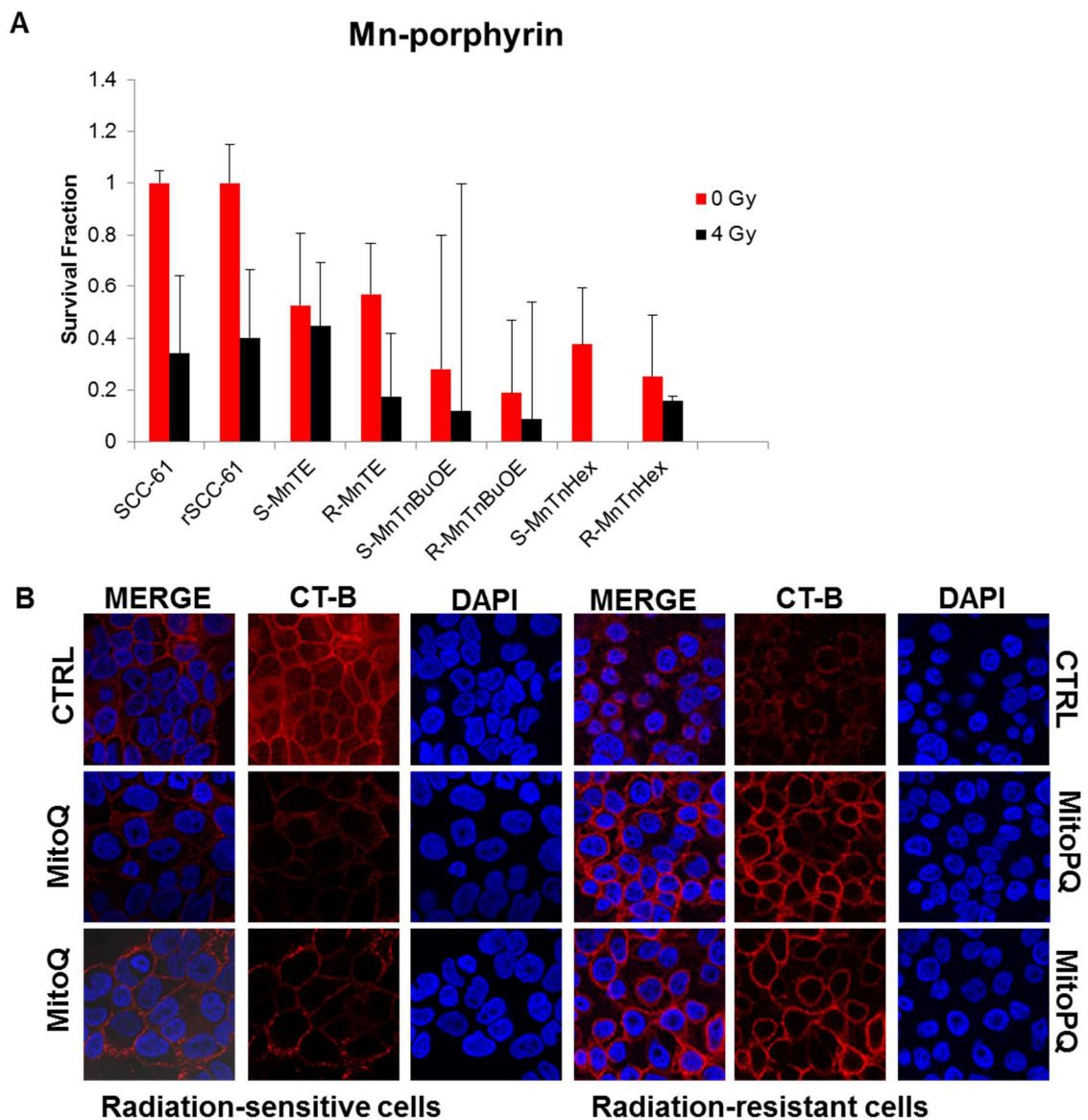


Figure 3 – Mitochondrial ROS Cycling **A.** Clonogenic assays of SCC-61 cells and rSCC-61 cells treated with MnTE, MnTnBuOE, MnTnHex in the absence and presence of 4 Gy radiation. **B.** Lipid raft stain of SCC-61 cells and rSCC-61 cells after treatment with either 10 μ M MitoQ or 50 μ M MitoPQ.

Literature Cited

Aravindan N, Aravindan S, Heramn TS, and Natarajan M. EGFR tyrosine kinase inhibitor pelitinib regulates radiation-induced p65-dependent telomerase activation in squamous cell carcinoma. *Radiat Res.* 179:304-312, 2013.

Bionda C, Hadchity E, Alphonse G, Chapet O, Rousson R, Rodriguez-Lafrasse C, and Ardail C. Radioresistance of human carcinoma cells is correlated to a defect in raft membrane clustering. *Free Radic Biol Med.* 43(5):681-94, 2007.

Clement MV and Pervaiz S. Reactive oxygen intermediates regulate cellular response to apoptotic stimuli: an hypothesis. *Free Radical Research,* 30(4): p. 247-52, 1999.

Kelso GF, Porteous CM, Coulter CV, Hughes G, Porteous WK, Ldegerwood EC, Smith RAJ, and Murphy MP. Selective targeting of a redox-active ubiquinone to mitochondria within cells. *J Biol Chem,* 276(7):4588-4596, 2001.

Li PL, Zhang Y, and Yi F. Lipid raft redox signaling platforms in endothelial dysfunction. *Antioxidants & Redox Signaling,* 9(9): p. 1457-70, 2007.

Moeller BJ, Batinic-Haberle I, Spasojevic I, Rabbani ZN, Anscher MS, Vujaskovic Z, and Dewhirst MW. A manganese porphyrin superoxide dismutase mimetic enhances tumor radioresponsiveness. *Int J Radiation Oncol Biol Phys,* 63(2): 545-552, 2005.

Pervaiz , Ramalingam JK, Hirpara JL and Clement MV. Superoxide anion inhibits drug-induced tumor cell death. *FEBS letters,* 459(3): p. 343-8, 1999.

Pike LJ. Lipid rafts: bringing order to chaos. *J Lipid Res.* 44:655-667, 2003.

Raghu H, Sodadas PK, Malla RR, Gondi CS, Estes N and Rao JS. Localization of uPAR and MMP-9 in lipid rafts is critical for migration, invasion and angiogenesis in human breast cancer cells. *BMC Cancer,* 10: p. 647, 2010.

CHAPTER 6 – DISCUSSION

HNSCC is developed from multifactorial interactions between the environment and genetic mutations. These interactions play a critical role in development, disease staging and response to therapy. Most patients present with locally advanced disease and patients rely on a combination of treatment options including surgery, radiation and chemotherapy (Bar-Ad 2014, Bernier 2004, Haque 2006). The current standard of care is (1) non-selective, (2) can cause damage to normal tissue, and (3) lacks predictors of response. To decrease therapy-associated side effects and resistance to chemoradiation, research focus and treatment plans have shifted towards the use of targeted agents alone or in combination with surgery, radiation or chemotherapy. Despite advances in HNSCC tumor biology over the last two decades, disease management remains complicated and determining an optimal therapeutic approach seems elusive. The goal of the studies presented in this dissertation was to establish a clinically relevant *in vitro* model of radiation resistance that allowed us to (1) investigate the mechanisms contributing to radiation resistance and EGFR drug targeted therapy, (2) investigate how redox regulation of signaling and metabolic pathways regulate response to radiation and (3) identify new radiosensitizing targets and biomarkers to be used in clinic.

HNSCC matched model. The translational impact of preclinical HNSCC studies lags significantly. HNSCC is very heterogeneous, due to origin and etiological factors, making it difficult to reproduce characteristic features of the disease and model clinical symptoms *in vivo* or *in vitro*. Most *in vitro* studies investigate resistance to radiation in HNSCC using comparative analysis of cancer cell lines established from patients with distinct genetic background and complex treatment history (Lee 2008). A better understanding of how tumors become resistant to radiation can be achieved by investigating radiation resistance in a clonal population derived from a matched cell line. This approach enables characterization of distinct molecular and cellular features between parental and clonal population and investigation of molecular mechanisms underlying radiation resistance in tumors. Using this methodology, we were able to select a clonal

population of radiation resistant cells after applying successive rounds of clinically relevant 2 Gy dose of IR to HPV⁻ radiation sensitive SCC-61 cells and develop a matched radiation resistant cell line (rSCC-61). Using systems biology, combining SILAC proteomics and redox proteomics, metabolomics, lipidomics, computational modeling and complementary biological techniques, we demonstrated radiation resistant cells converge signaling and metabolic networks through redox mechanisms to elicit protection against IR. The initial characterization in Chapter 2 identified three distinct properties in rSCC-61 cells compared to SCC-61 cells including (1) rSCC-61 cells are significantly more resistant to radiation, (2) rSCC-61 cells are more responsive or sensitive to treatment with EGFR TKI Erlotinib compared to SCC-61 cells, and (3) rSCC-61 cells display an epithelial phenotype as evidenced by increased E-cadherin expression compared to SCC-61 cells mesenchymal phenotype suggesting a mesenchymal-to-epithelial transition (MET) occurs after treatment with irradiation. Additional studies eluded to three critical signatures/hallmarks of HPV⁻ radiation resistant cells including (1) altered EGFR signaling and sensitivity to EGFR drug targeted therapy, (2) dysregulated cellular metabolism (e.g. increased FASN and “glucose addiction”), and (3) improved redox buffering capacity (e.g. increased antioxidant) to ultimately increase repair of DNA damage and cell proliferation and survival.

EGFR Signaling. EGFR status and signaling plays an ongoing role in HNSCC tumor development and progression as well as response to therapeutics. Epithelial cells exposed to CS have increased ROS, specifically H₂O₂, causing non-canonical phosphorylation of EGFR resulting in impaired degradation and perinuclear trafficking to enhance downstream activation of Akt and Erk to increase cell survival and proliferation (Goldkorn 2010). This phenomenon leads to 90 and 40% of mRNA and protein overexpression of EGFR in HNSCC patients making EGFR a potential target to improve locally advanced HNSCC. Despite the overexpression of EGFR in HNSCC, only 10–15% of patients respond to EGFR inhibition (Bonner 2006).

The data presented here showed strikingly different expression profiles of EGFR and response to EGFR TKI, Erlotinib. Radiation resistant rSCC-61 cells had 50% decreased EGFR

phosphorylation resulting in (a) decreased phosphorylation of downstream signaling target, Akt, and (b) increased sensitivity to Erlotinib compared to SCC-61 cells. Important to note, redox status plays a significant role in differential regulation between Akt isoforms, discussed later. The decreased phosphorylation of Akt also led to ~50% reduction of GSK-3 β phosphorylation in rSCC-61 cells compared to SCC-61 cells. GSK-3 β is a critical regulator of innate inflammatory processes and radiation induced apoptosis. Thus attenuation of GSK-3 β in rSCC-61 cells suppresses the expression of NF- κ B mediated pro-inflammatory genes, such as NOX or IL-6, and provides protection against IR-induced death (Li 2013). Additionally, PTEN, a negative regulator of Akt expression, was increased in rSCC-61 cells further increasing Akt inhibition and increasing response to Erlotinib. It is important to note the increased ROS in SCC-61 cells potentially causes oxidation of PTEN Cys124 residue yielding the phosphatase inactive and resulting in unchecked activity of PI3K/Akt pathway which requires higher, more toxic doses of EGFR TKI to achieve inhibition. This suggests EGFR overexpression alone cannot be used to stratify patient response to EGFR TKIs and potentially mAbs. Further, it supports the necessity to identify combinatory panels of biomarkers to predict therapeutic response.

Our findings identified two potential biomarkers including patient cholesterol levels and tumor redox status to predict patient response to radiation and Erlotinib. We found lipid rafts, composed of sphingomyelin and cholesterol, play a significant role in response to radiation and Erlotinib. Lipid rafts are signaling hubs that can be triggered to coalesce by radiation-induced ROS and when present, increase sensitivity to radiation but decrease sensitivity to Erlotinib. However, when lipid rafts are absent or decreased, the tumor phenotype is decreased sensitivity to radiation but increased sensitivity to Erlotinib. Data presented in Chapters 2 and 4 indicates radiation resistant rSCC-61 cells have decreased ROS and cholesterol with increased sensitivity to Erlotinib compared to radiation sensitive SCC-61 cells which have increased ROS and cholesterol with decreased sensitivity to Erlotinib. Taken together, these data establish a reciprocal regulatory relationship between levels of ROS and cholesterol content and their ability

to alter lipid raft formation and response to radiation and Erlotinib. Patient metabolic state also influences tumor redox state and therapeutic response. Exposure to CS has many effects including (1) reducing high density lipoprotein (HDL) cholesterol leading to the storage of cholesterol by low density lipoproteins (LDL), (2) toxins from cigarettes increase oxidized LDL in the bloodstream triggering inflammation thereby increasing ROS, and (3) smoking affects lipid metabolism thus raising total cholesterol, triglycerides and LDL numbers (Steinberg 1997, Yamaguchi 2005). In general, individuals who smoke have an unhealthy lifestyle and diet, such as intake of high cholesterol fatty foods, making them more susceptible to development of head and neck tumor formation. A pilot study completed at Wake Forest Baptist Health by Dr. Porosnicu and colleagues demonstrated active smokers required twice the dose of Erlotinib to achieve the same effect as individuals not actively smoking (Porosnicu 2011). This increased dose of Erlotinib can be due to (1) increased ROS leading to lipid raft formation which embeds the EGFR making it difficult for the drug to access and (2) increased inflammatory environment due to exposure to CS and decreased intake of dietary antioxidants leads to oxidation of EGFR or Erlotinib itself yielding it less effective.

These clinical data taken with our *in vitro* data demonstrates dietary intake low in antioxidants, increased cholesterol levels and ROS work synergistically to decrease sensitivity to Erlotinib but increase response to radiation. Therefore, tumor and plasma redox state and cholesterol levels can be used to predict patient response to radiation and TKIs. In addition, studies have shown that patients with increased dietary antioxidant (e.g. Vitamin D, carotenoids) intake before radiotherapy have prolonged PFS (Davies 2011). More recently, studies have shown that whole saliva can also be used as a non-invasive diagnostic tool in assessing lipid profile levels as well (Singh 2014). Together, patient lipid profile and redox state can be used to predict patient response to, both, radiation and Erlotinib.

Energy metabolism A major hallmark of cancer development is the reprogramming of cancer cell metabolism to ensure a steady supply of metabolites for generation of biomass and energy

(Barger 2010, Hanahan 2000, Hanahan 2011, Wise 2008). The Warburg effect, which converts glucose to lactate instead of pyruvate under aerobic conditions to support OXPHOS, is considered an advantageous process that builds up glycolytic intermediates to support rapid biosynthesis (Vander Heiden 2009).

The data presented in Chapter 3 demonstrates radiation resistant rSCC-61 cells deviate from the classical Warburg phenotype. Proteomics data in Chapter 2 revealed increased lactate dehydrogenase-B, which converts lactate to pyruvate in rSCC-61 cells. Lactic acid assay also confirmed decreased intra- and extracellular lactate in rSCC-61 cells compared to SCC-61 cells leading to conversion of glucose to pyruvate rather than glucose to lactic acid. Energy metabolism study in Chapter 3 further confirmed rSCC-61 cells are indeed “glucose addicted” as evidenced by increased GLUT1 expression and membrane localization and significant decrease in cell viability after inhibition with 2-DG. However, the data demonstrated the majority of glycolytic intermediates in rSCC-61 cells are routed into the PPP rather than flux through ETC to support OXPHOS. The decreased flux through mitochondrial ETC in rSCC-61 cells is another redox defense mechanism to reduce endogenous sources of ROS, specifically O_2^{\bullet} , while still maintaining ATP production to defend against radiation-induced damage. The increased reliance on PPP pathway for NADPH production and ribonucleotides is evident by the tight regulation of glycolytic intermediates through two mechanisms including (1) inhibiting glycolysis by TIGAR which promotes flux through PPP, and (2) upregulating key enzymes in the oxidative and non-oxidative phases of the PPP (e.g. G6PD, PGD). The increased ratio of NADPH/NADP⁺ in rSCC-61 cells compared to SCC-61 cells and FBA, discussed in Chapter 4, further validated PPP contribution to NADPH production. FBA also highlighted, together the PPP (i.e. PGD, G6PD), 1-C metabolism (i.e. MTHFD2, DHFR1/2) and isocitrate dehydrogenase (i.e. IDH1/2) enzymes are responsible for contributing 80–90% of the cellular NADPH production in HNSCC cells. FBA findings further supported proteomics data in Chapter 2, which revealed 1-C metabolism

enzymes, cytosolic MTHFD1 and mitochondrial SHMT2, are increased 6.3- and 4.0-fold change in rSCC-61 cells compared to SCC-61 cells. This infers a critical contribution of 1-C metabolism to coordinate maintenance of cellular NADPH reserve in cytosolic and mitochondrial compartments. This evidence was further substantiated by both (1) western blot analysis showing increased MTHFD2 protein in rSCC-61 cells, and (2) through knockdown of MTHFD2, inhibition of DHFR1 with MTX and combinatory inhibition of DHFR1 and PPP with MTX and CB83 in MTHFD2 knockdown cells led to 70–90% decreased cell survival in rSCC-61 cells compared to SCC-61 cells. Flux through PPP and 1-C pathways is essential for maintaining NADPH reserves and NADPH levels are critical to maintain redox homeostasis in cells after exposure to radiation. NADPH provides the reducing equivalents necessary for the regeneration of GSH by GR and for activity of NADPH-dependent TRX system to protect cells from oxidative damage. Lack of reducing equivalents increases ROS in rSCC-61 cells resulting in irreparable DNA damage. It is also important to note HIF's can also be active in aerobic conditions and play a critical role in activation of glycolytic enzymes, such as G6PD, to promote PPP and reduce aerobic respiration.

These data point to PPP and 1-C metabolism enzymes as potential biomarkers to diagnose head and neck tumor stage and determine optimal therapeutic response. For example, in prostate cancer, G6PD activity is four times higher in whole-tissue homogenates compared to normal cells and G6PD enzyme activity correlates with prostate tumor clinical stage (Zampella 1982). The human protein atlas (HPA) shows strong cytoplasmic activity of G6PD in HNSCC suggesting it can also be used to determine clinical stage in HNSCC. Oral administration of [U-¹³C₃]-glycerol followed by high resolution ¹³C NMR analysis of blood metabolites has been shown to accurately track PPP activity and flux through the mitochondria (Jin 2016). Therefore, G6PD tissue staining and tracking metabolic flux data can be used to determine HNSCC tumor stage and predict response to therapeutics before and after treatment. Greater flux through the

PPP after radiation therapy would suggest increased resistance to radiation and can be used to determine necessary doses and schedule of treatment with targeted therapies and chemotherapy, such as CB83 and MTX, in combination with radiation.

Additionally cancer cells have demonstrated the capacity to use alternate oxidizable substrates, such as fatty acids, for generation of biomass and energy (Diers 2012, Pike 2011, Weinberg 2010). Fatty acids (FAs) are essential for membrane construction, energy production, palmitoylation of signaling proteins and antioxidants and can be synthesized endogenously by FASN in a NADPH-dependent manner or exogenously-derived from the diet. Under normal conditions, FASN converts excess carbohydrates into FAs that are esterified as triacylglycerol's, which can provide energy when necessary through β -oxidation. However, tumors undergo endogenous FA biosynthesis irrespective of levels of extracellular lipids which correlates with increased glycolysis to provide energy and precursors for FA synthesis (Menendez 2007). Proteomics data from Chapter 2 identified a 6.8-fold increase in FASN and Western blot data in Chapter 3 confirmed FASN is overexpressed at least 3-fold in rSCC-61 cells compared SCC-61 cells. Further analysis of fatty acid metabolism (uptake, biosynthesis and oxidation) demonstrated rSCC-61 cells rely almost exclusively on endogenous FAs over exogenous FAs for energy production compared to SCC-61 cells. Pharmacologic inhibition of FASN by Orlistat or siRNA knockdown of FASN significantly disrupted OXPHOS activity and ATP generation in rSCC-61 cells with little to no effect in SCC-61 cells. Mathematical modeling, described in Chapter 4, accurately predicted AMPK, a master regulator of metabolism, is downregulated in rSCC-61 cells leading to uninhibited SREBP1c activity, which stimulates *FASN* transcription. In hormone-sensitive cells and cells with high lipid metabolism, FASN overexpression and regulation is due to constitutively active growth factors such as EGFR (Kao 2012). However, in HNSCC, the molecular mechanism of survival advantage by FASN overexpression is complicated and not well established. An independent study have shown FASN overexpression (1) can cause resistance to

chemoradiation, (2) is involved in lipid raft assembly and colocalization of EGFR with lipid rafts and (3) can inhibit p21 and BAX which inhibits DNA damage-induced apoptosis (Kao 2012). Based on our studies presented here and studies in liver and ovarian cancer (Bhattacharyya 2013, Modis 2014, Szabo 2013), there is a link between to FASN overexpression and enhanced cell proliferation, decreased apoptosis, and chemoradiation resistance that warrants further investigation.

AMPK also regulates SREBP2 which controls cholesterol metabolism. Our data showing increased AMPK activity and increased squalene and squalene synthase in rSCC-61 cells but decreased cholesterol is contradictory to the established paradigm in the literature. However, our mRNA data supports decreased *SREBP2* expression and decreased expression of its target genes (e.g. LDLR, HMGCR) in rSCC-61 cells compared to SCC-61 cells. While the rate of cholesterol influx and efflux is lower in rSCC-61 cells, it is possibly due to the fact there is less cholesterol to traffic. This data and the correlation between cholesterol content and ROS suggest *SREBP2* trafficking or post-translational modifications may be redox regulated resulting in downregulation of *SREBP2* activity and its target genes in radioresistant cells. For example, a study showed reversible sumoylation of lysine residue 464 in SREBP2 controls transcriptional activities of nuclear SREBP2 irrespective of sterol levels (Hirano 2003). It is also important to note squalene has antioxidant properties and may play a role in protecting cellular membranes from oxidative stress, cellular and systemic radioprotection (Goldstein 1982). It is also possible rSCC-61 cells are converting farnesyl pyrophosphate, substrate for squalene synthase, to produce farnesylated (i.e. Ras) and geranylgeranylated (i.e. Rho, Rab, Rac) proteins. Farnesyl and geranylgeranyl are isoprenoid groups that are attached post-translationally to proteins resulting in a thioether linkage between the isoprenoid and a cysteine residue at or near the C-terminus of the protein. Prenylation enhances interaction of the modified protein with the endoplasmic reticulum where further modifications can occur to aid in protein binding to membranes and induce cell

transformation. Farnesyl transferase inhibitors (FTIs) have been explored as anticancer agents, however, geranylgeranylation can substitute for farnesylation making FTIs ineffective (Brunner 2003). Further investigation into the regulation of cholesterol biosynthesis and its contribution to lipid raft formation is necessary to explore potential drug targets in the future.

Redox metabolism. Physiological levels of ROS are maintained by the cellular antioxidant system below the threshold at which DNA damage can occur while still enabling temporal and localized accumulation of these species when necessary for signaling. Radiation resistant rSCC-61 cells have altered signaling and metabolic pathways to (1) reduce contributors of endogenous ROS (e.g. decreased ETC and NOX activation in lipid rafts) and (2) increase metabolites (i.e. NADPH reserve) and enzymes (i.e. GSH, PRX) to survive insult from exogenous ROS and oxidative stress. These efforts require complex coordination between redox metabolism and cellular signaling and metabolic pathways. Under normal conditions, when ROS increases, cellular transcription factors, NRF2 and NF- κ B, are activated to help increase expression of enzymatic (e.g. GPX, PRX) and non-enzymatic (e.g. GSH) antioxidants (Sharma 2012). As described in Chapter 2, proteomics data confirmed by Western blot showed antioxidants, PRX1/2, which reduce H₂O₂ levels, and GSTpi, which metabolize xenobiotics, were significantly increased in rSCC-61 cells compared to SCC-61 cells correlating with decreased total ROS as evidenced by DCF and HyPer imaging assay. Radiation resistant rSCC-61 cells simultaneously decrease mitochondrial MnSOD and ETC activity but increase PRX3 by 2.1-fold change resulting in decreased O₂^{•-} and H₂O₂ as evidenced by MitoSOX imaging in Chapter 3 and HyPer-mito imaging in Chapter 4. Increasing mitochondrial ROS by treating with MitoPQ or with Mn-porphyrin compounds and radiation, as described in Chapter 5, causes oxidative stress and cell death in rSCC-61 cells.

Studies presented in Chapter 4 dived further into the role of metabolic reactions and enzymes contributing to redox maintenance in rSCC-61 cells. The cytosol is primarily maintained

under reducing conditions by the redox buffering capacity of intracellular thiols, GSH and TRX. GSH donates reducing equivalents to maintain protein reduced states and as a result becomes oxidized to GSSG. GSSG can be either excreted from the cell or reduced by GR in an NADPH-dependent manner. Therefore, NADPH reserve maintained by 1-C metabolism and PPP is intrinsically connected to the levels and the balance of reduced and oxidized GSH in cells. GSH and GSSG levels and ratio were found to be significantly increased in rSCC-61 cells compared to SCC-61 cells. TRX functions in the nucleus to activate redox-sensitive transcription factors (i.e. TP53 and NF- κ B), maintain mitochondrial proteins in the reduced state, and provide reducing equivalents to PRXs to detoxify H₂O₂. TRX and TR were also significantly increased 1.2- and 1.8-fold in rSCC-61 cells compared to SCC-61 cells. The TRX/TR system acts as a redundant mechanism with GSH/GR system highlighting the importance of redox buffering capacity of the cell for cellular signaling and metabolic functions. For example, the network in Chapter 4 highlighted differential regulation between Akt isoforms due to redox status. The phosphorylation of all Akt isoforms is downregulated in rSCC-61 cells compared to SCC-61 cells but due to isoform selective inhibition of Akt2 activity by H₂O₂ levels, Akt2 activity was predicted to be upregulated in the more reducing rSCC-61 cells. Western blot analysis in Chapter 4 confirmed increased Akt2 activity in rSCC-61 cells compared to SCC-61 cells. This further supported evidence of rSCC-61 cells “glucose addiction” as Akt2 regulates glucose uptake and membrane localization of GLUT1/4. These data point to the dual role of GSH and TRX to maintain redox homeostasis and also enable accumulation of these species necessary for signaling.

Despite increased GSH and GSSG in rSCC-61 cells, studies in Chapter 4 demonstrated a defect in glutathione biosynthesis and emphasized alternative pathways are employed to maintain GSH/GSSG ratio in rSCC-61 cells compared to SCC-61 cells. GSH synthesis involves condensation of glutamate and Cys by GCL making Cys availability the rate-limiting factor in GSH biosynthesis. Cysteine is derived from the diet, protein catabolism, methionine via transsulfuration or import of cystine via the X_c⁻ cystine/glutamate antiporter system. Our HPLC

methods were unable to precisely detect the levels of cysteine between SCC-61 cells and rSCC-61 cells. However, clonogenic cell survival assay inhibiting transport of cystine into the cell or removal of cysteine from the cellular microenvironment demonstrated the dependence on import of cystine to maintain cysteine availability for GSH biosynthesis. Western blot analysis of critical enzymes, CBS and CSE, showed increased expression of CBS and decreased expression of CSE in rSCC-61 cells compared to SCC-61 cells. HPA shows low or undetectable levels of CBS in head and neck normal tissue. These two enzymes work sequentially to synthesize cysteine from homocysteine and their decreased expression levels support a defect in glutathione biosynthesis in both cell lines. GC analysis in Chapter 4 confirmed a buildup of cystathionine and increased production of hydrogen sulfide (H₂S) in rSCC-61 cells as a result of increased CBS and decreased CSE.

Studies completed in colon and ovarian cancer demonstrated overexpression of CBS causes increased H₂S production and increases the rate of proliferation, bioenergetics and angiogenesis. While the mechanism of action is not well understood, several mechanisms have been proposed including (a) activation of PI3K/Akt pathway and inhibition of phosphatases, (b) the regulation of genes involved in cell cycle control, and (c) protecting cells against damage from leaky ETC by maintaining redox homeostasis (Bhattacharyya 2013, Modis 2014, Szabo 2013). The study in colon cancer also demonstrated silencing or inhibition of CBS attenuated ATP production, reduced glycolytic functions, and enhanced ROS generation. The effects of CBS inhibition and silencing in colon cancer are similar to inhibition and silencing of FASN described in Chapter 3 suggesting involvement of CBS in metabolic reprogramming in HNSCC as well. Studies completed in colon and ovarian cancer taken with our *in vitro* data showing increased CBS and H₂S production and decreased ROS in rSCC-61 cells compared to SCC-61 cells suggest (1) CBS plays a protective role in cancer cells leading to radiation resistance, (2) CBS to CSE ratio is a potential biomarker to monitor head and neck tumor progression, and (3) CBS is a potential therapeutic target for HNSCC. Overall, GSH/GSSG ratio is an indicative measure of

oxidative stress in the cell and is critical for maintaining redox homeostasis for efficient signaling and metabolism.

Cell Survival The signaling and metabolic pathways discussed converge to minimize the cytotoxic effects of radiotherapy by limiting free radical production and decreasing DNA damage. Cell cycle analysis showed 2 Gy irradiation induced significantly less G2/M arrest in rSCC-61 cells compared to SCC-61 cells. In the presence of cellular stressors, TP53 undergoes posttranslational modifications leading to its activation and cell cycle arrest in G1 phase giving cells time to repair DNA before replication and avoid propagation of nucleic acid alterations (Vousden 2002). Canonical pathway analysis of proteomics data in Chapter 2 and metabolic pathways analysis in Chapter 4 identified base excision repair, DNA replication and synthesis of nucleotides and ribonucleotides were significantly upregulated in rSCC-61 cells compared to SCC-61 cells. For example, proteomics data in Chapter 2, *Appendix* showed a 2.5-fold increase in poly (ADP-ribose) polymerase (PARP) which detects and initiates a cellular response to radiation-induced DNA SSBs. PARP binding to SSBs leads to recruitment of base excision repair proteins to repair DNA. Imaging data showing increased γ H2AX, an indicator of DNA DSBs, foci formation confirmed rSCC-61 cells repair DNA damage better than SCC-61 cells before and after irradiation.

Radiation resistant rSCC-61 cells ability to repair damage quickly parallels glycolytic flux diverted into PPP leading to an increase in precursors for nucleic acid biosynthesis. To enhance de novo ribonucleotide synthesis, in the second step of the oxidative branch of the PPP, 6-phosphogluconate dehydrogenase (PGD) makes a second molecule of NADPH and ribulose-5-phosphate (Ru5P). Ru5P quickly undergoes isomerization by ribulose-5-phosphate isomerase (RPIA) to generate ribose-5-phosphate (R5P) which is then converted to phosphoribosyl-pyrophosphate. Metabolomics and mRNA expression data showed R5P and PGD are increased 1.5- and 3.5-fold in rSCC-61 cells compared to SCC-61 cells. In lung cancer, genetic silencing of PGD results in increased flux through ETC resulting in ROS accumulation and a decrease in PPP

metabolites, however, NADPH/NADP did not change (Krushna 2014). Also, under oxidative stress, transketolase converts R5P to glyceraldehyde-3-phosphate (G3P) and sedoheptulose-7-phosphate to ultimately make fructose-6-phosphate (F6P) which can be either (1) converted back to G6P to replenish the NADPH reserve or (2) diverted to generate additional ribonucleotides. Glyceraldehyde 3-phosphate dehydrogenase (GAPDH) was identified as a redox regulated protein in Chapter 4 that is slightly more labeled, 1.2 fold, in rSCC-61 cells compared to SCC-61 cells. These data taken together establish a significant link between redox regulation and signaling and metabolic pathways to elicit protection against radiation induced damage that should be further explored (**Fig. 1**).

Innovation. The novelty of the work presented in this dissertation lie in the establishment of a preclinical *in vitro* matched model of HNSCC that enables the ability to determine how ROS interact with proteins and determines the consequences of this interaction on cellular signaling and metabolism relevant to radiation response in HNSCC. Also, the use of systematic investigation by developing a novel constraint-based computational method, COSM^{RO}, which combines multiple omics data sets including proteomics, redox proteomics, metabolomics, lipidomics and protein phosphorylation status. The novelty of the network lies in four components which when combined together provide insight into rSCC-61 cell specific redox-dependent changes.

1. Representing multi-omics data (i.e. metabolites, enzymes) from our *in vitro* matched model of HNSCC as ratios of concentrations in rSCC-61 cells relative to SCC-61 cells, we are able to develop a cell specific model connecting signaling and metabolic pathways regulated in radiation resistant HNSCC.
2. The analysis took into consideration the relationships among signaling protein activity by combining changes in oxidation, phosphorylation and total expression between the two cell lines. With nodes represented as activating or inhibitory reactions, we can accurately predict signaling reactions as up- or downregulated.

3. The metabolic subnetwork took into consideration the relationship among metabolic flux distribution, and metabolite thermodynamic and stoichiometric characteristics. This analysis combines enzyme concentration with metabolite flux allowing the prediction of flux direction as blocked and the ability to predict unknown enzyme concentrations.
4. This constraint model simplifies the network optimization process and gives the ability to simulate or quickly search for an optimal solution when components of the network are changed.

Overall, combining a matched model of radiation resistance in HNSCC with COSM^{RO}, we were able to identify clinically relevant radiation resistant HNSCC signatures including:

1. Transition from mesenchymal-to-epithelial phenotype.
2. Inverse relationship between response to radiation and EGFR TKI – radiation resistance, Erlotinib sensitive – due to a cyclic relationship between ROS, cholesterol level and lipid raft formation leading to alterations in EGFR signaling.
3. Upregulation of redox metabolism in radiation resistant cells leading to increased enzymatic and non-enzymatic antioxidants specifically PRXs, GSTpi, GSH, and TRX.
4. Glucose addiction diverted from classical Warburg phenotype to maintain low generation of ROS through mitochondrial ETC and increased flux through PPP to maintain NADPH reserve, ribonucleotide production and endogenous fatty acids.

Future Directions While our matched model of radiation resistance for HNSCC biological features parallel clinical tissue specimens, it is imperative to test these findings *in vivo*. To date, the most clinically relevant *in vivo* models are the orthotopic xenograft or orthotopic PDX models. PDX models are better able to recapitulate human tumor behavior (Anderson 2003, Chung 2004, Cutz 2006, Monsma 2012). SCC-61 cells and rSCC-61 cells have successfully been implanted orthotopically in nude mice with some associated metastases. This proves promising for testing potential biomarkers to stratify patients, predict patient response to therapeutics and personalize treatment plans based on findings in this dissertation. To further validate these

findings, other radiation resistant HNSCC cell lines should also be tested. This will help to establish signatures for HNSCC tumors based on tumor origin and associated etiological factors. The NCI-60 human tumor cell line panel, to identify and characterize novel compounds with growth inhibition, did not include HNSCC cell lines. The development of the NIH-NCI repository of cancer models derived from PDXs should include HNSCC PDXs to increase access to primary human cells and tissue and decrease the cost associated with *in vivo* models for future studies.

Biomarkers The lack of biomarkers leads to late detection of HNSCC and poor prediction of patient outcome. This dissertation was able to identify several biomarkers related to signaling and metabolism as well as redox status which should be explored *in vivo* and in clinical pilot studies. Evidence was presented in this dissertation showing the ability to monitor redox status with Cys-SOH probe BP1 in patient tissue samples and accurately predict patient response to radiation. The imaging showed distinct differences between radiation-sensitive versus radiation-resistant patients. Redox status should be further explored on a larger scale as a tool to predict patient response and outcome. In combination with redox status, development of tools to assess CBS:CSE and GSH:GSSG ratio may also be useful as biomarkers to measure tumor progression and oxidative stress. As previously mentioned, redox status can also be used in combination with patient lipid profile to further stratify patients response to radiation and EGFR TKI. Due to the increased toxicity of EGFR TKIs in HNSCC patients, better understanding how AKT overexpression and PTEN oxidation alter response to EGFR TKI thereby increasing toxicity is necessary to determine dose schedules to improve efficacy. It is also imperative to identify how ROS levels may impair post-processing of EGFR and EGFR drug targeted therapies which may be reducing drug efficacy. Future studies should also explore the relationship between ROS and cholesterol levels and its role in response to EGFR mAbs such as Cetuximab. Combination of EGFR expression, redox status, and lipid profile will help to not only stratify patients and predict

their response to therapy but also help to spare normal tissue toxicity by identifying an optimal treatment plan for patients in the future.

Drug Targets The coordination between signaling and metabolic pathways also implicated several novel targets of interest including lipid metabolism enzymes (i.e. FASN), pentose phosphate pathway (i.e. G6PD, PGD, and TIGAR), 1-C metabolism enzymes (i.e. MTHFD2, DHFR) and cell cycle (i.e. PARP). There are currently no FDA approved cancer drugs against these targets except, MTX against DHFR, which has not demonstrated increased efficacy and patient survival in HNSCC recurrent and/or metastatic clinical trials, and Olaparib (Lynparza®) against PARP for germline BRCA mutations in ovarian cancer. CB83, irreversible G6PD inhibitor, is being tested as an antimalarial drug. However, based on data presented here, its ability to induce continuous formation of ROS and deplete NADPH reserve makes it an ideal drug to treat radiation resistant HNSCC. Future studies should explore its mechanism of action *in vitro* and validate *in vivo* CB83's ability to reduce tumor growth. Better understanding of how these enzymes function in HNSCC and identifying which enzyme or pathway is a master regulator of redox-regulation would further current knowledge and help to identify new drug targets. These studies did not focus on immunotherapies which is an emerging focus of research in HNSCC. It would be ideal to use new drugs or immunotherapies against PD-1 or IDO1 in combination with radiation and/or novel drug targets described here to increase local regional control and overall survival.

Broadly, the studies presented here emphasize the role of redox regulation of signaling and metabolic pathways. Therefore, further research into understanding the associated molecular mechanisms and translating this research into clinic is critical for developing the next generation of therapeutics, increasing therapeutic efficacy of current drugs and increasing patient overall survival in HNSCC as well as other cancers.

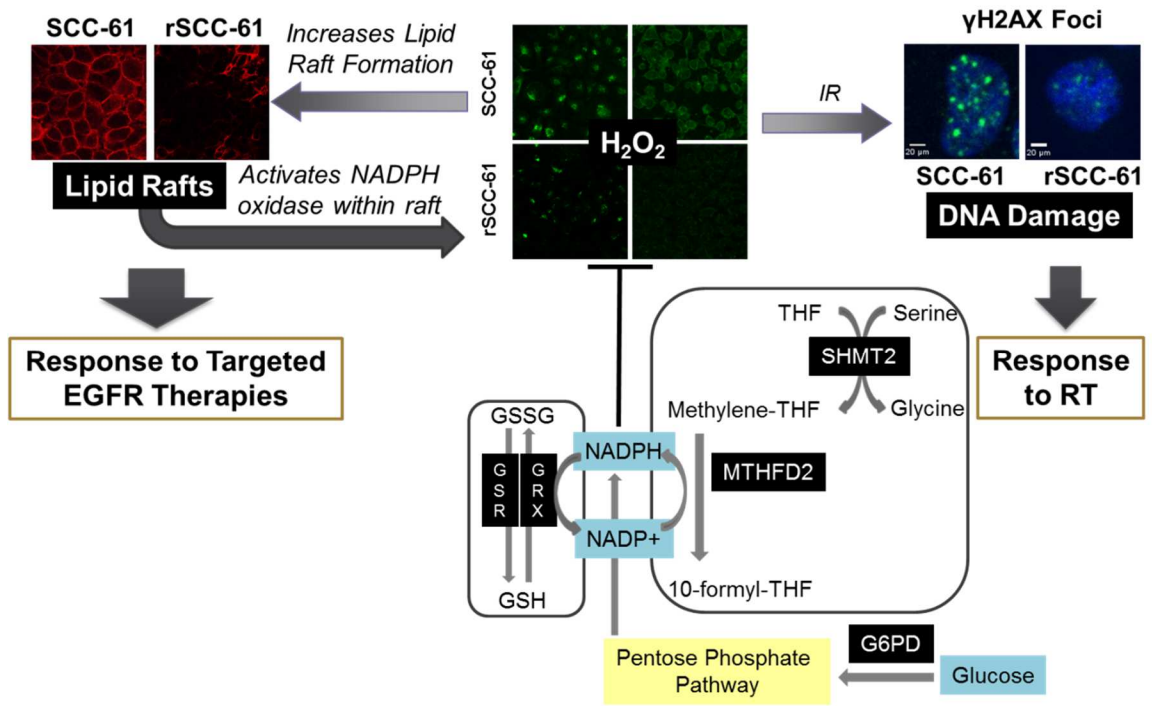


Figure 1 – Central role of reactive oxygen species and cholesterol metabolism and Head and Neck Squamous Cell Carcinoma response to therapies.

LITERATURE CITED

Anderson TM, Hess SD, Egilmez NK, Nwogu CE, Lenox JM, and Bankert RB. Comparison of human lung cancer/SCID mouse tumor xenografts and cell culture growth with patient clinical outcomes. *J Cancer Res Clin Oncol.* 129:565–568, 2003.

Bar-Ad V, Palmer J, Yang H, Cognetti D, Curry J, Luginbuhl A, Tuluc M, Campling B, and Azelrod R. Current management of locally advanced head and neck cancer: the combination of chemotherapy with locoregional treatments. *Semin Oncol.* 41(6):798-806, 2014.

Barger JF, Plas DR. Balancing biosynthesis and bioenergetics: metabolic programs in oncogenesis. *Endocr Relat Cancer.* 17:R287–304, 2010.

Bernier J, Domenge C, Ozsahin M, Matuszewska K, Lefebvre JL, Greiner RH, Giralt J, Maingon P, Rollan F, Bolla M, Cognetti F, Bourhis J, Kirkpatrick A, and van labeke M. Postoperative irradiation with or without concomitant chemotherapy for locally advanced head and neck cancer. *N Engl J Med.* 350(19):1945-52, 2004.

Bhattacharyya S, Saha S, Giri K, Lanza IR, Nair KS, Jennings NB, Rodriguez-Aguayo C, Lopez-Berestein G, Basal E, Weaver AL, Visscher DW, Cliby W, Sood AK, Bhattacharya R, and Mukherjee P. Cystathionine beta-synthase (CBS) contributes to advanced ovarian cancer progression and drug resistance. *PLoS One.* 8(11):e79167, 2013.

Bonner JA, Harari PM, Giralt J, Azarnia N, Shin DM, Cohen RB, Jones CU, Sur R, Raben D, Jassem J, Ove R, Kies MS, Baselga J, Youssoufian H, Amellal N, Rowinsky EK, and Ang KK. Radiotherapy plus cetuximab for squamous-cell carcinoma of the head and neck. *N Engl J Med* 354: 567–578, 2006.

Brunner TB, Hahn SM, Gupta AK, Muschel RJ, McKenna WG and Bernhard EJ. Farnesyltransferase inhibitors: an overview of the results of preclinical and clinical investigations. *Cancer Res.* 63(18):5656-68, 2003.

Chung CH, Parker JS, Karaca G, Wu J, Funkhouser WK, Moore D, Butterfoss D, Xiang D, Zanation A, Yin X, Shockley WW, Weissler MC, Dressler LG, Shores CG, Yarbrough WG and Perou CM. Molecular classification of head and neck squamous cell carcinomas using patterns of gene expression. *Cancer Cell*. 5:489–500, 2004.

Cutz JC, Guan J, Bayani J, Yoshimoto M, Xue H, Sutcliffe M, English J, Flint J, LeRiche J, Yee J, Squire JA, Gout PW, Lam S, and Wang YZ. Establishment in severe combined immunodeficiency mice of subrenal capsule xenografts and transplantable tumor lines from a variety of primary human lung cancers: potential models for studying tumor progression-related changes. *Clin Cancer Res*. 12:4043–4054, 2006.

Davies NJ, Batehup L and Thomas R. The role of diet and physical activity in breast, colorectal and prostate cancer survivorship: a review of the literature. *Br J Cancer*. 105 suppl 1:S52-73, 2011.

Diers AR, Broniowska KA, Chang CF, and Hogg N. Pyruvate fuels mitochondrial respiration and proliferation of breast cancer cells: effect of monocarboxylate transporter inhibition. *Biochem J*. 444:561–71, 2012.

Goldkorn T and Filosto S. Lung injury and cancer: mechanistic insights into ceramide and EGFR signaling under cigarette smoke. *Am J Respir Cell Mol Biol*. 4(3):259-268, 2010.

Goldstein JL and Brown MS. The LDL receptor defect in familial hypercholesterolemia. Implications for pathogenesis and therapy. *Med Clin Orth Am*. 66(2): p. 335-62, 1982.

Hanahan D, Weinberg RA. Hallmarks of cancer: the next generation. *Cell*. 144, 646–74, 2011.

Hanahan D, Weinberg RA. The hallmarks of cancer. *Cell*. 100:57–70, 2000.

Haque R, Contreras R, McNicoll MP, Eckberg EC, and Petitti DB. Surgical margins and survival after head and neck cancer surgery. *BMC Ear, Nose, and Throat Disord.* 6:2, 2006.

Hirano Y, Murata S, Tanaka K, Shimizu M and Sato R. Sterol regulatory element-binding proteins are negatively regulated through SUMO-1 modification independent of the ubiquitin/26 S proteasome pathway. *J Biol Chem.* 278(19): 16809-19, 2003.

Jin ES, Sherry AD, and Malloy CR. An oral load of [¹³C₃]glycerol and blood NMR analysis detect fatty acid esterification, pentose phosphate pathway and glycerol metabolism through tricarboxylic acid cycle in human liver. *J Biol Chem.* 291(36): 19031-41, 2016.

Kao YC, Lee SW, Lin LC, Chen LT, Hsing CH, Hsu HP, Huang HY, Shiue YL, Chen TJ, and Li CF. Fatty acid synthase overexpression confers an independent prognosticator and associates with radiation resistance in nasopharyngeal carcinoma. *Tumour Biol.* 34:759–68, 2012.

Krushna PC and Hay N. The pentose phosphate pathway and cancer. *Trends Biochem Sci.* 39(8):347-354, 2014.

Lee YS, Chang HW, Jeong JE, Lee SW, and Kim SY. Proteomic analysis of two head and neck cancer cell lines presenting different radiation sensitivity. *Acta Otolaryngol* 128: 86–92, 2008.

Li B, Zhang C, He F, Liu W, Yang Y, Liu H, Liu X, Wang J, Zhang L, Deng B, Gao F, Cui J, Liu C, and Cai J. GSK-3β Inhibition Attenuates LPS-Induced Death but Aggravates Radiation-Induced Death via Down-Regulation of IL-6. *Cell Physiol Biochem* 32: 1720–1728, 2013.

Menendez JA, Lupu R. Fatty acid synthase and the lipogenic phenotype in cancer pathogenesis. *Nat Rev Cancer* 7:763–77, 2007.

Modis K, Coletta C, Asimakopoulou A, Szczesny B, Chao C, Papaetropoulos A, Hellmich MR, and Szabo C. Effect of S-adenosyl-L-methionine (SAM), an allosteric activator of cystathionine- β -synthase on colorectal cancer cell proliferation and bioenergetics in vitro. *Nitric Oxide*. 41:146-56, 2014.

Monsma DJ, Monks NR, Cherba DM, Dylewski D, Eugster E, Jahn H, Srikanth S, Morad SA and Cabot MC. Ceramide-orchestrated signalling in cancer cells. *Nat Rev Cancer*. 13(1):51e65, 2013.

Pike LS, Smift AL, Croteau NJ, Ferrick DA, and Wu M. Inhibition of fatty acid oxidation by etomoxir impairs NADPH production and increases reactive oxygen species resulting in ATP depletion and cell death in human glioblastoma cells. *Biochim Biophys Acta* 1807:726–34, 2011.

Porosnicu M, Waltonen JD, Sullivan C, McWilliams L, Kucera GL, Thomas A, Plasser R, and Browne JD. Pilot study to evaluate the effect of erlotinib (E) administered before surgery in operable patients with squamous cell carcinoma of the head and neck (SCCHN). *J Clin Oncol*. 29:2011 (suppl; abstr 5568).

Sharma PK, Varshney R. 2-Deoxy-D-glucose and 6-aminonicotin-amide-mediated Nrf2 down regulation leads to radiosensitization of malignant cells via abrogation of GSH-mediated defense. *Free Radic Res*. 46:1446–57, 2012.

Singh S, Ramesh V, Oza N, Balamurali PD, Prashad KV and Balakrishnan P. Evaluation of serum and salivary lipid profile: a correlative study. *J Oral Maxillofac Pathol*. 18(1):4-8, 2014.

Steinberg D. Low density lipoprotein oxidation and its pathobiological significance. *J Biol Chem*. 272(34): 20963-6, 1997.

Szabo C, Coletta C, Chao C, Modis K, Szzeszny B, Papaetropoulos A and Hellmich MR. Tumor-derived hydrogen sulfide, produced by cystathionine- β -synthase, stimulates bioenergetics, cell proliferation, and angiogenesis in colon cancer. *Proc Natl Acad Sci USA*. 110(30):12474-9, 2013.

Vander Heiden MG, Cantley LC, and Thompson CB. Understanding the Warburg effect: the metabolic requirements of cell proliferation. *Science*. 324:1029–33, 2009.

Vousden KH and Lu X. Live or let die: the cell's response to p53. *Nat Rev Cancer*. 2:594–604, 2002.

Weinberg F, Hamanaka R, Wheaton WW, Weinberg S, Joseph J, Lopez M, Kalyanaraman B, Mutlu GM, Budinger GR and Chandel NS. Mitochondrial metabolism and ROS generation are essential for Kras-mediated tumorigenicity. *Proc Natl Acad Sci USA* 107:8788–93, 2010.

Wise DR, DeBerardinis RJ, Mancuso A, Sayed N, Zhang XY, Pfeiffer HK, Nissim I, Daikhin E, Yudkoff M, McMahon SB and Thompson CB. Myc regulates a transcriptional program that stimulates mitochondrial glutaminolysis and leads to glutamine addiction. *Proc Natl Acad Sci USA*. 105:18782–7, 2008.

Yamaguchi Y, Haginaka J, Morimoto S, Fujioka Y, and Kunitomo M. Facilitated nitration and oxidation of LDL in cigarette smoke. *Eur J Clin Invest*. 35(3):186-93, 2005.

Zampella EJ, Bradley EL Jr, and Pretlow TG 2nd. Glucose-6-phosphate dehydrogenase: a possible clinical indicator for prostatic carcinoma. *Cancer*. 49(2):384-7, 1982.

APPENDIX

Supplemental Information for Chapter II

Broad Phenotypic Changes Associated With Gain of Radiation Resistance in Head and Neck Squamous Cell Cancer

Jade Mims*¹, Nidhi Bansal*¹, Jeffrey G. Kuremsky², Amy L. Olex³, Weiling Zhao¹, Leimiao Yin¹, Revati Wani¹, Jiang Qian¹, Brian Center¹, Glen S. Marrs⁴, Mercedes Porosnicu⁵, Jacquelyn S. Fetrow³, Allen W. Tsang¹, Cristina M. Furdui¹

*authors contributed equally

The following manuscript was published in the *Antioxidant Redox Signaling*, volume 21, pages 221 – 236, March 2014 and is reprinted with permission. The stylistic variations are due to the requirements of the journal.

Materials and Methods

Reagents Antibodies were obtained from the following sources: rabbit anti-epidermal growth factor receptor (EGFR), Alexa 488 conjugated rabbit anti-EGFR, rabbit anti-pAkt, rabbit anti-Akt, anti-pMEK1/2, rabbit anti-pErk1/2, rabbit anti-cH2AX, anti-rabbit IgG (H + L), F(ab ϵ)₂ Fragment (Alexa Fluor 488 Conjugate), mouse anti-phosphotyrosine antibody (p-Tyr-100), and rabbit anti- β actin from Cell Signaling; rabbit anti-EGFR, rabbit anti-pEGFR, and rabbit anti-mouse IgG HRP from Santa Cruz Biotechnology; and goat anti-rabbit IgG HRP from Jackson Laboratories. Prx1 and 2, anti-peroxiredoxin-SO_{2/3}, superoxide dismutase (SOD), catalase, and GAPDH antibodies were from Abcam. DMEM/ F12 and fetal bovine serum were purchased from Gibco (Invitrogen). Phosphate-buffered saline (PBS) was purchased from Lonza. Erlotinib, Cell Proliferation Kit I (3-(4,5-dimethylthiazol-2-yl)-2,5-diphenyltetrazolium bromide [MTT]) was purchased from Roche. Cloned AMV cDNA kit, AlexaFluor594 conjugated cholera toxin subunit B (CT-B), AlexaFluo594 conjugated streptavidin, Topro-3-iodide, and Hoechst nucleic acid stains were purchased from Invitrogen. RNeasy Plus Micro kit (with genomic DNA removal columns) and RNA were later purchased from Qiagen. Bicinchoninic acid (BCA) protein estimation kit and Western Lightning Plus ECL were purchased from Thermo scientific. Glutathione Assay Kit and Lactate Assay Kit II were purchased from BioVision. Methyl- β -cyclodextrin (M β CD) and Lovastatin were purchased from Sigma.

Clonogenic cell survival assay Radiation-resistant rSCC-61 and the parental SCC-61 cells were trypsinized, resuspended in complete medium, and plated into the six-well culture dishes at a low density. After 4 h of incubation at 37 °C, each 6-well plate was subjected to radiation with different doses (0, 1, 2, 4, and 6 Gy) and allowed to incubate for further 10 days for the colony formation. Once formed, the colonies were fixed in methanol and acetic acid (1:1) solution and stained with 0.5% crystal violet. The colonies containing more than 50 cells were counted. The surviving fraction of the radiated cells was normalized using the plating efficiencies of their corresponding untreated control. The data were fitted to the multi-target and linear-quadratic

formulae, where survival (S) was related to dose (D) by the expression $S = 1 - (1 - e^{-D/D_0})^N$ and $S = e^{-\alpha D - \beta D^2}$ using Sigma Plot v.12 software. The survival curves were obtained, and the radiation-sensitivity parameters were calculated according to the published methods (12, 20).

MTT cell viability assay SCC-61 and rSCC-61 response to Erlotinib. The viability of SCC-61 and rSCC-61 cells in response to treatment with the EGFR tyrosine kinase inhibitor, Erlotinib (also known as OSI-744 or Tarceva) was determined using the MTT (Roche) assay. The cells were trypsinized, resuspended in complete DMEM/F12 medium, and seeded in 96-well plates at a density of 5000/well in 50 μ l. After overnight incubation at 37 °C, the cells were treated with Erlotinib (50 μ l) to the final concentrations of 0.5, 1, 10, 25, 50, and 100 μ M, respectively, and incubated for 72 h at 37 °C. After incubation, 10 μ l MTT (5 mg/ml in PBS) was added to each well, and the plates were further incubated for 4 h at 37°C. At the end of the incubation, 100 μ l solubilization solution was added to each well, and the absorbance was recorded at 570 nm. The resulting curves were fitted to a Hill equation with four parameters: $y = \text{min} + (\text{max} - \text{min}) / (1 + (x/IC_{50})^{(Hill\text{slope})})$ using SigmaPlot v.12 software. The 50% inhibitory concentration (IC₅₀) was then determined as the Erlotinib concentration causing a 50% reduction in the cell viability. Effects of lipid raft inhibition on the response to Erlotinib and radiation in SCC-61. 5 x 10⁴ cells/well were plated in 24-well plates and incubated overnight. Cells were then treated with 1 mM M β CD and 1 μ M Lovastatin for 24 h. Next, cells were either irradiated with 0.5 and 2 Gy or treated with 2 μ M Erlotinib. At 48 h post-treatment, MTT was added to the cultures, incubated for 4 h at 37 °C, and processed as described earlier.

Cell-cycle analysis The cell-cycle distribution of the SCC-61 and rSCC-61 cells was determined by flow cytometry. The SCC-61 and rSCC-61 cells were cultured in 100-mm dishes, radiated with a 2 Gy radiation dose, and incubated for 24 h at 37 °C. The next day, the cells were trypsinized and resuspended in 1 ml propidium iodide staining solution (1 μ g/ml) that was supplemented with 37 μ g/ml RNase A and 0.06% NP-40. The data were collected using the

Accuri C6 flow cytometer, and the cell-cycle distribution was analyzed by ModFit LT 3.2 DNA analysis software (Verity Software House).

Western blot analysis At 24 h after radiation, the cells were lysed with the modified RIPA buffer and supplemented with protease and phosphatase inhibitors (Complete Tablets Mini and Phos-STOP, respectively from Roche). The lysates were incubated on ice for 1 h followed by centrifugation at 10,000 g for 10 min. The lysates were then normalized for their protein concentration across different treatment conditions and subjected to SDS-PAGE. The separated proteins were then transferred to a nitrocellulose membrane (0.45 µm; BioRad) and probed for the indicated proteins after overnight incubation with the corresponding primary antibodies (Cell Signaling) that was diluted in 1% BSA in TBS-Tween20 buffer followed by incubation with respective HRP-conjugated secondary antibodies. The Western blots were developed using Western Lightning Plus-ECL reagents followed by exposure to autoradiography film (Blue Ultra Autorad Film from GeneMate).

Total RNA isolation and semi-quantitative RT-PCR Total RNA was extracted with RNeasy plus Micro kit (Qiagen). RNA (1 µg) was reverse transcribed with the SuperScript First-Strand cDNA Synthesis Kit (Invitrogen). Gene-specific primers were designed using Gene Runner 3.01 software. Semiquantitative PCR was performed to examine the relative expression of Vimentin and E-cadherin in SCC-61 and rSCC-61. 18S amplification was used as an endogenous control. The primers and PCR conditions are shown in Appendix Table 8.

Detection of reactive oxygen species Subconfluent SCC-61 and rSCC-61 cells were cultured in 6-well plates and assayed for intracellular reactive oxygen species by imaging at 1 h after radiation (2 Gy) using 2.5 µM CM-H₂DCFDA (dichlorofluorescein [DCF]; Invitrogen). DCF was added for 10 min and incubated at room temperature before imaging. The cells were rapidly washed twice with 1X PBS and visualized with an Arcturus PixCell II laser capture microscope under a

20X objective. Both the fluorescence and the corresponding phase images were captured from at least two random fields per condition.

Glutathione assay The concentration of total, oxidized, and reduced glutathione present in SCC-61 and rSCC-61 cells was determined using the o-phthalaldehyde-based glutathione assay kit (Biovision). Subconfluent cells were treated with 2 Gy radiation dose and incubated for 1 h post irradiation. The radiated and control SCC-61 and rSCC-61 cells were lysed using the assay buffer provided in the kit. The lysates were quickly added to the tubes containing prechilled perchloric acid (6N) and vortexed immediately. The samples were incubated on ice for 5 min and centrifuged at 13,000 g for 2 min to precipitate the proteins and separate the glutathione-containing supernatant. Ice-cold potassium hydroxide (KOH) (6N) was then added to the supernatant in order to neutralize the pH and to precipitate the perchloric acid. The supernatant was obtained by centrifugation at 13,000 g. For estimating total glutathione, oxidized glutathione (GSSG), and reduced glutathione (GSH), the samples were then diluted in the assay buffer in a 96-well plate with or without the glutathione reducing agent and reduced glutathione quencher (according to the manufacturer's instructions) and incubated with o-phthalaldehyde probe for 40 min at room temperature. Similar treatment was given to the reduced glutathione for generating the standard curve. The fluorescence was measured at k_{ex} 340 nm and k_{em} at 420 nm using the plate reader and reported as pmoles per μ g of protein in assay.

Cell migration assay The transwell migration assay was performed following the manufacturer's protocol. Briefly, the SCC-61 and rSCC-61 cells were serum starved for about 16 h. The next day, the cells were dissociated, counted and 2.5×10^4 cells/well were added to the upper chamber of the transwell plates (BD Biosciences) in 500 μ l serum-free medium. The lower chamber was filled with 500 μ l complete DMEM/F12 medium. After incubation for 20 h at 37 °C, the migrated cells were stained with 0.5% crystal violet and counted with the Olympus confocal microscope using a 20X objective. Lactic acid assay and extracellular pH analysis were utilized. SCC-61 and

rSCC-61 cells were dissociated with trypsin, counted, normalized, and cultured in six-well plates. After 4 h of incubation at 37 °C and 5% CO₂ (zero time point), the cells were harvested for estimating the intracellular lactate levels. The culture medium was also collected for measuring the extracellular pH and lactate levels. The extracellular pH was measured with a laboratory pH meter (S20 SevenEasy from Metler Toledo). The intracellular and extracellular lactate levels were estimated using the Lactate Assay Kit II from BioVision according to the manufacturer's protocol. Total protein was estimated using the BCA assay (Thermo Scientific). The intracellular and extracellular lactate and extra-cellular pH were measured at different time intervals (4, 8, 24, 48, and 72 h). The lactate levels were determined and expressed as nmoles/μg/μl of the total protein.

Immunostaining of lipid rafts and EGFR SCC-61/rSCC-61 comparison. SCC-61 and rSCC-61 cells were seeded in 1 ml microtek chambers at a density of 2 x 10⁴ cells/ml and incubated overnight at 37 °C and 5% CO₂. After overnight incubation, cells were treated with 2 Gy radiation. For lipid raft staining, the cells were incubated with 1 μg/ml of AlexaFluor594 conjugated CT-B for 15 min at 4 °C before cell fixation. Cells were fixed in 4% paraformaldehyde for 15 min and permeabilized with 0.1 TritonX-100 followed by blocking with 8% BSA for 1 h at 4°C. The cells were then incubated with 1:500 dilution of AlexaFluor488 conjugated anti-EGFR antibody (Millipore) for 1 h at 4 °C, washed, and mounted using Fluoromount (Sigma) for imaging. Imaging was performed using a Zeiss LSM710 confocal microscope and a 40X objective. The images were processed using the LSM image browser. Inhibition of lipid rafts was conducted in SCC-61 by MβCD, Lovastatin, and polyethylene glycol (PEG)-catalase. SCC-61 cells were seeded in 1 ml microtek chambers at a density of 2 x 10⁴ cells/ml and incubated overnight at 37 °C and 5% CO₂. After overnight incubation, cells were treated with (i) 1 mM MβCD, (ii) 2 μM Lovastatin, (iii) 1 mM MβCD plus 2 μM Lovastatin, and

(iv) PEG-catalase (2 and 20 U) in 1 ml medium. After 24 h treatment, the cells were stained with AlexaFluor594 conjugated CT-B and imaged as described earlier.

γ H2AX Immunofluorescence SCC-61 and rSCC-61 cells were seeded in 1 ml microtek chambers at a density of 2×10^4 cells/ml and incubated overnight at 37 °C and 5% CO₂. After overnight incubation, cells were treated with 2 Gy radiation. At 3 and 24 h post irradiation, cells were washed with cold PBS and fixed in 4% paraformaldehyde for 15-min, washed with 100% methanol for 1 min at 20 °C, and permeabilized with 0.1 TritonX-100 followed by blocking with 8% BSA for 1 h at room temperature. The cells were incubated with 1:500 dilution of γ H2AX overnight at 4°C followed by washing with PBS, incubation with 1:500 dilution of 2° anti-rabbit Alexa Fluor 488 Conjugate for 1 h at room temperature, and 10 min incubation with 1:100 Topro-3-iodide before mounting with Fluoromount (Sigma). Imaging was performed using a Zeiss LSM710 confocal microscope and a 63x objective.

Figure 1. Cellular localization and molecular functions of the 965 proteins identified in the proteomic analysis (A) and the subset of 45 proteins with less than 0.01 expression ratio in rSCC-61 vs SCC-61 cells (B).

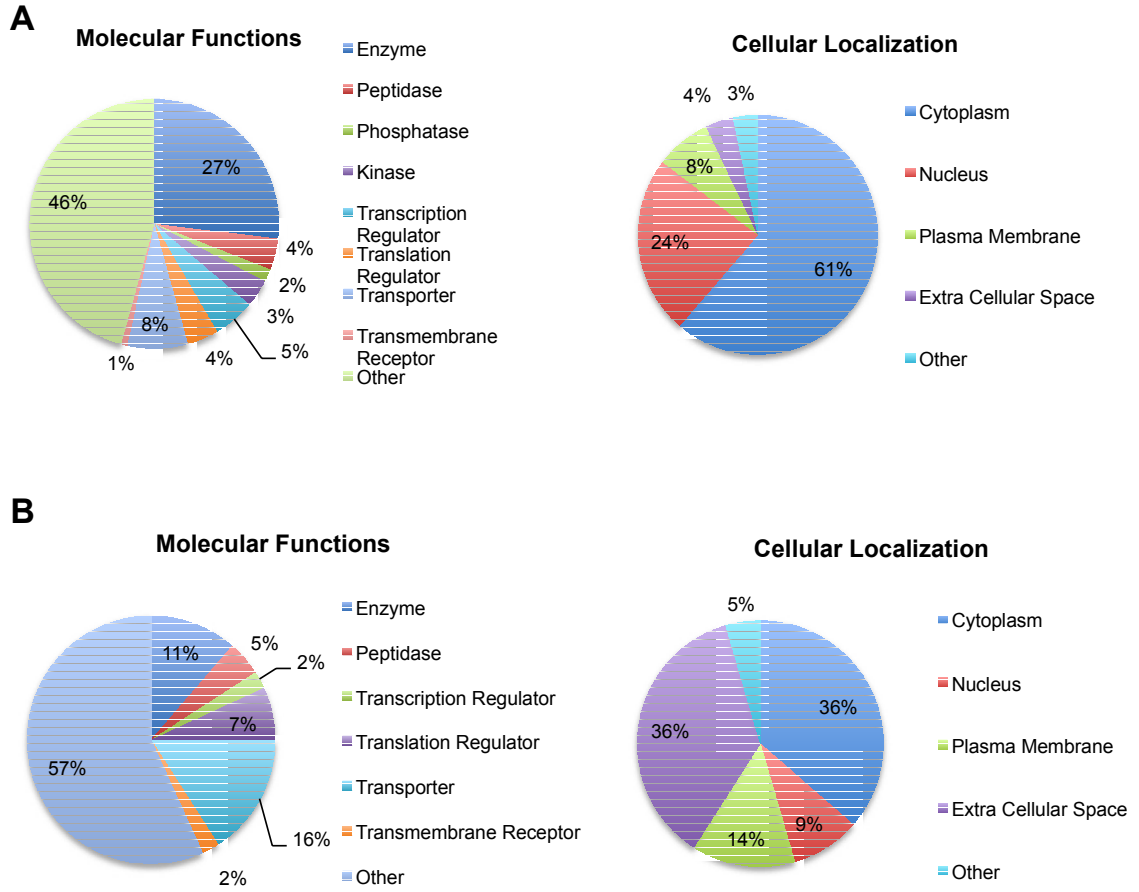
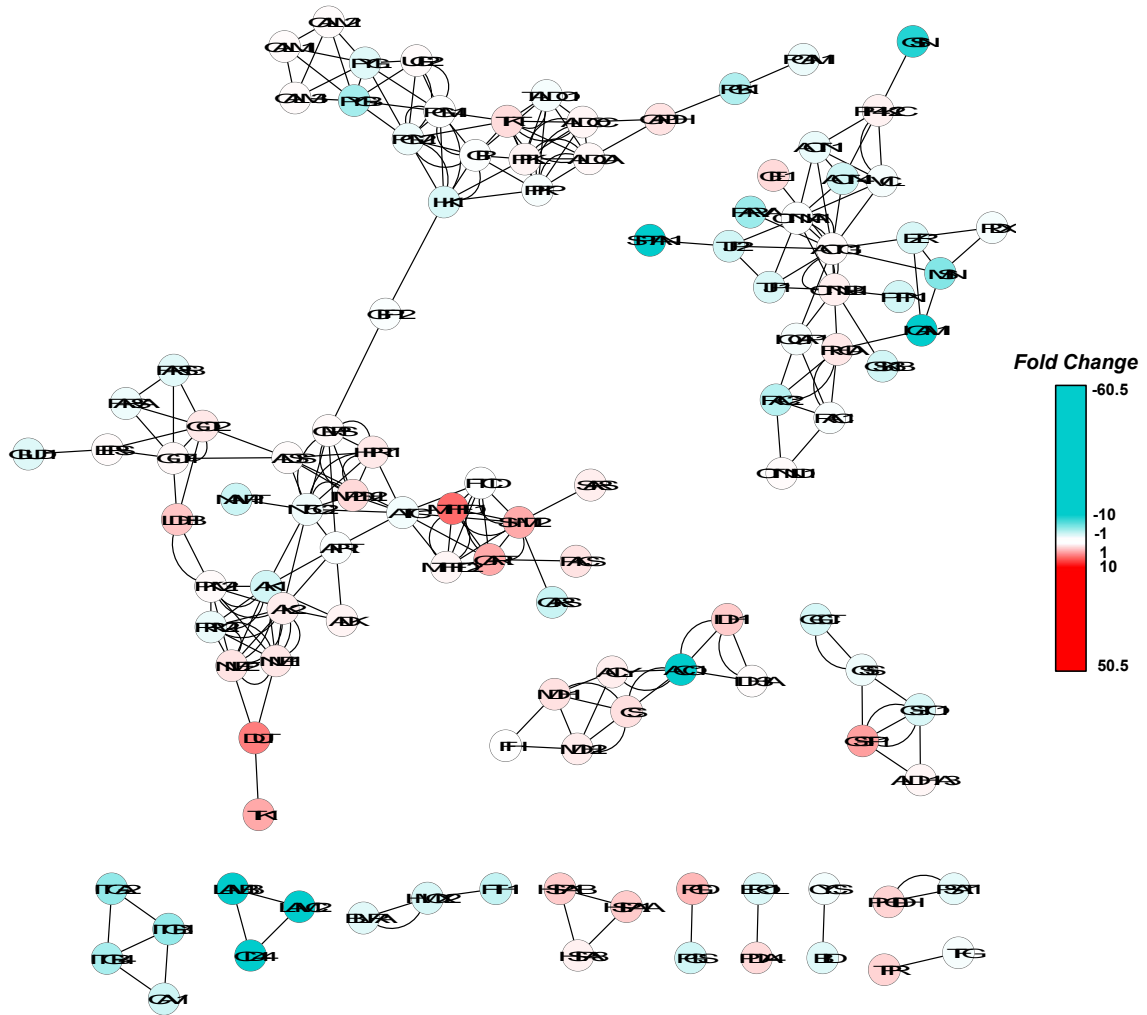


Figure 2. A. KEGG interaction subnetwork. Cytoscape was used to analyze MS data using interactions imported from the KEGG database. The figure shows subnetworks created from the global KEGG network by selecting all nodes (proteins) with a significant fold change (≥ 2.0 or ≤ -2.0) along with their first neighbors. Node colors represent fold change where red is up-regulation and blue is down-regulation as indicated by the fold-change bar. DAVID analysis of the Uniprot IDs of these significantly regulated nodes identified several overrepresented ($P < 0.05$) KEGG pathways in this network. The subnetwork that had a high density of proteins involved in regulation of actin cytoskeleton and focal adhesion is depicted on the right. **B.** List of significantly over-represented KEGG pathways and their corresponding P values.

A



B

| KEGG Pathway | P value |
|---|----------------|
| hsa00030:Pentose phosphate pathway | 1.34E-10 |
| hsa00010:Glycolysis / Gluconeogenesis | 1.24E-09 |
| hsa04520:Adherens junction | 2.72E-07 |
| hsa00020:Citrate cycle (TCA cycle) | 5.23E-07 |
| hsa04670:Leukocyte transendothelial migration | 5.00E-06 |
| hsa00230:Purine metabolism | 1.88E-05 |
| hsa00630:Glyoxylate and dicarboxylate metabolism | 2.04E-05 |
| hsa00670:One carbon pool by folate | 2.91E-05 |
| hsa04810:Regulation of actin cytoskeleton | 6.16E-05 |
| hsa04510:Focal adhesion | 1.03E-04 |
| hsa00052:Galactose metabolism | 3.60E-04 |
| hsa00500:Starch and sucrose metabolism | 4.97E-04 |
| hsa00520:Amino sugar and nucleotide sugar metabolism | 6.42E-04 |
| hsa00480:Glutathione metabolism | 1.28E-03 |
| hsa05200:Pathways in cancer | 2.52E-03 |
| hsa00250:Alanine, aspartate and glutamate metabolism | 6.55E-03 |
| hsa00051:Fructose and mannose metabolism | 9.12E-03 |
| hsa04530:Tight junction | 1.67E-02 |
| hsa00970:Aminoacyl-tRNA biosynthesis | 1.75E-02 |
| hsa00860:Porphyrin and chlorophyll metabolism | 4.63E-02 |
| hsa00270:Cysteine and methionine metabolism | 4.99E-02 |

Table 1. List of calculated values of D_0 , α and β parameters for the clonogenic assays in SCC-61 and rSCC-61. In the multi-target model, D_0 parameter indicates the amount of radiation required to reduce the survival fraction to approximately 0.37. In the linear-quadratic model, there are two components of cell killing: one is proportional to the IR dose (αD) and the other is proportional to the square of the IR dose (βD^2).

| Cell Lines | D_0 | N | α | β | PE | SF ₁ | SF ₂ | SF ₄ | SF ₆ |
|------------|-------|------|----------|---------|-------|-----------------|-----------------|-----------------|-----------------|
| rSCC-61 | 2.04 | 2.20 | 0.13 | 0.04 | 49.0% | 0.88 | 0.64 | 0.30 | 0.10 |
| SCC-61 | 1.32 | 1.95 | 0.27 | 0.09 | 28.8% | 0.71 | 0.39 | 0.09 | 0.03 |

PE: plating efficiency, SF: surviving fraction.

Table 2. List of proteins with expression ratio <0.01 in rSCC-61 and SCC-61 generated by the SILAC proteomics analysis.

| Proteins |
|--|
| Adenosine deaminase |
| Afamin |
| Alpha-1B-glycoprotein |
| Alpha-2-macroglobulin |
| Alpha-actinin-3 |
| Alpha-aminoadipicsemialdehyde dehydrogenase |
| Ankyrin-3 |
| Apolipoprotein E |
| BTB/POZ domain-containing protein KCTD12 |
| Desmoglein-3 |
| Eukaryotic peptide chain release factor subunit |
| Fibronectin type III domain-containing protein 3B |
| HEAT repeat-containing protein 2 |
| Helicase SKI2W |
| Hematopoietic lineage cell-specific protein |
| Hemoglobin subunit alpha |
| Hemoglobin subunit epsilon |
| HLA class I histocompatibility antigen, A-25 alpha chain |
| Insulin-like growth factor 2 mRNA-binding protein 2 |
| Insulin-like growth factor 2 mRNA-binding protein 3 |
| Integrin alpha-6 |
| Inter-alpha-trypsin inhibitor heavy chain H2 |
| Involucrin |
| Lactotransferrin |
| Neutrophil gelatinase-associated lipocalin |
| Normal mucosa of esophagus-specific gene 1 protein |
| Nuclear pore complex protein Nup205 |
| Plasminogen activator inhibitor |
| Plasminogen activator inhibitor 2 |
| Plastin-2 |
| Pregnancy zone protein |
| Protein S100-A7 |
| Protein S100-A8 |
| Protein S100-A9 |
| Protein-glutamine gamma-glutamyltransferase 2 |
| Putative FAM75-like protein FLJ44082 |
| Serum albumin |
| Serum amyloid A protein |
| Succinate dehydrogenase [ubiquinone] flavoprotein subunit, mitochondrial |
| Thrombomodulin |
| Thrombospondin-1 |
| Thyroxine-binding globulin O |
| Translocon-associated protein subunit alpha |
| Trypsin-3 |
| Vitronectin |

Table 3. List of the top upregulated proteins in rSCC-61 generated by the SILAC proteomics analysis

| Proteins | Fold Change (rSCC-61/SCC-61) |
|---|---------------------------------|
| Keratin Type II cytoskeletal 8 (KRT8) | 50.5 |
| Keratin Type I Cytoskeletal 18 (KRT18) | 13.8 |
| Keratin Type I Cytoskeletal 17 (KRT17) | 8.9 |
| Fatty Acid Synthase (FASN) | 6.8 |
| C-1-tetrahydrofolate synthase | 6.3 |
| Deoxyuridine 5'-triphosphate nucleotidohydrolase (DUT) | 5.6 |
| Periplakin | 4.8 |
| Structural maintenance of chromosome flexible hinge domain containing protein 1 | 4.7 |
| Protein S100-A16 | 4.5 |
| Glutathione S-transferase pi (GSTpi) | 4.4 |
| Trifunctional purine biosynthetic protein adenosine-3 | 4.0 |
| Serine hydroxymethyltransferase (SHMT2) | 4.0 |
| Activator of 90kDa heat shock protein ATPase homolog 1 | 3.9 |

Table 4. Fold change in a subset of proteins predicted to decrease cell death and apoptosis in rSCC-61 obtained from the SILAC proteomics analysis.

| Protein | Fold Change (rSCC-61/SCC-61) |
|--|------------------------------|
| Keratin Type II cytoskeletal 8 (KRT8) | 50.5 |
| Keratin Type I Cytoskeletal 18 (KRT18) | 13.8 |
| Fatty Acid Synthase (FASN) | 6.8 |
| Glutathione S-transferase pi (GSTpi) | 4.4 |
| Activator of 90 kDa heat shock protein ATPase homolog 1 (AHSA1) | 3.9 |
| A-kinase anchor protein 12 (AKAP12) | 2.9 |
| Desmoplakin (DSP) | 2.9 |
| Serine/arginine-rich splicing factor 5 (SRSF5) | 2.5 |
| Proliferation-associated 2G4, 38kDa (PA2G4) | 2.5 |
| Peroxiredoxin (PRDX3) | 2.1 |
| Serpin peptidase inhibitor, clade B (ovalbumin), member 5 (SERPINB5) | -30.6 |
| Intercellular adhesion molecule 1 (ICAM1) | -19.9 |
| SH3-domain kinase binding protein 1 (SH3KBP1) | -15.9 |
| Reticulon 4 (RTN4) | -14.9 |
| CD44 molecule (Indian blood group) | -11.6 |
| Microtubule-associated protein 1 light chain 3 alpha (MAP1LC3A) | -6.0 |
| FK506 binding protein 1A, 12kDa (FKBP1A) | -5.3 |
| Integrin, beta 1 (fibronectin receptor, beta polypeptide, antigen CD29 includes MDF2, MSK12) (ITGB1) | -4.7 |
| BH3 interacting domain death agonist (BID) | -2.1 |

Table 5A. Fold change in a subset of proteins involved in DNA replication and base-excision repair obtained from the SILAC proteomics analysis.

| Proteins | Fold Change (rSCC-61/SCC-61) |
|---|-------------------------------------|
| Minichromosome maintenance complex component 7 (MCM7) | 2.9 |
| Minichromosome maintenance complex component 2 (MCM2) | 2.8 |
| Minichromosome maintenance complex component 6 (MCM6) | 2.6 |
| Minichromosome maintenance complex component 3 (MCM3) | 2.7 |
| Poly (ADP-ribose) polymerase 1 (PARP1) | 2.5 |
| APEX nuclease (multifunctional DNA repair enzyme) 1 (APEX1) | 2.5 |
| Ligase I, DNA, ATP-dependent (LIG1) | 2.5 |
| High mobility group box 1 (HMGB1) | 2.3 |

Table 5B. Fold change in a subset of proteins involved in ECM-receptor interaction obtained from the SILAC proteomics analysis.

| Proteins | Fold Change (rSCC-61/SCC-61) |
|------------------------------------|-------------------------------------|
| Laminin, beta 3 (LMB3) | -20.0 |
| Laminin, gamma 2 (LMC2) | -18.6 |
| CD44 molecule (Indian blood group) | -11.6 |
| Integrin, beta 1 (ITGB1) | -4.8 |
| Integrin, alpha 2 (ITGA2) | -4.8 |
| Integrin, beta 4 (ITGB4) | -4.0 |

Table 5C. Fold change in a subset of proteins involved in regulation of cell cycle obtained from the SILAC proteomics analysis.

| Proteins | Fold Change (rSCC-61/SCC-61) |
|--|-------------------------------------|
| Minichromosome maintenance complex component 7 (MCM7) | 2.9 |
| Glycogen synthase kinase 3 beta (GSK3B) | -2.6 |
| Structural maintenance of chromosomes 1A (SMC1A) | 2.3 |
| Minichromosome maintenance complex component 2 (MCM2) | 2.8 |
| Protein kinase, DNA-activated, catalytic polypeptide (PRKDC) | 2.3 |
| Minichromosome maintenance complex component 6 (MCM6) | 2.6 |
| Minichromosome maintenance complex component 3 (MCM3) | 2.8 |

Table 5D. Fold change in a subset of proteins involved in focal adhesion obtained from the SILAC proteomics analysis.

| Proteins | Fold Change (rSCC-61/SCC-61) |
|--|-------------------------------------|
| Laminin, beta 3 (LMB3) | -20.0 |
| Laminin, gamma 2 (LMC2) | -18.6 |
| Integrin, beta 1 (ITGB1) | -4.8 |
| Integrin, alpha 2 (ITGA2) | -4.8 |
| Parvin, alpha (PARVA) | -4.5 |
| Integrin, beta 4 (ITGB4) | -4.0 |
| Ras-related C3 botulinum toxin substrate 2 (RAC2) | -3.5 |
| Caveolin 1 (CAV1) | -2.7 |
| Actinin alpha 4 (ACTN4) | -2.7 |
| Glycogen synthase kinase 3 beta (GSK3B) | -2.6 |
| Ras homolog family member A (RHOA) | 1.8 |
| catenin (cadherin-associated protein), beta 1 (CTNNB1) | 1.5 |

Table 5E. Fold change in a subset of proteins involved in regulation of actin cytoskeleton obtained from the SILAC proteomics analysis.

| Proteins | Fold Change (rSCC-61/SCC-61) |
|---|-------------------------------------|
| Gelsolin (GELS) | -8.8 |
| Moesin (MOES) | -5.4 |
| Integrin, beta 4 (ITGB4) | -4.0 |
| Integrin, alpha 2 (ITGA2) | -4.8 |
| Integrin, beta 1 (ITGB1) | -4.8 |
| Ras-related C3 botulinum toxin substrate 2 (RAC2) | -3.5 |
| Actinin alpha 4 (ACTN4) | -2.7 |
| Ezrin (EZR) | -2.4 |
| Actinin alpha 1 (ACTN1) | -1.7 |
| Cofilin-1 (COF1) | 2.3 |
| Ras homolog family member A (RHOA) | 1.8 |

Table 6. Fold change in proteins predicted to decrease ROS in rSCC-61 obtained from the SILAC proteomics analysis.

| Proteins | Fold Change (rSCC-61/SCC-61) |
|---------------------------------------|---|
| Peroxiredoxin 1 | 2.2 |
| Peroxiredoxin 3 | 2.1 |
| Glutathione S-transferase pi (GST pi) | 4.4 |

Table 7. Fold change in expression of subset of proteins predicted to decrease DNA damage in rSCC-61 obtained from the SILAC proteomic analysis.

| Protein | Fold Change (rSCC-61/SCC-61) |
|--|-------------------------------------|
| Glutathione S-transferase pi 1 (GSTP1) | 4.4 |
| Poly (ADP-ribose) polymerase 1 (PARP1) | 2.5 |
| Ligase I, DNA, ATP-dependent (LIG1) | 2.5 |
| Protein kinase, DNA-activated, catalytic polypeptide (PRKDC) | 2.3 |
| Nucleophosmin (NPM1) | 2.3 |
| Peroxiredoxin 1 (PRDX1) | 2.2 |
| MutS homolog 6 (MSH6) | 1.9 |
| Nucleoside diphosphate kinase 1 (NME1) | 1.8 |

Table 8. Primers and PCR conditions for Vimentin and E-cadherin.

| <i>Gene</i> | 5'-3' Sequence (Forward primer [F], Reverse primer [R]) | Length (bp) |
|-------------------|--|--------------------|
| <i>E-cadherin</i> | F: CTCCCATCAGCTGCCAGAA R: TCAGGATCTTGGCTGAGGATG | 454 |
| <i>Vimentin</i> | F: AAGCAGGAGTCCACTGAGTAC R: GGTATCAACCAGAGGGAGTGA | 372 |
| <i>18S</i> | F: GTGGTGTGAGGAAAGCAGACA R: TGATCACACGTTCCACCTCATC | 98 |

PCR conditions: 95°C for 5 min; 28 cycles of 95°C for 30 sec, 54°C for 30 sec and 72°C for 30 sec; and a final extension step for 5 min at 72°C.

APPENDIX

Supplemental Information for Chapter VI

Integration of Signaling and Metabolism in a Head and Neck Cancer Cell Model of Radiation Resistance using COSM^{RO}

Zhiwei Ji^{1,2}, Jade Mims³, Nelmi O. Devarie-Baez³, Hanzhi Wu³, Elsa I. Silva Lopez³, Joshua Lewis⁵, Victor Vitvitsky⁵, Jing Su², Melissa L. Kemp⁴, Ruma Banerjee⁵, Allen W. Tsang³, Xiaobo Zhou^{2,*}, Cristina M. Furdai^{3,*}

The following manuscript is in preparation to be submitted to *Cell*. The stylistic variations are due to the requirements of the journal.

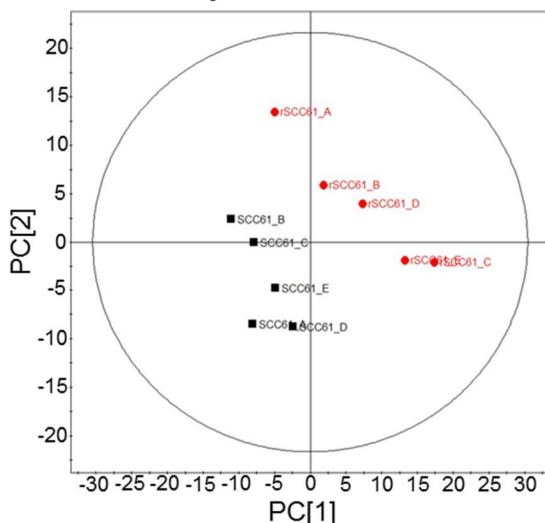
| REAGENT or RESOURCE | SOURCE | IDENTIFIER |
|---|-------------------------------|-----------------|
| Antibodies | | |
| Phospho-IGF-I Receptor β (Y1135/1136) | Cell Signaling | Cat#3024 |
| Phospho-ASK1 (Ser83) | Cell Signaling | Cat#3761 |
| Phospho-PDK1 (Ser241) | Cell Signaling | Cat#3061 |
| Phospho-SAPK/JNK (Thr183/Tyr185) | Cell Signaling | Cat#9251 |
| Phospho-PKD/PKC μ (Ser744/748) | Cell Signaling | Cat#2054 |
| Phospho-Akt (Ser473) | Cell Signaling | Cat#9271 |
| Phospho-Akt (Thr308) XP Rabbit mAb | Cell Signaling | Car#13038 |
| Phospho-Stat3 (Tyr705) | Cell Signaling | Cat#9145 |
| Phospho-Stat1 (Tyr701) | Cell Signaling | Cat#8062 |
| Phospho-LKB1 (Ser428) | Cell Signaling | Cat#3482 |
| Phospho-S6 Ribosomal Protein (Ser235/236) | Cell Signaling | Cat#4858 |
| Phospho-4E-BP1 (Thr37/46) | Cell Signaling | Cat#2855 |
| Phospho-Akt2 (Ser474) | Cell Signaling | Cat#8599 |
| Phospho-GSK-3 β (Ser 9) | Cell Signaling | Cat#9336 |
| Phospho-AMPK α (Thr172) Rabbit mAb | Cell Signaling | Cat#2535 |
| AMPK α | Cell Signaling | Cat#5831 |
| Phospho-Acetyl-CoA Carboxylase (Ser79) Rabbit mAb | Cell Signaling | Cat#11818 |
| Acetyl-CoA Carboxylase Rabbit mAb | Cell Signaling | Cat#3676 |
| Phospho-Histone H2A.X (Ser139) Rabbit mAb | Cell Signaling | Cat#9718 |
| GAPDH XP Rabbit mAb | Cell Signaling | Cat#5174 |
| Anti-rabbit IgG, HRP-linked Antibody | Cell Signaling | Cat#7074 |
| MTHFD2 Rabbit mAb | Cell Signaling | Cat#41377 |
| TIGAR (E-10) | Santa Cruz Biotechnology | Cat#sc-166291 |
| P53 (FL-393) | Santa Cruz Biotechnology | Cat#sc-6243 |
| Anti-PRX1 | Abcam | Cat#ab211292 |
| Anti-Peroxiredoxin-SO3 | Abcam | Cat#ab16830 |
| Anti-c-myc (phospho T58/S62) | Abcam | Cat#ab32029 |
| SRXN1 | Novus Biologicals | Cat#NBP1-36991 |
| <i>CBS</i> | | |
| CTH (F-1) | Santa Cruz Biotechnology | Cat#sc-374249 |
| Horseradish Peroxidase Goat Anti-Chicken IgY | Aves labs, Inc. | Cat#H-1004 |
| xCT/SLC7A11 Antibody | Novus Biologicals | Cat#NB300-318SS |
| β -Actin | Cell Signaling | Cat#4967S |
| ABCA1 | | |
| Biological Samples | | |
| human APOA1 | John Parks, WFSM | |
| ABCA1 full length protein | John Parks, WFSM | |
| Mouse ABCA1 knockout protein | John Parks, WFSM | |
| Human CBS | Ruma Banerjee, UofM-Ann Arbor | |
| Human CSE | Ruma Banerjee, UofM-Ann Arbor | |

| Chemicals, Peptides, and Recombinant Proteins | | |
|--|-----------------------------------|------------------|
| Cholera Toxin Subunit (Recombinant), Alexa Fluor 594 Conjugate | Thermo Scientific | Cat#C34777 |
| Pierce™ High Capacity Streptavidin Agarose | Thermo Scientific | Cat#20361 |
| Sulfasalazine | Tocris Bioscience | Cat#599-79-1 |
| Lovastatin | Santa Cruz Biotechnology | Cat#75330-75-5 |
| Methyl-β-cyclodextrin | Sigma-Aldrich | Cat#C4555 |
| Cholesterol | Sigma-Aldrich | Cat#C3045 |
| Tert-Butyl hydroperoxide | Sigma-Aldrich | Cat#B2633 |
| Catalase-polyethylene glycol | Sigma Aldrich | Cat#C4963 |
| pHyPer-cyto | Evrogen | Cat#FP941 |
| pHyPer-dMito | Evrogen | Cat#FP942 |
| Geneticin® Selective Antibiotic (G418 Sulfate) | Thermo Scientific | Cat#10131035 |
| Methotrexate hydrate | Sigma-Aldrich | Cat#M8407 |
| CB83 | Gift | |
| Cholesterol, [1,2- ³ H(N)] | PerkinElmer | Cat#NET139001 MC |
| Isopropanol | Fisher Scientific | Cat#A962 |
| Adenosine 3',5'-cyclic monophosphate sodium salt monohydrate | Sigma-Aldrich | Cat#A6885 |
| Critical Commercial Assays | | |
| Pierce BCA Protein Assay Kit | Thermo Scientific | Cat#23225 |
| Western Lightning® Plus-ECL, Enhance Chemiluminescence Substrate | PerkinElmer | Cat#NEL103001 |
| Clarity Western ECL Substrate | Bio-Rad | Cat#1705060 |
| Blue Autoradiography Film | Genemate | Cat#F-9023-8X10 |
| Lipofectamine® 2000 | Thermo Scientific | Cat#11668019 |
| Dialyzed Fetal Bovine Serum | Thermo Scientific | Cat#26400044 |
| Sep-Pak tC18 1 cc Vac Cartridge | Waters | Cat#WAT036820 |
| Roche mini complete EDTA free | Roche | Cat#11836170001 |
| PhosSTOP™ | Roche | Cat#04906837007 |
| Puromycin Dihydrochloride | Thermo Scientific | Cat#A1113802 |
| Crystal violet, 0.5 % stain | Fisher Scientific | Cat# |
| Experimental Models: Cell Lines | | |
| SCC-61 | Ezra Cohen, University of Chicago | |
| rSCC-61 | Cristina Furdui, WFSM | |
| Sequence-Based Reagents | | |
| MTHFD2 shRNA plasmid | Santa Cruz Biotechnology | Cat#sc-75937-SH |
| Control shRNA Plasmid-A | Santa Cruz Biotechnology | Cat#sc-108060 |
| Software and Algorithms | | |
| SIMCA-P 12.0.1 Software | Umetrics | Cat#Q625 |

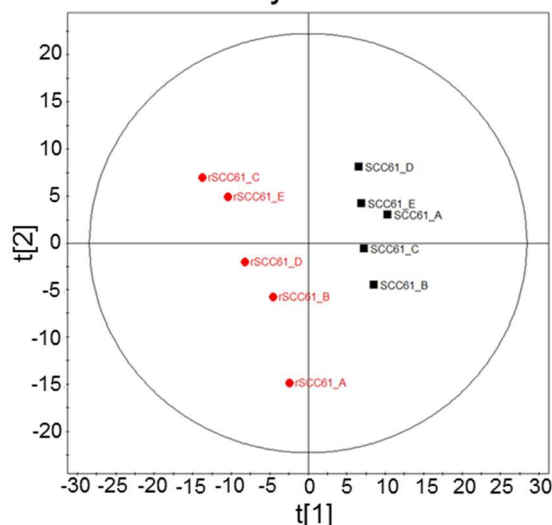
| | | |
|----------------------------|-------------------|----------------------------|
| NIST MS Search v.2.0g | NIST | |
| XCalibur™ v.2.1 Software | Thermo Scientific | Cat#OPTON-20487 |
| Proteome Discoverer™ v.1.4 | Thermo Scientific | Cat#IQLAAEGA BSFAKJMAUH |
| SigmaPlot v.12 Software | SigmaPlot | |
| ChromaTOF-GC Software | Leco | |

Figure 1. Metabolomics Analysis. A. Principal component analysis B. Supervised partial least square discriminant analysis C. Selected list of top 25 differential metabolites in rSCC-61 versus SCC-61 cells

A: PCA Analysis



B: PLS-DA Analysis



C: Selected list of differential metabolites in rSCC-61 versus SCC-61 cells used in computational modeling.

| NO | Compounds name | VIP ^a | <i>p</i> ^b | FC ^c |
|----|----------------------------|------------------|-----------------------|-----------------|
| 1 | Uracil | 1.64 | 1.08E-07 | 0.08 |
| 2 | Guanine | 1.6 | 1.14E-05 | 0.12 |
| 3 | Xanthine | 1.59 | 1.34E-05 | 0.3 |
| 4 | L-Cysteine | 1.53 | 1.74E-04 | 0.38 |
| 5 | Inosine | 1.52 | 2.26E-04 | 0.38 |
| 6 | Thymine | 1.5 | 3.98E-04 | 0.22 |
| 7 | Glutamate | 1.48 | 5.41E-04 | 0.46 |
| 8 | Hypoxanthine | 1.48 | 5.76E-04 | 0.48 |
| 9 | Uridine | 1.46 | 8.30E-04 | 0.22 |
| 10 | Adenosine, 5'-phosphate | 1.4 | 2.32E-03 | 2.53 |
| 11 | Putrescine | 1.4 | 2.44E-03 | 0.27 |
| 12 | Spermidine | 1.39 | 2.61E-03 | 0.51 |
| 13 | phosphate | 1.36 | 3.87E-03 | 1.52 |
| 14 | d-Glucose, phosphate | 1.34 | 4.80E-03 | 2.98 |
| 15 | Hypotaurine | 1.34 | 5.01E-03 | 0.68 |
| 16 | Adenine | 1.31 | 6.93E-03 | 2.25 |
| 17 | Uridine-5'-monophosphate | 1.23 | 1.51E-02 | 1.92 |
| 18 | Guanosine | 1.21 | 1.68E-02 | 0.33 |
| 19 | Glycine | 1.2 | 1.89E-02 | 0.74 |
| 20 | Adenosine | 1.18 | 2.13E-02 | 0.09 |
| 21 | Ornithine | 1.17 | 2.36E-02 | 0.65 |
| 22 | Thymidine 5'-monophosphate | 1.17 | 2.39E-02 | 1.74 |
| 23 | 5-oxoproline | 1.08 | 4.13E-02 | 0.75 |
| 24 | L-Serine | 1.08 | 4.14E-02 | 1.5 |
| 25 | D-Ribose, 5-phosphate | 1.07 | 4.54E-02 | 1.54 |

^a variable importance in the projection (VIP) was obtained from PLS-DA with a threshold of 1.0; ^b *p*-value was calculated from Student's *t* Test; ^c Fold change with a value larger than 1 indicates a relatively higher concentration in the rSCC-61 samples, while a value less than 1 means a relatively lower concentration as compared to SCC-61 samples.

Figure 2. Redox Proteomics. **A.** Biotin-tagged 1, 3-cyclopentanedione (BP1) probe. **B.** nanoLC-MS and MS/MS workflow to label protein sulfenic (Cys-SOH) acids with biotin-tagged BP1 probe and identify 272 redox regulated proteins. **C.** Plot of $\log_2(\text{Normalized rSCC-61 versus SCC-61 ratio})$ to show proteins increased/decreased labeling. **D.** Ingenuity pathway analysis showing (**upper**) distribution of proteins subcellular locations and (**lower**) distribution of molecular functions in redox-regulated proteins in rSCC-61 cells versus SCC-61 cells.

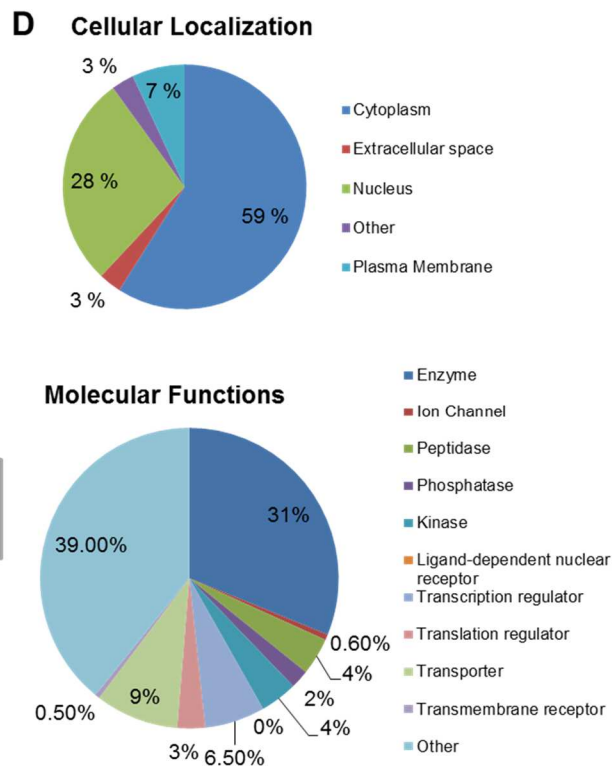
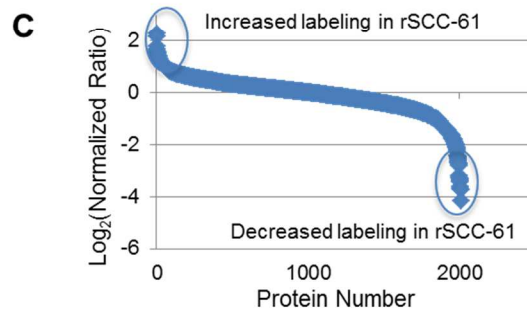
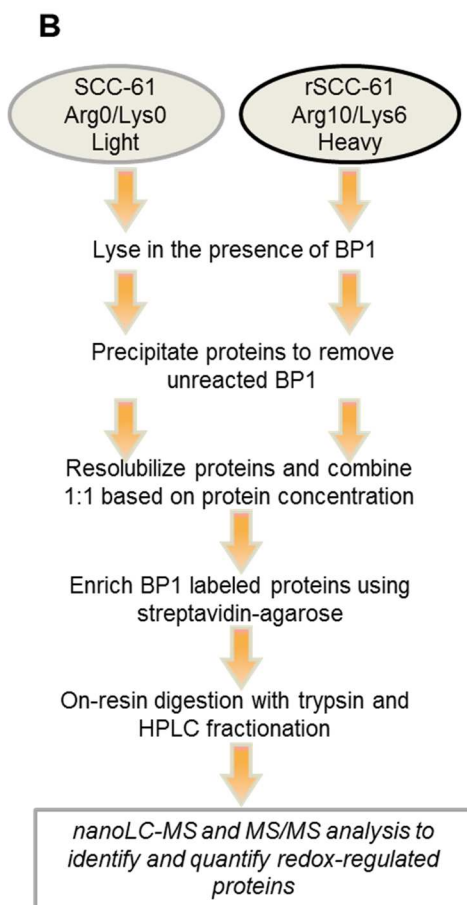
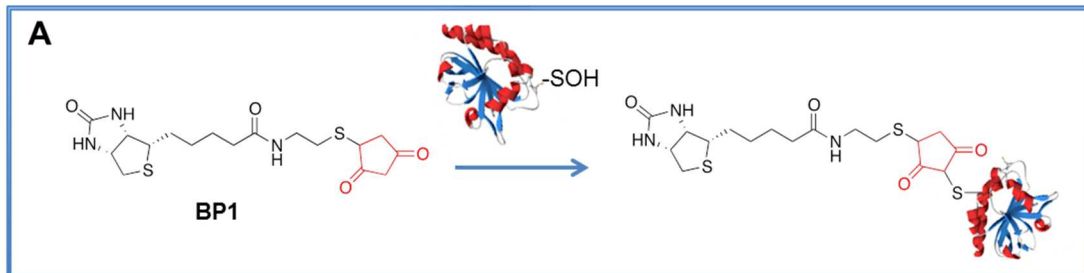


Figure 3. Targeted Western Blot Analysis. **A.** Western blot analysis to determine total protein expression of 5 proteins: TIGAR, TP53, PRX1, PRX-SO_{2/3}, SRX. **B.** Western blot analysis to determine phosphorylation status of 12 proteins: IGFR, JNK1, myc, RPS6, PKC, Akt, PDK1, STAT3, ASK1, LKB1, STAT1, and 4E-BP1. *0.05, **0.01-0.001, ***<0.001

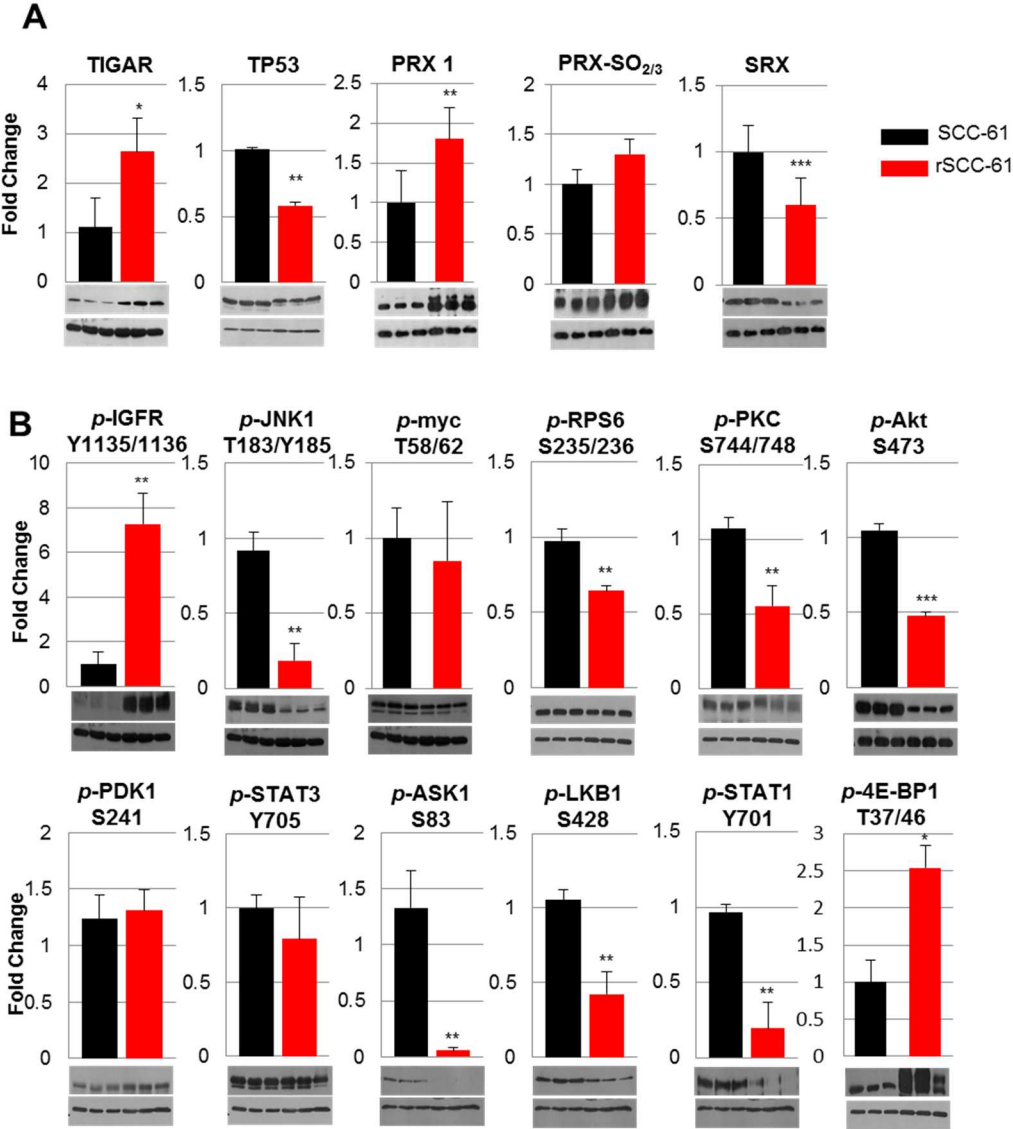


Figure 4. Generic Network. Network composed of integrated signaling and metabolic networks by selecting enriched signaling pathways, metabolic pathways and ROS-regulated pathways using four types of analysis (proteomics, redox proteomics, metabolomics, and protein phosphorylation). Blue circles = enzymes connecting signaling and metabolic pathways. White box = signaling proteins. Orange line = metabolic reactions. --- = ROS-regulated pathways. Blue line = signaling reactions.

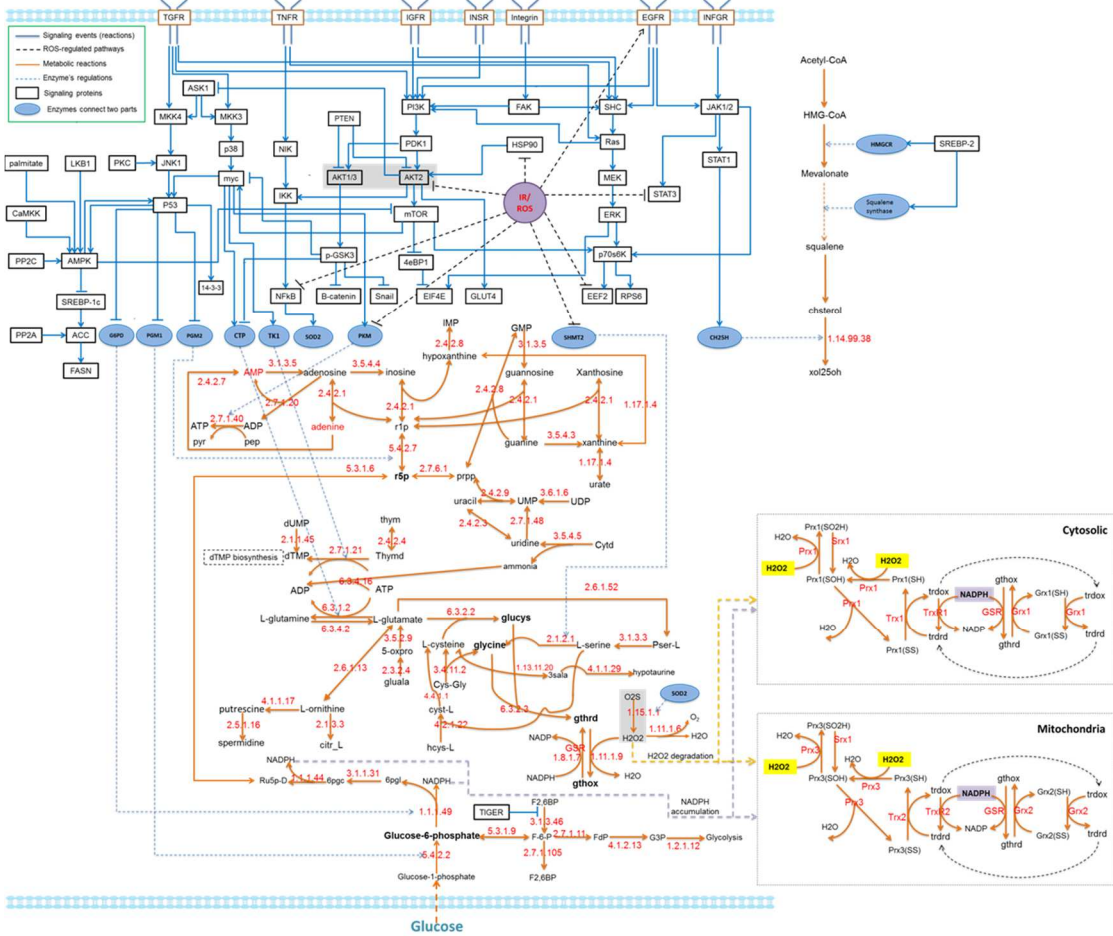
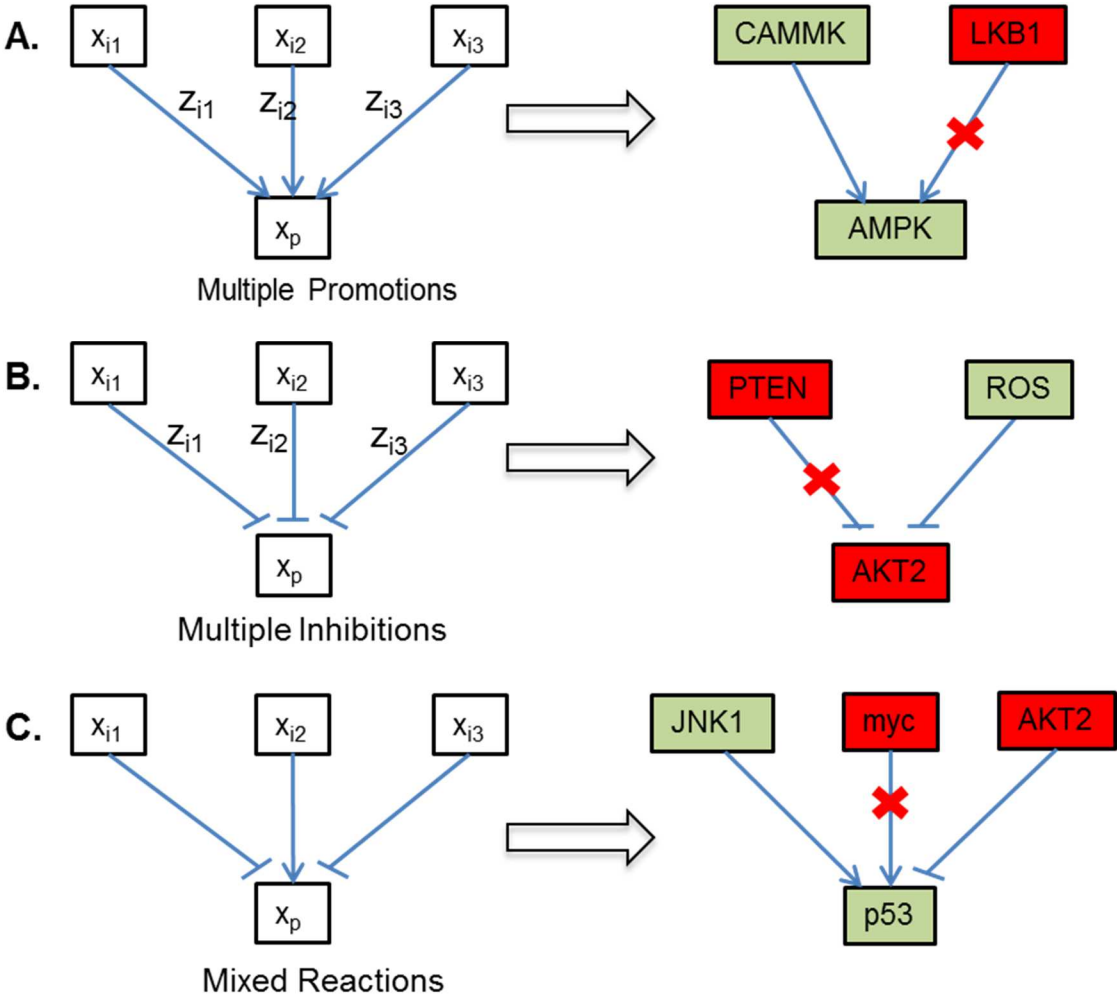


Figure 5. Signaling Sub-Network Represented as a Boolean Network. A. Schematic and example of multiple promotions. B. Schematic and example of multiple inhibitions. C. Schematic and example of mixed reactions.



S6. Cholesterol Synthesis and Trafficking. A. (upper) Schematic of cholesterol synthesis and efflux regulation by SREBP2 and LXR and **(lower)** mRNA expression levels of SREBP2 and LXR target genes extracted from the HumanHT-12 v4 Expression BeadChip data. **B. (left)** Schematic of cholesterol efflux and **(right)** western blot of ABCA1 transporter in SCC-61 cells and rSCC-61 cells with full length ABCA1 as positive control, ABCA1 knockout as negative control and B-actin as loading control. **C.** mRNA expression levels of genes that inactivate SREBP2 extracted from the HumanHT-12 v4 Expression BeadChip data. *0.05, **0.01-0.001, ***<0.001

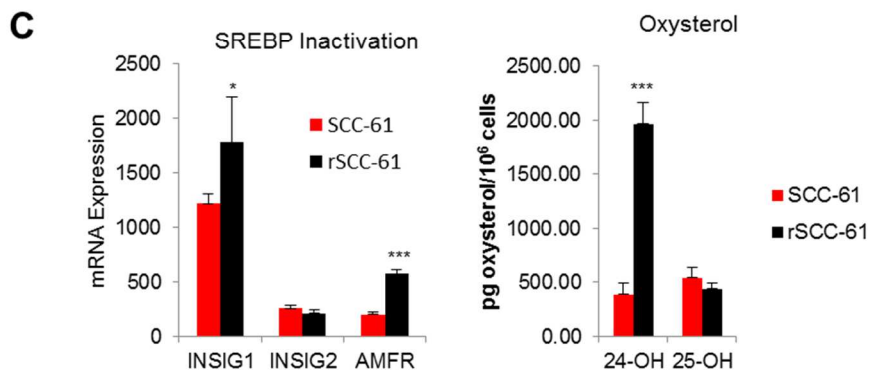
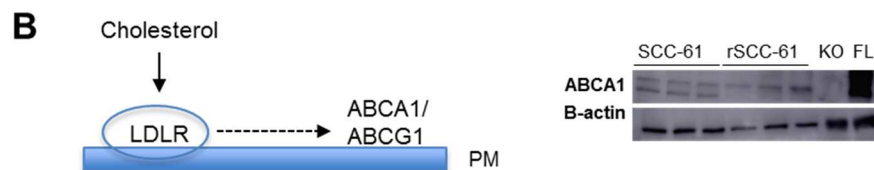
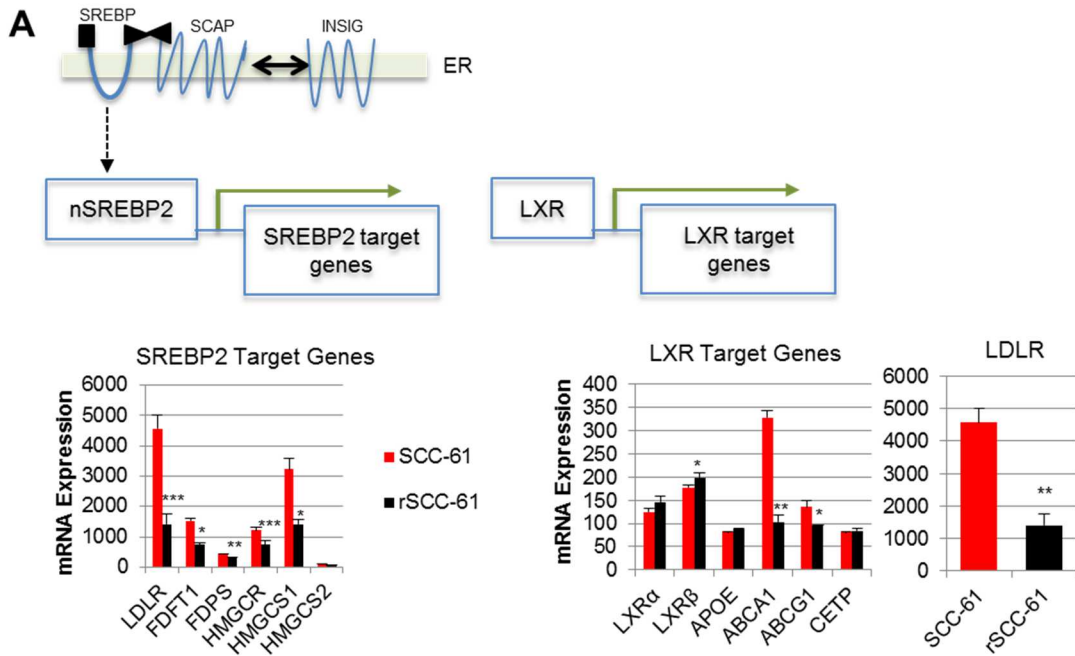


Table 1. The screened redox-sensitive proteins from redox proteomics data.

| Uniprot ID | Proteins | Oxidation Ratio | Description |
|-------------------|-----------------|------------------------|--------------------|
| P40763 | STAT3 | 0.533 | Signaling proteins |
| P00533 | EGFR | 0.637 | Signaling proteins |
| P13639 | EEF2 | 0.554 | Signaling proteins |
| P08238 | HSP90 | 0.969 | Signaling proteins |
| P48506 | GCLC | 3.114 | Metabolic Enzyme |
| P14618 | PKM | 1.228 | Metabolic Enzyme |

Table 2. Redox-regulated pathways.

| NO. | Redox-regulated reactions | Annotations |
|------------|----------------------------------|-------------------------|
| 1 | “IR/ROS” ⊣ STAT3 | PMID: 3226362, 20807804 |
| 2 | “IR/ROS” → EGFR | PMID: 22158416 |
| 3 | “IR/ROS” ⊣ EEF2 | PMID: 18768473 |
| 4 | “IR/ROS” ⊣ HSP90 | PMID: 15579467 |
| 5 | “IR/ROS” ⊣ PKM | PMID: 21275844 |
| 6 | “IR/ROS” ⊣ AKT2 | PMID: 21670275 |
| 7 | “IR/ROS” ⊣ SHMT2 | PMID: 25186948 |
| 8 | “IR/ROS” ⊣ NF-κB | PMID: 1903539 |

Table 3. Validation for the prediction of our optimized specific pathway network on five interested proteins.

| Proteins | Total expression | Phosphorylation | Oxidation | Predicted activity's changes |
|-----------------|-------------------------|------------------------|------------------|-------------------------------------|
| AKT2 | 1 | 0.83 | | Up-regulated |
| GSK-3 | 0.38 | 0.38 | | Down-regulated |
| B-catenin | 1.55 | | | Up-regulated |
| EEF2 | | 1.99 | 0.554 | Up-regulated |
| AMPK | 0.58 | 0.13 | | Down-regulated |

Dataset 1 Redox Proteomics (# AAs – number of amino acids; MW – molecular weight)

| Accession | Description | Score | Coverage | rSCC-61/SCC-61 | # AAs | MW [kDa] | calc. pI |
|-----------|--|-------------|----------|----------------|-------|-------------|-------------|
| P07384 | Calpain-1 catalytic subunit OS=Homo sapiens GN=CAPN1 PE=1 SV=1 - [CAN1_HUMAN] | 37.95 | 1.4 | 9.281537758 | 714 | 81.8381919 | 5.668457031 |
| P43355 | Melanoma-associated antigen 1 OS=Homo sapiens GN=MAGEA1 PE=1 SV=1 - [MAGA1_HUMAN] | 34.28 | 2.91 | 8.318917708 | 309 | 34.32039731 | 4.855957031 |
| P49327 | Fatty acid synthase OS=Homo sapiens GN=FASN PE=1 SV=3 - [FAS_HUMAN] | 21934.56443 | 54.32 | 8.294511584 | 2511 | 273.2543005 | 6.442871094 |
| Q9H3U1 | Protein unc-45 homolog A OS=Homo sapiens GN=UNC45A PE=1 SV=1 - [UN45A_HUMAN] | 431.7350928 | 6.57 | 6.786789767 | 944 | 103.0114943 | 6.074707031 |
| P11586 | C-1-tetrahydrofolate synthase, cytoplasmic OS=Homo sapiens GN=MTHFD1 PE=1 SV=3 - [C1TC_HUMAN] | 2008.812263 | 25.99 | 6.194239569 | 935 | 101.4953107 | 7.298339844 |
| O60814 | Histone H2B type 1-K OS=Homo sapiens GN=HIST1H2BK PE=1 SV=3 - [H2B1K_HUMAN] | 73.10427064 | 7.14 | 5.799126339 | 126 | 13.88156321 | 10.31591797 |
| Q14247 | Src substrate cortactin OS=Homo sapiens GN=CTTN PE=1 SV=2 - [SRC8_HUMAN] | 1652.648416 | 27.09 | 5.09534554 | 550 | 61.54853429 | 5.401855469 |
| P50991 | T-complex protein 1 subunit delta OS=Homo sapiens GN=CCT4 PE=1 SV=4 - [TCPD_HUMAN] | 568.2543526 | 21.15 | 5.061300293 | 539 | 57.88776398 | 7.825683594 |
| Q96DB2 | Histone deacetylase 11 OS=Homo sapiens GN=HDAC11 PE=1 SV=1 - [HDA11_HUMAN] | 24.01 | 4.03 | 4.571011162 | 347 | 39.15848159 | 7.649902344 |
| Q6UB35 | Monofunctional C1-tetrahydrofolate synthase, mitochondrial OS=Homo sapiens GN=MTHFD1L PE=1 SV=1 - [C1TM_HUMAN] | 76.22 | 1.64 | 4.534518038 | 978 | 105.7237418 | 8.060058594 |
| O15067 | Phosphoribosylformylglycinamide synthase OS=Homo sapiens GN=PFAS PE=1 SV=4 - [PUR4_HUMAN] | 782.548165 | 13.53 | 4.18284039 | 1338 | 144.6428974 | 5.757324219 |
| P55060 | Exportin-2 OS=Homo sapiens GN=CSE1L PE=1 SV=3 - [XPO2_HUMAN] | 9398.193934 | 46.45 | 4.027160089 | 971 | 110.3462865 | 5.770019531 |
| P05141 | ADP/ATP translocase 2 OS=Homo sapiens GN=SLC25A5 PE=1 SV=7 - [ADT2_HUMAN] | 1551.93819 | 32.55 | 3.901370239 | 298 | 32.83115249 | 9.686035156 |
| Q99832 | T-complex protein 1 subunit eta OS=Homo sapiens GN=CCT7 PE=1 SV=2 - [TCPH_HUMAN] | 810.37 | 16.21 | 3.879261598 | 543 | 59.32892712 | 7.649902344 |
| P68104 | Elongation factor 1-alpha 1 OS=Homo sapiens GN=EEF1A1 PE=1 SV=1 - [EF1A1_HUMAN] | 4359.556489 | 38.96 | 3.2659644 | 462 | 50.10911075 | 9.012207031 |
| Q9BQE3 | Tubulin alpha-1C chain OS=Homo sapiens GN=TUBA1C PE=1 SV=1 - [TBA1C_HUMAN] | 15837.70879 | 46.55 | 3.260493546 | 449 | 49.86346453 | 5.097167969 |
| Q9NUQ9 | Protein FAM49B OS=Homo sapiens GN=FAM49B PE=1 SV=1 - [FA49B_HUMAN] | 51.95 | 4.01 | 3.242358215 | 324 | 36.72464952 | 6.062011719 |
| Q13435 | Splicing factor 3B subunit 2 OS=Homo sapiens GN=SF3B2 PE=1 SV=2 - [SF3B2_HUMAN] | 194.0837771 | 7.6 | 3.190496007 | 895 | 100.1649822 | 5.668457031 |
| P48506 | Glutamate--cysteine ligase catalytic subunit OS=Homo sapiens GN=GCLC PE=1 SV=2 - [GSH1_HUMAN] | 106.5577404 | 6.28 | 3.114190408 | 637 | 72.71934692 | 6.087402344 |
| P05787 | Keratin, type II cytoskeletal 8 OS=Homo sapiens GN=KRT8 PE=1 SV=7 - [K2C8_HUMAN] | 4239.080268 | 12.01 | 3.047233048 | 483 | 53.6711355 | 5.592285156 |
| Q00839 | Heterogeneous nuclear ribonucleoprotein U OS=Homo sapiens GN=HNRNPU PE=1 SV=6 - [HNRPU_HUMAN] | 636.409961 | 12.48 | 2.989227658 | 825 | 90.52800912 | 5.998535156 |
| P22102 | Trifunctional purine biosynthetic protein adenosine-3 OS=Homo sapiens GN=GART PE=1 SV=1 - [PUR2_HUMAN] | 949.0778177 | 23.27 | 2.987594737 | 1010 | 107.6990051 | 6.697753906 |

| | | | | | | | |
|--------|---|-------------|-------|-------------|------|-------------|-------------|
| P49411 | Elongation factor Tu, mitochondrial OS=Homo sapiens GN=TUFM PE=1 SV=2 - [EFTU_HUMAN] | 217.7461303 | 11.95 | 2.949657004 | 452 | 49.51018362 | 7.605957031 |
| P13489 | Ribonuclease inhibitor OS=Homo sapiens GN=RNH1 PE=1 SV=2 - [RINI_HUMAN] | 205.7914142 | 5.64 | 2.92782334 | 461 | 49.94108966 | 4.817871094 |
| P07814 | Bifunctional glutamate/proline--tRNA ligase OS=Homo sapiens GN=EPRS PE=1 SV=5 - [SYEP_HUMAN] | 183.3697383 | 3.77 | 2.897507976 | 1512 | 170.4831032 | 7.327636719 |
| P56192 | Methionine--tRNA ligase, cytoplasmic OS=Homo sapiens GN=MARS PE=1 SV=2 - [SYMC_HUMAN] | 37.19 | 1.33 | 2.865604059 | 900 | 101.0519105 | 6.163574219 |
| P23396 | 40S ribosomal protein S3 OS=Homo sapiens GN=RPS3 PE=1 SV=2 - [RS3_HUMAN] | 41.45 | 5.35 | 2.846272632 | 243 | 26.67143165 | 9.656738281 |
| P28340 | DNA polymerase delta catalytic subunit OS=Homo sapiens GN=POLD1 PE=1 SV=2 - [DPOD1_HUMAN] | 163.8945012 | 1.9 | 2.79449098 | 1107 | 123.5526066 | 7.034667969 |
| P06748 | Nucleophosmin OS=Homo sapiens GN=NPM1 PE=1 SV=2 - [NPM_HUMAN] | 30.94 | 2.38 | 2.710316345 | 294 | 32.55484332 | 4.779785156 |
| P51003 | Poly(A) polymerase alpha OS=Homo sapiens GN=PAPOLA PE=1 SV=4 - [PAPOA_HUMAN] | 67.9 | 3.22 | 2.69778306 | 745 | 82.79101993 | 7.371582031 |
| P62826 | GTP-binding nuclear protein Ran OS=Homo sapiens GN=RAN PE=1 SV=3 - [RAN_HUMAN] | 80.29 | 9.72 | 2.678591747 | 216 | 24.4076189 | 7.488769531 |
| P52597 | Heterogeneous nuclear ribonucleoprotein F OS=Homo sapiens GN=HNRNPF PE=1 SV=3 - [HNRPF_HUMAN] | 81.45 | 4.1 | 2.502242987 | 415 | 45.64285734 | 5.579589844 |
| P27708 | CAD protein OS=Homo sapiens GN=CAD PE=1 SV=3 - [PYR1_HUMAN] | 541.2958913 | 4.27 | 2.488308241 | 2225 | 242.8294673 | 6.455566406 |
| P31943 | Heterogeneous nuclear ribonucleoprotein H OS=Homo sapiens GN=HNRNPH1 PE=1 SV=4 - [HNRH1_HUMAN] | 77.84 | 3.79 | 2.367135055 | 449 | 49.19841117 | 6.303222656 |
| O14980 | Exportin-1 OS=Homo sapiens GN=XPO1 PE=1 SV=1 - [XPO1_HUMAN] | 2686.807315 | 31.19 | 2.331528324 | 1071 | 123.3061015 | 6.062011719 |
| Q01813 | 6-phosphofructokinase type C OS=Homo sapiens GN=PFKP PE=1 SV=2 - [K6PP_HUMAN] | 35.35 | 1.28 | 2.274708352 | 784 | 85.54153581 | 7.547363281 |
| Q15021 | Condensin complex subunit 1 OS=Homo sapiens GN=NCAPD2 PE=1 SV=3 - [CND1_HUMAN] | 96.97902142 | 0.71 | 2.180407554 | 1401 | 157.0824525 | 6.609863281 |
| P27824 | Calnexin OS=Homo sapiens GN=CANX PE=1 SV=2 - [CALX_HUMAN] | 224.65 | 7.94 | 2.166065498 | 592 | 67.52585354 | 4.602050781 |
| O43719 | HIV Tat-specific factor 1 OS=Homo sapiens GN=HTATSF1 PE=1 SV=1 - [HTSF1_HUMAN] | 48.84 | 2.12 | 2.130271544 | 755 | 85.80056555 | 4.398925781 |
| Q9UJS0 | Calcium-binding mitochondrial carrier protein Aralar2 OS=Homo sapiens GN=SLC25A13 PE=1 SV=2 - [CMC2_HUMAN] | 37.89 | 1.19 | 2.044556148 | 675 | 74.12864688 | 8.616699219 |
| Q5H9R7 | Serine/threonine-protein phosphatase 6 regulatory subunit 3 OS=Homo sapiens GN=PPP6R3 PE=1 SV=2 - [PP6R3_HUMAN] | 191.1 | 4.7 | 2.010061733 | 873 | 97.60763973 | 4.602050781 |
| P26640 | Valine--tRNA ligase OS=Homo sapiens GN=VAR5 PE=1 SV=4 - [SYVC_HUMAN] | 837.4683505 | 14.56 | 2.002696252 | 1264 | 140.3873808 | 7.591308594 |
| P15924 | Desmoplakin OS=Homo sapiens GN=DSP PE=1 SV=3 - [DESP_HUMAN] | 3421.097988 | 19.54 | 1.992490629 | 2871 | 331.568719 | 6.814941406 |
| P41252 | Isoleucine--tRNA ligase, cytoplasmic OS=Homo sapiens GN=IARS PE=1 SV=2 - [SYIC_HUMAN] | 234.9441992 | 5.78 | 1.989992756 | 1262 | 144.4060415 | 6.150878906 |
| Q9P2J5 | Leucine--tRNA ligase, cytoplasmic OS=Homo sapiens GN=LARS PE=1 SV=2 - [SYLC_HUMAN] | 140.0966667 | 4 | 1.971053007 | 1176 | 134.379482 | 7.298339844 |
| Q13509 | Tubulin beta-3 chain OS=Homo sapiens GN=TUBB3 PE=1 SV=2 - [TBB3_HUMAN] | 3684.26095 | 34.67 | 1.945717148 | 450 | 50.40025728 | 4.932128906 |
| Q15393 | Splicing factor 3B subunit 3 OS=Homo sapiens GN=SF3B3 PE=1 SV=4 - [SF3B3_HUMAN] | 55.98 | 1.97 | 1.927335504 | 1217 | 135.4917469 | 5.262207031 |
| Q13085 | Acetyl-CoA carboxylase 1 OS=Homo sapiens GN=ACACA PE=1 SV=2 - | 1481.796753 | 11.68 | 1.90733594 | 2346 | 265.3848622 | 6.366699219 |

| | | | | | | | |
|--------|---|-------------|-------|-------------|------|-------------|-------------|
| | [ACACA_HUMAN] | | | | | | |
| P53992 | Protein transport protein Sec24C OS=Homo sapiens GN=SEC24C PE=1 SV=3 - [SC24C_HUMAN] | 146.2475998 | 5.39 | 1.900925262 | 1094 | 118.2491564 | 7.063964844 |
| P68371 | Tubulin beta-4B chain OS=Homo sapiens GN=TUBB4B PE=1 SV=1 - [TBB4B_HUMAN] | 8395.860469 | 58.88 | 1.886412751 | 445 | 49.79900427 | 4.894042969 |
| O00429 | Dynamin-1-like protein OS=Homo sapiens GN=DNM1L PE=1 SV=2 - [DNM1L_HUMAN] | 83.3295437 | 5.03 | 1.810621225 | 736 | 81.82611638 | 6.814941406 |
| Q9UJC3 | Protein Hook homolog 1 OS=Homo sapiens GN=HOOK1 PE=1 SV=2 - [HOOK1_HUMAN] | 109.23 | 3.85 | 1.810598457 | 728 | 84.59483793 | 5.147949219 |
| Q8TEQ6 | Gem-associated protein 5 OS=Homo sapiens GN=GEMIN5 PE=1 SV=3 - [GEM5_HUMAN] | 66.7 | 1.92 | 1.79462546 | 1508 | 168.4828577 | 6.624511719 |
| P25705 | ATP synthase subunit alpha, mitochondrial OS=Homo sapiens GN=ATP5A1 PE=1 SV=1 - [ATPA_HUMAN] | 108.47 | 6.87 | 1.788928415 | 553 | 59.71359642 | 9.129394531 |
| P17987 | T-complex protein 1 subunit alpha OS=Homo sapiens GN=TCP1 PE=1 SV=1 - [TCPA_HUMAN] | 72.86 | 2.7 | 1.754159688 | 556 | 60.30558528 | 6.112792969 |
| Q06830 | Peroxisredoxin-1 OS=Homo sapiens GN=PRDX1 PE=1 SV=1 - [PRDX1_HUMAN] | 92.69027465 | 10.55 | 1.742072897 | 199 | 22.09627988 | 8.133300781 |
| P49368 | T-complex protein 1 subunit gamma OS=Homo sapiens GN=CCT3 PE=1 SV=4 - [TCPG_HUMAN] | 303.5412517 | 8.62 | 1.69706278 | 545 | 60.49532076 | 6.493652344 |
| P05023 | Sodium/potassium-transporting ATPase subunit alpha-1 OS=Homo sapiens GN=ATP1A1 PE=1 SV=1 - [AT1A1_HUMAN] | 7913.777124 | 41.25 | 1.683398661 | 1023 | 112.8238851 | 5.490722656 |
| Q08J23 | tRNA (cytosine(34)-C(5))- methyltransferase OS=Homo sapiens GN=NSUN2 PE=1 SV=2 - [NSUN2_HUMAN] | 64.7 | 1.43 | 1.67956425 | 767 | 86.41580653 | 6.770996094 |
| O43175 | D-3-phosphoglycerate dehydrogenase OS=Homo sapiens GN=PHGDH PE=1 SV=4 - [SERA_HUMAN] | 953.5097838 | 14.82 | 1.651094387 | 533 | 56.61440725 | 6.712402344 |
| P53396 | ATP-citrate synthase OS=Homo sapiens GN=ACLY PE=1 SV=3 - [ACLY_HUMAN] | 3993.159671 | 41.24 | 1.591365983 | 1101 | 120.7618867 | 7.327636719 |
| P40227 | T-complex protein 1 subunit zeta OS=Homo sapiens GN=CCT6A PE=1 SV=3 - [TCPZ_HUMAN] | 416.6987651 | 8.85 | 1.558948734 | 531 | 57.98760023 | 6.683105469 |
| Q00325 | Phosphate carrier protein, mitochondrial OS=Homo sapiens GN=SLC25A3 PE=1 SV=2 - [MPCP_HUMAN] | 58.86 | 3.31 | 1.553956509 | 362 | 40.06873926 | 9.378417969 |
| O14929 | Histone acetyltransferase type B catalytic subunit OS=Homo sapiens GN=HAT1 PE=1 SV=1 - [HAT1_HUMAN] | 83.18 | 3.1 | 1.548368926 | 419 | 49.48079141 | 5.693847656 |
| Q15149 | Plectin OS=Homo sapiens GN=PLEC PE=1 SV=3 - [PLEC_HUMAN] | 53.34 | 0.79 | 1.523432054 | 4684 | 531.466012 | 5.960449219 |
| P55265 | Double-stranded RNA-specific adenosine deaminase OS=Homo sapiens GN=ADAR PE=1 SV=4 - [DSRAD_HUMAN] | 37.27 | 0.98 | 1.502860351 | 1226 | 135.9808998 | 8.645996094 |
| Q8WUM4 | Programmed cell death 6-interacting protein OS=Homo sapiens GN=PDCD6IP PE=1 SV=1 - [PDC6I_HUMAN] | 379.4484665 | 6.91 | 1.467899608 | 868 | 95.96312482 | 6.521972656 |
| P63261 | Actin, cytoplasmic 2 OS=Homo sapiens GN=ACTG1 PE=1 SV=1 - [ACTG_HUMAN] | 4312.087539 | 51.73 | 1.450036783 | 375 | 41.76579469 | 5.478027344 |
| O75874 | Isocitrate dehydrogenase [NADP] cytoplasmic OS=Homo sapiens GN=IDH1 PE=1 SV=2 - [IDHC_HUMAN] | 400.8312035 | 17.63 | 1.432202081 | 414 | 46.62951655 | 7.005371094 |
| Q9UI26 | Importin-11 OS=Homo sapiens GN=IPO11 PE=1 SV=1 - [IPO11_HUMAN] | 108.6033333 | 2.46 | 1.424658462 | 975 | 112.4627632 | 5.249511719 |
| P38646 | Stress-70 protein, mitochondrial OS=Homo sapiens GN=HSPA9 PE=1 SV=2 - [GRP75_HUMAN] | 53.08 | 1.62 | 1.391909706 | 679 | 73.6347763 | 6.163574219 |
| Q9UL46 | Proteasome activator complex subunit 2 OS=Homo sapiens GN=PSME2 PE=1 SV=4 - [PSME2_HUMAN] | 103.2668304 | 15.9 | 1.381638694 | 239 | 27.38431693 | 5.731933594 |

| | | | | | | | |
|--------|---|-------------|-------|-------------|------|-------------|-------------|
| Q92990 | Glomulin OS=Homo sapiens GN=GLMN PE=1 SV=2 - [GLMN_HUMAN] | 89.71 | 4.55 | 1.360359633 | 594 | 68.16456641 | 5.325683594 |
| P31153 | S-adenosylmethionine synthase isoform type-2 OS=Homo sapiens GN=MAT2A PE=1 SV=1 - [METK2_HUMAN] | 147.1687277 | 3.8 | 1.355768003 | 395 | 43.63333654 | 6.480957031 |
| Q86UP2 | Kinectin OS=Homo sapiens GN=KTN1 PE=1 SV=1 - [KTN1_HUMAN] | 56.07 | 0.88 | 1.338759942 | 1357 | 156.1793111 | 5.643066406 |
| P68363 | Tubulin alpha-1B chain OS=Homo sapiens GN=TUBA1B PE=1 SV=1 - [TBA1B_HUMAN] | 16597.85633 | 55.43 | 1.329831073 | 451 | 50.11960685 | 5.059082031 |
| Q8WWM7 | Ataxin-2-like protein OS=Homo sapiens GN=ATXN2L PE=1 SV=2 - [ATX2L_HUMAN] | 39.39 | 2.14 | 1.325460874 | 1075 | 113.3035467 | 8.587402344 |
| O75694 | Nuclear pore complex protein Nup155 OS=Homo sapiens GN=NUP155 PE=1 SV=1 - [NUI155_HUMAN] | 316.0953516 | 6.47 | 1.316580897 | 1391 | 155.1002762 | 6.163574219 |
| O95347 | Structural maintenance of chromosomes protein 2 OS=Homo sapiens GN=SMC2 PE=1 SV=2 - [SMC2_HUMAN] | 66.50262885 | 1.75 | 1.314540592 | 1197 | 135.5718331 | 8.426269531 |
| Q6NUK1 | Calcium-binding mitochondrial carrier protein SCaMC-1 OS=Homo sapiens GN=SLC25A24 PE=1 SV=2 - [SCMC1_HUMAN] | 56.99 | 3.35 | 1.309853965 | 477 | 53.32034536 | 6.328613281 |
| Q9UBF2 | Coatmer subunit gamma-2 OS=Homo sapiens GN=COPG2 PE=1 SV=1 - [COPG2_HUMAN] | 61.23 | 1.38 | 1.290304517 | 871 | 97.55958744 | 5.808105469 |
| Q12769 | Nuclear pore complex protein Nup160 OS=Homo sapiens GN=NUP160 PE=1 SV=3 - [NUI160_HUMAN] | 42.46 | 1.25 | 1.286588475 | 1436 | 162.0169585 | 5.503417969 |
| P30153 | Serine/threonine-protein phosphatase 2A 65 kDa regulatory subunit A alpha isoform OS=Homo sapiens GN=PPP2R1A PE=1 SV=4 - [2AAA_HUMAN] | 136.1311109 | 7.81 | 1.284010971 | 589 | 65.26691645 | 5.109863281 |
| P52732 | Kinesin-like protein KIF11 OS=Homo sapiens GN=KIF11 PE=1 SV=2 - [KIF11_HUMAN] | 1095.522761 | 20.36 | 1.279022016 | 1056 | 119.0850394 | 5.643066406 |
| P04843 | Dolichyl-diphosphooligosaccharide-- protein glycosyltransferase subunit 1 OS=Homo sapiens GN=RPN1 PE=1 SV=1 - [RPN1_HUMAN] | 129.8555422 | 8.57 | 1.250921149 | 607 | 68.52681096 | 6.379394531 |
| P07437 | Tubulin beta chain OS=Homo sapiens GN=TUBB PE=1 SV=2 - [TBB5_HUMAN] | 8841.768787 | 59.01 | 1.241299738 | 444 | 49.63897361 | 4.894042969 |
| P61978 | Heterogeneous nuclear ribonucleoprotein K OS=Homo sapiens GN=HNRNPK PE=1 SV=1 - [HNRPK_HUMAN] | 181.9243456 | 16.85 | 1.238844611 | 463 | 50.94440521 | 5.541503906 |
| P46060 | Ran GTPase-activating protein 1 OS=Homo sapiens GN=RANGAP1 PE=1 SV=1 - [RAGP1_HUMAN] | 116.5523416 | 4.77 | 1.233805907 | 587 | 63.50230751 | 4.678222656 |
| P14618 | Pyruvate kinase isozymes M1/M2 OS=Homo sapiens GN=PKM PE=1 SV=4 - [KPYM_HUMAN] | 895.2699179 | 25.24 | 1.227920666 | 531 | 57.90002631 | 7.840332031 |
| O43264 | Centromere/kinetochore protein zw10 homolog OS=Homo sapiens GN=ZW10 PE=1 SV=3 - [ZW10_HUMAN] | 236.29 | 4.24 | 1.226737713 | 779 | 88.77287343 | 6.265136719 |
| P43243 | Matrin-3 OS=Homo sapiens GN=MATR3 PE=1 SV=2 - [MATR3_HUMAN] | 48.73 | 2.48 | 1.218439354 | 847 | 94.56480206 | 6.252441406 |
| P52292 | Importin subunit alpha-2 OS=Homo sapiens GN=KPNA2 PE=1 SV=1 - [IMA2_HUMAN] | 52.5 | 2.84 | 1.204720313 | 529 | 57.82594988 | 5.401855469 |
| Q6ZRP7 | Sulfhydryl oxidase 2 OS=Homo sapiens GN=QSOX2 PE=1 SV=3 - [QSOX2_HUMAN] | 139.1 | 2.29 | 1.203737686 | 698 | 77.47961564 | 7.723144531 |
| A5YKK6 | CCR4-NOT transcription complex subunit 1 OS=Homo sapiens GN=CNOT1 PE=1 SV=2 - [CNOT1_HUMAN] | 119.7438696 | 1.09 | 1.1987073 | 2376 | 266.7679086 | 7.107910156 |
| Q92667 | A-kinase anchor protein 1, mitochondrial OS=Homo sapiens GN=AKAP1 PE=1 SV=1 - [AKAP1_HUMAN] | 459.0244444 | 2.66 | 1.197455509 | 903 | 97.28094918 | 4.944824219 |
| O75534 | Cold shock domain-containing protein E1 OS=Homo sapiens GN=CSDE1 PE=1 SV=2 - [CSDE1_HUMAN] | 608.4774664 | 13.41 | 1.196653634 | 798 | 88.82887622 | 6.252441406 |
| Q06323 | Proteasome activator complex subunit 1 OS=Homo sapiens GN=PSME1 PE=1 | 589.6155323 | 22.49 | 1.186778858 | 249 | 28.70501612 | 6.023925781 |

| | | | | | | | |
|--------|---|-------------|-------|-------------|------|-------------|-------------|
| | SV=1 - [PSME1_HUMAN] | | | | | | |
| P42704 | Leucine-rich PPR motif-containing protein, mitochondrial OS=Homo sapiens GN=LRPPRC PE=1 SV=3 - [LRPPRC_HUMAN] | 3459.633002 | 37.45 | 1.169040423 | 1394 | 157.8051234 | 6.125488281 |
| P21333 | Filamin-A OS=Homo sapiens GN=FLNA PE=1 SV=4 - [FLNA_HUMAN] | 5814.167929 | 23.46 | 1.167989229 | 2647 | 280.5638863 | 6.062011719 |
| Q14694 | Ubiquitin carboxyl-terminal hydrolase 10 OS=Homo sapiens GN=USP10 PE=1 SV=2 - [UBP10_HUMAN] | 29.95 | 1.75 | 1.167969347 | 798 | 87.07975952 | 5.312988281 |
| P48643 | T-complex protein 1 subunit epsilon OS=Homo sapiens GN=CCT5 PE=1 SV=1 - [TCPE_HUMAN] | 158.43 | 3.14 | 1.164600167 | 541 | 59.63281064 | 5.655761719 |
| P16615 | Sarcoplasmic/endoplasmic reticulum calcium ATPase 2 OS=Homo sapiens GN=ATP2A2 PE=1 SV=1 - [AT2A2_HUMAN] | 3589.470641 | 28.21 | 1.160256645 | 1042 | 114.6825651 | 5.338378906 |
| P04406 | Glyceraldehyde-3-phosphate dehydrogenase OS=Homo sapiens GN=GAPDH PE=1 SV=3 - [G3P_HUMAN] | 428.3270858 | 8.66 | 1.148095058 | 335 | 36.03039959 | 8.455566406 |
| Q9UP83 | Conserved oligomeric Golgi complex subunit 5 OS=Homo sapiens GN=COG5 PE=1 SV=3 - [COG5_HUMAN] | 89.86 | 1.67 | 1.143024056 | 839 | 92.68479971 | 6.595214844 |
| P50454 | Serpin H1 OS=Homo sapiens GN=SERPINH1 PE=1 SV=2 - [SERPH_HUMAN] | 52.07 | 6.22 | 1.073408863 | 418 | 46.41117943 | 8.689941406 |
| P46940 | Ras GTPase-activating-like protein IQGAP1 OS=Homo sapiens GN=IQGAP1 PE=1 SV=1 - [IQGAP1_HUMAN] | 2099.809166 | 18.11 | 1.053247615 | 1657 | 189.1338062 | 6.480957031 |
| Q9BSJ8 | Extended synaptotagmin-1 OS=Homo sapiens GN=ESYT1 PE=1 SV=1 - [ESYT1_HUMAN] | 255.6549351 | 3.89 | 1.023201159 | 1104 | 122.7799541 | 5.833496094 |
| O60506 | Heterogeneous nuclear ribonucleoprotein Q OS=Homo sapiens GN=SYNCRIP PE=1 SV=2 - [HNRPQ_HUMAN] | 320.0105751 | 7.7 | 1.018163015 | 623 | 69.55960051 | 8.587402344 |
| P23526 | Adenosylhomocysteinase OS=Homo sapiens GN=AHCY PE=1 SV=4 - [SAHH_HUMAN] | 96.34 | 2.78 | 1.017486555 | 432 | 47.68520607 | 6.341308594 |
| O75153 | Clustered mitochondria protein homolog OS=Homo sapiens GN=CLUH PE=1 SV=2 - [CLU_HUMAN] | 652.4511871 | 8.71 | 1.000242787 | 1309 | 146.577167 | 6.125488281 |
| Q04637 | Eukaryotic translation initiation factor 4 gamma 1 OS=Homo sapiens GN=EIF4G1 PE=1 SV=4 - [IF4G1_HUMAN] | 43.88 | 0.56 | 0.999757272 | 1599 | 175.3822744 | 5.325683594 |
| O00148 | ATP-dependent RNA helicase DDX39A OS=Homo sapiens GN=DDX39A PE=1 SV=2 - [DX39A_HUMAN] | 48.12 | 2.34 | 0.995620196 | 427 | 49.09795769 | 5.681152344 |
| Q96P70 | Importin-9 OS=Homo sapiens GN=IPO9 PE=1 SV=3 - [IPO9_HUMAN] | 1397.253333 | 16.81 | 0.982375309 | 1041 | 115.8887431 | 4.805175781 |
| Q15365 | Poly(rC)-binding protein 1 OS=Homo sapiens GN=PCBP1 PE=1 SV=2 - [PCBP1_HUMAN] | 267.4627416 | 11.52 | 0.973126377 | 356 | 37.47394517 | 7.093261719 |
| P08238 | Heat shock protein HSP 90-beta OS=Homo sapiens GN=HSP90AB1 PE=1 SV=4 - [HS90B_HUMAN] | 6190.378751 | 38.67 | 0.969497805 | 724 | 83.21210592 | 5.033691406 |
| Q92973 | Transportin-1 OS=Homo sapiens GN=TNPO1 PE=1 SV=2 - [TNPO1_HUMAN] | 1911.196341 | 21.71 | 0.967685404 | 898 | 102.2887863 | 4.982910156 |
| P10809 | 60 kDa heat shock protein, mitochondrial OS=Homo sapiens GN=HSPD1 PE=1 SV=2 - [CH60_HUMAN] | 4102.480735 | 47.99 | 0.954117285 | 573 | 61.01638505 | 5.871582031 |
| O14974 | Protein phosphatase 1 regulatory subunit 12A OS=Homo sapiens GN=PPP1R12A PE=1 SV=1 - [MYPT1_HUMAN] | 203.24 | 1.65 | 0.933172614 | 1030 | 115.2113165 | 5.401855469 |
| Q8TEX9 | Importin-4 OS=Homo sapiens GN=IPO4 PE=1 SV=2 - [IPO4_HUMAN] | 2342.114948 | 27.38 | 0.92884343 | 1081 | 118.6395571 | 4.957519531 |
| Q58FF6 | Putative heat shock protein HSP 90-beta 4 OS=Homo sapiens GN=HSP90AB4P PE=5 SV=1 - [H90B4_HUMAN] | 272.1428101 | 5.15 | 0.927822025 | 505 | 58.22758048 | 4.729003906 |
| Q93009 | Ubiquitin carboxyl-terminal hydrolase 7 OS=Homo sapiens GN=USP7 PE=1 SV=2 - [UBP7_HUMAN] | 174.57 | 3.27 | 0.920438086 | 1102 | 128.2203389 | 5.554199219 |
| Q6PIU2 | Neutral cholesterol ester hydrolase 1 | 610.3320592 | 10.05 | 0.919341435 | 408 | 45.77873015 | 7.225097656 |

| | | | | | | | |
|--------|--|-------------|-------|-------------|------|-------------|-------------|
| | OS=Homo sapiens GN=NCEH1 PE=1 SV=3 - [NCEH1_HUMAN] | | | | | | |
| P45880 | Voltage-dependent anion-selective channel protein 2 OS=Homo sapiens GN=VDAC2 PE=1 SV=2 - [VDAC2_HUMAN] | 478.5372958 | 28.57 | 0.912110597 | 294 | 31.54654776 | 7.562011719 |
| P07900 | Heat shock protein HSP 90-alpha OS=Homo sapiens GN=HSP90AA1 PE=1 SV=5 - [HS90A_HUMAN] | 3362.02908 | 17.08 | 0.87106352 | 732 | 84.60668521 | 5.020996094 |
| Q9Y490 | Talin-1 OS=Homo sapiens GN=TLN1 PE=1 SV=3 - [TLN1_HUMAN] | 1637.643692 | 11.73 | 0.867851014 | 2541 | 269.5990627 | 6.074707031 |
| O15027 | Protein transport protein Sec16A OS=Homo sapiens GN=SEC16A PE=1 SV=3 - [SC16A_HUMAN] | 30.93 | 0.5 | 0.865541988 | 2179 | 233.3725181 | 5.630371094 |
| P68032 | Actin, alpha cardiac muscle 1 OS=Homo sapiens GN=ACTC1 PE=1 SV=1 - [ACTC_HUMAN] | 2634.248811 | 24.93 | 0.847724074 | 377 | 41.99188264 | 5.389160156 |
| Q00610 | Clathrin heavy chain 1 OS=Homo sapiens GN=CLTC PE=1 SV=5 - [CLH1_HUMAN] | 876.089429 | 10.93 | 0.840324811 | 1675 | 191.4925326 | 5.693847656 |
| P42166 | Lamina-associated polypeptide 2, isoform alpha OS=Homo sapiens GN=TMPO PE=1 SV=2 - [LAP2A_HUMAN] | 347.7670792 | 8.79 | 0.832563674 | 694 | 75.44563409 | 7.664550781 |
| P11142 | Heat shock cognate 71 kDa protein OS=Homo sapiens GN=HSPA8 PE=1 SV=1 - [HSP7C_HUMAN] | 982.5814502 | 13.31 | 0.797363865 | 646 | 70.8542269 | 5.516113281 |
| P35221 | Catenin alpha-1 OS=Homo sapiens GN=CTNNA1 PE=1 SV=1 - [CTNA1_HUMAN] | 258.5895579 | 5.19 | 0.791412397 | 906 | 100.0085301 | 6.290527344 |
| Q659C4 | La-related protein 1B OS=Homo sapiens GN=LARP1B PE=1 SV=2 - [LAR1B_HUMAN] | 74.49 | 1.53 | 0.777499756 | 914 | 105.2574839 | 7.605957031 |
| Q01650 | Large neutral amino acids transporter small subunit 1 OS=Homo sapiens GN=SLC7A5 PE=1 SV=2 - [LAT1_HUMAN] | 288.08 | 6.71 | 0.761793019 | 507 | 54.97428151 | 7.723144531 |
| Q5T6F2 | Ubiquitin-associated protein 2 OS=Homo sapiens GN=UBAP2 PE=1 SV=1 - [UBAP2_HUMAN] | 39.03 | 1.34 | 0.73346086 | 1119 | 117.0439184 | 7.342285156 |
| P58107 | Epiplakin OS=Homo sapiens GN=EPPK1 PE=1 SV=2 - [EPIPL_HUMAN] | 2103.977754 | 14.56 | 0.724278224 | 5090 | 555.2790018 | 5.604980469 |
| Q14974 | Importin subunit beta-1 OS=Homo sapiens GN=KPNB1 PE=1 SV=2 - [IMB1_HUMAN] | 7019.082613 | 41.55 | 0.711075461 | 876 | 97.10801929 | 4.779785156 |
| Q92945 | Far upstream element-binding protein 2 OS=Homo sapiens GN=KHSRP PE=1 SV=4 - [FUBP2_HUMAN] | 657.082487 | 14.06 | 0.70678432 | 711 | 73.07002776 | 7.298339844 |
| Q15366 | Poly(rC)-binding protein 2 OS=Homo sapiens GN=PCBP2 PE=1 SV=1 - [PCBP2_HUMAN] | 119.05 | 6.85 | 0.702356904 | 365 | 38.55559337 | 6.785644531 |
| Q14139 | Ubiquitin conjugation factor E4 A OS=Homo sapiens GN=UBE4A PE=1 SV=2 - [UBE4A_HUMAN] | 149.28 | 4.13 | 0.69278349 | 1066 | 122.4819766 | 5.236816406 |
| P22223 | Cadherin-3 OS=Homo sapiens GN=CDH3 PE=1 SV=2 - [CADH3_HUMAN] | 126.9966667 | 3.62 | 0.690229798 | 829 | 91.36159599 | 4.754394531 |
| P49736 | DNA replication licensing factor MCM2 OS=Homo sapiens GN=MCM2 PE=1 SV=4 - [MCM2_HUMAN] | 75.53 | 1.44 | 0.679716428 | 904 | 101.8321629 | 5.516113281 |
| Q6P2E9 | Enhancer of mRNA-decapping protein 4 OS=Homo sapiens GN=EDC4 PE=1 SV=1 - [EDC4_HUMAN] | 75 | 1.14 | 0.671034841 | 1401 | 151.5666899 | 5.858886719 |
| Q8TCT9 | Minor histocompatibility antigen H13 OS=Homo sapiens GN=HM13 PE=1 SV=1 - [HM13_HUMAN] | 62.39906709 | 2.39 | 0.670841974 | 377 | 41.46155063 | 6.430175781 |
| O43847 | Nardilysin OS=Homo sapiens GN=NRD1 PE=1 SV=2 - [NRDC_HUMAN] | 29.58 | 1.04 | 0.65987522 | 1150 | 131.488496 | 4.995605469 |
| P63010 | AP-2 complex subunit beta OS=Homo sapiens GN=AP2B1 PE=1 SV=1 - [AP2B1_HUMAN] | 38.9 | 2.24 | 0.654141079 | 937 | 104.4860467 | 5.376464844 |
| Q9Y5L0 | Transportin-3 OS=Homo sapiens GN=TNPO3 PE=1 SV=3 - [TNPO3_HUMAN] | 98.72229901 | 1.84 | 0.650286017 | 923 | 104.1360787 | 5.566894531 |
| Q86VP6 | Cullin-associated NEDD8-dissociated protein 1 OS=Homo sapiens | 5083.260229 | 37.07 | 0.646898324 | 1230 | 136.288666 | 5.782714844 |

| | | | | | | | |
|--------|--|-------------|-------|-------------|------|-------------|-------------|
| | GN=CAND1 PE=1 SV=2 - [CAND1_HUMAN] | | | | | | |
| Q04695 | Keratin, type I cytoskeletal 17 OS=Homo sapiens GN=KRT17 PE=1 SV=2 - [K1C17_HUMAN] | 3113.256146 | 19.21 | 0.641006113 | 432 | 48.07604632 | 5.020996094 |
| P00533 | Epidermal growth factor receptor OS=Homo sapiens GN=EGFR PE=1 SV=2 - [EGFR_HUMAN] | 159.032191 | 2.89 | 0.637633045 | 1210 | 134.190257 | 6.683105469 |
| Q9BZQ8 | Protein Niban OS=Homo sapiens GN=FAM129A PE=1 SV=1 - [NIBAN_HUMAN] | 216.78 | 2.91 | 0.634051857 | 928 | 103.0700066 | 4.779785156 |
| Q96RU2 | Ubiquitin carboxyl-terminal hydrolase 28 OS=Homo sapiens GN=USP28 PE=1 SV=1 - [UBP28_HUMAN] | 74.43 | 2.14 | 0.631593648 | 1077 | 122.4136649 | 5.198730469 |
| O60518 | Ran-binding protein 6 OS=Homo sapiens GN=RANBP6 PE=1 SV=2 - [RANBP6_HUMAN] | 392.8466667 | 4.71 | 0.614017046 | 1105 | 124.6333321 | 5.008300781 |
| Q14008 | Cytoskeleton-associated protein 5 OS=Homo sapiens GN=CKAP5 PE=1 SV=3 - [CKAP5_HUMAN] | 273.7035478 | 2.76 | 0.611510768 | 2032 | 225.3517848 | 7.796386719 |
| P02786 | Transferrin receptor protein 1 OS=Homo sapiens GN=TFRC PE=1 SV=2 - [TFR1_HUMAN] | 88.88833458 | 1.84 | 0.604782884 | 760 | 84.81794733 | 6.609863281 |
| P22314 | Ubiquitin-like modifier-activating enzyme 1 OS=Homo sapiens GN=UBA1 PE=1 SV=3 - [UBA1_HUMAN] | 209.4248263 | 4.25 | 0.580709754 | 1058 | 117.7743346 | 5.757324219 |
| P13639 | Elongation factor 2 OS=Homo sapiens GN=EEF2 PE=1 SV=4 - [EF2_HUMAN] | 5719.858382 | 42.07 | 0.553776281 | 858 | 95.27695382 | 6.829589844 |
| O95373 | Importin-7 OS=Homo sapiens GN=IPO7 PE=1 SV=1 - [IPO7_HUMAN] | 6431.674561 | 38.15 | 0.545477345 | 1038 | 119.4398756 | 4.817871094 |
| Q9NZM1 | Myoferlin OS=Homo sapiens GN=MYOF PE=1 SV=1 - [MYOF_HUMAN] | 568.0048659 | 6.94 | 0.541528145 | 2061 | 234.5606126 | 6.176269531 |
| Q92797 | Symplekin OS=Homo sapiens GN=SYMPK PE=1 SV=2 - [SYMPK_HUMAN] | 40.62 | 1.81 | 0.516853191 | 1274 | 141.0592116 | 6.125488281 |
| Q9Y3P9 | Rab GTPase-activating protein 1 OS=Homo sapiens GN=RABGAP1 PE=1 SV=3 - [RBGP1_HUMAN] | 73.18 | 2.62 | 0.514894693 | 1069 | 121.6604259 | 5.249511719 |
| P08865 | 40S ribosomal protein SA OS=Homo sapiens GN=RPSA PE=1 SV=4 - [RSSA_HUMAN] | 81.35 | 4.41 | 0.511731915 | 295 | 32.83343464 | 4.868652344 |
| Q04206 | Transcription factor p65 OS=Homo sapiens GN=RELA PE=1 SV=2 - [TF65_HUMAN] | 53.86 | 4.17 | 0.501724967 | 551 | 60.18137974 | 5.681152344 |
| P60842 | Eukaryotic initiation factor 4A-1 OS=Homo sapiens GN=EIF4A1 PE=1 SV=1 - [IF4A1_HUMAN] | 93.04373328 | 5.17 | 0.491603526 | 406 | 46.12455781 | 5.478027344 |
| P06733 | Alpha-enolase OS=Homo sapiens GN=ENO1 PE=1 SV=2 - [ENOA_HUMAN] | 759.3534411 | 17.51 | 0.489051116 | 434 | 47.13932161 | 7.386230469 |
| O15118 | Niemann-Pick C1 protein OS=Homo sapiens GN=NPC1 PE=1 SV=2 - [NPC1_HUMAN] | 83.49 | 0.94 | 0.48643706 | 1278 | 142.0735604 | 5.363769531 |
| P35579 | Myosin-9 OS=Homo sapiens GN=MYH9 PE=1 SV=4 - [MYH9_HUMAN] | 83.78 | 1.02 | 0.466615596 | 1960 | 226.3916023 | 5.604980469 |
| O75369 | Filamin-B OS=Homo sapiens GN=FLNB PE=1 SV=2 - [FLNB_HUMAN] | 2798.750091 | 14.68 | 0.462727297 | 2602 | 277.990071 | 5.731933594 |
| Q00341 | Vigilin OS=Homo sapiens GN=HDLBP PE=1 SV=2 - [VIGLN_HUMAN] | 244.9450973 | 3.39 | 0.452427639 | 1268 | 141.3681479 | 6.873535156 |
| P62937 | Peptidyl-prolyl cis-trans isomerase A OS=Homo sapiens GN=PPIA PE=1 SV=2 - [PPIA_HUMAN] | 111.6273752 | 10.91 | 0.450273165 | 165 | 18.00088618 | 7.811035156 |
| O43156 | TELO2-interacting protein 1 homolog OS=Homo sapiens GN=TTI1 PE=1 SV=3 - [TTI1_HUMAN] | 137.6155252 | 1.19 | 0.449918633 | 1089 | 121.9916998 | 5.973144531 |
| P40763 | Signal transducer and activator of transcription 3 OS=Homo sapiens GN=STAT3 PE=1 SV=2 - [STAT3_HUMAN] | 214.6633333 | 5.58 | 0.444057083 | 770 | 88.01138051 | 6.303222656 |
| Q9NV11 | Fanconi anemia group 1 protein OS=Homo sapiens GN=FANCI PE=1 SV=4 - [FANCI_HUMAN] | 108.5087875 | 1.13 | 0.443947192 | 1328 | 149.2289812 | 6.741699219 |
| P16144 | Integrin beta-4 OS=Homo sapiens GN=ITGB4 PE=1 SV=5 - [ITB4_HUMAN] | 222.457001 | 4.61 | 0.43437887 | 1822 | 202.0386432 | 6.087402344 |

| | | | | | | | |
|--------|---|-------------|-------|-------------|------|-------------|-------------|
| P0CG48 | Polyubiquitin-C OS=Homo sapiens GN=UBC PE=1 SV=3 - [UBC_HUMAN] | 1335.300373 | 44.67 | 0.422603315 | 685 | 76.99153793 | 7.664550781 |
| P12814 | Alpha-actinin-1 OS=Homo sapiens GN=ACTN1 PE=1 SV=2 - [ACTN1_HUMAN] | 281.7355609 | 4.26 | 0.417197934 | 892 | 102.9926373 | 5.414550781 |
| P08195 | 4F2 cell-surface antigen heavy chain OS=Homo sapiens GN=SLC3A2 PE=1 SV=3 - [4F2_HUMAN] | 1371.35418 | 21.11 | 0.413681898 | 630 | 67.9517307 | 5.008300781 |
| O00410 | Importin-5 OS=Homo sapiens GN=IPOS PE=1 SV=4 - [IPOS_HUMAN] | 8430.713181 | 44.94 | 0.410781005 | 1097 | 123.5498651 | 4.944824219 |
| Q96JB2 | Conserved oligomeric Golgi complex subunit 3 OS=Homo sapiens GN=COG3 PE=1 SV=3 - [COG3_HUMAN] | 98.91145756 | 1.81 | 0.409599155 | 828 | 94.03633732 | 5.566894531 |
| O43592 | Exportin-T OS=Homo sapiens GN=XPOT PE=1 SV=2 - [XPOT_HUMAN] | 62.29 | 1.56 | 0.405292367 | 962 | 109.8933046 | 5.389160156 |
| P49588 | Alanine--tRNA ligase, cytoplasmic OS=Homo sapiens GN=AARS PE=1 SV=2 - [SYAC_HUMAN] | 2269.756535 | 21.59 | 0.405109635 | 968 | 106.7432296 | 5.528808594 |
| Q9UIA9 | Exportin-7 OS=Homo sapiens GN=XPO7 PE=1 SV=3 - [XPO7_HUMAN] | 73.91 | 1.38 | 0.401056613 | 1087 | 123.8279817 | 6.315917969 |
| P27816 | Microtubule-associated protein 4 OS=Homo sapiens GN=MAP4 PE=1 SV=3 - [MAP4_HUMAN] | 92.04931773 | 3.82 | 0.395803607 | 1152 | 120.9298323 | 5.427246094 |
| P02545 | Prelamin-A/C OS=Homo sapiens GN=LMNA PE=1 SV=1 - [LMNA_HUMAN] | 188.2486208 | 5.87 | 0.394518154 | 664 | 74.09471168 | 7.020019531 |
| Q9Y6E2 | Basic leucine zipper and W2 domain- containing protein 2 OS=Homo sapiens GN=BZW2 PE=1 SV=1 - [BZW2_HUMAN] | 76.69983407 | 4.77 | 0.378957017 | 419 | 48.13197517 | 6.683105469 |
| Q9NQW6 | Actin-binding protein anillin OS=Homo sapiens GN=ANLN PE=1 SV=2 - [ANLN_HUMAN] | 275.6685151 | 7.38 | 0.378818955 | 1124 | 124.121876 | 8.074707031 |
| P20810 | Calpastatin OS=Homo sapiens GN=CAST PE=1 SV=4 - [ICAL_HUMAN] | 187.4698638 | 4.8 | 0.374646575 | 708 | 76.52627137 | 5.071777344 |
| P11021 | 78 kDa glucose-regulated protein OS=Homo sapiens GN=HSPA5 PE=1 SV=2 - [GRP78_HUMAN] | 574.6037819 | 10.4 | 0.374245702 | 654 | 72.28843987 | 5.160644531 |
| P13797 | Plastin-3 OS=Homo sapiens GN=PLS3 PE=1 SV=4 - [PLST_HUMAN] | 114.0801837 | 2.86 | 0.372738655 | 630 | 70.76621213 | 5.604980469 |
| Q07157 | Tight junction protein ZO-1 OS=Homo sapiens GN=TJP1 PE=1 SV=3 - [ZO1_HUMAN] | 43.31 | 0.74 | 0.363871239 | 1748 | 195.3399768 | 6.697753906 |
| Q9C0E2 | Exportin-4 OS=Homo sapiens GN=XPO4 PE=1 SV=2 - [XPO4_HUMAN] | 159.4760926 | 4.87 | 0.357588209 | 1151 | 130.0562555 | 5.046386719 |
| Q96R06 | Sperm-associated antigen 5 OS=Homo sapiens GN=SPAG5 PE=1 SV=2 - [SPAG5_HUMAN] | 101.85 | 2.35 | 0.352433722 | 1193 | 134.3378056 | 4.995605469 |
| O60664 | Perilipin-3 OS=Homo sapiens GN=PLIN3 PE=1 SV=3 - [PLIN3_HUMAN] | 313.8581104 | 11.06 | 0.347746628 | 434 | 47.04594807 | 5.439941406 |
| Q8N4X5 | Actin filament-associated protein 1-like 2 OS=Homo sapiens GN=AFAP1L2 PE=1 SV=1 - [AF1L2_HUMAN] | 105.8357866 | 4.28 | 0.337522791 | 818 | 91.24311538 | 5.312988281 |
| O43143 | Putative pre-mRNA-splicing factor ATP- dependent RNA helicase DHX15 OS=Homo sapiens GN=DHX15 PE=1 SV=2 - [DHX15_HUMAN] | 74.4 | 1.51 | 0.301437631 | 795 | 90.87516973 | 7.459472656 |
| Q6P179 | Endoplasmic reticulum aminopeptidase 2 OS=Homo sapiens GN=ERAP2 PE=1 SV=2 - [ERAP2_HUMAN] | 51.79 | 1.35 | 0.297272234 | 960 | 110.3911009 | 6.712402344 |
| Q9C0C2 | 182 kDa tankyrase-1-binding protein OS=Homo sapiens GN=TNKS1BP1 PE=1 SV=4 - [TB182_HUMAN] | 239.1704934 | 2.14 | 0.295299331 | 1729 | 181.6850283 | 4.855957031 |
| Q01970 | 1-phosphatidylinositol 4,5-bisphosphate phosphodiesterase beta-3 OS=Homo sapiens GN=PLCB3 PE=1 SV=2 - [PLCB3_HUMAN] | 31.5 | 1.62 | 0.289812273 | 1234 | 138.71272 | 5.896972656 |
| P14923 | Junction plakoglobin OS=Homo sapiens GN=JUP PE=1 SV=3 - [PLAK_HUMAN] | 87.85241083 | 4.16 | 0.289379583 | 745 | 81.692734 | 6.138183594 |
| P53618 | Coatomer subunit beta OS=Homo sapiens GN=COPB1 PE=1 SV=3 - | 108.06 | 1.89 | 0.286211521 | 953 | 107.0737539 | 6.049316406 |

| | | | | | | | |
|--------|--|-------------|-------|-------------|------|-------------|-------------|
| | [COPB_HUMAN] | | | | | | |
| Q9NQC3 | Reticulon-4 OS=Homo sapiens GN=RTN4 PE=1 SV=2 - [RTN4_HUMAN] | 63.90072035 | 1.09 | 0.258438484 | 1192 | 129.8511941 | 4.500488281 |
| A6NMY6 | Putative annexin A2-like protein OS=Homo sapiens GN=ANXA2P2 PE=5 SV=2 - [AXA2L_HUMAN] | 118.6288059 | 7.96 | 0.243051486 | 339 | 38.63482876 | 6.946777344 |
| P78527 | DNA-dependent protein kinase catalytic subunit OS=Homo sapiens GN=PRKDC PE=1 SV=3 - [PRKDC_HUMAN] | 60.98 | 0.34 | 0.242502725 | 4128 | 468.7879323 | 7.122558594 |
| Q92616 | Translational activator GCN1 OS=Homo sapiens GN=GCN1L1 PE=1 SV=6 - [GCN1L_HUMAN] | 477.1613169 | 5.24 | 0.194259349 | 2671 | 292.5724832 | 7.474121094 |
| Q96TA1 | Niban-like protein 1 OS=Homo sapiens GN=FAM129B PE=1 SV=3 - [NIBL1_HUMAN] | 117.8439121 | 5.63 | 0.175893877 | 746 | 84.08472636 | 6.188964844 |
| Q13751 | Laminin subunit beta-3 OS=Homo sapiens GN=LAMB3 PE=1 SV=1 - [LAMB3_HUMAN] | 509.3413333 | 10.41 | 0.16677581 | 1172 | 129.4886098 | 7.210449219 |
| Q13200 | 26S proteasome non-ATPase regulatory subunit 2 OS=Homo sapiens GN=PSMD2 PE=1 SV=3 - [PSMD2_HUMAN] | 160.7623875 | 3.96 | 0.16315673 | 908 | 100.1357944 | 5.198730469 |
| Q7L1Q6 | Basic leucine zipper and W2 domain- containing protein 1 OS=Homo sapiens GN=BZW1 PE=1 SV=1 - [BZW1_HUMAN] | 195.6224869 | 10.5 | 0.153626757 | 419 | 48.01274847 | 5.922363281 |
| Q9UMD9 | Collagen alpha-1(XVII) chain OS=Homo sapiens GN=COL17A1 PE=1 SV=3 - [COHA1_HUMAN] | 335.2407848 | 5.48 | 0.149295329 | 1497 | 150.3264977 | 8.792480469 |
| Q9BYX2 | TBC1 domain family member 2A OS=Homo sapiens GN=TBC1D2 PE=1 SV=3 - [TBD2A_HUMAN] | 32.15 | 2.59 | 0.141418102 | 928 | 105.3480384 | 6.580566406 |
| P04083 | Annexin A1 OS=Homo sapiens GN=ANXA1 PE=1 SV=2 - [ANXA1_HUMAN] | 61.73 | 6.94 | 0.14021179 | 346 | 38.68998096 | 7.020019531 |
| Q9HAV4 | Exportin-5 OS=Homo sapiens GN=XPO5 PE=1 SV=1 - [XPO5_HUMAN] | 1044.982069 | 18.11 | 0.131754745 | 1204 | 136.2221535 | 5.795410156 |
| P35527 | Keratin, type I cytoskeletal 9 OS=Homo sapiens GN=KRT9 PE=1 SV=3 - [K1C9_HUMAN] | 24543.45409 | 61.8 | 0.114460904 | 623 | 62.02681761 | 5.236816406 |
| Q5VYK3 | Proteasome-associated protein ECM29 homolog OS=Homo sapiens GN=ECM29 PE=1 SV=2 - [ECM29_HUMAN] | 536.0126322 | 6.29 | 0.113269139 | 1845 | 204.1603993 | 7.122558594 |
| P23229 | Integrin alpha-6 OS=Homo sapiens GN=ITGA6 PE=1 SV=5 - [ITA6_HUMAN] | 76.99 | 1.42 | 0.111400292 | 1130 | 126.526188 | 6.609863281 |
| O15533 | Tapasin OS=Homo sapiens GN=TAPBP PE=1 SV=1 - [TPSN_HUMAN] | 98.8406285 | 6.92 | 0.096965074 | 448 | 47.59567689 | 7.151855469 |
| P30508 | HLA class I histocompatibility antigen, Cw-12 alpha chain OS=Homo sapiens GN=HLA-C PE=2 SV=2 - [1C12_HUMAN] | 318.7879743 | 24.04 | 0.092760619 | 366 | 40.86014693 | 6.303222656 |
| Q13753 | Laminin subunit gamma-2 OS=Homo sapiens GN=LAMC2 PE=1 SV=2 - [LAMC2_HUMAN] | 572.9173652 | 13.24 | 0.082361831 | 1193 | 130.8916845 | 6.188964844 |
| P05120 | Plasminogen activator inhibitor 2 OS=Homo sapiens GN=SERPINB2 PE=1 SV=2 - [PAI2_HUMAN] | 247.4530468 | 18.55 | 0.08155557 | 415 | 46.56614894 | 5.630371094 |
| P13647 | Keratin, type II cytoskeletal 5 OS=Homo sapiens GN=KRT5 PE=1 SV=3 - [K2C5_HUMAN] | 6373.309817 | 37.8 | 0.065049408 | 590 | 62.33997999 | 7.737792969 |
| P35908 | Keratin, type II cytoskeletal 2 epidermal OS=Homo sapiens GN=KRT2 PE=1 SV=2 - [K22E_HUMAN] | 23379.67284 | 68.86 | 0.059593403 | 639 | 65.39322034 | 8.001464844 |
| O14787 | Transportin-2 OS=Homo sapiens GN=TNPO2 PE=1 SV=3 - [TNPO2_HUMAN] | 331.843763 | 3.9 | 0.058455813 | 897 | 101.3222349 | 5.008300781 |
| O60443 | Non-syndromic hearing impairment protein 5 OS=Homo sapiens GN=DFNA5 PE=1 SV=2 - [DFNA5_HUMAN] | 83.99 | 2.22 | 0.056966691 | 496 | 54.52035395 | 5.173339844 |
| Q07065 | Cytoskeleton-associated protein 4 OS=Homo sapiens GN=CKAP4 PE=1 SV=2 - [CKAP4_HUMAN] | 704.3510698 | 23.59 | 0.052131765 | 602 | 65.98273486 | 5.922363281 |
| P13645 | Keratin, type I cytoskeletal 10 OS=Homo | 45735.79777 | 66.44 | 0.011754191 | 584 | 58.79169631 | 5.211425781 |

| | | | | | | | |
|--------|--|-------------|-------|--|------|-------------|-------------|
| | sapiens GN=KRT10 PE=1 SV=6 - [K1C10_HUMAN] | | | | | | |
| Q7Z5M8 | Abhydrolase domain-containing protein 12B OS=Homo sapiens GN=ABHD12B PE=2 SV=1 - [AB12B_HUMAN] | 33.76572807 | 1.66 | | 362 | 40.74995339 | 8.279785156 |
| Q562R1 | Beta-actin-like protein 2 OS=Homo sapiens GN=ACTBL2 PE=1 SV=2 - [ACTBL_HUMAN] | 1655.274818 | 15.69 | | 376 | 41.97596926 | 5.592285156 |
| P60709 | Actin, cytoplasmic 1 OS=Homo sapiens GN=ACTB PE=1 SV=1 - [ACTB_HUMAN] | 4097.889283 | 51.73 | | 375 | 41.70973209 | 5.478027344 |
| P12236 | ADP/ATP translocase 3 OS=Homo sapiens GN=SLC25A6 PE=1 SV=4 - [ADT3_HUMAN] | 734.7241811 | 30.54 | | 298 | 32.84519063 | 9.744628906 |
| P02768 | Serum albumin OS=Homo sapiens GN=ALB PE=1 SV=2 - [ALBU_HUMAN] | 21451.32838 | 10.84 | | 609 | 69.32149882 | 6.277832031 |
| Q10567 | AP-1 complex subunit beta-1 OS=Homo sapiens GN=APIB1 PE=1 SV=2 - [APIB1_HUMAN] | 33.6 | 2.21 | | 949 | 104.5700772 | 5.059082031 |
| Q9UBB4 | Ataxin-10 OS=Homo sapiens GN=ATXN10 PE=1 SV=1 - [ATX10_HUMAN] | 83.53 | 2.32 | | 475 | 53.45481763 | 5.249511719 |
| Q494V2 | Coiled-coil domain-containing protein 37 OS=Homo sapiens GN=CCDC37 PE=2 SV=1 - [CCD37_HUMAN] | 35.79 | 1.15 | | 611 | 71.07315416 | 7.107910156 |
| P81605 | Dermcidin OS=Homo sapiens GN=DCD PE=1 SV=2 - [DCD_HUMAN] | 745.1835552 | 20 | | 110 | 11.27682818 | 6.536621094 |
| Q99615 | DnaJ homolog subfamily C member 7 OS=Homo sapiens GN=DNAJC7 PE=1 SV=2 - [DNJC7_HUMAN] | 41.88 | 2.63 | | 494 | 56.40467488 | 6.961425781 |
| Q96JB1 | Dynein heavy chain 8, axonemal OS=Homo sapiens GN=DNAH8 PE=1 SV=2 - [DYH8_HUMAN] | 29.17 | 0.16 | | 4490 | 514.3348892 | 6.315917969 |
| Q9NZ08 | Endoplasmic reticulum aminopeptidase 1 OS=Homo sapiens GN=ERAP1 PE=1 SV=3 - [ERAP1_HUMAN] | 116.4604251 | 1.38 | | 941 | 107.1662625 | 6.455566406 |
| Q01469 | Fatty acid-binding protein, epidermal OS=Homo sapiens GN=FABP5 PE=1 SV=3 - [FABP5_HUMAN] | 80.82529169 | 13.33 | | 135 | 15.15455203 | 7.005371094 |
| Q5D862 | Filaggrin-2 OS=Homo sapiens GN=FLG2 PE=1 SV=1 - [FILA2_HUMAN] | 95.48 | 0.5 | | 2391 | 247.9278232 | 8.309082031 |
| P09211 | Glutathione S-transferase P OS=Homo sapiens GN=GSTP1 PE=1 SV=2 - [GSTP1_HUMAN] | 62.08 | 5.24 | | 210 | 23.34102375 | 5.643066406 |
| P11166 | Solute carrier family 2, facilitated glucose transporter member 1 OS=Homo sapiens GN=SLC2A1 PE=1 SV=2 - [GTR1_HUMAN] | 132.4533333 | 3.05 | | 492 | 54.04853842 | 8.719238281 |
| Q16777 | Histone H2A type 2-C OS=Homo sapiens GN=HIST2H2AC PE=1 SV=4 - [H2A2C_HUMAN] | 160.4766667 | 22.48 | | 129 | 13.979842 | 10.90185547 |
| P0C0S5 | Histone H2A.Z OS=Homo sapiens GN=H2AFZ PE=1 SV=2 - [H2AZ_HUMAN] | 55.91 | 22.66 | | 128 | 13.54455269 | 10.57958984 |
| P69905 | Hemoglobin subunit alpha OS=Homo sapiens GN=HBA1 PE=1 SV=2 - [HBA_HUMAN] | 184.9866667 | 8.45 | | 142 | 15.24792627 | 8.675292969 |
| P02042 | Hemoglobin subunit delta OS=Homo sapiens GN=HBD PE=1 SV=2 - [HBD_HUMAN] | 236.2544444 | 6.8 | | 147 | 16.04529062 | 8.045410156 |
| Q86Y56 | HEAT repeat-containing protein 2 OS=Homo sapiens GN=HEATR2 PE=1 SV=4 - [HEAT2_HUMAN] | 112.8710609 | 3.86 | | 855 | 93.46206862 | 6.417480469 |
| Q9ULT8 | E3 ubiquitin-protein ligase HECTD1 OS=Homo sapiens GN=HECTD1 PE=1 SV=3 - [HECD1_HUMAN] | 46.89 | 0.46 | | 2610 | 289.2030834 | 5.351074219 |
| Q86YZ3 | Hornerin OS=Homo sapiens GN=HRNR PE=1 SV=2 - [HORN_HUMAN] | 47.96905986 | 3.89 | | 2850 | 282.2276372 | 10.03759766 |
| Q8NI35 | InaD-like protein OS=Homo sapiens GN=INADL PE=1 SV=3 - [INADL_HUMAN] | 50.73229438 | 0.33 | | 1801 | 196.2474017 | 4.944824219 |
| P02533 | Keratin, type I cytoskeletal 14 OS=Homo sapiens GN=KRT14 PE=1 SV=4 - [K1C14_HUMAN] | 6276.115516 | 32.63 | | 472 | 51.52938654 | 5.160644531 |
| P08779 | Keratin, type I cytoskeletal 16 OS=Homo sapiens GN=KRT16 PE=1 SV=4 - | 4595.112807 | 36.36 | | 473 | 51.23620491 | 5.046386719 |

| | | | | | | | |
|--------|---|-------------|-------|--|------|-------------|-------------|
| | [K1C16_HUMAN] | | | | | | |
| Q7Z794 | Keratin, type II cytoskeletal 1b OS=Homo sapiens GN=KRT77 PE=2 SV=3 - [K2C1B_HUMAN] | 2973.399925 | 8.3 | | 578 | 61.86351303 | 5.985839844 |
| P04264 | Keratin, type II cytoskeletal 1 OS=Homo sapiens GN=KRT1 PE=1 SV=6 - [K2C1_HUMAN] | 44909.99234 | 57.45 | | 644 | 65.99900395 | 8.118652344 |
| P02538 | Keratin, type II cytoskeletal 6A OS=Homo sapiens GN=KRT6A PE=1 SV=3 - [K2C6A_HUMAN] | 7017.112607 | 37.41 | | 564 | 60.0082771 | 8.001464844 |
| P04259 | Keratin, type II cytoskeletal 6B OS=Homo sapiens GN=KRT6B PE=1 SV=5 - [K2C6B_HUMAN] | 8639.350598 | 35.82 | | 564 | 60.03029381 | 8.001464844 |
| Q7RTS7 | Keratin, type II cytoskeletal 74 OS=Homo sapiens GN=KRT74 PE=1 SV=2 - [K2C74_HUMAN] | 672.9641625 | 5.1 | | 529 | 57.82964422 | 7.708496094 |
| Q9Y2K7 | Lysine-specific demethylase 2A OS=Homo sapiens GN=KDM2A PE=1 SV=3 - [KDM2A_HUMAN] | 64.67540984 | 0.52 | | 1162 | 132.707543 | 7.576660156 |
| Q13136 | Liprin-alpha-1 OS=Homo sapiens GN=PPF1A1 PE=1 SV=1 - [LIPA1_HUMAN] | 77.55 | 1.25 | | 1202 | 135.6950084 | 6.290527344 |
| P61626 | Lysozyme C OS=Homo sapiens GN=LYZ PE=1 SV=1 - [LYSC_HUMAN] | 92.64 | 8.11 | | 148 | 16.52628464 | 9.158691406 |
| Q9NU22 | Midasin OS=Homo sapiens GN=MDN1 PE=1 SV=2 - [MDN1_HUMAN] | 37.38453332 | 0.13 | | 5596 | 632.4201854 | 5.681152344 |
| Q00653 | Nuclear factor NF-kappa-B p100 subunit OS=Homo sapiens GN=NFKB2 PE=1 SV=4 - [NFKB2_HUMAN] | 35.94 | 1.11 | | 900 | 96.68892937 | 6.252441406 |
| Q29RF7 | Sister chromatid cohesion protein PDS5 homolog A OS=Homo sapiens GN=PDS5A PE=1 SV=1 - [PDS5A_HUMAN] | 43.22 | 1.12 | | 1337 | 150.7343038 | 7.913574219 |
| P12273 | Prolactin-inducible protein OS=Homo sapiens GN=PIP PE=1 SV=1 - [PIP_HUMAN] | 29.74 | 5.48 | | 146 | 16.56179653 | 8.045410156 |
| Q8TF05 | Serine/threonine-protein phosphatase 4 regulatory subunit 1 OS=Homo sapiens GN=PPP4R1 PE=1 SV=1 - [PP4R1_HUMAN] | 56.75 | 2.42 | | 950 | 106.9359614 | 4.767089844 |
| Q03181 | Peroxisome proliferator-activated receptor delta OS=Homo sapiens GN=PPARD PE=1 SV=1 - [PPARD_HUMAN] | 30.58 | 1.59 | | 441 | 49.87118982 | 7.591308594 |
| P62333 | 26S protease regulatory subunit 10B OS=Homo sapiens GN=PSMC6 PE=1 SV=1 - [PRS10_HUMAN] | 69.04 | 3.86 | | 389 | 44.14510118 | 7.488769531 |
| P46782 | 40S ribosomal protein S5 OS=Homo sapiens GN=RPS5 PE=1 SV=4 - [RS5_HUMAN] | 84.93 | 7.35 | | 204 | 22.86205347 | 9.715332031 |
| P31151 | Protein S100-A7 OS=Homo sapiens GN=S100A7 PE=1 SV=4 - [S10A7_HUMAN] | 40.27 | 18.81 | | 101 | 11.46356499 | 6.770996094 |
| A6NHL2 | Tubulin alpha chain-like 3 OS=Homo sapiens GN=TUBAL3 PE=1 SV=2 - [TBAL3_HUMAN] | 423.7888983 | 9.42 | | 446 | 49.87673246 | 6.049316406 |
| P78371 | T-complex protein 1 subunit beta OS=Homo sapiens GN=CCT2 PE=1 SV=4 - [TCPB_HUMAN] | 28.13 | 2.24 | | 535 | 57.45213278 | 6.455566406 |
| P10599 | Thioredoxin OS=Homo sapiens GN=TXN PE=1 SV=3 - [THIO_HUMAN] | 240.4882861 | 12.38 | | 105 | 11.72974219 | 4.919433594 |
| P21796 | Voltage-dependent anion-selective channel protein 1 OS=Homo sapiens GN=VDAC1 PE=1 SV=2 - [VDAC1_HUMAN] | 69.93 | 3.53 | | 283 | 30.75357144 | 8.543457031 |
| Q96JF6 | Zinc finger protein 594 OS=Homo sapiens GN=ZNF594 PE=2 SV=3 - [ZNF594_HUMAN] | 44.6 | 2.6 | | 807 | 93.84681203 | 8.704589844 |

Dataset 2 Signaling Proteins

| Pname | total expression | phosphorylation | phospho-sites | Consequence at Site | references (phosphorylation) | oxidation ratio | Consequence of Oxidation | reference (oxidation) | change of activity |
|-----------|---|-----------------|---------------|---------------------|------------------------------|-----------------|--------------------------|-----------------------|--------------------|
| ROS | | | | | | | | | 0 |
| TNFR | 0.81 | | | | | | | | 0 |
| INTEGRIN | 0.2 | | | | | | | | 0 |
| IGF1R | | 7.31 | Y1135/1136 | Activate | PMID:20007139 | | | | 1 |
| EGFR | 1 | 0.4 | Y1109 | Activate | PMID22158416 | 0.638 | Activate | PMID:22158416 | 0 |
| ASK1 | 0.39 | 0.045 | S83 | Activate | PMID:11689443 | | | | 0 |
| FAK | 0.32 | | | | | | | | 0 |
| PDK1 | 1.04 | 1.06 | S241 | Activate | PMID:1061613 | | | | 1 |
| HSP90 | 1.798 | | | | | 0.969 | Inhibit | PMID:15579467 | 1 |
| PKC | 0.98 | 0.51 | S744/748 | Activate | PMID:11440359 | | | | 0 |
| MEK | 0.647 | | | | | | | | 0 |
| MYC | 1.99 | | | | | | | | 1 |
| JNK1 | 0.79 | 0.2 | T183/Y185 | Activate | PMID:533995 | | | | 0 |
| LKB1 | 1.01 | 0.4 | S428 | Activate | PMID:19858366 | | | | 0 |
| P53 | 0.58 | | | | | | | | 0 |
| STAT1 | 0.796 | 0.2 | Y701 | Activate | PMID:10071751 | | | | 0 |
| 14-3-3 | 1.007 | | | | | | | | 1 |
| 4EBP1 | | 0.84 | | | | | | | 0 |
| STAT3 | | 0.79 | Y705 | Activate | PMID:2859454 | 0.533 | Inhibit | PMID:3226362,20807804 | 1 |
| EIF4E | 1.272 | | | | | | | | 1 |
| RPS6 | | 0.66 | | | | | | | 0 |
| PTEN | 2.2 | | | | | | | | 1 |
| AKT1/3 | 0.85 | 0.13 | | | | | | | 0 |
| ROS | | | | | | | | | 0 |
| TNFR | 0.81 | | | | | | | | 0 |
| INTEGRIN | 0.2 | | | | | | | | 0 |
| IGF1R | | 7.31 | Y1135/1136 | Activate | PMID:20007139 | | | | 1 |
| EGFR | 1 | 0.4 | Y1109 | Activate | PMID22158416 | 0.638 | Activate | PMID:22158416 | 0 |
| ASK1 | 0.39 | 0.045 | S83 | Activate | PMID:11689443 | | | | 0 |
| FAK | 0.32 | | | | | | | | 0 |
| PDK1 | 1.04 | 1.06 | S241 | Activate | PMID:1061613 | | | | 1 |
| HSP90 | 1.798 | | | | | 0.969 | Inhibit | PMID:15579467 | 1 |
| PKC | 0.98 | 0.51 | S744/748 | Activate | PMID:11440359 | | | | 0 |
| MEK | 0.647 | | | | | | | | 0 |
| MYC | 1.99 | | | | | | | | 1 |
| | | | | | | | | | |
| AMPK | 0.58 | 0.12 | | | | | | | ? |
| ACC | 5.11 | 1.36 | | | | | | | |
| AKT2 | 0.61 | 0.68 | | | | | Inhibit | PMID:21670275 | ? |
| GSK3 | 0.38 | 0.39 | | | | | Inhibit | | ? |
| B-CATENIN | 1.546 | | | | | | | | ? |
| EEF2 | | 1.99 | | | | 0.554 | Inhibit | ? | ? |
| | | | | | | | | | |
| | proteins were used in training of the model | | | | | | | | |
| | proteins were used to validate the predicted values | | | | | | | | |

Dataset 3 Signaling Reactions

| | Upstream | Downstream | Regulations | | Downstream | Regulations | Upstream |
|----|----------|------------|-------------|--------------|------------|---------------|----------|
| 1 | ROS | AKT2 | 0 | 45 | AKT1/3 | GSK3-β | 1 |
| 2 | ROS | HSP90β | 0 | 46 | AKT2 | IKK | 1 |
| 3 | ROS | EGFR | 1 | 47 | AKT2 | ASK1 | 0 |
| 4 | ROS | STAT3 | 0 | 48 | AKT2 | mTOR | 1 |
| 5 | ROS | NFKB | 0 | 49 | AKT2 | GLUT4 | 1 |
| 6 | ROS | EEF2 | 0 | 50 | MEK | ERK | 1 |
| 7 | TGFR | MKK3 | 1 | 51 | P53 | AMPK | 1 |
| 8 | TGFR | MKK4 | 1 | 52 | P53 | 14-3-3 | 1 |
| 9 | TGFR | SHC | 1 | 53 | IKK | NFKB | 1 |
| 10 | TGFR | PI3K | 1 | 54 | mTOR | 4EBP1 | 0 |
| 11 | TNFR | Ras | 1 | 55 | mTOR | P70S6K | 1 |
| 12 | TNFR | NIK | 1 | 56 | mTOR | MYC | 1 |
| 13 | INSR | PI3K | 1 | 57 | ERK | EIF4E | 1 |
| 14 | IGF1R | PI3K | 1 | 58 | ERK | P70S6K | 1 |
| 15 | IGF1R | SHC | 1 | 59 | CaMKK | AMPK | 1 |
| 16 | INTEGRIN | FAK | 1 | 60 | AMPK | SREBP-1c | 0 |
| 17 | EGFR | PI3K | 1 | 61 | AMPK | mTOR | 0 |
| 18 | EGFR | SHC | 1 | 62 | AMPK | P53 | 1 |
| 19 | EGFR | JAK1/2 | 1 | 63 | AMPK | SREBP-2 | 0 |
| 20 | INFGR | JAK1/2 | 1 | 64 | AMPK | ACC | 0 |
| 21 | ASK1 | MKK3 | 1 | 65 | GSK3-β | B-CATENIN | 0 |
| 22 | ASK1 | MKK4 | 1 | 66 | GSK3-β | Snail | 0 |
| 23 | MKK4 | JNK1 | 1 | 67 | GSK3-β | MYC | 0 |
| 24 | MKK3 | P38 | 1 | 68 | 4EBP1 | EIF4E | 0 |
| 25 | PTEN | AKT1/3 | 0 | 69 | P70S6K | EEF2 | 1 |
| 26 | PTEN | AKT2 | 0 | 70 | P70S6K | RPS6 | 1 |
| 27 | PI3K | PDK1 | 1 | 71 | palmitate | AMPK | 1 |
| 28 | FAK | PI3K | 1 | 72 | SREBP-1c | FASN | 1 |
| 29 | FAK | SHC | 1 | 73 | SREBP-1c | ACC | 1 |
| 30 | SHC | Ras | 1 | 74 | PP2C | AMPK | 0 |
| 31 | JAK1/2 | P70S6K | 1 | 75 | PP2A | ACC | 1 |
| 32 | JAK1/2 | STAT1 | 1 | 76 | SREBP-2 | HMGCR | 1 |
| 33 | JAK1/2 | STAT3 | 1 | 77 | ROS | SHMT2 | 0 |
| 34 | PKC | JNK1 | 1 | 78 | ROS | PKM | 0 |
| 35 | JNK1 | P53 | 1 | 79 | MYC | CTP | 1 |
| 36 | P38 | MYC | 1 | 80 | MYC | TK1 | 1 |
| 37 | NIK | IKK | 1 | 81 | MYC | PKM | 1 |
| 38 | PDK1 | AKT1/3 | 1 | 82 | P53 | G6PD | 0 |
| 39 | PDK1 | AKT2 | 1 | 83 | P53 | PGM1 | 0 |
| 40 | HSP90β | AKT2 | 1 | 84 | P53 | PGM2 | 0 |
| 41 | Ras | PI3K | 1 | 85 | STAT1 | CH25H | 1 |
| 42 | Ras | MEK | 1 | 86 | NFKB | SOD2 | 1 |
| 43 | LKB1 | AMPK | 1 | 87 | GSK3-β | CTP | 0 |
| 44 | MYC | P53 | 1 | 1: promotion | | 0: inhibition | |

Dataset 4 Metabolites

| | Metabolites | KEGGid | Concentration(rSCC/SCC) | | Metabolites | KEGGid | Concentration(rSCC/SCC) |
|----|------------------|--------|-------------------------|-----|-------------|--------|-------------------------|
| 1 | adenosine | C00212 | 0.09 | 55 | akg | C00026 | |
| 2 | H ₂ O | C00001 | 1 | 56 | glu5sa | C01165 | |
| 3 | inosine | C00294 | 0.38 | 57 | dUMP | C00365 | |
| 4 | phosphate | C00009 | 1.52 | 58 | dhf | C00415 | |
| 5 | hypoxanthine | C00262 | 0.48 | 59 | UDP | C00015 | |
| 6 | adenine | C00147 | 2.25 | 60 | UTP | C00075 | |
| 7 | guanosine | C00387 | 0.33 | 61 | CTP | C00063 | |
| 8 | guanine | C00242 | 0.12 | 62 | cbp | C00169 | |
| 9 | xanthine | C00385 | 0.3 | 63 | g6p | C00092 | |
| 10 | r5p | C00117 | 1.54 | 64 | O2 | C00007 | |
| 11 | AMP | C00020 | 2.53 | 65 | 3sala | C00606 | |
| 12 | Glycine | C00037 | 0.74 | 66 | ppi | C00013 | |
| 13 | ATP | C00002 | 0.36 | 67 | IMP | C00130 | |
| 14 | L-Cysteine | C00097 | 0.44 | 68 | 6pgl | C01236 | |
| 15 | 5oxpro | C01879 | 0.75 | 69 | Cytidine | C00475 | |
| 16 | L-Glutamate | C00025 | 0.5 | 70 | pyr | C00022 | |
| 17 | L-serine | C00065 | 1.5 | 71 | H2O2 | C00027 | 0.74426 |
| 18 | Thymine | C00178 | 0.22 | 72 | NADPH | C00005 | 0.8386 |
| 19 | dTMP | C00364 | 1.74 | 73 | NADP | C00006 | 0.536 |
| 20 | L-ornithine | C00077 | 0.65 | 74 | o2s | C00704 | |
| 21 | putrescine | C00134 | 0.27 | 75 | 6pgc | C00345 | |
| 22 | UMP | C00105 | 1.92 | 76 | ru5p-D | C00199 | |
| 23 | L-Glutamine | C00064 | 1.1793 | 77 | ametam | C01137 | |
| 24 | citr-L | C00327 | 1.631789 | 78 | 5mta | C00170 | |
| 25 | glp | C00103 | 2.98 | 79 | NH3 | C00014 | |
| 26 | hypotaurine | C00519 | 0.68 | 80 | cyst-L | C02291 | |
| 27 | uridine | C00299 | 0.22 | 81 | hcys-L | C00155 | |
| 28 | uracil | C00106 | 0.08 | 82 | 2obut | C00109 | |
| 29 | gthrd | C00051 | 1.26 | 83 | f26bp | C00265 | |
| 30 | gthox | C00127 | 1.4 | 84 | f6p | C00085 | |
| 31 | chsterol | C00187 | 0.3 | 85 | fdp | C00354 | |
| 32 | xol25oh | C15519 | 0.8 | 86 | dhap | C00111 | |
| 33 | spermidine | C00315 | 0.51 | 87 | g3p | C00118 | |
| 34 | NH4 | C01342 | | 88 | glycolysis | C00236 | |
| 35 | r1p | C00442 | | 89 | Trx1(SS) | C00343 | |
| 36 | xanthosine | C01762 | | 90 | Trx1(SH)2 | C00342 | |
| 37 | NAD | C00003 | | 91 | Trx2(SS) | C00343 | |
| 38 | NADH | C00004 | | 92 | Trx2(SH)2 | C00342 | |
| 39 | GMP | C00144 | | 93 | Prx1(SH)2 | C00000 | |
| 40 | prpp | C00119 | | 94 | Prx1(SOH) | C00000 | |
| 41 | urate | C00366 | | 95 | Prx1(SS) | C00000 | |
| 42 | glucys | C00669 | | 96 | Prx1(SO2H) | C00000 | |
| 43 | ADP | C00008 | | 97 | Prx3(SH)2 | C00000 | |
| 44 | pep | C00074 | | 98 | Prx3(SOH) | C00000 | |
| 45 | Cys-Gly | C01419 | | 99 | Prx3(SS) | C00000 | |
| 46 | gluala | C03740 | | 100 | Prx3(SO2H) | C00000 | |
| 47 | ala-L | C00041 | | 101 | Grx1(SS) | C00000 | |
| 48 | 3php | C03232 | | 102 | Grx1(SH)2 | C00000 | |
| 49 | psr-L | C01005 | | 103 | Grx2(SS) | C00000 | |
| 50 | thf | C00101 | | 104 | Grx2(SH)2 | C00000 | |
| 51 | mlthf | C00143 | | 105 | Acetyl-CoA | C00024 | |
| 52 | thymd | C00214 | | 106 | Mevalonate | C00418 | |
| 53 | 2drp | C00672 | | 107 | Squalene | C00751 | 15.14 |
| 54 | CO2 | C00011 | | | | | |

Dataset 4 Metabolic Reactions

| | EC_number | enzyme | UniprotID | Enzyme_value | Reversible? | Kc | T | Substrates | Products |
|----|------------|--------------------------|-----------|--------------|-------------|----------|--------|----------------------------|-------------------------------|
| 1 | 3.5.4.4 | ADA | P00813 | 0.01 | 0 | 1175 | 298.15 | adenosine,H2O | NH4,inosine |
| 2 | 2.4.2.1 | PNP | P00491 | | 1 | 0.0164 | 310.15 | phosphate,inosine | hypoxanthine,r1p |
| 3 | 2.4.2.1 | PNP | P00491 | | 1 | 0.063 | 310.15 | phosphate,adenosine | adenine,r1p |
| 4 | 2.4.2.1 | PNP | P00491 | | 1 | 9.26E-03 | 311.15 | phosphate,guanosine | guanine,r1p |
| 5 | 2.4.2.1 | PNP | P00491 | | 1 | 0.0156 | 311.15 | phosphate,xanthosine | xanthine,r1p |
| 6 | 5.4.2.7 | PGM2 | Q96G03 | | 1 | 26 | 311.15 | r1p | r5p |
| 7 | 3.1.3.5 | NT5C2 | P49902 | 0.674 | 0 | 176 | 311.15 | AMP,H2O | phosphate,adenosine |
| 8 | 3.1.3.5 | NT5C2 | P49902 | 0.674 | 0 | 176 | 311.15 | GMP,H2O | phosphate,guanosine |
| 9 | 1.17.1.4 | XDH | P47989 | | 1 | | | hypoxanthine,H2O,NAD | NADH,xanthine |
| 10 | 1.17.1.4 | XDH | P47989 | | 1 | | | xanthine,H2O,NAD | urate,NADH |
| 11 | 3.5.4.3 | GDA | Q9Y2T3 | | 0 | 1.50E+03 | 298.15 | guanine,H2O | NH4,xanthine |
| 12 | 6.3.2.3 | GSS | P48637 | 0.645 | 0 | | | ATP,Glycine,glucys | phosphate,ADP,gthrd |
| 13 | 3.4.11.2 | ANPEP | P15144 | | 0 | | | Cys-Gly,H2O | L-Cysteine,Glycine |
| 14 | 2.3.2.4 | GGCT | O75223 | 0.406 | 0 | | | gluala | 5oxpro,ala-L |
| 15 | 6.3.2.2 | GCLC | P48506 | | 0 | | | L-Cysteine,ATP,L-Glutamate | ADP,phosphate,glucys |
| 16 | 3.5.2.9 | OPLAH | O14841 | | 0 | | | 5oxpro,ATP,H2O | phosphate,ADP,L-Glutamate |
| 17 | 2.6.1.52 | PSAT1 | Q9Y617 | 0.517 | 0 | 0.01117 | 311.15 | pser-L,akg | L-Glutamate,3php |
| 18 | 3.1.3.3 | PSPH | P78330 | | 0 | 47.4 | 311.15 | H2O,pser-L | phosphate,L-serine |
| 19 | 2.1.2.1 | SHMT2 | P34897 | 4.015 | 0 | 14.9 | 310.15 | Glycine,m1thf,H2O | L-serine,thf |
| 20 | 2.4.2.4 | TYMP | P19971 | | 1 | | | phosphate,thymd | Thymine,2dr1p |
| 21 | 2.7.1.21 | TK1 | P04183 | 4.025 | 0 | 8700 | 298.15 | ATP,thymd | ADP,dTMP |
| 22 | 4.1.1.17 | ODC1 | P11926 | | 0 | | | L-ornithine | putrescine,CO2 |
| 23 | 2.6.1.13 | OAT | P04181 | 2.422 | 1 | 71 | 310.15 | akg,L-ornithine | L-Glutamate,glu5sa |
| 24 | 2.1.1.45 | TYMS | P04818 | | 0 | 1.30E+07 | 298.15 | dUMP,m1thf | dTMP,dhf |
| 25 | 3.6.1.6 | ENTPD5/UDPase | O75356 | | 0 | 8.90E+05 | 298.15 | UDP,H2O | phosphate,UMP |
| 26 | 6.3.4.2 | CTP | P17812 | | 0 | | | ATP,L-Glutamine,UTP | ADP,CTP,L-Glutamate,phosphate |
| 27 | 2.1.3.3 | OTC | P00480 | | 0 | 1.00E+05 | 310.15 | cbp,L-ornithine | citr-L,phosphate |
| 28 | 6.3.4.16 | CPS1 | P31327 | | 0 | 3.20E+03 | 289.15 | ATP,ATP,NH4,CO2,H2O | cbp,phosphate,ADP,ADP |
| 29 | 5.4.2.2 | PGM1 | P36871 | | 0 | 17.4 | 311.15 | g1p | g6p |
| 30 | 6.3.1.2 | GLUL | P15104 | | 0 | 1233 | 310.15 | L-Glutamate,ATP,NH4 | ADP,L-Glutamine,phosphate |
| 31 | 1.13.11.20 | CDO1 | Q16878 | | 0 | 5.34E-06 | 311.15 | L-Cysteine,O2 | 3sala |
| 32 | 4.1.1.29 | CSAD | Q9Y600 | | 1 | 4.20E-05 | 308.15 | 3sala | CO2,hypotaurine |
| 33 | 2.4.2.8 | HPRT1 | P00492 | 1.793 | 0 | 1.00E+05 | 311.15 | hypoxanthine,prpp | IMP,ppi |
| 34 | 2.4.2.8 | HPRT1 | P00492 | 1.793 | 1 | 1.00E+05 | 311.5 | guanine,prpp | GMP,ppi |
| 35 | 2.4.2.7 | APRT | P07741 | 0.882 | 0 | 2.00E+03 | 311.15 | prpp,adenine | AMP,ppi |
| 36 | 2.7.6.1 | PRPS1 | P60891 | | 1 | 28.6 | 310.15 | r5p,ATP | AMP,prpp |
| 37 | 2.7.1.20 | ADK | P55263 | 1.39 | 0 | 2080 | 298.15 | adenosine,ATP | AMP,ADP |
| 38 | 1.1.1.49 | G6PD | P11413 | 2.26 | 0 | 52 | 298.15 | g6p,NADP | 6pgl,NADPH |
| 39 | 3.5.4.5 | CDA | P32320 | | 0 | 10300 | 298.15 | Cytidine,H2O | NH4,uridine |
| 40 | 2.4.2.3 | UPP1 | Q16831 | | 1 | 0.031 | 310.15 | uridine,phosphate | uracil,r1p |
| 41 | 2.7.1.48 | UCK2 | Q9BZX2 | | 0 | 8800 | 298.15 | uridine,ATP | ADP,UMP |
| 42 | 2.7.1.40 | PKM | P14618 | 1.177 | 0 | 0.000155 | 303.15 | ATP,pyr | ADP,pep |
| 43 | 1.15.1.1 | SOD2 | P04179 | 0.233 | 0 | 1.00E+28 | 298.15 | o2s,o2s | H2O2,O2 |
| 44 | 1.11.1.6 | CAT | P04040 | 0.864 | 0 | 2.60E+15 | 298.15 | H2O2,H2O2 | H2O,O2 |
| 45 | 3.1.1.31 | PGLS | O95336 | 0.375 | 0 | 83000 | 311.15 | 6pgl,H2O | 6pgc |
| 46 | 2.4.2.9 | UPP | Q980Q4 | | 1 | 0.031 | 310.15 | UMP,ppi | uracil,prpp |
| 47 | 1.1.1.44 | PGD | P52209 | 3.49 | 0 | 0.076 | 298.15 | 6pgc,NADP,H2O | CO2,NADPH,ru5p-D |
| 48 | 5.3.1.6 | RPIA | P49247 | | 1 | 0.28 | 310.15 | r5p | ru5p-D |
| 49 | 2.5.1.16 | SRM | P19623 | | 0 | | | ametam,putrescine | 5mta,spermidine |
| 50 | 1.8.1.7 | GSR(GR) | P00390 | 0.89 | 0 | 800 | 298.15 | gthox,NADPH | gthrd,NADP |
| 51 | 4.2.1.22 | CBS | P35520 | 1.61 | 0 | 0.61 | 310.15 | L-serine,hcys-L | cyst-L,H2O |
| 52 | 4.4.1.1 | CTH(CSE) | P32929 | 0.72 | 0 | 1.7 | 310.15 | cyst-L,H2O | L-Cysteine,NH4,2obut |
| 53 | 3.1.3.46 | TIGAR induced inhibition | Q9NQ88 | 0.362 | 0 | 0.019 | 310.15 | f26bp,H2O | f6p,phosphate |
| 54 | 2.7.1.105 | PFK2 | Q9UBT0 | | 0 | | | f6p,ATP | f26bp,ADP |
| 55 | 5.3.1.9 | G9Pi | P06744 | | 1 | | | g6p | f6p |
| 56 | 2.7.1.11 | PFK1 | P16861 | | 0 | 150 | 303.15 | f6p,ATP | ADP,f6p |
| 57 | 4.1.2.13 | ALDOC | P09972 | | 0 | | | f6p | dhap,g3p |
| 58 | 1.2.1.12 | GAPD | P04406 | | 0 | | | g3p,NAD,phosphate | NADH,glycolysis |
| 59 | 1.11.1.9 | GPX1(GPx1) | P07203 | 1.06 | 0 | 0.2 | 310.15 | gthrd,gthrd,H2O2 | gthox,H2O,H2O |
| 60 | 1.8.1.9 | TXNRD1(TrxR1) | Q16881 | 1.75 | 0 | 48 | | NADPH,Trx1(SS) | NADP,Trx1(SH)2 |
| 61 | 1.8.1.9 | TXNRD2(TrxR2) | Q9NNW7 | 0.98 | 0 | 48 | | NADPH,Trx2(SS) | NADP,Trx2(SH)2 |
| 62 | 1.11.1.15 | PRDX1(Prx1) | Q06830 | 2.2 | 0 | | | Prx1(SH)2,H2O2 | Prx1(SOH),H2O |
| 63 | 1.11.1.15 | PRDX1(Prx) | Q06830 | 2.2 | 0 | | | Prx1(SOH) | Prx1(SS),H2O |

| | | | | | | | | | |
|----|------------|-------------------|--------|-------|---|---------|--------|---|---|
| | | l) | | | | | | | |
| 64 | 1.11.1.15 | PRDX1(Prx1) | Q06830 | 2.2 | 0 | | | Prx1(SOH),H2O2 | Prx1(SO2H),H2O |
| 65 | 1.11.1.15 | PRDX3(Prx3) | P30048 | 2.1 | 0 | | | Prx3(SH)2,H2O2 | Prx3(SOH),H2O |
| 66 | 1.11.1.15 | PRDX3(Prx3) | P30048 | 2.1 | 0 | | | Prx3(SOH) | Prx3(SS),H2O |
| 67 | 1.11.1.15 | PRDX3(Prx3) | P30048 | 2.1 | 0 | | | Prx3(SOH),H2O2 | Prx3(SO2H),H2O |
| 68 | 1.8.98.2 | SRXN1(Srx1) | Q9BYN0 | 0.37 | 0 | | | Prx1(SO2H),ATP,gthrd,gthrd | Prx1(SOH),ADP,phosphate,gthox |
| 69 | 1.8.98.2 | SRXN1(Srx1) | Q9BYN0 | 0.37 | 0 | | | Prx3(SO2H),ATP,gthrd,gthrd | Prx3(SOH),ADP,phosphate,gthox |
| 70 | 0.0.0.0 | TXN(Trx1) | P10599 | 0.69 | 0 | | | Trx1(SH)2,Prx1(SS) | Trx1(SS),Prx1(SH)2 |
| 71 | 0.0.0.0 | TXN2(Trx2) | Q99757 | 1.22 | 0 | | | Trx2(SH)2,Prx3(SS) | Trx2(SS),Prx3(SH)2 |
| 72 | 1.1.1.34 | HMGCR | P04035 | | 0 | | 310.15 | Acetyl-CoA,NADPH | Mevalonate,NADP |
| 73 | 2.5.1.21 | Squalene synthase | P37268 | 1.8 | 0 | | 310.15 | Mevalonate,ATP,ATP,ATP,NADPH | Squalene,ADP,ADP,ADP,NADP |
| 74 | 0.0.0.0 | XXX | XXX | | 0 | | 310.15 | Squalene, NADPH,NADPH,NADPH,NADPH, NADPH,NADPH,NADPH,NADPH, NADPH,NADPH,NAD,NAD,NAD,NAD,NAD,NAD | chsterol,NADH,NA DH,NADH,NADH, NADH,NADH,NA DP,NADP,NADP,N ADP,NADP,NADP, NADP,NADP,NAD P,NADP,NADP,NA DP,NADP,NADP |
| 75 | 1.11.1.15 | Prx6 | P30041 | 1.535 | 0 | 3 x 106 | | gthrd,gthrd,H2O2 | gthox,H2O,H2O |
| 76 | 1.14.99.38 | CH25H | Q95992 | | 0 | | | chsterol,NADPH,O2 | xo125oh,NADP,H2 O |

Jade T. Moore, PhD

Medical Center Blvd, NRC 239 · Winston-Salem, NC 27157 ·
jadmims@wakehealth.edu

EDUCATION

Wake Forest School of Medicine, Winston-Salem, NC, May 2017

Howard University, Washington, DC, Bachelor of Science in Biology, *magna cum laude*, May 2011

RESEARCH EXPERIENCE

Wake Forest School of Medicine, Winston-Salem, NC

Graduate Research, Principal Investigator: Cristina M. Furdui, May 2013 – May 2017

National Institute of Health, National Cancer Institute, Gaithersburg, MD

Cancer Research Intern, Principal Investigator: Mike Emmert-Buck, May 2009 – May 2010

RELATED EXPERIENCE

Association of University Technology Manager Technology Transfer Career Transition Training Program

Burroughs Wellcome Fund AUTM Transition Scholar, September 2016 – August 2017

- Training: AUTM's **TOOLS Course** – Patents, Value Proposition, Jointly Owned IP, Anatomy of a License agreement and **Essentials Course** – Evaluating Invention Disclosures, Valuation, Marketing, Negotiations

Wake Forest Innovations, Winston-Salem, NC

Technology Innovation & Commercialization Intern, September 2015 – December 2017

Winston-Salem State University, Winston-Salem, NC

Teaching Assistant, fall 2015

GRANTS

Integrative Lipid Metabolism, Inflammation and Chronic Diseases Training Grant, National Institute of Health, July 2015 – July 2017

Pre-Doctoral Fellowship in Structural and Computational Biophysics, July 2013 – July 2015

Ruth L. Kirschstein National Research Service Award, National Institute of Health

HONORS & DISTINCTIONS

Scholar-in-Training Travel Award, Radiation Research Society Conference, 2016

Co-Chair of Gordon Research Seminar, Thiol-Based Redox Regulation and Signaling, Stowe, VT, 2016

Molecular Medicine & Translational Science Travel Award, 2016

Scholar-in-Training Travel Award, Radiation Research Society Conference, 2015

Scholar-in-Training Travel Award, Radiation Research Society Conference, **2014**

Gordon Research Conference Travel Award, Thiol-Based Redox Regulation and Signaling Seminar, **2014**

Graduate Symposium Three Minute Thesis Finalist, Wake Forest School of Medicine, **2014**

SERVICE & LEADERSHIP

Winston Salem State University Scholarship Day Poster Judge, April 2015 & 2016

Geeks-N-Taps Advisory Board, December 2014 – present

PROFESSIONAL MEMBERSHIPS

Member, American Association for the Advancement of Science, **2016**

Member, Radiation Research Society, **2014**

Member, National Institute of Science, **2010**

SKILLS/TRAININGS

- Mammalian Cell Culture; Stable Isotope Labeling of Amino Acids in Cell Culture and In-Gel/Solution Digestion of Proteins to Detect by Mass Spectrometry; Fluorescence and Confocal Microscopy; Western Blot; Isolation of Cellular Compartments using Ultracentrifugation; Cell Survival Assays (i.e. Clonogenic, SR B, and MTT Assay); Flow Cytometry; Transfection (i.e. chemical based and electroporation); Seahorse; Immunohistochemistry and H&E staining;
- **Computer Skills:** Proficient in MS Office, Adobe Photoshop, Sigma Plot, Endnote, FlowJo, Ingenuity Pathway Analysis
- **Other:** primary technology evaluations, material transfer agreements, non-confidential disclosures

PRESENTATIONS

Oral Presentations

“Integration of Redox-Regulated Signaling and Metabolism in Head and Neck Cancer”, Gordon Research Conference – Thiol-Based Redox Regulation and Signaling Conference, Stowe, VT, 2016

“A Redox-Centered View of Radiation Resistance in Head and Neck Cancer”, Gordon Research Conference – Thiol-Based Redox Regulation and Signaling Seminar and Conference, Spain, 2014

Poster Presentations

“Role of Reactive Oxygen Species and Lipid Rafts in Head and Neck Cancer Treatment”, Radiation Research Society Conference, Weston, FL, 2015

“Integrated “omics” Approach to Discover Therapies for Radiation Resistant Head and Neck Cancer.”, Radiation Research Society Conference, Las Vegas, NV 2014

“A Redox-Centered View of Radiation Resistance in Head and Neck Cancer”, Gordon Research Conference – Thiol-Based Redox Regulation and Signaling Conference, Spain, 2014

PEER-REVIEWED PUBLICATIONS

Swanner J., **Mims J.**, Akman S., Furdui C.M., Torti S., Carroll D., Singh R. (2015) “Differential Cytotoxic and Radiosensitizing Effects of Silver Nanoparticles on Triple-Negative Breast Cancer and Non-Triple Negative Breast Cells”. *Int J Nanomedicine*. 10:3937-53

Chen X., Liu L., **Mims J.**, Punska E.C., Williams K.E., Zhao W. Arcaro K.F., Tsang A.W., Zhou X., Furdui C.M. (2015) “Analysis of DNA Methylation and Gene Expression in Radiation Resistant Head and Neck Tumors”. *Epigenetics*. 10(6):545-61.

Mims J., Bansal N., Bharadwaj M.S., Chen X., Molina A.J., Tsang A.W., Furdui C.M. (2015) “Energy Metabolism in a Matched Model of Radiation Resistance for Head and Neck Squamous Cell Cancer”. *Radiat Res*. 2015; 183(3):291-304.

Mims J.*, Bansal N.*, Kuremsky J.G., Olex A.L., Zhao W., Yin L., Wani R., Qian J., Center B., Marrs G.S., Porosnicu M., Fetrow J.S., Tsang A.W., **Furdui C.M. (2014)** “Broad Phenotypic Changes Associated with Gain of Radiation Resistance in HNSCC”. *Antioxid Redox Signal*. 21(2):221-36.*authors contributed equally